Exploration of complex environments by microorganisms : application to motile E. coli under confinement and penetration of a gut mucus barrier

Renaud Baillou

Thèse de doctorat de RENAUD BAILLOU

au Laboratoire de Physique et Mécanique des Milieux Hétérogènes

sous la direction d'Éric Clément

et codirection de Karine Clément - Nutriomics, Pitié-Salpêtrière, SU

Programme doctoral interdisciplinaire IPV : Interface Pour le Vivant

École Doctorale n°564 : Physique en Ile-de-France

Exploration of complex environments by microorganisms : application to motile *E. coli* under confinement and penetration of a gut mucus barrier

Directeur du jury : Maria Barbi - Sorbonne-Université, LPTMC
Rapporteur : Charles Baroud - Institut Pasteur and Ecole Polytechnique, LadHyX
Rapporteur : Éric Grelet - Université de Bordeaux, CRPP
Examinateur : Marianne Grognot - Uniklinik RWTH Aachen, IMM
Examinateur : Muriel Mercier-Bonin - INRAE Toulouse, Toxalim
Invité : Fernando Peruani - Université de Cergy-Pontoise, LPTM

February 16, 2024

Remerciements

Trois années de thèse, c'est à la fois une période longue et parsemée de difficultés. C'est aussi une période très riche, dont le quotidien est tout sauf monotone et qui, finalement, passe à un rythme fou.

Je tiens en premier lieu à remercier Eric, pour toute la passion et le savoir qu'il transmet au quotidien. Son suivi assidu, plein de créativités, et son sens des responsabilités ont été très bénéfiques pour m'aider à surmonter les doutes et les épreuves. Sa vision de la recherche et ses prises de position m'ont beaucoup questionné et apporté dans mon développement scientifique. Je remercie les autres personnes qui ont participé à la relecture de cette thèse, d'abord dans le laboratoire : Philippe B, Lara et Guillaume puis tous les membres du jury dont les remarques ont été précieuses pour finaliser le manuscrit. Je tiens à souligner l'excellence des retours écrits de mes rapporteurs. Mes partenaires de laboratoire ensuite, de tous horizons : Hector, Guillaume, Changsong, Peixin, Benja, Alex, Andrew, Solène, Jeanne... Au delà de l'entraide pour les manips, partager et maintenir une salle de laboratoire dans un état praticable n'est pas une mince affaire et chacun y a mis du sien, que ce soit pour la propreté ou la gestion des stocks. Une équipe internationale jusque dans les anti-bactériens, du Pisco au Baijiu. Une mention spéciale pour Thierry avec qui j'ai lutté sans relâche pour débogger et dépasser les limitations du système de tracking, c'était très prenant ! Merci aussi à mes collègues du côté biologie : Marta, experte en charcuterie, et Tiphaine, qui ne pense qu'à manger des crêpes ! Nos échanges, encadrés par Karine, m'ont permis de mettre un pied dans l'univers passionnant de la biologie.

Les nombreux évènements conviviaux auront largement contribué à mon insertion dans le laboratoire, avec notamment le PMM'oucHes et le Burger Quiz génial de Roméo ou encore le moulin d'Andé et la mémorable session de contradance de Stéphane. Un remerciement particulier pour Magdalena et Chloé, pour les folies aux Vinaigriers, et Juan, maitre du barbecue et blagueur de tous les jours, et leur entrain beaucoup trop prononcé pour les tournées de shooters ! Je remercie aussi Pierre-Ewen, Nathan J, Manon Q, Samantha, Alexis, José, Evelyne, Maud et ceux que j'oublie, pour leur bienveillance et leur sympathie. Une pensée pour Jules et Nathan qui se sont un peu trop illustrés à mon pot de thèse ! Enfin, un grand merci à Damien, Philippe P, Fred et Claudette qui assurent avec brio la cohésion et la bonne atmosphère au laboratoire.

Mes années au PMMH ont aussi signé un important retour au sport : d'abord porté par Mathieu et son nom d'équipe douteux "PhDK", puis marqué par la préparation au marathon de Paris avec Vincent, la course en équipe avec notamment Magdalini et Anumita, les sessions natation du samedi matin avec la bienveillance et la passion du triathlon de Gatien, et les sorties vélos en Chevreuse avec Francisco, Antoine, Guillaume, Philippe B, Ramiro ainsi que les nombreux futsal en compagnie de mon voisin de bureau Lars, Zhibo, Joo-Won... qui me laisseront beaucoup de souvenirs.

Je remercie finalement ma famille et mes amis de longue date pour leur soutien sans faille depuis tant d'années.

Résumé en français / French summary

Cette thèse s'intéresse à la motilité de micronageurs bactériens (E. coli) dans deux conditions physiologiquement importantes : premièrement dans le cas d'une géométrie confinée entre deux surfaces parallèles, puis dans du mucus intestinal d'origine animale.

Le premier chapitre présente le contexte biophysique de la thèse, dans lequel les problématiques physiques de la matière active dans les environnements complexes sont reliées aux problématiques biologiques et médicales d'infections bactériennes à travers le mucus intestinal.

L'omniprésence des microorganismes, que ce soit dans les océans, dans les sols ou dans le système digestif d'autres êtres vivants est présenté ainsi que les différents mécanismes qu'ils utilisent pour se propager et coloniser de nouveaux territoires. Le lien historique entre les microorganismes et les avancées médicales sont retracées au travers des plus grandes découvertes.

Les différentes problématiques de la matière active en interaction avec des environnements d'une certaine complexité, au sens large, ainsi que la complémentarité entre physique et biologie dans ce domaine, sont discutées succinctement, avant d'ouvrir la problématique principale de la thèse : "les propriétés géométriques et mécaniques de la barrière de mucus, qui tapisse les parois de l'intestin, sont-elles des éléments-clés dans la compréhension des infections bactériennes qui peuvent y avoir lieu, dont l'importance de la motilité bactérienne est de plus en plus attestée dans de récentes études". D'éventuelles brèches dans la barrière de mucus ainsi que les propriétés structurelles du mucus (un réseau enchevêtré de protéines) sont rapportées, qui sont à la base des deux études expérimentales développées dans cette étude.

Dans le second chapitre, les propriétés de nage des microorganismes, ainsi que leurs processus d'exploration sont introduits. Un intérêt spécifique est dédié à Escherichia coli, cette bactérie largement étudiée par les microbiologistes, qui est le microorganisme modèle que nous utiliserons.

Celle-ci se compose principalement d'un corps ellipsoidal d'environ 2 micromètres de long pour 1 micromètre de large sur lequel est implanté typiquement entre 2 et 6 flagelles d'une dizaine de micromètres, disposés de façon aléatoire. Ces flagelles ont une forme hélicoïdale et leur rotation, qui conduit à une propulsion d'environ 20 à 30 microns par seconde, est assurée par un moteur flagellaire qui fait le lien entre le corps et le flagelle. Ce moteur peut alterner des phases de rotation dans le sens horaire et antihoraire, ce qui conduit à des différences dans la cinématique de la bactérie.

La nage des microorganismes est ensuite introduite sous le spectre de l'hydrodynamique. De manière importante, le nombre de Reynolds qui régit la mécanique des fluides est très petit pour les micronageurs. Dans ce régime, les effets inertiels n'existent pas contrairement au monde dans lequel nous sommes habitués à évoluer. L'hydrodynamique de la propulsion des micronageurs est bien comprise et classifiés en deux catégories : les "pushers" tels qu'Escherichia coli dont le faisceau hélicoïdal de flagelles pousse le fluide derrière lui, et les "pullers" tels que la microalgue modèle Chlamydomonas reinhardtii qui tirent le fluide qui leur fait face. Un modèle simple composé d'un corps sphérique et d'une hélice, une version simplifiée d'E. coli, permet ensuite de mettre en équation les concepts de l'hydrodynamique à bas Reynolds. Le micronageur est un système sur lequel les résultantes des forces et des couples sont nulles et le couplage entre la cinématique et les forces mises en jeu se font au travers d'une matrice de résistance. Un modèle reliant le couple du moteur à sa vitesse de rotation permet de fermer les équations. Des questions plus actuelles de nage dans les fluides complexes sont ensuite traitées dans une revue de littérature internationale. Elle traite de différentes récentes avancées, principalement d'ordre expérimental et principalement avec E. coli, qui ont eu lieu dans des fluides viscoelastiques de différentes natures : dans les fluides à seuil, un couple est nécessaire pour enclencher un

mouvement. Dans les fluides rhéofluidifiants, la rotation rapide du flagelle entraîne localement une diminution de la viscosité. Dans les billes d'hydrogels, la bactérie peut se retrouver bloquée dans un "cul-de-sac" et doit prendre le temps de se réorienter pour reprendre sa nage... La partie hydrodynamique se termine sur les interactions avec une surface : il résulte un alignement de la bactérie avec la surface, qui l'empêche de s'échapper, ainsi qu'un mouvement qui n'est plus en ligne droite, mais circulaire.

Le processus stochastique de "run & tumble" est ensuite décrit : une séquence de lignes droites interrompues par des réorientations. Le déplacement quadratique moyen (MSD) qui en résulte est alors balistique aux temps courts puis diffusif aux temps longs. Lorsque tous les flagelles tournent dans le sens antihoraire, les flagelles s'assemblent hydrodynamiquement, formant un faisceau appelé "bundle", et la bactérie se déplace en ligne droite, ce qu'on appelle un "run". Le processus de réorientation, appelé "tumble", résulte d'un changement de sens de rotation d'un flagelle (du sens antihoraire à horaire). Lorsque le flagelle reprend son sens de rotation initial (antihoraire), un nouveau "run" prend place. Un formalisme mathématique, analogue à l'étalement spatial d'une chaîne à articulations libres, est ensuite introduit pour calculer les quantités statistiques d'un tel processus, spécialement le coefficient de diffusion, qui dépend notamment des deux premiers moments de la distribution des longueurs de "run". Le modèle de variabilité comportementale ("BV model"), qui sera la base de la modélisation du chapitre suivant, est ensuite présenté. Dans ce modèle, la large distribution des temps de run observée dans des expériences passées est imputée, non pas à une variabilité phénotypique, mais aux fluctuations d'une variable interne qui contrôle "l'humeur" de la bactérie : selon son "humeur", la bactérie enclenche des réorientations plus ou moins fréquemment. Ce modèle a par exemple permis d'expliquer la distribution log-normale des temps de résidence à la surface lors d'une précédente étude.

Le troisième chapitre est la première étude expérimentale de cette thèse : l'exploration bactérienne dans un fluide sous confinement.

Une suspension bactérienne est prise en sandwich entre deux lames de verre séparées par une distance choisie, qu'on fera varier entre 50 et 220 microns pour évaluer son impact sur les propriétés de transport des bactéries. Les bactéries sont suivies par un système de tracking Lagrangian conçu au laboratoire : la lame de microscope est déposée sous microscope, sur une plate-forme motorisée dans les trois directions de l'espace. Il est alors possible de sélectionner une bactérie et le dispositif se met alors à la suivre en focus automatiquement. Il est ainsi possible d'obtenir des trajectoires individuelles 3D de bactéries de plusieurs centaines de secondes, ainsi que la visualisation de son corps et de ses flagelles pendant le suivi. Un inconvénient du tracking Lagrangian, en comparaison à un tracking Eulérien (vue fixe), est de ne pouvoir suivre qu'une bactérie à la fois, rendant fastidieux l'obtention de statistiques.

Nous étudions dans un premier temps des bactéries à la surface de lame de verre. Nous utilisons pour ce cas des bactéries mutantes, dont le gène responsable pour les "tumbles" a été supprimé. Ces bactéries, dites "smooth-swimmer", restent ainsi très longtemps à la surface. Les trajectoires observées à la surface sont circulaires et le centre de leur orbite se déplace progressivement dans le temps, décrivant un processus diffusif. Une théorie simple permet, à partir de la mesure des propriétés cinématiques de la nage (la vitesse de nage, le rayon de gyration et le coefficient de diffusion rotationnel) de prédire le coefficient de diffusion translationnel, mesurable directement à partir du déplacement quadratique moyen.

Les paramètres cinématiques d'un individu sont constants au cours du temps, mais il existe une grande variabilité au sein d'une population. Nous tirons alors profit de notre dispositif de "tracking", qui permet aussi de visualiser l'objet suivi, pour caractériser l'anatomie de chaque bactérie et la mettre en lien avec ses propriétés de nage. En plus de la longueur du corps et de la longueur du faisceau de flagelles, une méthode est élaborée pour déterminer le nombre de

flagelles. Les résultats sont les suivants : Le coefficient de diffusion rotationnel est expliqué par la taille du corps et des flagelles dans une simple théorie brownienne. La vitesse de nage est indépendante du nombre de flagelles. Finalement, un scénario basé sur le nombre de flagelles et leur disposition est proposé pour expliquer les rayons de gyration. Dans ce scénario les flagelles repoussent le corps de la surface par encombrement stérique, réduisant l'interaction hydrodynamique avec la surface. Ceci expliquerait la tendance du rayon de gyration à croitre avec le nombre de flagelles, tandis que la disposition aléatoire sur le corps explique la variabilité observée à nombre de flagelles fixé.

Nous passons alors au coeur de l'étude. Des bactéries, qui cette fois peuvent déclencher des "tumbles", sont suivies entre deux plaques parallèles, alternant des phases de nage dans le "bulk" avec des phases de nage à la surface. La distance entre les plaques est variée de quelques dizaines à plusieurs centaines de microns, et une centaine de trajectoires bactériennes de plusieurs centaines de secondes sont mesurées. Nous mesurons les paramètres cinématiques ainsi que le coefficient de diffusion latérale qui traduit l'exploration de la bactérie. Nous montrons que l'exploration latérale diminue avec la hauteur de confinement et augmente avec le rayon de gyration. Les temps de résidence, à la fois aux surfaces et dans le bulk, sont aussi mesurés et décrits. Un modèle numérique basé sur le "BV model", calibré dans une précédente étude, et complété par des règles simplistes à la surface, reproduit quantitativement l'ensemble des résultats expérimentaux, sans paramètre ajustable.

Nous identifions deux effets du confinement sur les propriétés de transport. D'abord, le confinement contrôle la fraction du temps que la bactérie passe aux surfaces. Comme la diffusion globale est principalement une moyenne pondérée de la diffusion dans le bulk et à la surface, alors plus l'environnement est confiné, plus la diffusion à la surface est prépondérante. Dans la limite des faibles rayons de gyration, le confinement diminue la diffusion. Dans la limite des grands rayons de gyration, à l'inverse, le confinement augmente la diffusion. Le second effet provient du fait que les "runs" venant du bulk peuvent être interrompus par les surfaces. Le confinement induit alors des "runs" plus petits dans le bulk en moyenne, ce qui entraine une diminution de la diffusion dans le bulk, qui diminue finalement la diffusion globale.

Le quatrième chapitre est la seconde étude expérimentale de cette thèse : la pénétration bactérienne dans une barrière de mucus.

Le microbiote intestinal, composé d'environ 10^{14} bactéries, soit plus que le nombre de nos cellules, est introduit au sein du système digestif. Ces bactéries peuvent être bénéfiques en favorisant la digestion de certains aliments, mais d'autres sont des pathogènes qui peuvent envahir nos cellules. Nos intestins sont munis d'une barrière biologique pour prévenir les infections bactériennes : c'est le rôle de la barrière de mucus, sécrétée par les cellules calciformes ("goblet cells") de notre paroi intestinale. Le mucus est principalement constitué d'un réseau de macromolécules appelées "mucin" qui forment un réseau enchevêtré dynamique, dont la structure est complexe. Cette barrière de mucus peut être détériorée en conditions pathologiques comme les pathologies inflammatoires de l'intestin, favorisées par des régimes alimentaires basés sur des émulsifiants très présents dans l'industrie alimentaire.

En collaboration avec une équipe de biologistes du laboratoire Nutriomics, nous avons récolté du mucus sur des intestins de cochons. Ces cochons provenaient d'une cohorte séparée en deux groupes basés sur leur alimentation. Nous avons purifié ce mucus pour éliminer au mieux les impuretés et résidus chimiques, et ainsi se concentrer sur les propriétés mécaniques du réseau de "mucin".

Le coeur de ce travail est la mise en place d'une expérience basée sur une cellule microfluidique dans laquelle une suspension bactérienne est mise en contact avec du mucus, délimité par une interface nette. Deux heures après la mise en contact, la position des bactéries est relevée : la plupart des bactéries ont migré dans le mucus et sont immobiles, pointant vers un

état stationnaire. Le profil de concentration bactérienne à travers la barrière de mucus est le suivant : un maximum est observé peu après l'interface suivi d'une décroissance exponentielle. On peut alors extraire une "longueur de pénétration" qui caractérise une "qualité du mucus". Cette mesure est complétée par des mesures optiques, caractérisée par deux tailles de structure, ainsi que par des mesures rhéologiques de courbe d'écoulement. La reproductibilité des expériences est attestée par des mesures répétées sur un cochon donné.

Six extraits de mucus purifié, provenant de cochons équitablement répartis entre les deux groupes, ont été caractérisés de cette manière. Les longueurs de pénétration sont très variables, de 200 à plus de 800 microns, indépendantes des mesures rhéologiques qui quant à elles sont toutes du même ordre de grandeur. Les mesures rhéologiques présentent des différences qualitatives : certains mucus montrent une dépendance à leur historique de cisaillement tandis que les autres en sont indépendants. Il est à noter que quatre des six échantillons testés présentent la même "longueur de pénétration" ainsi que les mêmes tailles de structure. Ces observations pointent vers une importance majeure des tailles de structure, plus que des mesures de macrorhéologie.

Un modèle heuristique est ensuite proposé pour expliquer le profil de concentration des bactéries obtenu dans le mucus dans un régime stationnaire. Dans ce modèle, les bactéries motiles diffusent dans la suspension bactérienne et dans le mucus. Cependant dans le mucus, celles-ci peuvent se retrouver piégées avec une certaine probabilité, conduisant à la décroissance exponentielle observée à travers le mucus. Le maximum observé peu après l'interface peu quant à lui provenir d'une hydratation du mucus à l'interface, diminuant localement la probabilité de piégeage, mais peut aussi être expliqué par un effet de la chimiotaxie. Une vision temporelle du processus de pénétration est nécessaire pour affiner le modèle.

Ce chapitre se termine sur une discussion dans laquelle les limitations de cette étude ainsi que des solutions sont énoncées, tel qu'un rapprochement vers des situations in vivo, l'utilisation de techniques optiques plus adaptées comme la microscopie OCT, la caractérisation des tailles du réseau de mucin par diffusion de neutrons, ou encore des mesures de microrhéologie à l'échelle des flagelles.

Le cinquième et dernier chapitre de cette thèse est dédié à l'extension des possibilités d'utilisation du tracking Lagrangien, notamment pour son utilisation dans des environnements optiquement complexes tels que nos extraits de mucus. Une nouvelle méthode est développée basée sur l'intelligence artificielle, en collaboration avec des chercheurs de l'université de Göteborg spécialiste de l'intelligence artificielle appliquée à microscopie pour la matière active. Le principe de cette méthode est d'entrainer un réseau de neurones dans le but d'associer une image à sa distance au plan focal. Une collection d'images labellisées est produite expérimentalement dans les conditions similaires aux conditions de "tracking" désirées. Une fois le réseau entrainé, il est porté sur l'ordinateur de tracking pour l'utiliser dans le cadre du suivi en temps réel. Cette méthode a été implémentée avec succès, offrant de nouvelles possibilités comme le suivi de bactéries non fluorescentes ou encore un suivi à plus haute fréquence.

Remarquablement, cette méthode a aussi porté ses fruits pour suivre des bactéries fluorescentes dans un extrait de mucus, menant à la première trajectoire Lagrangienne 3D de bactéries dans du mucus. Les propriétés de la nage dans le mucus sont différentes de celles observées dans l'eau : la vitesse est sensiblement identique mais des phases d'arrêt et des réorientations plus fréquentes apparaissent, en cohérence avec des expériences rapportées dans des fluides modèles. La bactérie s'arrête définitivement au bout de quelques dizaines de secondes, en cohérence avec une probabilité de piégeage.

Une conclusion générale est finalement proposée, rappelant les différents résultats obtenus et les principales perspectives. Les résultats principaux de cette thèse consistent en de nouvelles

mesures de la nage bactérienne en géométrie confinée et une nouvelle méthodologie pour étudier leur accumulation dans le mucus. Les résultats et les nouveaux protocoles expérimentaux enrichissent l'état de l'art dans le sujet de l'exploration bactérienne et de leur pénétration dans des fluides viscoélastiques. Ce travail ouvre de nombreuses perspectives et pourrait constituer la base de futures études.

Abstract

Microorganisms are ubiquitous on Earth. They developed self-propulsion to explore their environment and colonize new ecological niche. Some of them are pathogens and trigger inflammation when in contact with epithelial cells. While the hydrodynamical nature of their motion is rather well understood in Newtonian fluids, there is still much to understand when they interact mechanically with their environment either through the presence of geometric obstacles or stemming from the non-Newtonian nature of their swimming environments.

We perform experiments with E. coli using an in-house tracking device allowing to get bacteria trajectories while visualizing their body and flagella for long time. In relation with the medical problem of bacterial infection in the gut, we use it to understand the impact of surfaces when they explore a confined environment. Confinement slows E. coli spreading, that we rationalize with a stochastic model accounting for the complex internal dynamics from which result E. coli active reorientations. Motion at surfaces is specifically studied, and the interindividual variability observed in the swimming properties are questioned under the prism of their morphologies, especially their number of flagella.

We then turn into understanding the motion of E. coli in intestinal mucus, that is extracted from two distinct groups of piglets that are compared. After a purification process, the different samples are characterized by an original in-vitro experiment in which bacteria have penetrated a mucus barrier, from which emerges a "penetration length", and complemented by rheological and optical measurements. Different rheological signatures are observed, not linked with interindividual variability in the bacterial penetration.

To get a temporal picture of the penetration process, machine learning is used to extend the use of the Lagrangian tracking device to optically complex fluids, successfully implemented for mucus. Bacteria are shown to explore mucus ten times slower than water, and to get blocked after a few minutes.

The results and experimental protocols developed in this thesis extend the state-of-the-art on the subject of microswimmers in methodological terms, while also providing some new data on swimming patterns and penetration into viscoelastic fluids.

Table des matières

Chapter I

Bacteria in interaction with mucus : biological and physical problems

I.1 Microorganisms : invisible but ubiquitous

Microorganisms, also known as microbes, are unicellular organisms that can only be seen individually by using a microscope. Despite their small size, they account for about 20% of the total biomass [1]. The first traces of micro-organisms, found in stromatolites, date back to more than three billion years ago. These primitive life forms have colonized many territories in which they play an essential role, for instance :

- in the oceans, phytoplankton fix carbon and produce oxygen.
- in soils, soil bacteria recycle organic compounds and in symbiosis with fungi increase water and nutrient absorption of roots [2].
- in other living organisms, intestinal bacteria known as the microbiota participate in the digestive system.

Microorganisms spread passively on a macroscopic scale through water currents, winds but also through the movement of other living organisms where they settle. At the microscopic scale (their own scale) they can explore the environment passively through Brownian motion

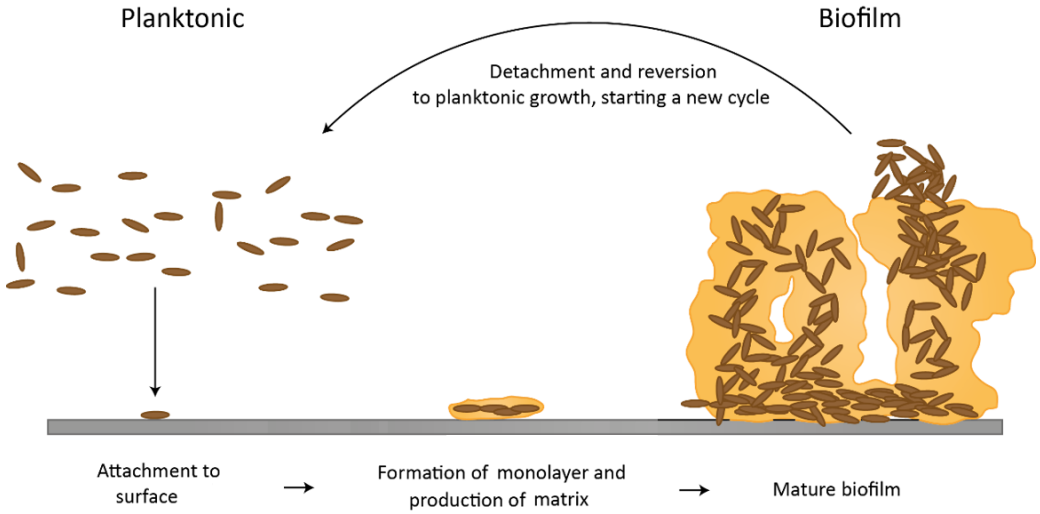

FIGURE I.1 – Life cycle of a bacterium. Bacteria explore their environment in the planktonic state until they attach to a surface where they form a protective biofilm made by replication and aggregation of other bacteria by the production of extracellular matrix. At maturation, some bacteria escape the biofilm aiming at colonizing a new place. Adapted from [3].

but some species have developed a more efficient way to discover their ecological niche : an active propulsion mechanism [4]. They can use this active propulsion to explore their environment in the "planktonic" state while they can also form dense static aggregates called "biofilms" to colonize it (see figure I.1).

A brief historic is depicted in figure I.2 : humans have suspected the existence of microorganisms only since the second half of the 17th century and the observations of Antoni van Leeuwenhoek in a microscope that he personally designed. Louis Pasteur published his seminal work on spontaneous generation in 1861. In 1885 he developed the rabies vaccine [5], while its German rival Robert Koch isolated the bacterium responsible for tuberculosis in 1882 [6]. Together, they definitively brought the field of microbiology into the realm of modern medicine. At the same time, the pediatrician Theodor Escherich noted the appearance of rod-shaped microorganisms ("bacilli") in the stools of diarrheic newborns. This is the discovery of Escherichia coli, bacteria that will become a reference model for fundamental research in microbiology.

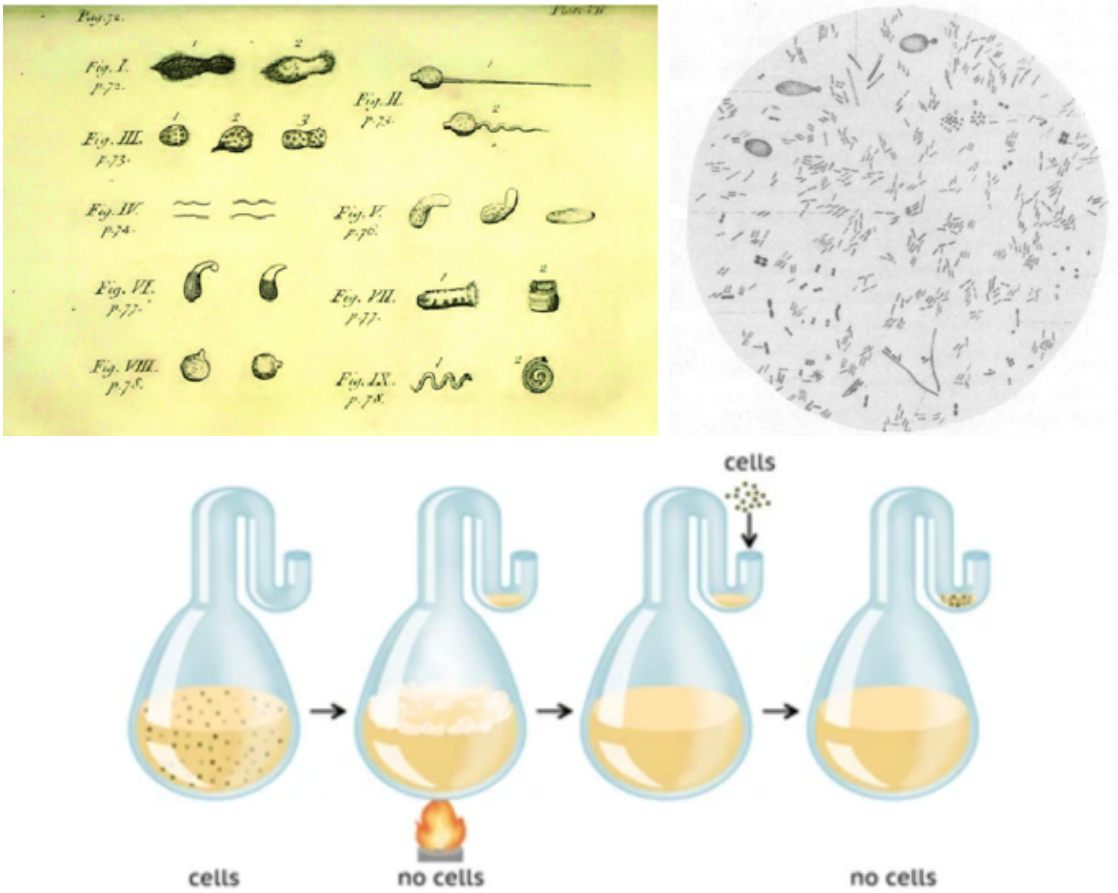

FIGURE I.2 – Key discoveries in the early age of microbiology. (left) First drawings of microorganisms by A. Van Leeuwenhoek (1676) collected from pond water [7]. (right) Sample from a diarrheic 2-month old child feces observed by T. Escherich with a large amount of rod-shaped bacteria (1885) [8]. (bottom) Sketch of L. Pasteur's experiment proving the absence of spontaneous life generation (1861) [9]. A nutritive fluid containing cells is heated, killing the organisms and filling the "U" by condensation. Invaders can contaminate the "U" but can never reach the flask which stay sterile. No organism grow in the sterile nutritive fluid (no spontaneous generation).

The study of microorganisms has led to great medical advances but their understanding is still very incomplete, as reflected by the numerous recent studies on the microbiome (more information in [10]). Bringing physicists in the field, with their experimental tools and mechanical concepts far from traditional microbiology, open new perspectives to understand unsolved medical problems.

I.2 A physicist view : active matter in complex environments

Active matter is matter that consumes energy in order to exert mechanical forces, especially to move. This is the case of motile microorganisms. Systems composed of active matter are intrinsically out-of-equilibrium and emerging counter-intuitive phenomena (i.e. compared to passive systems) can occur, mainly inherent to the persistent direction of the motion (see fig.I.3 for the example of MIPS).

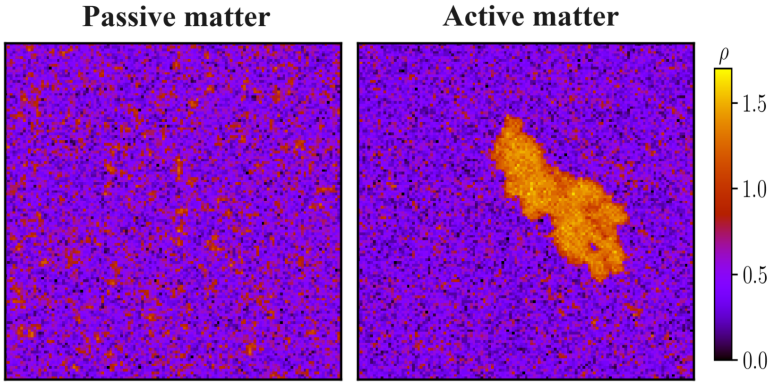

FIGURE I.3 – Motility-induced phase separation (MIPS). Numerical simulations : snapshots of the density of particles ρ at large time for : passive Brownian particles (left) and active Brownian particles (right). Density field is homogeneous for passive particles whereas active particles eventually form a dense cluster. Adapted from [11].

Active matter in complex environments is a broad field of research in physics, close to biological problems. It is a very active domain whether in experiments, but also in numerics and theory, as shown by the following large number of recent reviews [12, 13, 14, 15, 16, 17, 18]. I had the chance to attend several international high-level workshops on this topic :

1. July 2021/2022/2023 - the transdisciplinary "PSL Soft and Living Matter days" organized in ESPCI, Paris.
2. October 2021 - "UCA fall program - Mobility, self-organization and swimming strategies" in the beautiful Campus Valrose, Nice, Côte d'Azur.
3. October 2022 - "Active matter and complex media" in the wonderful Institut d'Etudes Scientifiques of Cargèse, Corsica.
4. November 2022 - "ETN - PHYMOT - Physics of microbial motility" in the modern Institut Pierre-Gilles de Gennes, ESPCI, Paris.
5. June 2023 - "Active Matter at Surfaces and in Complex Environments" in the prestigious Max Planck Institute for the Physics of Complex Systems (MPI-PKS), Dresden, Germany.

Nature brings a large choice of diverse models of active matter : the motile microorganisms (algae [19], worms [20], sperms [21], cilia [22] or bacteria [23]), complementary to artificial

systems (diffusiophoresis [24], Janus particles [25], swimming droplets [26, 27], magnetic micro-rotors [28]), to question the physics underneath active matter. For instance many progress are being led to control the motion of bacteria (with or without genetic modifications) throughout the external environment (magnetic field [29], chemical gradients [30, 31], light [32]) that would be very hard to mimick synthetically. It makes them a very nice support in the study of fundamental statistical physics of active matter.

At the same time, the study of their fundamental interactions with complex environments paves the way to new understanding of ecological and medical problems. The complexity of the environment, often modeling the natural environments of microorganisms, can range from the presence of geometric obstacles (confined geometries [33], surface texture [34], maze [35], pillars [36], colloids [37], porous media [38, 39]) to non-Newtonian fluids [40] (liquid crystals [41], viscoelastic fluids [42], hydrogels [43], yield stress fluids [44], biological fluids like mucus [45], polymers [46] shown in figure I.4).

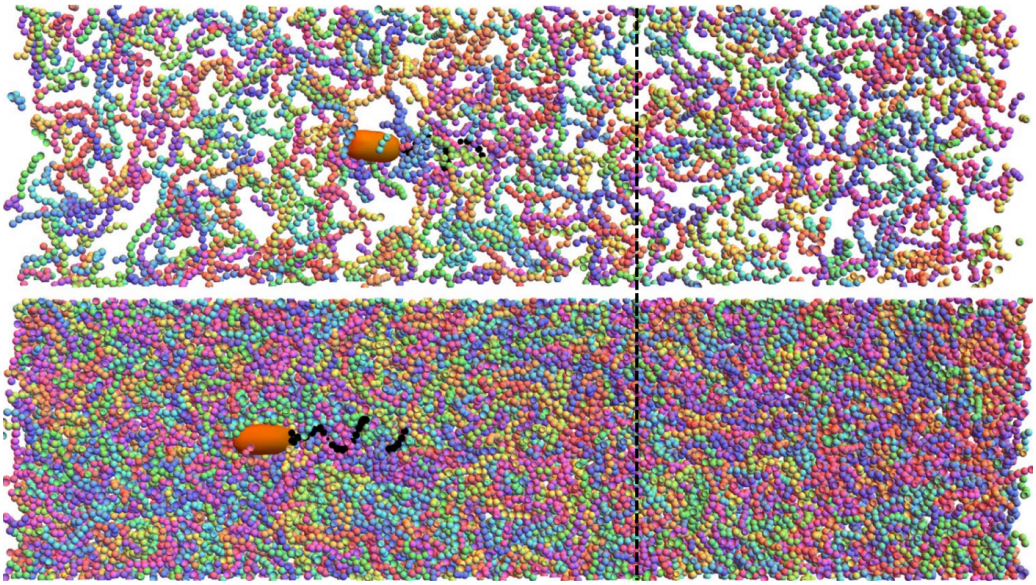

FIGURE I.4 – Simulations of a model monoflagellated bacterium E.coli-like swimming in a dense macromolecular polymer solution. Typical simulation snapshots of the bacterial dynamics in fluids consisting of a Newtonian background fluid and including semiflexible polymers. The starting position of the cell body is indicated by the black dashed line, showing that the bacterium can swim faster in the more concentrated suspension. The colours of individual polymers are to aid visualization. From [46].

There is thus a mutual relationship between physics and biology : physics can help to understand biology and biology can provide model systems and inspiration for physical studies. In this thesis, we study the problem of bacterial infection taking place in the gut where the "mucus barrier quality" [47, 48, 49] and bacterial motility [50, 49] have been shown to be important factors.

I.3 Geometrical and mechanical properties of the mucus barrier : key factors for motility-induced infection ?

Bacteria are omnipresent in the gastrointestinal tract and form the so-called "gut microbiota". Symbiotic bacteria take part in the digestive process but pathogens can cause inflammation by infecting intestinal cells. In normal conditions, intestinal cells secrete a mucus barrier that covers intestinal walls preventing pathogens to invade host cells. However in pathological

conditions, for instance induced by diet (food emulsifiers [47] in figure I.5a, western-style [48]), the mucus barrier can lose its protective function. Studies suggest that it can be due to (see figure I.5b) :

1. holes in the mucus barrier offering a narrow (i.e. geometrically confined) path that bacteria can exploit to access intestinal cells [49].

2. an alteration of the mechanical properties of the mucus mesh [48].

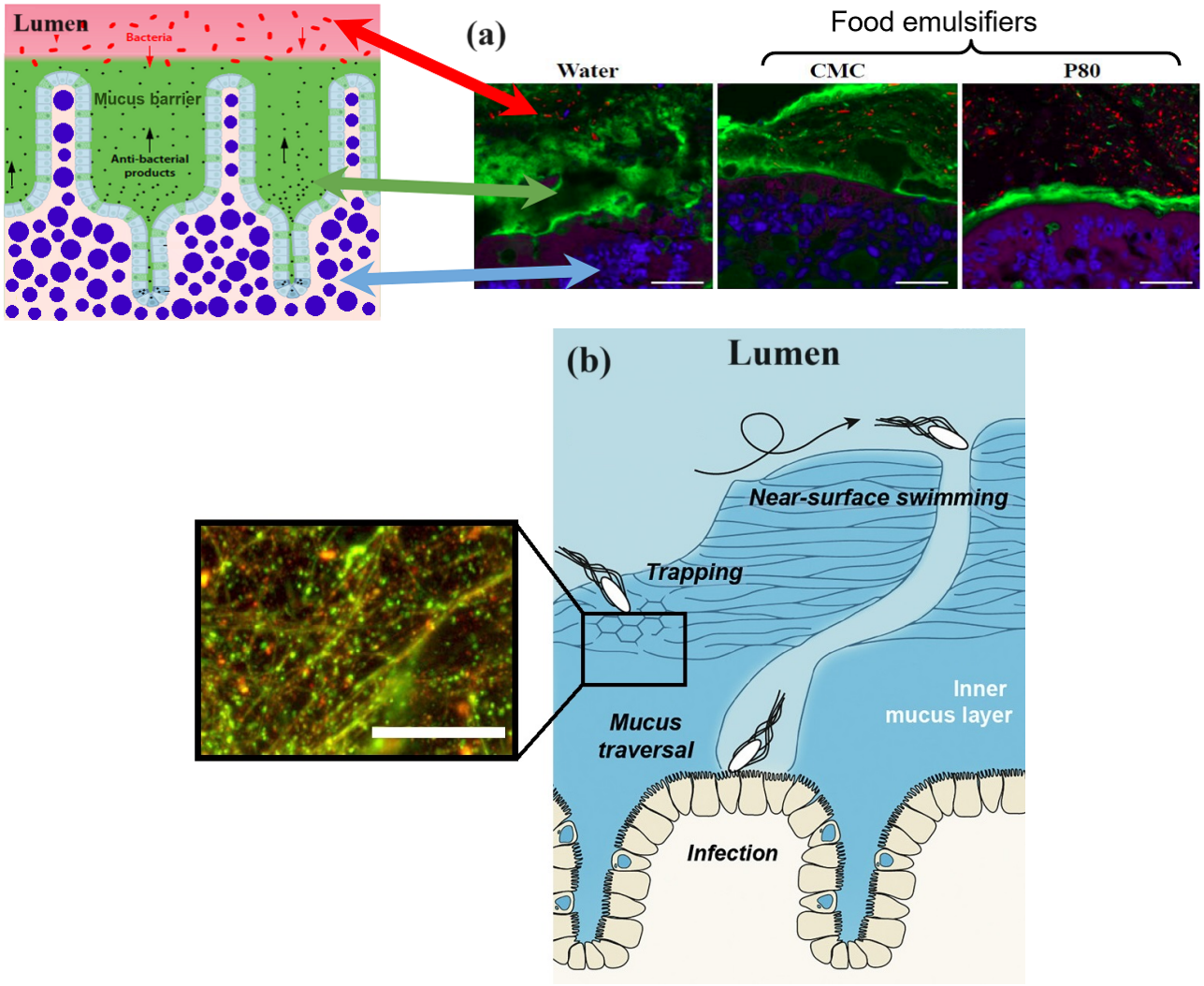

FIGURE I.5 – Mucus barrier properties and mechanisms of bacterial infection. (a) In the lumen (inside of the intestine), the mucus barrier (green) prevents bacteria (red) from invading our intestinal cells (blue). Sketch of the situation (left) and experiments (right) on mice fed with different diets. In normal (water) conditions, the mucus barrier keeps the bacteria away from intestinal cells. Under specific diets, bacteria can penetrate the mucus barrier (CMC) or the mucus barrier is drastically reduced (P80). Scale bar = 20 μm. Extracted from [47]. (b) Motile bacteria Salmonella Typhimurium can swim in the lumen and on the surface of the inner mucus layer where their motion is circular, allowing them to find holes in the mucus barrier, possibly leading to infection. They can also penetrate the inner mucus layer until getting trapped. Adapted from [49]. Inset : Ex-vivo confocal imagery of mucus stained with WGA (red) and UEA1 (green) revealing a granulous mesh pointing mechanical heterogeneities at micron scale. Scale bar is 50 μm. From [48].

In this thesis, we aim at shedding light on the fundamental mechanisms linking geometrical and mechanical heterogeneities of the mucus barrier to infection by motile bacteria. After an introduction to microswimmers in simple and complex environments, we first track E. coli bacteria during their motion in a simple fluid geometrically confined between two parallel plates : we clarify their exploration on solid surfaces, taking the opportunity to challenge the impact of morphology on the observed kinematic variability between individuals, and demonstrate the importance of confinement on their transport properties. Then, mucus from two groups of piglets fed under different diet are extracted and systematically characterized not only with optic and rheology but also with an original experiment probing the bacterial penetration. Finally, the tracking apparatus is improved with a method of machine learning to extend its use in optically complex fluid leading to the first 3D trajectory of a bacterium in mucus.

Chapter II

Microswimmers in simple and complex fluids : a focus on E. coli

II.1 E. coli : a model bacterium

II.1.1 Cell structure

E. coli, a reference model for fundamental research in microbiology, is composed of an ellipsoidal body of typical length 2 μm and width 1 μm on which are attached external structures (see figure II.1) :

- the pili (length : 1 μm, diameter : 7 nm) are known to play a role both in the exchange of plasmids between individuals and in the adhesion process (to form aggregated colony called biofilms or to attach to a surface).
- the flagella (length : 4-10 μm, diameter : 20 nm) used for locomotion (when they are in the planktonic state).

The body is composed of three membranes : an outer membrane (capsule) full of lipopolysaccharides protecting the bacteria, a rigid cell wall with peptidoglycans maintaining the cell shape and an inner membrane (plasma membrane) made of phospholipids controlling the molecular exchange between the inside and the outside of the cell [52].

The cytoplasm is composed of ribosomes that synthesize proteins and two kinds of genetic material : the nucleoid containing most of the DNA, but also some other small circular pieces called plasmids. Genetic modifications performed by either inserting a new plasmid or changing

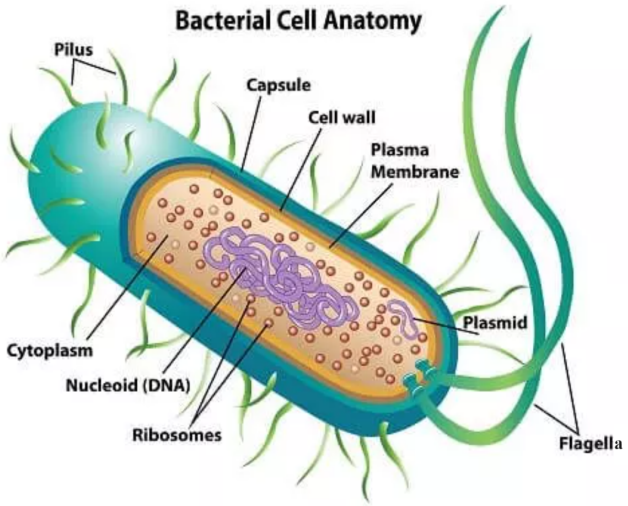

FIGURE II.1 – Sketch of the bacterial structure (after [51]).

the genome directly, allow to control the protein production by bacteria, thus monitoring specific functions [53].

II.1.2 Propulsion machinery

The motion of bacteria emerges from the active rotation of helicoidal flagella. This rotation is induced by a motor (figure II.2) converting a flux of proton into mechanical energy, known as proton motive force. The balance of protons is regulated by proton pumps that can act either aerobically (i.e, only in presence of oxygen) but also anaerobically (i.e, no oxygen) via a metabolic pathway called "glycolysis" extracting energy from glucose [54].

The motor is composed of stator units that drive the rotor (C-ring). Stator units can adapt their number depending on the required torque, that can be interpreted as "mechanosensing" [55] recently modeled via mechano-chemical concepts in [56]. The flagellum can rotate clockwise (CW) or counterclockwise (CCW) depending on the rotor conformation [57, 58] led by the presence of CheY-P proteins, controlled by a complex sensory and signaling chemotactic (i.e, motion influenced by the chemical environment) machinery.

The flagellum is made of a concatenation of proteins called flagellin that are constrained to a limited number of configurations (known as "polymorphism" [59]) leading to either left-handed or right-handed helicity. Multiple flagella can interact together hydrodynamically to form a unique helix called the "bundle". The link between the outer flagellum and its inner motor is ensured by a flexible hook. The hook must be compliant to enable bundle formation yet rigid to withstand large hydrodynamical forces [60].

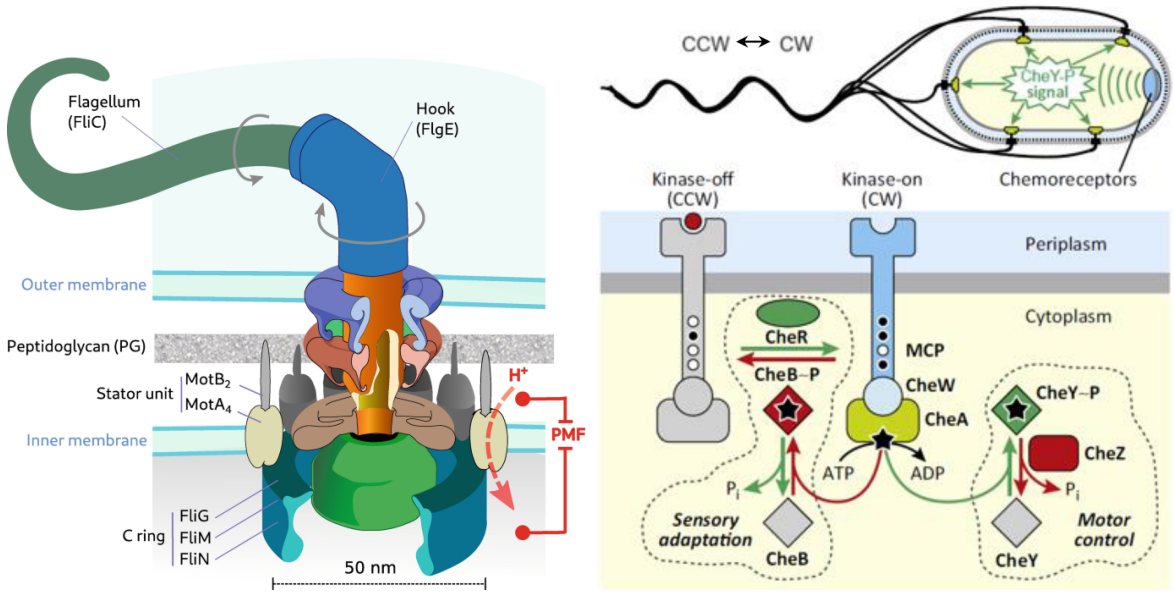

FIGURE II.2 – Sketch of the flagellar motor machinery. (left) Main mechanical units (from [61]). Motors are located at the inner membrane. Proton pumps maintain a proton flux, from the periplasm to the cytoplasm, which makes the stators rotate. This mechanism is called proton motive force (PMF). It leads to the rotation of the C-ring rotor via a gear-like mechanism. The C-ring is linked to the flagellum by an elastic hook. (right) Chemotactic machinery. Chemicals of the surrounding fluid bind to the chemoreceptors that can activate or disable a kinase. When activated, the kinase triggers a complex chemical cascade that ultimately catalyzes the production of the CheY-P protein controlling the motor rotation direction. Adapted from [62].

The helical flagella rotation and conformations control the motion of motile micro-swimmers such as E. coli, exerting forces on the surrounding fluids allowing self-propulsion and active reorientations. The compound of fluid mechanics and also stochastic dynamics are thus necessary to understand the inherent complexity of the motion of motile micro-swimmers.

II.2 Hydrodynamics of microswimming

This section is suited to give an elementary but reasonable understanding of the locomotion of flagellated microorganisms, especially E. coli.

II.2.1 The low Reynolds world

The dynamics of a mass m is ruled by Newton's second law :

$$m\frac{d\mathbf{v}}{dt} = \sum \mathbf{F} \tag{II.1}$$

which yields for the fluid mechanics of a viscous fluid the Navier-Stokes equation :

$$\rho\left(\frac{\partial \mathbf{u}}{\partial t} + (\mathbf{u}.\nabla)\mathbf{u}\right) = -\nabla p + \eta\boldsymbol{\Delta}\mathbf{u} + \rho\mathbf{f} \tag{II.2}$$

This equation links the flow field $\mathbf{u}$ to the force field (caused by internal pressure p, external massic force $\mathbf{f}$ and viscosity η). By comparing, with dimensional analysis, the inertial term $\rho(\mathbf{u}.\nabla)\mathbf{u} \propto \rho U^2/L$ and the viscous term $\eta\boldsymbol{\Delta}\mathbf{u} \propto \eta U/L^2$, inertia is dominated by viscous force if $\rho LU/\eta = Re \ll 1$ with Re the Reynolds number. The Reynolds number is thus the ratio of inertial forces upon viscous forces. Typically, for E. coli swimming in water : $\rho = 1\times10^3\,\mathrm{kg\,m^{-3}}$, $L = 1\times10^{-6}\,\mathrm{m}$, $U = 30\times10^{-6}\,\mathrm{m\,s^{-1}}$ and $\eta = 1\times10^{-3}\,\mathrm{Pa\,s}$ resulting in the very low Reynolds number $Re \sim 10^{-5} \ll 1$. Microswimmers thus experience the Stokes regime which yields in the absence of external force :

$$\eta\boldsymbol{\Delta}\mathbf{u} - \nabla p = 0 \tag{II.3}$$

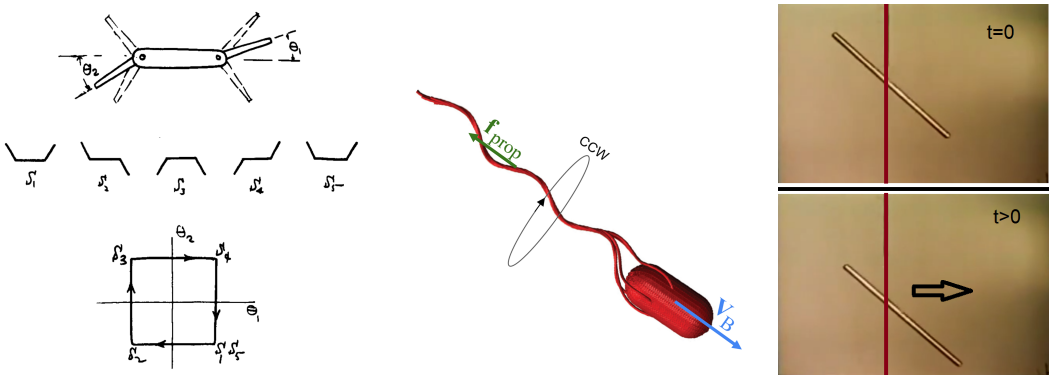

FIGURE II.3 – (left) Minimalist swimmer designed by Purcell : the sequence of motion is not reciprocal allowing the object to have a net motion after a cycle. Drawing from [63]. (middle) E. coli as desgined in hydrodynamics simulation [64]. Rotation of the helix induces a force pushing the fluid behind it. Consequently the bacterium moves forward. (right) Anisotropy of the drag force makes the slender rod moves not only down but also to the right whereas the only force is the vertical gravity (full video [65]).

The time-independence of this equation implies that :

- the system can be considered in the quasi-static limit. Fluid displacement is instantaneous : dynamics stops instantaneously when kinematics stops. To fix the idea let's do a simple computation in the idea of Purcell [63] : What is the coasting distance Δx that a sphere of radius $R = 1\mu m$ moving initially at $U_0 = 30\mu m/s$ will run before stopping ? The drag force is given by Stokes' law : $F = -6\pi\eta RU$. Solving $F = ma$ with $m = (4/3)\pi R^3\rho$ results in the coasting distance $\Delta x = U_0/\tau \approx 0.01nm$ with a typical coasting time $\tau = (4/18)\rho L^2/\eta \approx 0.2\mu s$. All timescales greater than this will thus reach the quasi-static limit.
- the system is time-reversible (perfectly illustrated in the video [66]). A net displacement cannot be obtained by a mere reciprocal motion, meaning that a symmetry must be broken during a motion cycle. This is known as the "scallop theorem" [63] and implies that one degree of freedom is not sufficient to get a net motion in a Newtonian fluid. A minimal swimmer with two degrees of freedom is shown on figure II.3a.

Thus micro-organisms have developed locomotion strategies adapted to the low Reynolds regime, that can be quite surprising (a common picture is to compare microswimming to a human swimming in very viscous fluid, like honey, where the Reynolds number would be comparable). For instance, E. coli are propelled by a rotating helix (figure II.3b) taking advantage of a viscous drag effect called "anisotropy of the drag force" (figure II.3c).

II.2.2 Pusher / Puller

Most microswimmers can be classified into two categories depending on the way they swim (figure II.4) :

- the pushers push the fluid behind and in front of them (and as a consequence fluid arrives by the side to achieve mass conservation). E. coli is the archetypal pusher.
- the pullers pull the fluid behind and in front of them (and as a consequence fluid is ejected by the side). The archetypal puller is Chlamydomonas reinhardtii. Its swimming cycle is similar to a breaststroke.

Pushers (resp. Pullers) can be modeled by a simple repulsive (resp. attractive) force dipole.

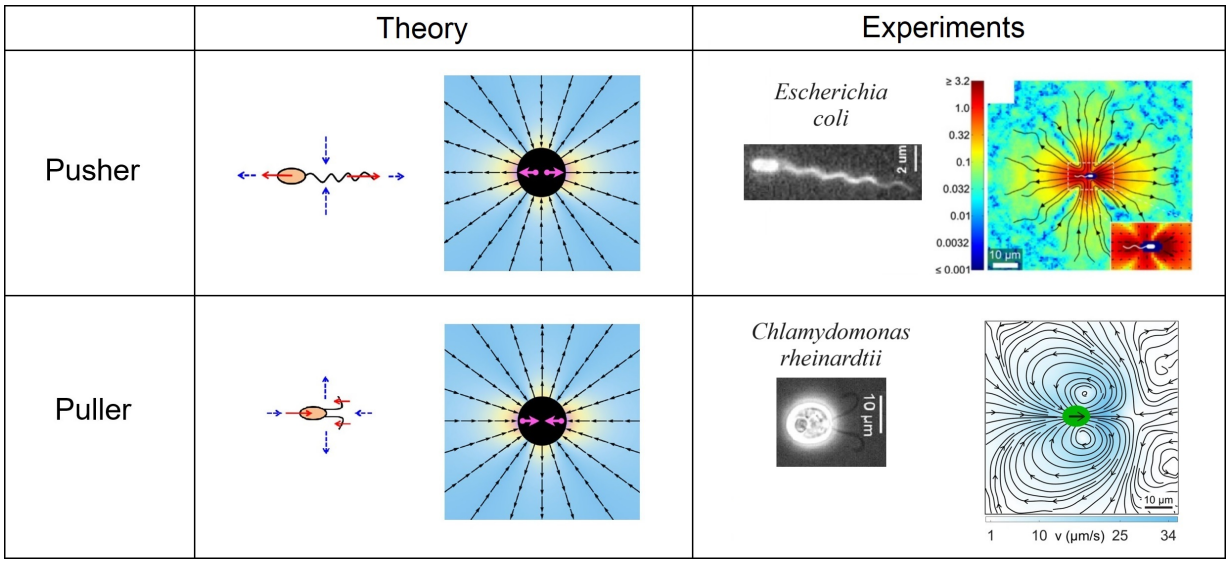

FIGURE II.4 – Theory : Sketch of pusher/puller force-dipole (left) and associated theoretical flow field (right). Point forces are the red arrows. Color code represents flow intensity. Figures from [67, 15]. Experiments : Real imaging with flagella (left) and measured experimental flow field (right) of E. coli / C. reinhardtii. Figures from [68, 69] / [70].

The resulting flow field can be computed (figure II.4-left) since the response to a point force is known in the Stokes regime :

$$\mathbf{u}(\mathbf{r}) = \mathbf{F}.\mathbb{J}(\mathbf{r}) \text{ with } \mathbb{J}(\mathbf{r}) = \frac{1}{8\pi\eta}\left(\frac{\mathbb{I}}{|\mathbf{r}|} + \frac{\mathbf{rr}}{|\mathbf{r}|^3}\right) \tag{II.4}$$

where $\mathbb{J}(\mathbf{r})$ is known as the "Stokeslet" and $\mathbf{F}$ a point force applied at the origin. Considering a force dipole of strength p centered in $r = 0$ aligned with the elongated direction of the cell (as sketched in figure II.4-left), which is also the swimming direction, results in :

$$\mathbf{u}(\mathbf{r}) = \frac{p}{8\pi\eta r^3}(3\cos^2\theta - 1)\mathbf{r} \tag{II.5}$$

The velocity field thus generically decays as $1/r^2$ in the far-field of an individual microswimmer. For pushers $p > 0$ whereas for pullers $p < 0$. $|p| = 2d|F|$ where d is the distance between the two point forces constituting the force dipole.

Experimentalists were able to visualize directly the flow field around micro-swimmers using micro-PIV techniques [69, 70] (figure II.4-right), in good agreement with this simple dipole of force model, especially for E. coli.

II.2.3 A simple model for swimming E. coli

A flagellated bacterium can be modelled as the combination of a spherical body of radius R_B and an effective helix of length L, pitch λ, radius r and thickness r_0 linked by a motor of rotation speed Ω_M. All the parameters of the problem are sketched in figure II.5. The idea is now to derive an expression for the speed V.

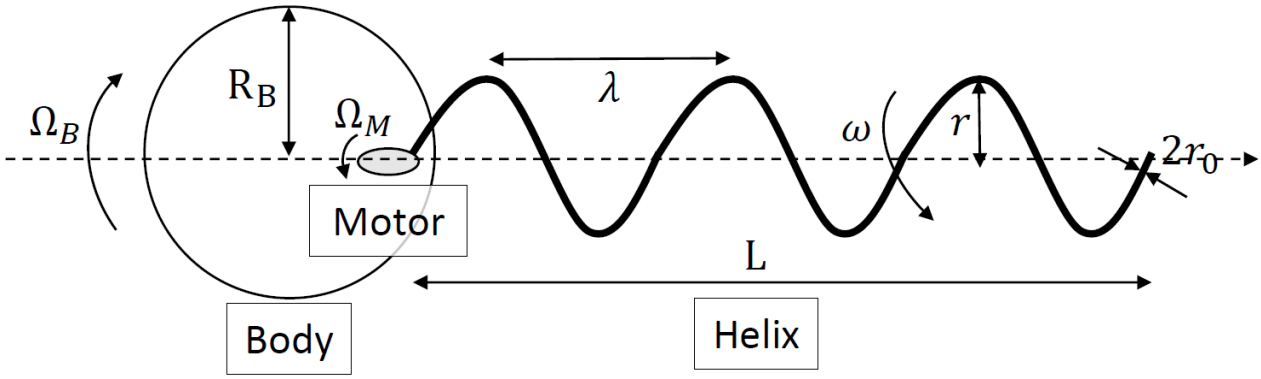

FIGURE II.5 – Sketch of a bacterium and its geometrical properties.

First, kinematics imply that the rotation speed of the body Ω_B and the helix ω are linked via the motor Ω_M : $\Omega_B = \omega - \Omega_M$.

Then, an active micro-swimmer is force-free and torque-free (in the absence of inertia). Considering no coupling between the body and the helix, one can compute the resistance matrix which links force and torque to translational and rotation speed at low Re :

$$\begin{pmatrix} F \\ T \end{pmatrix} = \begin{pmatrix} 0 \\ 0 \end{pmatrix} = \eta \left[\begin{pmatrix} A_{11} & 0 \\ 0 & A_{22} \end{pmatrix} \begin{pmatrix} V \\ \Omega_B \end{pmatrix} + \begin{pmatrix} B_{11} & B_{12} \\ B_{12} & B_{22} \end{pmatrix} \begin{pmatrix} V \\ \omega \end{pmatrix} \right] \tag{II.6}$$

where η is the viscosity of the fluid, $A_{11}V$ (resp. $B_{11}V$) is the drag of the translating sphere (resp. helix), $A_{22}\Omega_B$ (resp. $B_{22}\omega$) is the torque of the rotating sphere (resp. helix), $B_{12}\omega$ is the thrust produced by the rotating helix and $B_{21}V$ is the torque produced by the translating

helix. The reciprocal relationship between the force on a rotating element and the torque on this translating element [71] imposes $B_{12} = B_{21}$.

One can now apply resistive force theory (RFT) to compute all the coefficients. It has been solved theoretically for both a sphere (Stokes-Einstein) and a helix [72]. The idea of such a theory is to compute the resulting parallel and perpendicular drag coefficients of the helix by an infinite sum of small segments along its shape. While experiments show some limits to this theory for a helix [73], numerical improvements can be made by taking into account the coupling between the flow field induced by each small segment (known as "slender body theory" [74]). We can get an expression for the speeds :

$$V = -\frac{A_{22}B_{21}}{(A_{22}+B_{22})(A_{11}+B_{11}) - B_{12}^2}\Omega_M \tag{II.7}$$

$$\omega = -\frac{(A_{11}+B_{11})A_{22}}{(A_{22}+B_{22})(A_{11}+B_{11}) - B_{12}^2}\Omega_M \tag{II.8}$$

Finally, the motor has been shown to adapt to the external torque by recruiting stator units (see figure II.2.left) [75]. Then the bacterial description requires a model for the motor, linking the internal torque to the rotation speed. This has been studied extensively experimentally [76, 77, 55]. One can use the empirical expression :

$$T_{int}(x) = T_M\,(1 - x^n)\,/\,(1 + x^n) \tag{II.9}$$

with $x = \Omega_M/\Omega^*$. T_M denotes the maximal torque that can be delivered by the motor, $\Omega*$ is a characteristic rotation speed and $n = 2.5$ an empirical power (see figure II.6).

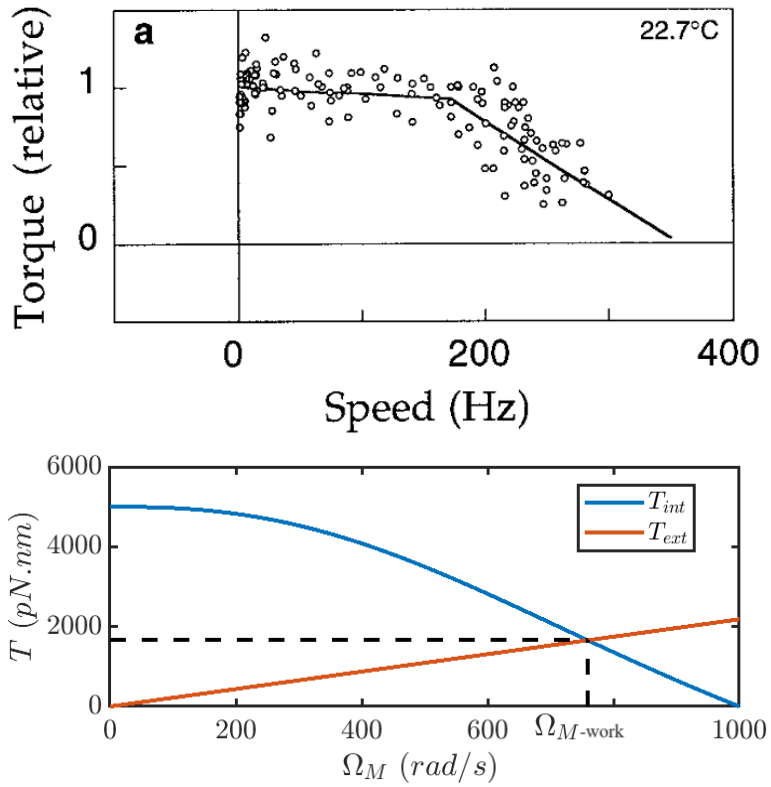

FIGURE II.6 – Motor torque-speed relationship. (top) Experimental measurements from [76]. (bottom) Empirical numerical profile from equation II.9. Internal torque (blue) balances the external torque (orange) to determine the working speed of the motor Ω_{M-work}.

The power dissipated in the fluid must be equal to the power delivered by the motor :

$$P_{diss} = T_{ext}\Omega_M \tag{II.10}$$
$$= \eta\left[A_{11}V^2 + (B_{11}V + B_{12}\omega)V + A_{22}\Omega_B^2 + (B_{21}V + B_{22}\omega)\omega\right] \tag{II.11}$$
$$= P_{mot} = T_{int}\Omega_M \tag{II.12}$$

that can be solved numerically provided a model for the internal torque (equation II.9).

The model is now complete. One can choose parameters from the literature [78, 79]. For the body : $V_B = 1.4\,\mu\text{m}^3 => R_B = 0.7\,\mu\text{m}$, for the helix : $L = 6\,\mu\text{m}$, $\lambda = 2.1\,\mu\text{m}$, $r = 0.2\,\mu\text{m}$, $r_0 = 10\,\text{nm}$ and for the motor : $T_M = 3000\,\text{pN nm}$, $\Omega^* = 150\,\text{Hz}$.

This model predicts that speed is maximal for a given length of the helix (figure II.7a) and describes experimental data done in viscous fluids (figure II.7b).

Despite its apparent simplicity, this model already captures most of the important features of bacterial locomotion in viscous fluids while providing good insights.

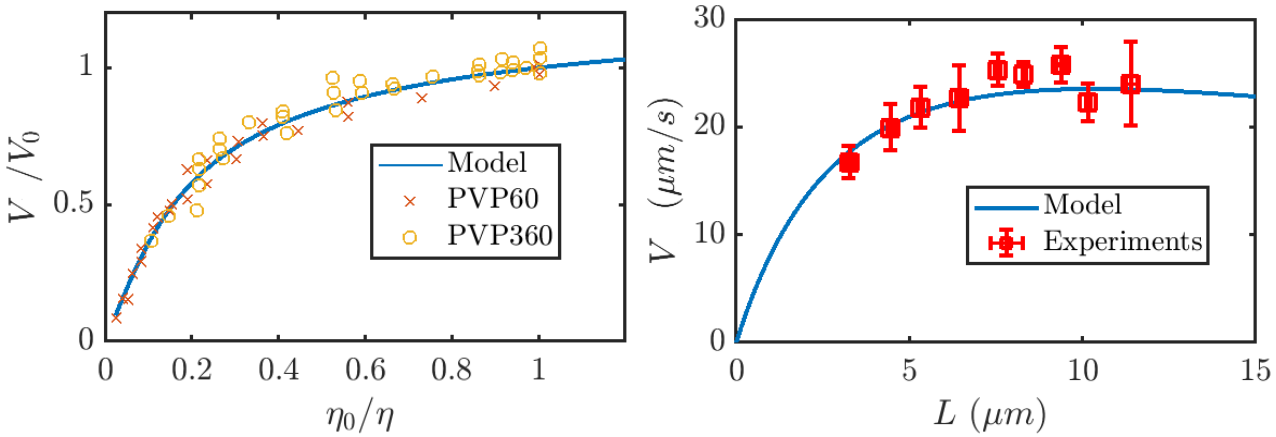

FIGURE II.7 – Results of the model. (left) Bacterial speed as a function of the fluidity (defined as the inverse of the viscosity). The external torque is proportional to viscosity, the motor adapts its speed consequently. Experiments from [80]. (right) Bacterial speed as a function of flagella length. Speed increases with flagella length until reaching a quasi-plateau. Error bars are errors of the mean. Data from private communication with a former PhD in the group, Gaspard Junot. Note : From (left) is calibrated $V_0 = 22.03\,\mu\text{m/s}$, $\Omega* = 1050\,\text{rad/s}$, $T_M = 2600\,\text{pN nm}$. Then results (right).

However, microswimmers generally live in polymeric fluids, such as mucus, whose properties are more complex (viscoelasticity, shear-thinning, yield stress...) and in confined environments characterized by the presence of surfaces. The state-of-the-art of the hydrodynamic interactions with such elements are discussed below.

II.2.4 Swimming in complex fluids

We saw that, as the fluid viscosity increases, the speed of E. coli decreases. However most of the biological fluids in which bacteria settle cannot be simply described by a Newtonian viscosity. Indeed, for example they can be composed of polymers that can crosslink and create elasticity in the fluid or internal structures such as soft gel inclusions. This elasticity can lead to different rheological behaviors such as viscoelastic response or yield stress. Due to the inherent microscale of polymers, the resulting rheology can be different if it is measured on macroscopic scale (with a rheometer) or on microscope scale (through beads diffusion). Dimensionless numbers are usually used to characterize the different regimes :

- Oldroyd-B fluids are characterized by a relaxation time λ and the dimensionless number to describe the resulting properties is related with the Deborah number De which measures the degree of elasticity of a viscoelastic fluid. Surprising properties emerge : some swimming strategies that would not lead to any motion in a Newtonian fluid can conversely generate motion in viscoelastic fluids, like the swimmer presented in figure II.8a from [81]. These fluids are shown in figure II.8f to reduce the rotational diffusion and the wobbling (i.e the helical motion of the body due to asymmetry in flagellar location [64]) while viscosity is suspected to reduce the tumbling rate [82].
- Shear thinning fluids are materials whose local viscosity $\eta(\dot{\gamma})$ decrease with the shear rate $\dot{\gamma}$: the more it is stressed, the easier it will flow. They are commonly described with a shear-thinning index n describing the decay of the viscosity with shear rate. In such fluids, since the effective shear rate of the flagellum $\dot{\gamma}_f = \omega_f/(R/r_0) \approx 10^4\,\mathrm{s}^{-1}$ with ω_f the rotation rate, R the helix radius and r_0 the filament radius is far higher than the effective shear rate produced by the counter-rotating body $\dot{\gamma}_b \approx 10^2\,\mathrm{s}^{-1}$, both elements don't feel the same viscosity and this can lead to speed enhancement while the measured macroscopic shear viscosity increases [80, 83] (figure II.8c).
- Yield-stress fluids need a sufficient stress to start flowing, the yield-stress σ_0. A model combining shear-thinning and yield stress is the Herschel–Bulkley fluid and the Bingham number $Bi = \sigma_0/\eta\dot{\gamma}$ with η the fluid viscosity is mainly used. In these fluids, microswimmers are shown to experience three phases with increasing torque (see figure II.8d) : 1) Blocked. 2) In-place rotation. 3) Net motion. [44].
- In jammed hydrogels particles, described by a typical pore size, E. coli is shown to be confined (trapped) in a close area until it can escape (hop) to a new one as shown in figure II.8e. The statistics of trapping/hopping with pore size is studied in [43] : the larger the pore size, the longer the hops.
- In colloidal suspensions, characterized by a colloid radius R and a volume fraction ϕ, E. coli is shown to increase its speed when passing near a colloid of size $R \sim 1\,\mu$m. Indeed its wobbling is reduced due to hydrodynamic interactions leading to a straighter trajectory of the body and then a speed enhancement [37].

Interaction of living organisms with complex fluids (see [12] for a more general review) can be contradictory because rheological effects are combined with biochemical effects. For instance, a shear-thinning fluid without elasticity (and conversely) bio-compatible has not been found yet, to be able to decipher their impact separately [12, 83]. It is also now clear that polymer solutions must be dialyzed to make reliable comparisons, as small polymer fragments can serve as extra fuel for bacteria thus changing the metabolism [83]. Finally, recent experiments by [84] have shown that bacterial accumulation at surfaces, that are omnipresent in the living habitats of micro-organisms, are reduced in viscoelastic media.

II.2.5 Swimming at solid surfaces

"Pushers", like most of flagellated bacteria, are known to accumulate at surfaces [85]. This property is related to the no-slip boundary condition at surface : the pusher swims with its virtual image on the opposite side of the surface [86], tending to keep it aligned with the surface (figure II.9a). The strength of this hydrodynamic force depends on the distance between the object and the wall [87] that has been measured experimentally by internal reflection aqueous fluorescence microscopy [88] ($h < 100\,\mathrm{nm}$) as well as the surface properties via the slip length [89]. Numerical studies [86] ($h > 300\,\mathrm{nm}$) fail to capture the order of magnitude of experimental measurements yet. This distance is probably mediated by an interplay between hydrodynamic attraction and electrostatic repulsion that can be screened by adding ions in the solution. Escape can thus come from passive rotational diffusion [90, 91] or mainly by active reorientations [92]

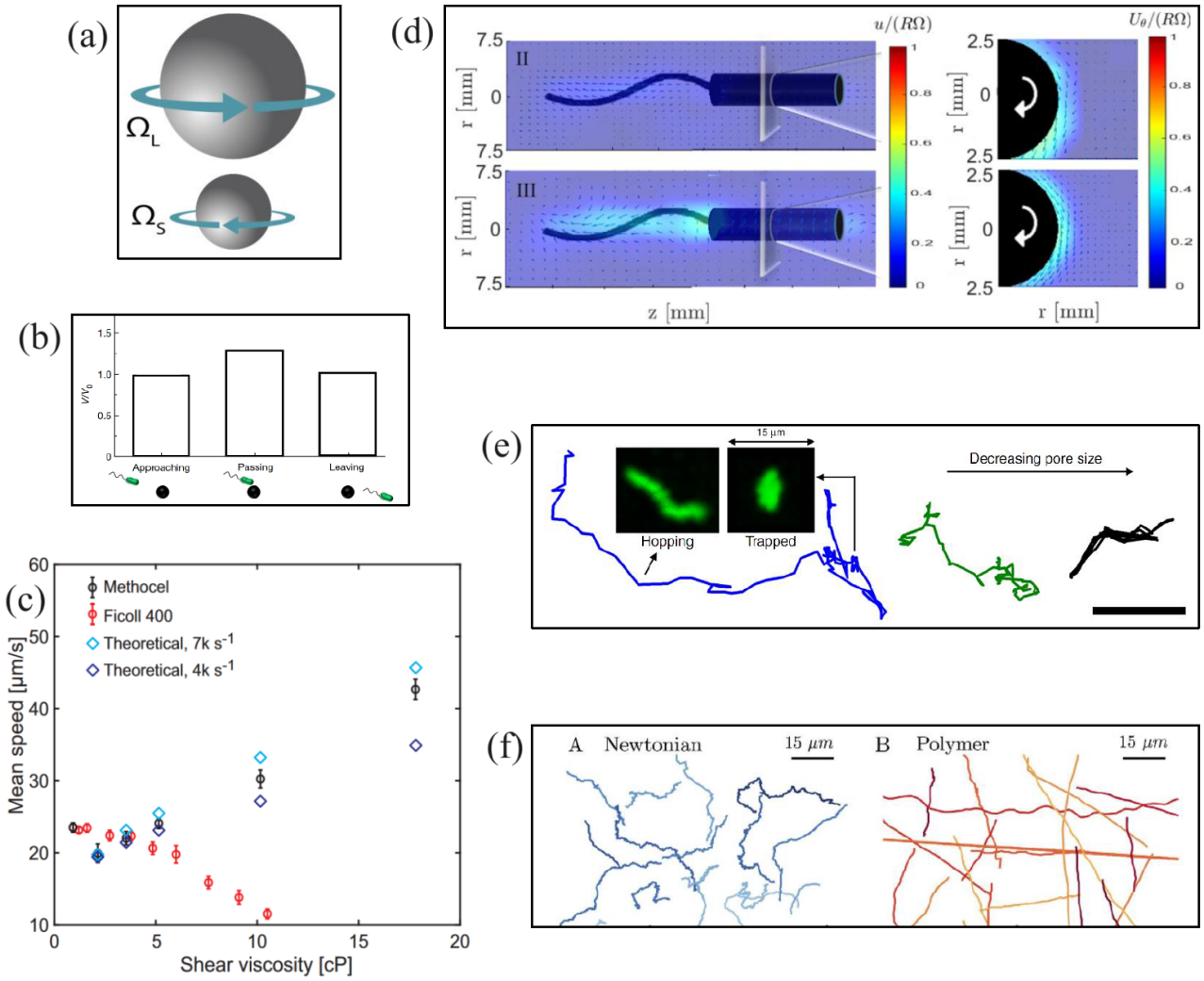

FIGURE II.8 – Interaction of microswimmers with complex fluids. (a) A two-sphere model by [81]. Two spheres of different sizes are maintained at a certain distance one of each other and rotate in an opposite way. In a viscoelastic fluid (Oldroyd-B model), unlike in a Newtonian fluid, it generates a net motion in the direction of the large sphere. (b) E. coli enhances its speed when passing near a colloid. It is due to wobbling suppression. Adapted from [37]. (c) Shear-thinning fluid (Methocel) enhances bacterial speed [83], in contradiction with the measured viscosity, explained theoretically by a reduced viscosity experienced by the flagellum due to its local shear rate. (d) Combination of a cylinder (with permanent magnet) and a helix under magnetic field in a yield stress fluid. Three phases are defined with increasing rotating speed. I) Below a critical magnetic torque, the swimmer is fully blocked. 2) Magnetic torque becomes sufficient for in-place rotation but no net motion occurs. 3) Magnetic force rotates the swimmer sufficiently fast : net motion occurs. Adapted from [44]. (e) In hydrogels particles, E. coli can be trapped some time in a pore space, possibly escaping from it [43]. Pore size affects the dynamics. (f) In CMC, a polymeric viscoelatic fluid, E. coli rotational diffusion and tumbles are hindered [82].

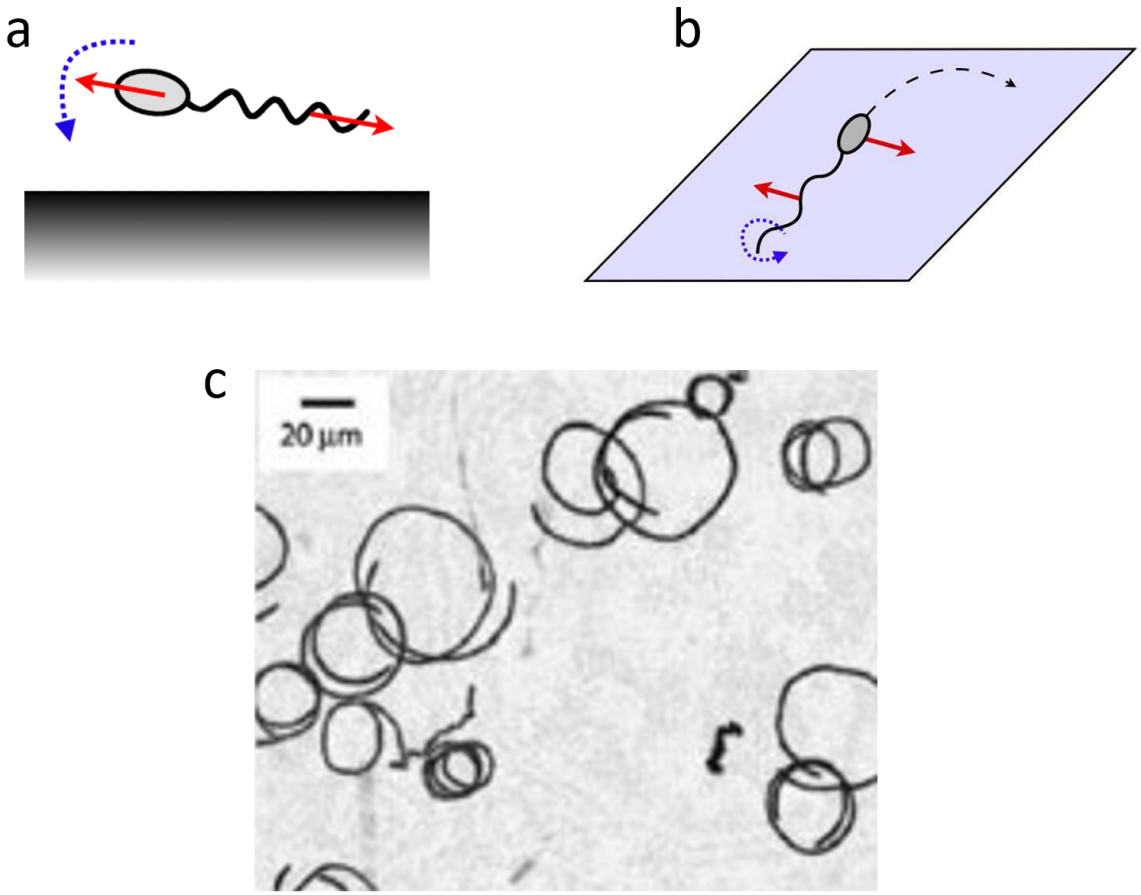

FIGURE II.9 – Interactions of E. coli (and more generally "pushers") with surfaces. (a) Hydrodynamic interaction tends to align the bacteria to the surface (from [67]). (b) Principle of the circular motion (from [85]). (c) Circular trajectories of bacteria on surface (from [85]).

if the attraction is too strong to be overcome passively.

In addition to the accumulation, E. coli is also known to swim at surface in clockwise (CW) circular motion [93]. Examples of trajectories are shown on figure II.9c. The circular motion can be understood with simple arguments : flagella rotate CCW and, because the bacterium is torque-free and force-free, the body counter-rotates (i.e. CW). The interaction of these rotations with the surface results in two forces of opposite direction located on the body and on the flagella leading to a global torque perpendicular to the surface as sketched on figure II.9b. From an elementary hydrodynamic model, the gyration radius is shown to depend on the gap between the surface and the bacterium and the strength of the force dipole [94], as well as the body shape [93]. Experimentally, the near-field emerging from a swimming bacterium close to a surface is not shown to differ from bulk with micro-PIV techniques [69]. An asymmetry in the flow field close to surface, related to the circular motion of the bacterium, could remain to be demonstrated. Besides the flow field emerging in the vertical direction is also studied [95].

Deformable interfaces [96] and the case of air-liquid interfaces, where E. coli is shown to swim counter-clockwise (CCW) [97], unlike at solid-liquid interfaces (except in special conditions [98]), are also sources of interest.

Hydrodynamics is not sufficient to understand the bacterial exploration. Self-propulsion is indeed combined with active reorientation processes triggered stochastically by a complex biochemical machinery.

II.3 Run & Tumble (R&T) exploration

Bacteria can explore their environment combining self-propulsion and reorientations which can be purely passive or combined with more elaborated active processes :

- Monoflagellated bacteria, such as Myxococcus xanthus [99] (resp. Vibro alginolyticus [100]), can perform "reversals" (resp. "flicks"), i.e reorientations of 180° (resp. 90°).
- Peritrichous bacteria, such as E. coli, perform stochastic reorientations called "tumbles".

The sequence of a straight motion ("run") followed by a reorientation ("tumble") allows the bacterium to explore its environment. Denoting τ_r the typical run time, the mean square displacement (MSD) of such an object is ballistic (exponent 2) at short time $\Delta t \ll \tau_c$ and then diffusive (exponent 1) at large time $\Delta t \gg \tau_c$ due to the reorientations (figure II.10) where $\tau_c \propto \tau_r$ is the characteristic time at which the transition from ballistic to diffusive regime occurs [101]. The diffusion coefficient D, which is the slope of the MSD in the diffusive regime divided by twice the spatial dimension d of $\mathbf{X}$, is then the measure of the exploration at large time :

$$D \underset{\Delta t \to \infty}{=} \frac{\Delta \mathbf{X}^2}{2d\Delta t} \tag{II.13}$$

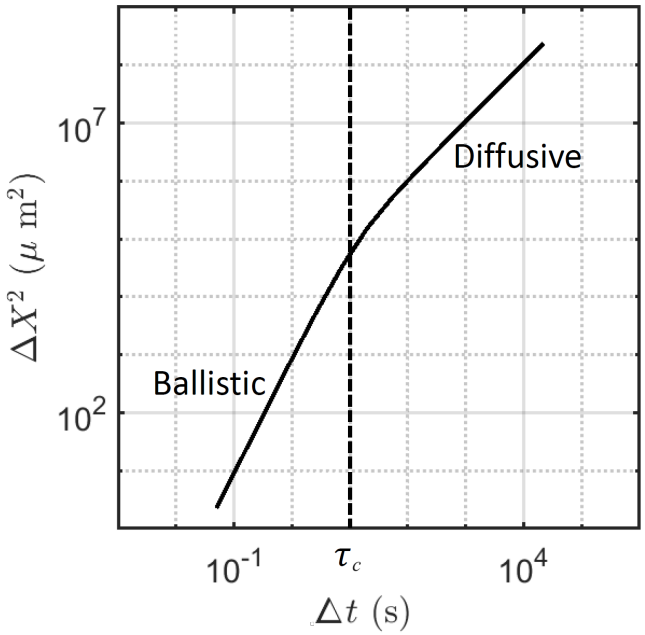

FIGURE II.10 – Typical mean square displacement of a run & tumbler. During a time window Δt, in average (mean), the square of the distance between the original position and the final position (displacement) is $\Delta \mathbf{X}^2$.

II.3.1 Mechanisms and statistics of the reorientations

Each flagellum is composed of a motor that can turn clockwise (CW) or counter-clockwise (CCW). The sense of rotation of the motors is associated to two different swimming modes (figure II.11a) :

- the run mode during which all the flagella turn CCW and assemble into a unique helix. The flagella inside the helix rotate propelling the bacterium straight.
- the tumble mode during which at least one flagellum turns CW, getting out of the bundle ("debundling") and resulting in a reorientation of the bacterium. When the flagellum turns CCW again, the bundle reforms ("bundling") and a new straight run start.

The tumble process is observed experimentally [68]. When the CW rotation starts, the flagellum switches from conformation "normal" to "semi coiled 1" and, after a certain time, to "curly 1" (conformations 2,4 and 5 in figure II.11b). When the motor rotates CCW again, the flagellum gets back to a "normal" conformation. The hydrodynamic origin of the reorientation is addressed in [102] suggesting that most of the reorientation happens in the "bundling" phase. However, the question is still open. Reorientation angles are shown to have a non-trivial distribution [103] peaked around $\theta_t = 45°$ (figure II.11c) that can be modeled via a rotational diffusion during a distribution of tumble time [104]. The distribution of tumble time (of order $\tau_t = 0.4\,\mathrm{s}$) decays exponentially whereas the distribution of run time (of order $\tau_r = 10\,\mathrm{s}$) decays with a power-law [105, 106] (figure II.11d).

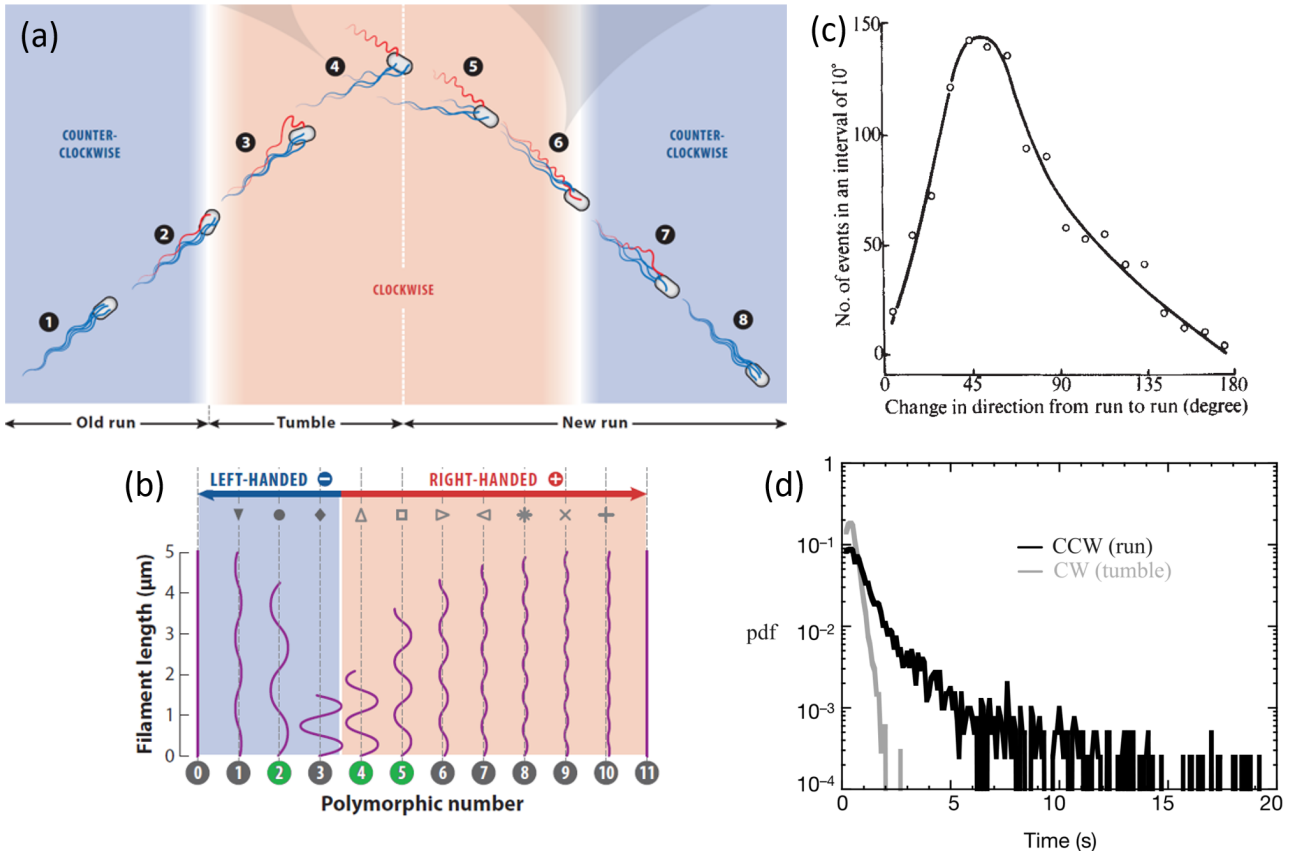

FIGURE II.11 – E. coli run & tumble dynamics. (a) Sketch of the association / dissociation of the flagella bundle occurring during the run / tumble phases induced by the change of rotation direction of a flagellum. (b) Possible conformations of a flagellum : conformations 2,4 and 5 are the most observed and are respectively referred as "normal", "semi coiled 1" and " curly 1". Figures (a) and (b) from [59]. (c) Distribution of reorientation angles (from [103]) (d) Distribution of tumble times (gray) and run times (black). Distribution of tumble times is exponential whereas distribution of run times is not exponential. Adapted from [105].

II.3.2 Mathematical framework

Definition

We provide here a mathematical description of a run & tumble process (only in two dimensions for the sake of clarity). In the following set of equations, the position $\mathbf{X}(t)$ evolves at a constant speed v with translational noise D_t. The orientation angle $\theta(t)$ can vary through rotational diffusion D_r and through tumbles modeled by shot noises at time T_i with a reorientation

angle $\Delta\theta_i$:

$$\frac{d\mathbf{X}(t)}{dt} = \mathbf{V}(t) = V\mathbf{e}(t) + \sqrt{2D_t}\boldsymbol{\xi}(t) \tag{II.14}$$

$$\mathbf{e}(t) = \begin{pmatrix} \cos\left[\theta(t)\right] \\ \sin\left[\theta(t)\right] \end{pmatrix} \tag{II.15}$$

$$\frac{d\theta(t)}{dt} = \sqrt{2D_r}\xi(t) + \sum_i \Delta\theta_i \delta(t - T_i) \tag{II.16}$$

with $\xi(t)$ a white noise. For E. coli, $D_t \sim 0.2\,\mu\text{m}^2/\text{s}$ [107] and $D_r \sim 0.01\,\text{rad}^2/\text{s}$ [108]. Without the shot noise, the process describes an active brownian particle (ABP) [109] like our mutant bacteria, introduced later in section III.1.1, that do not tumble (also denoted as "smooth swimmer").

Analogy with polymer physics

In the 1970's Lovely and Dahlquist found a strong analogy between a run & tumble trajectory and a freely jointed chain : both are sequences of straight lines with reorientations, known as a random walk process. Physicists already worked a lot on freely jointed chain to explain the spatial extension of polymers [110, 111] and the same tools can be applied to describe the exploration of the run & tumble trajectory of bacteria, sketched in figure II.12.

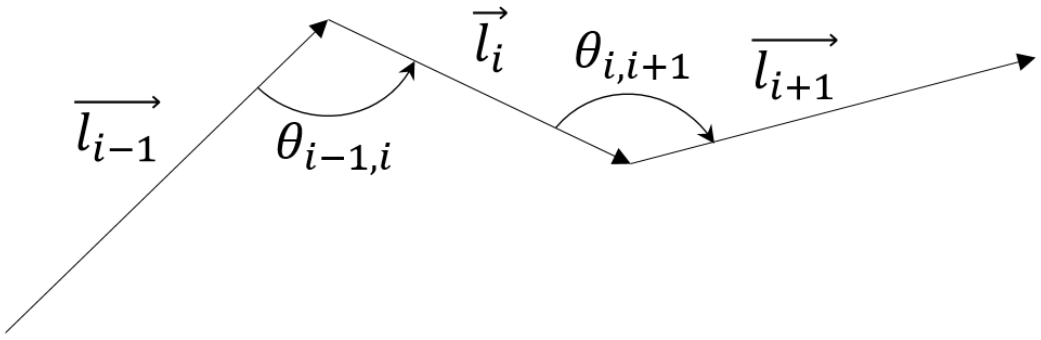

FIGURE II.12 – Sketch of a run and tumble trajectory, or freely jointed chain, with the run vector $\vec{l_i}$ and the angles between successive runs $\theta_{i,i+1}$.

The mean square displacement $\left\langle \Delta\mathbf{X}^2 \right\rangle$ can then be computed as :

$$\left\langle \Delta\mathbf{X}^2 \right\rangle = \left\langle \left(\sum_{i=1}^{N} \vec{l_i} \right)^2 \right\rangle = \sum_{i=1}^{N} \left\langle \vec{l_i}^2 \right\rangle + 2 \sum_{i=1}^{N} \sum_{j>i}^{N} \left\langle \vec{l_i}.\vec{l_j} \right\rangle \tag{II.17}$$

with $\vec{l_i}$ are the runs. $\left\langle \vec{l_i}^2 \right\rangle \equiv \langle l^2 \rangle$ and $\left\langle \vec{l_i} \right\rangle \equiv l$ then $\left\langle \vec{l_i}.\vec{l_j} \right\rangle = l^2 \langle cos(\theta_{i,j}) \rangle$ with $\theta_{i,j}$ the angle between the vectors $\vec{u_i}$ and $\vec{u_j}$. Let's note α the mean cosine between two successive monomers :

$$\alpha = \langle cos(\theta_{i,i+1}) \rangle = \langle cos(\theta_{i+1} - \theta_i) \rangle \tag{II.18}$$

The cosine function here is multiplicative ($\langle cos(a+b) \rangle = \langle cos(a) \rangle \langle cos(b) \rangle$) due to the symmetry of the reorientation along the original vector (then $\langle sin(a) \rangle = \langle sin(b) \rangle = 0$), then :

$$\langle cos(\theta_{i,j}) \rangle = \alpha^{j-i} \tag{II.19}$$

Thus :

$$\left\langle \vec{l_i}.\vec{l_j} \right\rangle = l^2 \alpha^{j-i} \tag{II.20}$$

Then we just have to compute :

$$\sum_{i=1}^{N} \sum_{j>i}^{N} \alpha^{j-i} = \sum_{i=1}^{N-1} N\alpha^i - \sum_{i=1}^{N-1} i\alpha^i \tag{II.21}$$

where the sums have been rearranged. The resulting sums are both analytically solvable and the result holds :

$$\sum_{i=1}^{N-1} N\alpha^i - \sum_{i=1}^{N-1} i\alpha^i = \frac{N(\alpha^N - \alpha)}{\alpha - 1} - \frac{(N-1)\alpha^{N+1} - N\alpha^N + \alpha}{(\alpha - 1)^2} \tag{II.22}$$

When $N \to \infty$ it simplifies :

$$\sum_{i=1}^{N-1} N\alpha^i - \sum_{i=1}^{N-1} i\alpha^i \underset{N\to\infty}{\longrightarrow} \frac{N\alpha}{1-\alpha} - \frac{\alpha}{(1-\alpha)^2} = \frac{N\alpha}{1-\alpha} \tag{II.23}$$

Then by replacing in II.17 and simplifying it holds :

$$\left\langle \Delta \mathbf{X}^2 \right\rangle = \lim_{N\to\infty} N \left\langle l^2 \right\rangle \frac{1 + \alpha \left(2 \left\langle l \right\rangle^2 / \left\langle l^2 \right\rangle - 1 \right)}{1 - \alpha} \tag{II.24}$$

Then to adapt this expression for a run & tumble trajectory (following [101]), the number of monomers N is replaced by $t/(\tau_r + \tau_t)$ with τ_r the mean run time and τ_t the mean tumble time. The monomeric length l is replaced by the run length $V\tau_r$ where V is the speed. Finally one gets an expression for the diffusion coefficient D :

$$D = \frac{\left\langle \Delta \mathbf{X}^2 \right\rangle}{2d} = \frac{V^2 S}{2d\tau_r} \frac{1 + \alpha(2\tau_r^2/S - 1)}{1 - \alpha} f \tag{II.25}$$

where d is the number of dimension of the trajectory, $f = \tau_r/(\tau_r + \tau_t)$ is the running fraction and $S = \langle \tau_r^2 \rangle$. For an exponential distribution of run times (Poisson process) $\langle \tau_r^2 \rangle = 2\tau_r^2$, it holds :

$$D_p = \frac{V^2 \tau_r}{d} \frac{f}{1 - \alpha} \tag{II.26}$$

In the special case of processes ensuring random reorientations such that $\alpha = 0$ and in the limit of negligible tumbling time $f = 1$:

$$D_p = \frac{V^2 \tau_r}{d} \tag{II.27}$$

The diffusion coefficient D of motile E. coli is estimated to $200 - 400\,\mu\mathrm{m}^2/\mathrm{s}$ [112, 4]. Formula II.25 is exact for any distribution of run times as long as its first and second moments are defined and stem from a Markovian process.

II.3.3 Behavioral Variability (BV) model for the run times

Pioneer experiments of bacterial 3D tracking from Berg in 1972 [103] have allowed to access for the first time the distribution of bacterial run times (see figure II.13). This amazing achievement led to consider an exponential distribution for the run times, and thus a Poisson process to describe their dynamics. The main limitation of Berg's apparatus was the tracking duration : limited to a few seconds. Much later, in 2004, Korobkova et al measured the CW and CCW rotation times by attaching a bead to a flagellum of trapped bacteria. It was then

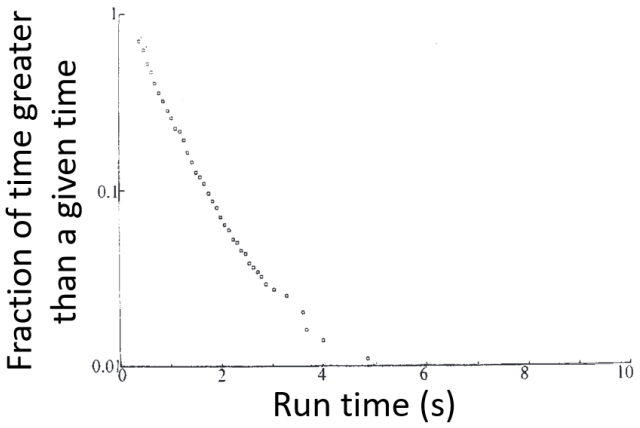

FIGURE II.13 – Fraction of run times greater than a given run time measured by H. Berg [103]. The distribution of run times is mostly exponential. The run times measurement is limited to 5 s.

possible to measure more precisely and on timescales of the order of hours the CCW (run phase) and CW (tumble phase) distributions. They have shown that the run times distribution is actually described by a power-law decay. We present in this section the "behavior variability" (BV) model developed earlier in the group that aims at describing quantitatively the run times dynamics of a generic E. coli bacterium.

Experimental considerations

First of all, bacteria can sense chemical environments through sensors linked to a chemotactic machinery regulating the production of a protein called CheY-P. In the motor vicinity, this protein responsible for the motor rotation mediates the tumble rate. Thus, if a bacterium is sensing more and more attractants (sugars, amino-acids...), the CheY-P production decreases such as to lengthen the run, whereas if it is sensing more and more repellents (fatty acids, alcohol...) the production of CheY-P increases to trigger more frequent tumbles [113]. Statistically, this will lead the bacteria to follow gradients of attractants or eventually escape harmful environments. This process is called "chemotaxis". The tumble occurs because CheY-P binds to the rotor which induces a change of conformation of the rotor (figure II.14a) making the flagellum rotates from CCW to CW. A video illustrating this mechanism can be watched in ref [114].

In an homogeneous chemical environment, the distribution of CCW times (closely related to run times) is shown to decay with a power-law with an exponent close to -2 [105] (figure II.14c).

Finally, it has been found in the group that the run times dynamics possess a memory time [115] as shown by the exponential decay of the log of the persistence times self-correlation function (figure II.14c) leading to a "behavioral variability" (BV) model for the run times [115].

A model based on the internal biomachinery

Even in absence of chemical environment, the CheY-P concentration around the motor $Y(t)$ fluctuates and the timescale of these fluctuations is the memory time T_M (figure II.14d). Modelling the evolution of $Y(t)$ through an Orstein-Uhlenbeck process takes into account this memory time and leads to a normal distribution for Y :

$$\dot{Y}(t) = \frac{Y(t) - \bar{Y}}{T_M} + \eta(t) \tag{II.28}$$

where $\bar{Y}$ is the mean value of Y and $\eta(t)$ is a white noise resulting in fluctuations of Y of amplitude σ_Y. Then let's consider the two-state model (run and tumble) of figure II.14e where an energy barrier ΔG_0 has to be overcome to trigger a tumble (and a constant energy barrier has to be exceeded to bring it back to the run mode). Let's make ΔG_0 depends linearly with Y (expansion to the first order) :

$$\frac{\Delta G_0[Y(t)]}{k_b T} = \frac{\Delta G_0[\bar{Y}]}{k_b T} - \Delta_0 \frac{Y(t) - \bar{Y}}{\sigma_Y} + ... \tag{II.29}$$

where Δ_0 is the sensitivity to Y fluctuations. Finally, the time needed to overcome this barrier is given on average by an Arrhenius law :

$$\tau_s(t) = \tau_0 \exp(-\Delta_0 \frac{Y(t) - \bar{Y}}{\sigma_Y}) \tag{II.30}$$

where τ_s is the switching time and τ_0 is the switching time for $Y = \bar{Y}$. Thus the normal distribution of Y is transformed into a log-normal distribution for the switching times τ_s. The switching times must reflect the run times $\tau_s \approx \tau_r$.

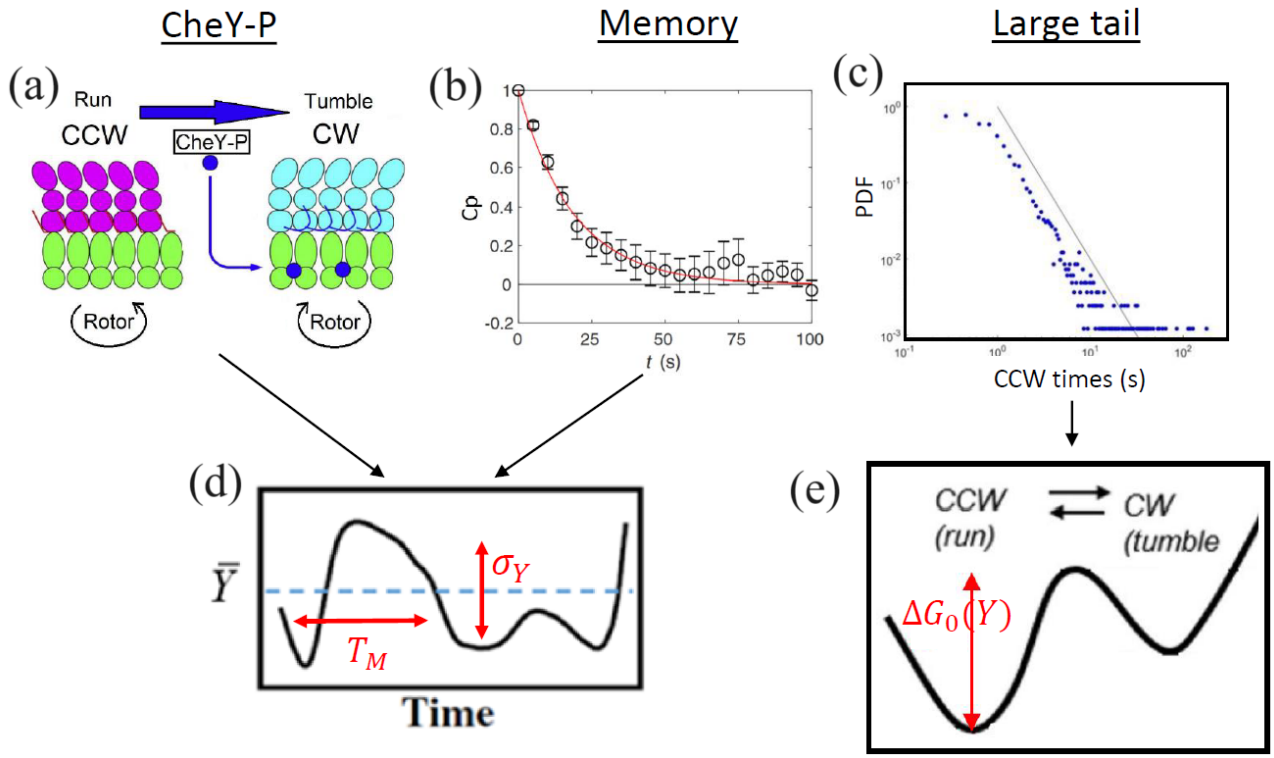

FIGURE II.14 – Behavioral variability (BV) model. Experimental considerations (a,b,c) leading to a minimal model for the run times with an internal slow variable representing fluctuations of the CheY-P protein (d,e). (a) Sketch of the rotor of the flagellar motor. CheY-P binds to the rotor, triggering a conformational change that makes it switch briefly to CW rotation (from [114]). (b) Self-correlation function of the log of the persistence times, with exponential fit (red line) of characteristic a memory time $T_M = 19\,\mathrm{s}$ (from [115]). (c) Distribution of the CCW rotation sequence as a direct proxy for the run times (data from [105]). Solid line : power law of exponent -2. (d) CheY-P concentration Y as a function of time fluctuates around its mean value $\bar{Y}$ with a standard deviation σ_Y and is temporally correlated on a typical memory time T_M. (e) Switch from run to tumble state is mediated by the varying energy barrier $\Delta G_0(Y)$. This transforms the Gaussian distribution of Y into a log-normal distribution of run times τ_r.

Success of the BV model

As a consequence this model provides an internal dimensionless variable :

$$\delta X(t) = \frac{Y(t) - \bar{Y}}{\sigma_Y} \tag{II.31}$$

describing an apparent "mood" of the bacterium defining its run times preferences at a given time. When $\delta X \gg 1$ the bacterium forages its near-environment whereas for $\delta X \ll 1$ it explores a larger area (figure II.15a).
The parameters of the model are calibrated in [115]. Among other things, it has successfully described the distribution of surface residence times [92] (see figure II.15b).

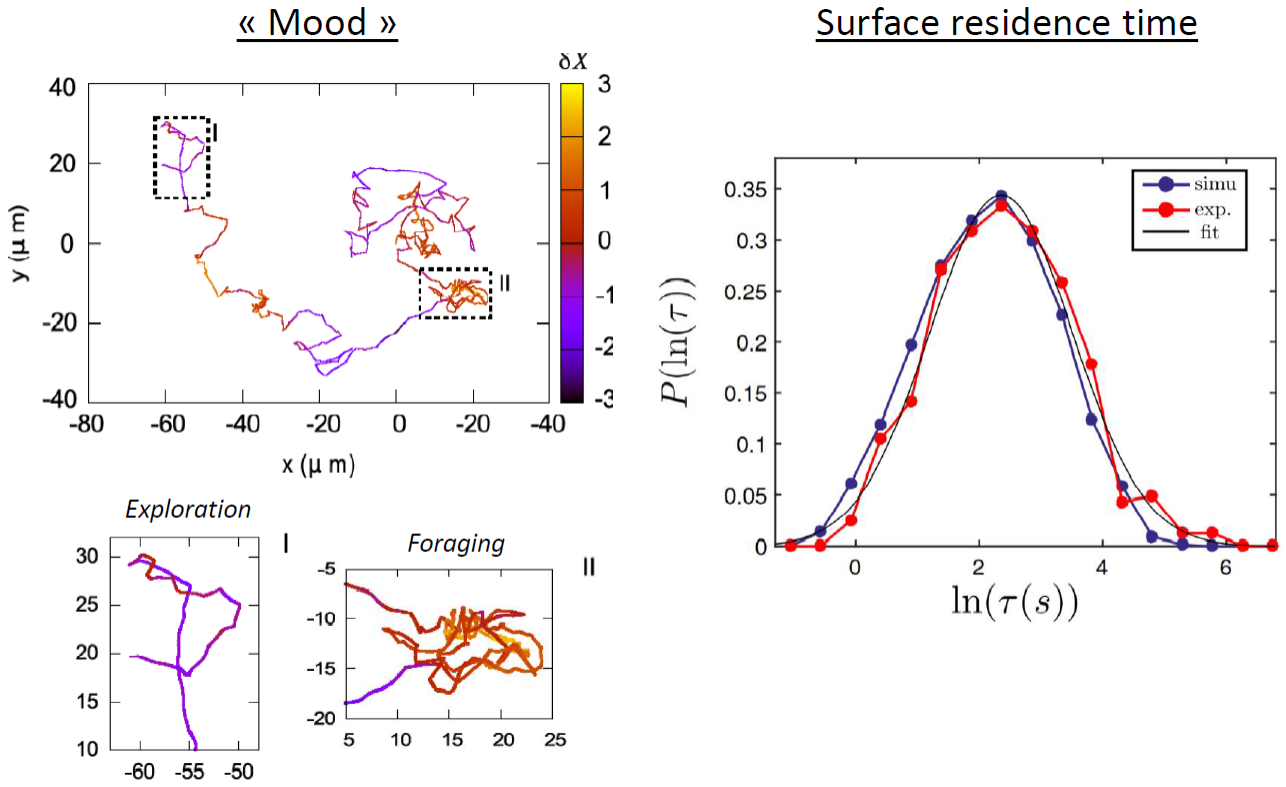

FIGURE II.15 – Consequences of the BV model on the behavioral variations of the sequence of run times experience by an individual. (a) A typical numerical trajectory implementing the BV model with the "mood" in color (2D projection of a 3D track). Sometimes the same swimmer forages (I : $\delta X < 1$), sometimes it explores (II : $\delta X > 1$). (b) Distribution of the logarithm of surface residence times τ. BV model reproduces the log-normal distribution observed experimentally for wild-type E. coli (from [92]).

We will study the fundamental implications on the large-scale transport properties of such a large and temporal run times dynamics, specifically under confinement, in the following chapter III.

Chapter III

Bacteria exploring simple fluids under confinement

In their natural environment, peritrichous bacteria such as E. coli undergo run and tumble kinematics, alternating between three-dimensional swimming and quasi-2D exploration of surfaces. In the absence of boundaries and in a chemically uniform environment, the combination of run and tumble leads to a 3D diffusive process [4]. In numerous practical situations, such as mucus barriers, physiological ducts, natural soils, porous media, the presence of low-dimensional substrates alters this simple picture and appears as a key to control the large-scale transport and contamination properties [116, 117]. However, while studied in detail for passive particles [118, 119] and despite these crucial practical consequences, the interplay between 3D and 2D motion for microswimmers remains poorly understood both theoretically and experimentally. Here, we address this fundamental question by combining experiment and theory using a simple prototypical setup in which bacteria swim in an environment bounded only by the presence of two parallel surfaces separated by a height H (see figure III.1). We show that the emerging dispersion process along the plane differs from the boundless limit and explicitly depends on the confinement height as well as on specific features of the surface kinematics. To describe the exploration process, we use the "behavioral variability" (BV) model [115], which has recently been shown to be successful in describing bacterial residence time [92] and backflow contamination [120]. This model incorporates the fluctuations of a slowly varying internal molecular variable, called "the mood", that triggers the run-to-tumble events. In this work we have adapted it to additionally take into account the circular kinematics at surfaces.

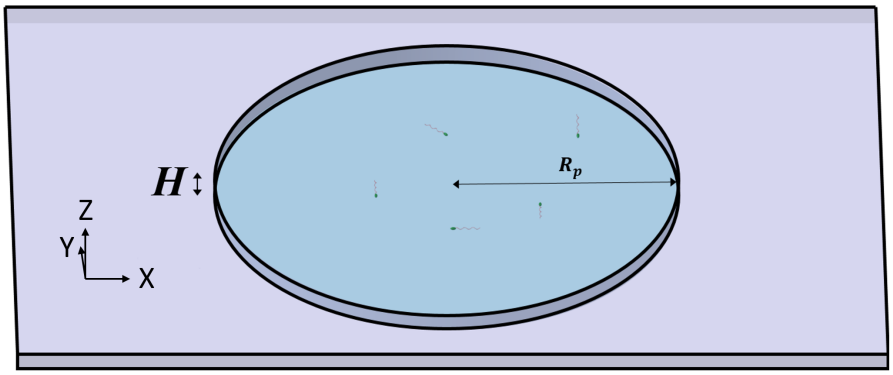

FIGURE III.1 – Sketch of the experimental cell. Bacteria swim in a pool delimited by two parallel plates separated by a confinement height H. The other dimension of the pool $R_p \sim 1\,\text{cm}$ can be considered as infinite when compared to bacterial exploration distances during the time of the experiment. Bacteria inside the pool are magnified for visualization. (Illustration by Xavier Benoit-Gonin, PMMH)

To understand the impact of confinement under the influence of surfaces, on the exploration of microorganisms and after introducing the experimental setup, we first study the surface kinematics of a "smooth-swimmer" (i.e non-tumbling) E. coli strain. We take the opportunity to question the observed kinematic variability through the prism of morphology. Armed with this knowledge, we finally study the exploration of "wild-type" bacteria under variable confinement heights (see figure III.1).

III.1 3D Lagrangian tracking of fluorescent E. coli

In the PMMH laboratory, it has been developed since 2015 [121] a motorized microscope suited to track bacteria which has led to successful achievements in the understanding of bacterial exploration processes such as temporal variability in the run times [115], Bretherton-Jeffery trajectories in Poiseuille flow [122], log-normal distribution of surface residence times [92] or frustrated run and tumble in nematic liquid crystals [41]. In this section, I briefly summarize the setup, provide the settings I used and highlight the problems I fixed.

III.1.1 Bacterial strains

The E. coli strains AD62 and AD63 [54] we use are derived from the strain AB1157, itself derived from a K-12 : the first strain to be used in a lab isolated in 1922. AB1157 has been genetically modified (fliC mutation) so that the flagella can be tagged by a fluorophore (Alexa 647 C2 malmeide) giving rise to AD62. AD63 is a genetically modified version of AD62 where the gene responsible for the bacterial reorientation has been suppressed. These genetic modifications can be simply written this way in the biological literature :

- AD62 = AB1157 fliC(S353C)
- AD63 = AD62 Δ(cheY)

Moreover, a plasmid has been added to the strains so that they become resistant to ampicillin (an antibiotic) and express Green Fluorescent Protein (GFP). In simple words : AD62 and AD63 are fluorescent when cultured with ampicillin and their flagella can bind with a fluorophore (as Alexa 647 C2 malmeide). AD62 can tumble and will be referred as "wild-type" (WT) whereas AD63 cannot (ΔcheY) and will therefore be referred as "smooth-runner" (SR).

III.1.2 Motorized microscope

The inverted optical microscope has a mounted 3D motorized stage (two mechanical motors on the horizontal plane and a piezo motor for the vertical plane) that holds the glass slides. It is possible to use it in bright field (transmitted light) but also in fluorescence (reflected light) thanks to the LED source. A CCD camera can capture the images in focus and transmit them to the computer. The computer can control the 3D platform and a TTL trigger is used to synchronize the position of the platform with its associated image at given frequency (figure III.2). Objective "C-Apochromat 63x/1,20 W Korr M27" (referred as 63xW) is used with both the blue and the red source to excite respectively the GFP (on the body) and the Alexa Red fluorophore (on the flagella). Combined with reflector 90HE, a dichroic mirror then splits the wavelength emitted by the body and the flagella on two different areas of the camera chip (top and bottom). These two area are adjusted and calibrated with a sight before each use to then be able to combine them adequately in post-processing.

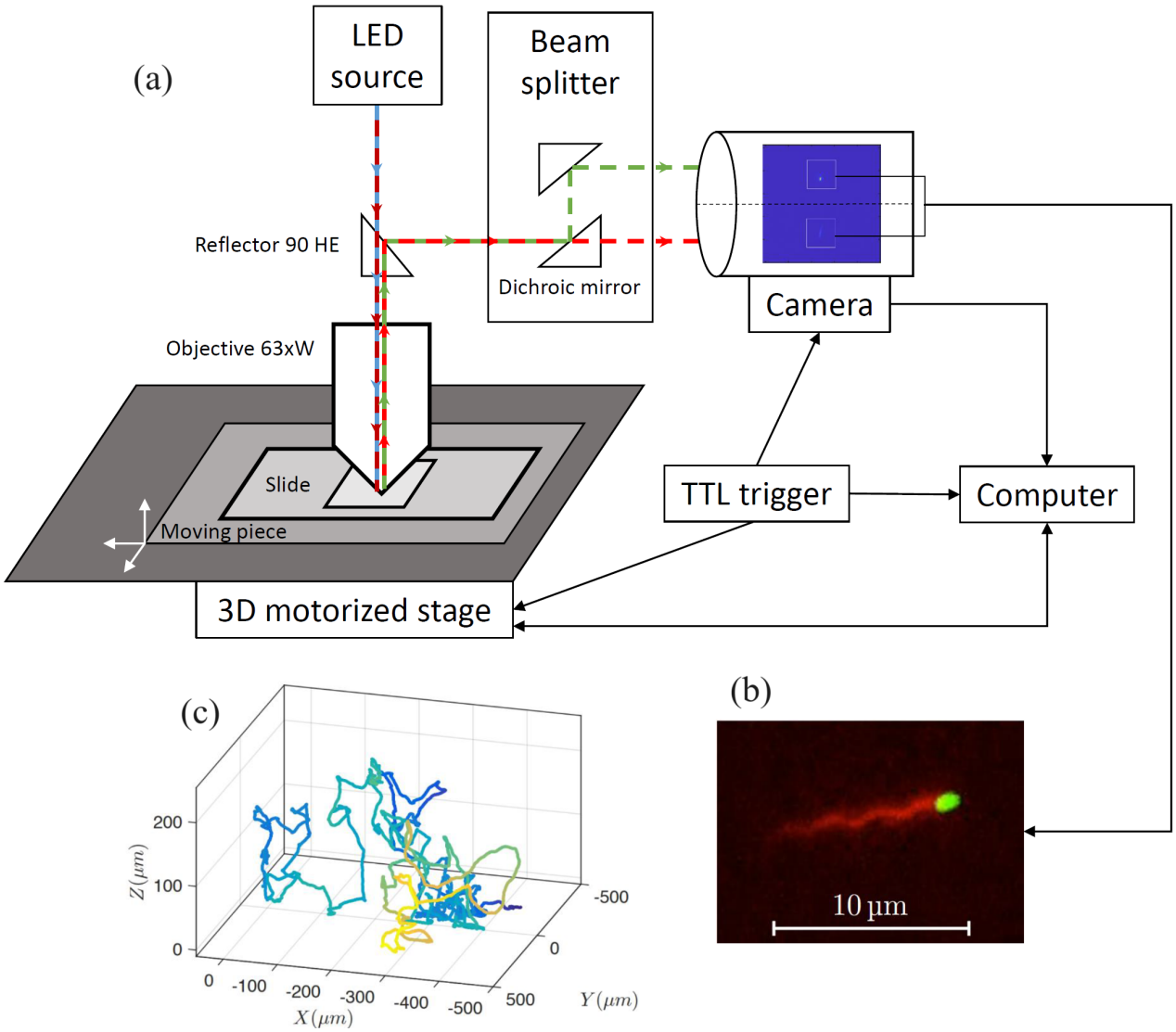

FIGURE III.2 – Tracking system. (a) Experimental set-up : The LED source emits light beams at chosen wavelengths. Fluorescent bacteria are excited and emit light (green for the body and red for the flagella) that is reflected to the camera. A dichroic mirror guide the different wavelengths at different locations on the camera chip. The image is treated by the computer to determine the displacement of the 3D motorized stage in order to keep the bacteria in focus and in the center of the image. The 3D motorized stage informs its current position. Every element is synchronized through a TTL trigger. Finally, we can visualize both the body (in green) and the flagella (in red) while getting the trajectory (color is for the tracking time, scale is not known). Bacterial image (b) and trajectory (c) from [123].

Algorithm rules

Beyond engineering considerations, all what is needed to track an object is to know its current displacement from the focal point at the intersection of the focal plane and the optical axis. In the XY plane (plane of visualization), this displacement can be obtained by finding the object closest to the center and taking its center of mass (where the mass is the pixel intensity). It is more difficult to find the displacement in the Z plane (orthogonal to the plane of visualization). Actually the method takes the advantage that the defocusing pattern of the object is not symmetric along Z (due to spherical aberrations). Indeed, when looking from above the focal plane, a ring appears around the object (airy disk) whereas when looking from below, the object gets blurred and loses intensity. This assessment especially holds when the

correction ring of the objective (which is here to apply an optical correction of the glass slide) is put on 0.19 μm for a coverslip#1. In addition the profile is more robust with z variations with this setting. We then adopt this configuration.

To keep the bacterium in focus, the algorithm aims at minimizing a robust quantity : the peak width at half maximum PW extracted from the radial intensity profile. It is minimal when the object is in focus $\Delta z = 0$ (see figure III.3). Without other criteria, it is difficult to know if the object is above or below its focus point. To keep the object in focus, the vertical position must be constantly readjusted then leading to inherent noise in vertical direction definition. Note that a zero-crossing method (developed in chapter V), instead of this method of minimum, would indeed improve the accuracy of the tracking.

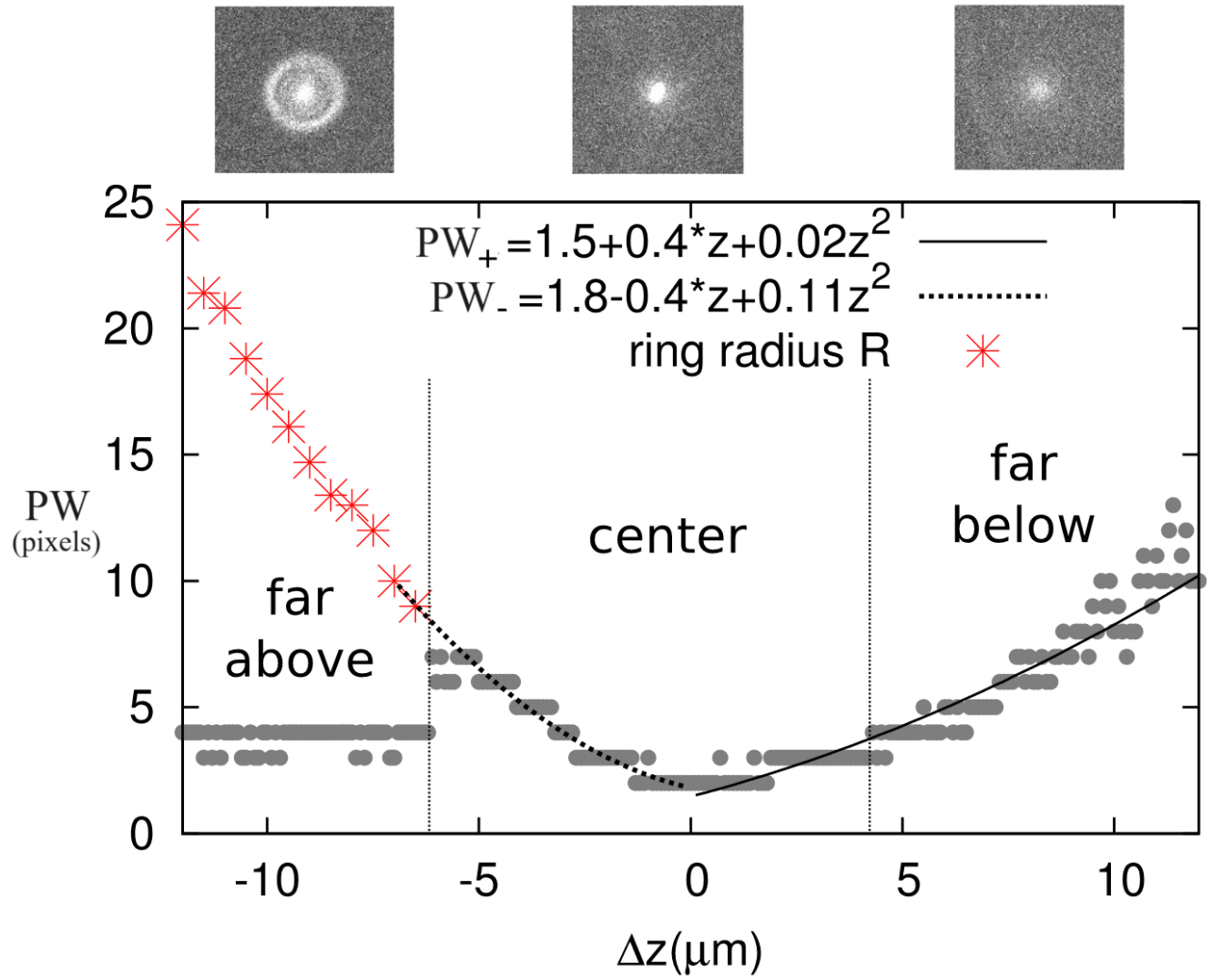

FIGURE III.3 – Peak width at half-maximum PW as a function of displacement Δz from focal position. In the center area, for a given PW there are two solutions for the displacement Δz : one cannot predict deterministically if the object is above or below its focus position, leading to oscillations around the focus position $\Delta z = 0$. Far above and far below the focus, some criteria allow to know the displacement deterministically (namely the presence of an optical ring when far above and a loss of signal when far below). Adapted from [121].

Correction of the regressions

When I arrived at the lab, impacted by the covid crisis, the tracking experiment did not work fully and reliably and it took some time to fix the regressions (i.e, new settings or imple-

mentations leading to malfunction). Actually, two problems were combined making it harder to put it back in working conditions :

1. an algorithm was used to adjust the maximal value of intensity at focus during the track, which decayed due to photobleaching. This algorithm was not robust and we first replaced it by changing the value manually during the track.
2. the correction ring of the objective, originally used to apply an optical correction to the glass thickness of the coverslip, had been set to 0.19 mm when developing the algorithm whereas it was set on 0.15 μm at my arrival. This led to important differences in the Z-pattern as shown in figure III.4, directly impacting the quality of the tracking.

After fixing those issues, ultimately more than a year after the beginning of my PhD, the tracking experiment was enjoyably back on its feets.

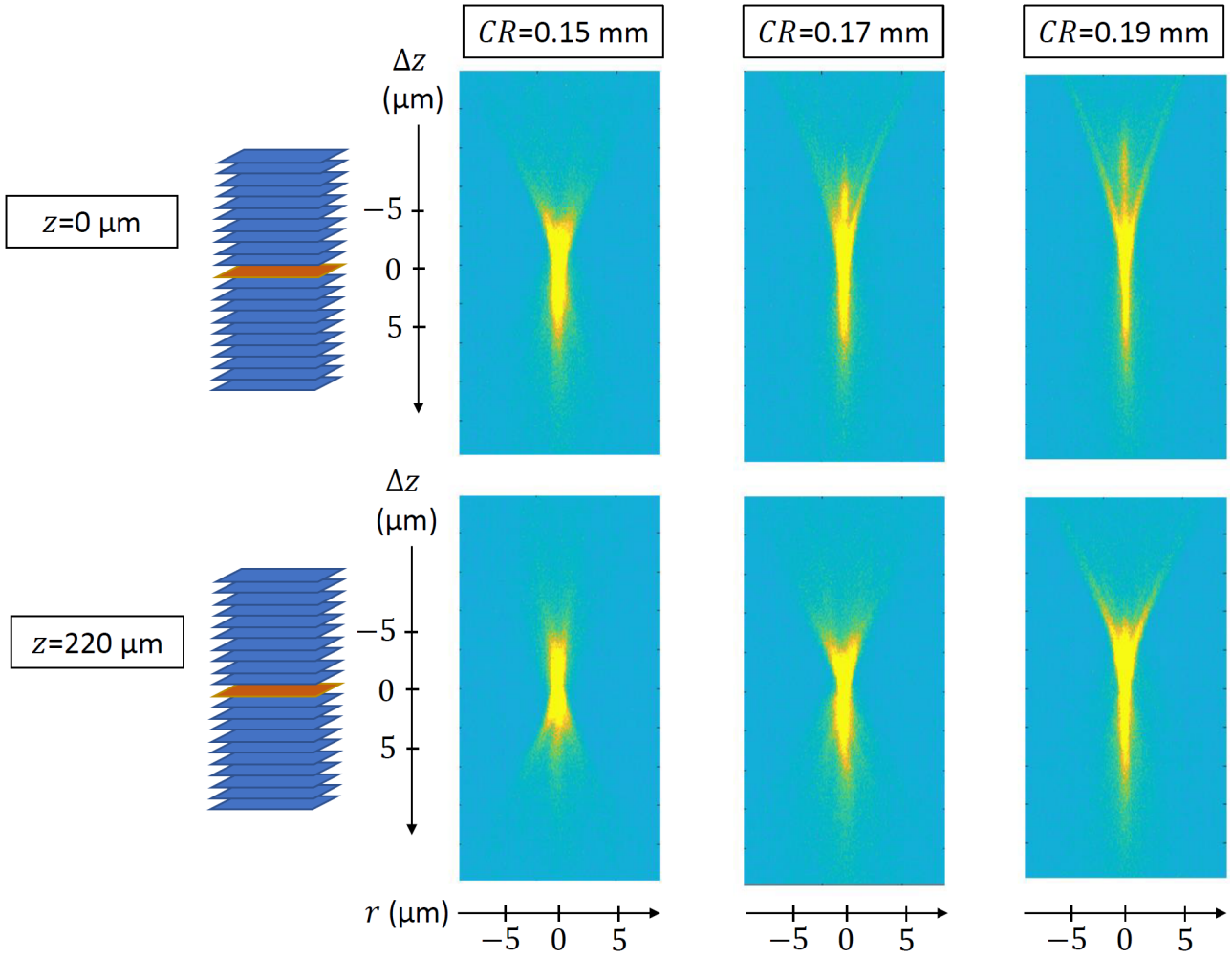

FIGURE III.4 – Z-pattern : Radial intensity (in color) at different defocussed planes Δz, and at different distances z from the surface and for different values of the correction ring CR. Z-pattern is influenced by CR and z. It depends less on z when $CR = 0.19$ mm. The algorithm is optimized for $CR = 0.19$ mm.

III.1.3 Microfluidic cell

The experimental cell consists in a spacer drilled in its center between which a bacterial solution is sandwiched. We use ultraclean thick slides to eliminate bending and minimize impurities on one side and a coverslip #1 on the other side facing the microscope objective. The

spacer is made of a double-sided adhesive (for instance, Gudy 804 of nominal thickness 105 μm) hollow-punched $\varnothing = 14$ mm. This forms a "pool" in which bacteria swim in an environment only limited by the presence of two parallel surfaces separated by a distance (height) H (see figure III.5).

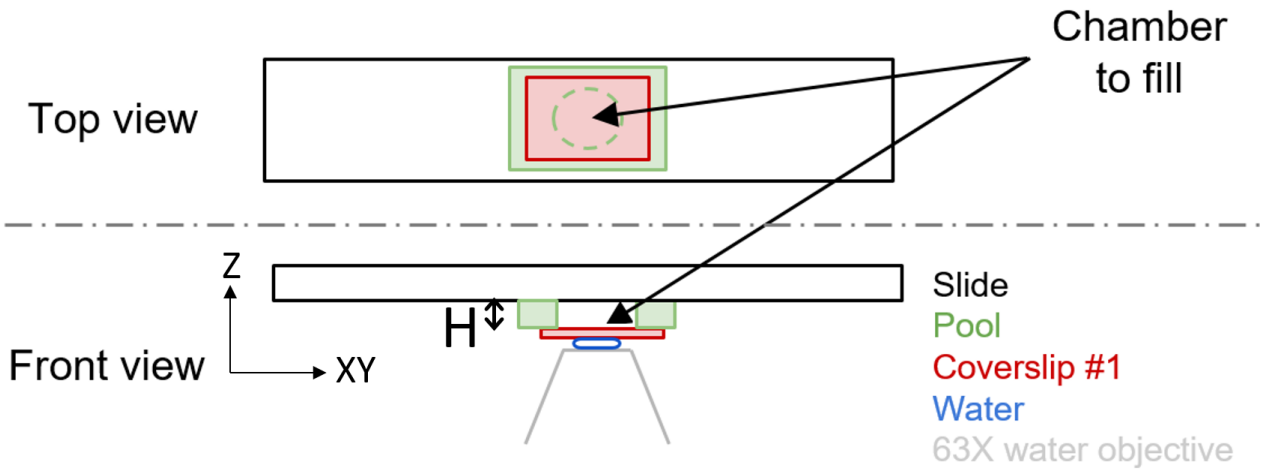

FIGURE III.5 – Sketch of the experimental cell. Bacteria are sandwiched between two slides separated by a distance $H = 50 - 220\,\mu$m, while freely exploring laterally their environment.

III.2 Smooth-swimmer E. coli exploration of solid surfaces

The presence of surface is ubiquitous in natural habitats of microorganisms such as in the gut inner mucus layer [49], cell walls in our body linked with biofilms formation [124] and ultimately infectious diseases [125]. Hydrodynamic interactions bring and trap [85] pusher-type microswimmers on flat surfaces where they swim circularly instead of straight [93]. The main mechanism to escape flat surfaces has been shown to be tumbling processes [92]. Here we study a non-tumbling mutant strain of E. coli that we refer to as a "smooth-swimmer" from which the protein CheY whose phosphorylation to CheY-P is responsible for the tumbling process has been genetically removed. This mutant displays very long residence times on surfaces [123] characterized by a noisy chiral motion leading to a diffusive exploration at large times. This surface exploration can be affected by several intrinsic and external parameters :

- passive thermal noise acting on the body and on the flagella [107].
- gyration radius, speed and speed fluctuations [126].
- presence of obstacles [36].
- intermittent motion with on-place rotation [127].

We show how the surface exploration of the E. coli smooth-swimmer mutant we study here mostly depend on few parameters easily accessible, even for short trajectories : the speed, the gyration radius and a passive rotational diffusion coefficient.

III.2.1 Stochastic model of surface kinematics

Equations for noisy chiral motion in 2D can be written :

$$\frac{d\mathbf{r}(t)}{dt} = \mathbf{V}(t) = V\mathbf{e}(t) \tag{III.1}$$

$$\mathbf{e}(t) = \begin{pmatrix} \cos\left[\theta(t)\right] \\ \sin\left[\theta(t)\right] \end{pmatrix} \tag{III.2}$$

$$\frac{d\theta(t)}{dt} = \Omega + \sqrt{2D_r}\xi(t) \tag{III.3}$$

where V is the swimming speed, Ω is the rotation rate, D_r is the rotational diffusion coefficient and ξ a white noise (see figure III.6).

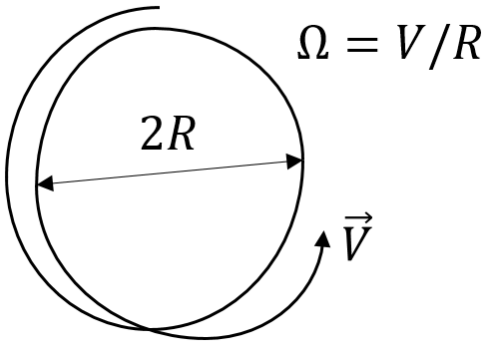

FIGURE III.6 – Sketch of a 2D noisy chiral trajectory of parameters V the swimming velocity and Ω the rotation rate. The circle is not perfect because of a rotational diffusion coefficient D_r.

We aim at computing the diffusion coefficient :

$$D = \lim_{t\to\infty} \frac{\langle \mathbf{r}^2(t)\rangle}{4t} \tag{III.4}$$

The mean square displacement $\langle \mathbf{r}^2(t)\rangle$ is then :

$$\left\langle \mathbf{r}^2(t)\right\rangle = \int_0^t \int_0^t \langle \dot{\mathbf{r}}(t_1)\dot{\mathbf{r}}(t_2)\rangle \; dt_1\, dt_2 \tag{III.5}$$

$$\langle \dot{\mathbf{r}}(t_1)\dot{\mathbf{r}}(t_2)\rangle = V^2 \langle \mathbf{e}(t_1)\mathbf{e}(t_2)\rangle \tag{III.6}$$

The computation of $\langle \mathbf{e}(t_1)\mathbf{e}(t_2)\rangle$ is provided in [126] and leads to :

$$\langle \mathbf{e}(t_1)\mathbf{e}(t_2)\rangle = e^{-D_r|t_1-t_2|}\cos\left(\Omega|t_1-t_2|\right) \tag{III.7}$$

By symmetry of the absolute value function :

$$\int_0^t \int_0^t e^{-D_r|t_1-t_2|}\cos\left(\Omega|t_1-t_2|\right)\; dt_1\, dt_2 = 2\int_{t_1=0}^t \int_{t_2=0}^{t_1} e^{-D_r(t_1-t_2)}\cos\left[\Omega\left(t_1-t_2\right)\right]\; dt_1\, dt_2 \tag{III.8}$$

This integral can be derived by developing the cosine and first integrating on t_2 :

$$\begin{aligned}\int_0^t \int_0^t \langle \mathbf{e}(t_1)\mathbf{e}(t_2)\rangle \; dt_1\, dt_2 = 2\Bigg[&\int_0^t e^{-D_r t_1}\cos\Omega t_1 \left(\int_{t_2=0}^{t_1} e^{D_r t_2}\cos\Omega t_2\, dt_2\right)\; dt_1 \\ &- \int_0^t e^{-D_r t_1}\sin\Omega t_1 \left(\int_{t_2=0}^{t_1} e^{D_r t_2}\sin\Omega t_2\, dt_2\right)\; dt_1\Bigg]\end{aligned}$$

from which the exact solution is :

$$\left\langle r^2(t)\right\rangle = 2V^2\left[\frac{D_r t}{D_r^2+\Omega^2} + \frac{(D_r^2-\Omega^2)\left(e^{-D_r t}\cos\Omega t - 1\right)}{\left(D_r^2+\Omega^2\right)^2} + \frac{2D_r\Omega e^{-D_r t}\sin\Omega t}{\left(D_r^2+\Omega^2\right)^2}\right] \tag{III.9}$$

This expression will be used to fit the experimental trajectories.
Taking the limit finally leads to :

$$D = \lim_{t\to\infty}\frac{\langle \mathbf{r}^2(t)\rangle}{4t} = \frac{V^2 D_r}{2(D_r^2+\Omega^2)} \tag{III.10}$$

III.2.2 A typical experimental trajectory

The tracking setup allows for very long trajectories at surface. A typical trajectory of 500 s is shown in figure III.7.a : circles of constant radii appear and their time-local centers move with time. The speed distribution shown in figure III.7.b can be fitted by a Gaussian curve and its mode defines a swimming speed V. Indeed fluctuations mostly come from our experimental measurements and strongly depend on the smoothing time we use for the analysis (0.2 s in this study), whereas the mode determination is, as a maximum, robust. The orientation auto-correlation function (ACF) shown in figure III.7.c displays damped oscillations fitted by an exponentially decaying function (of characteristic time τ_p) in a sinusoidal envelope (of pulsation Ω) :

$$f_{ACF} = e^{-t/\tau_p}\cos\Omega t \tag{III.11}$$

The fit is done only on the 3 first seconds of the ACF and is shown to describe very well longer times for most trajectories. The self-averaged MSD of figure III.7.d is defined as :

$$\left\langle \Delta\mathbf{r}^2(\Delta t)\right\rangle = \frac{1}{T-\Delta t}\int_0^{T-\Delta t}\left[\mathbf{r}(t+\Delta t)-\mathbf{r}(t)\right]^2\,dt \tag{III.12}$$

with T the duration of the track. The expression III.9 is used with the parameters V, $R = V/\Omega$ and $D_r = 1/\tau_p$ extracted before (shown in solid line) very close to the best possible fit (shown in dashed line). The theoretical curves describe very well the oscillations and the diffusion coefficient (i.e, the slope at large time lags). Note that we restrain the study of the MSD and the orientation ACF to $\Delta t < 10\% T_{obs}$ due to statistical reasons of self-averaged quantities.

We have seen that the theory derived above can describe our experimental measurements and that we can estimate the diffusion coefficient from the speed distribution and the orientation ACF fitted on the three first seconds. Let's notice that, sometimes, the circle center displaces abruptly or the bacterium escapes the surface. It is rare but can be observed and such sharp reorientations are out of the theoretical picture we present here. Let's have a look at what could cause those particularities.

III.2.3 Mechanisms for non-tumbling reorientations

We hypothesize different mechanisms responsible for reorientations without active tumbling :

- Hitting dust impurities stuck on the surface.
- Flagellar reorganisation due to hydrodynamic instabilities in the bundle.
- Passive rotational diffusion (thermal fluctuations) inducing off plane kinematics, that can be coupled with wobbling.

We did not have time to study all this in detail. Tools are ready to check the role of impurities. Indeed, impurities cannot be seen in fluorescence, but we can now "replay" a track, i.e follow the same trajectory of a previously tracked object. In this case, by using white light instead of fluorescence, we would indeed see if an impurity is present when the bacterium escapes or

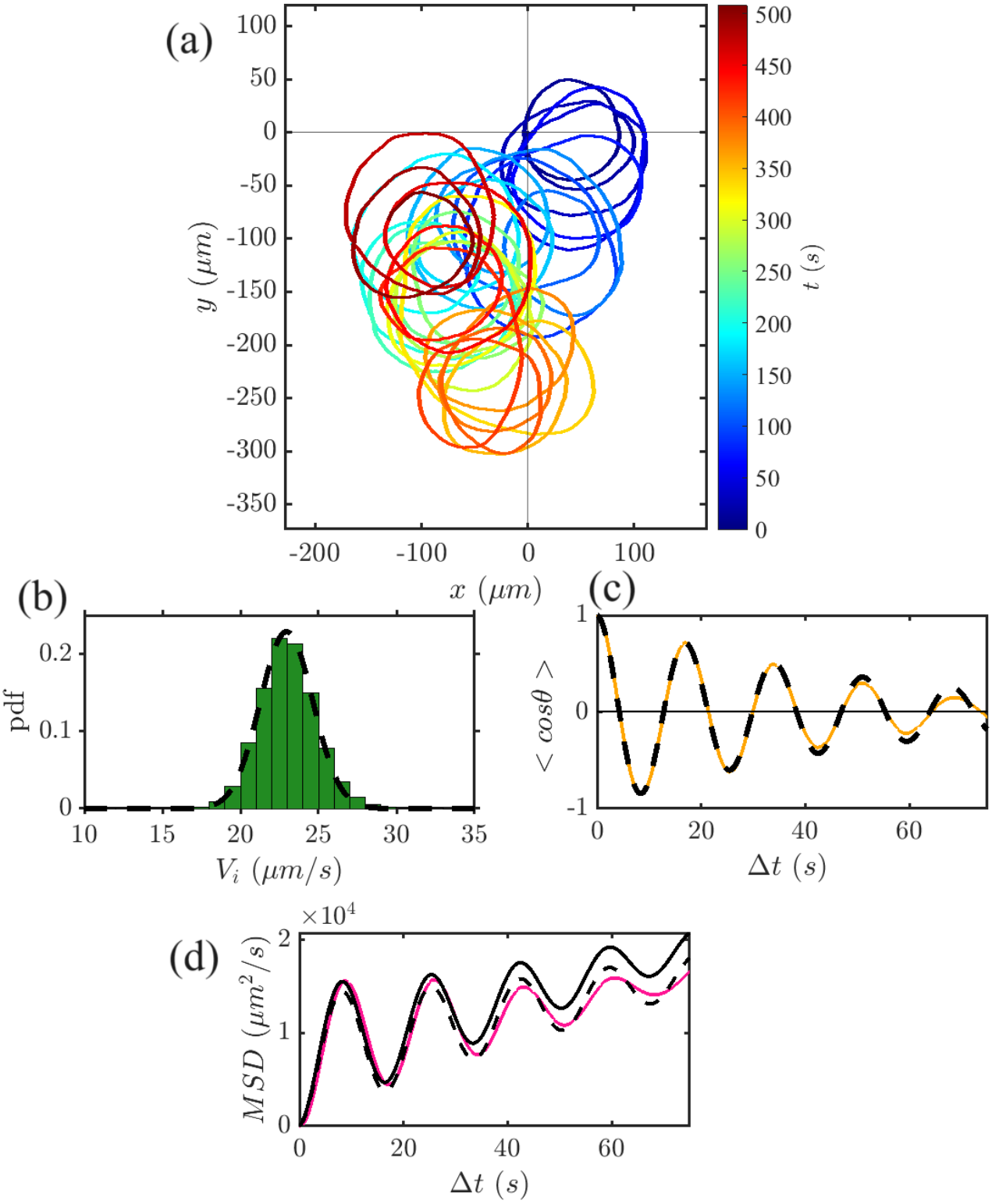

FIGURE III.7 – (a) 2D trajectory resulting from a tracking experiment with a smooth-swimmer followed during 500 s at a solid surface. (b) Distribution of instantaneous speeds V_i (green) and Gaussian fit of parameters V,σ_V (dashed line). (c) Orientation ACF (orange) and fit on $\Delta t < 3$ s with formula III.11 (dashed line). (d) Self-averaged MSD (pink) and theoretical prediction (solid black) from III.9 (with parameters fitted in previous graphs) and best fit (dashed black).

reorient sharply at surface. We also noticed, by monitoring reconstructed movies of bacteria with their flagella, that the bundle sometimes rearrange. For instance the body has been seen to perform a flip : the flagella that were at the back of the body (respectively to the motion) turn at the front and vice-versa. Passive (thermal) rotational diffusion is also a possibility for escaping the surface [90] and the eventual role of wobbling, i.e the body precession, is unclear [128].

We studied very long trajectories of non-tumbling E. coli at surface from which we can extract the main kinematic parameters : the swimming speed V, the rotation rate Ω and a rotational diffusion coefficent D_r. These parameters are sufficient to describe the diffusion coefficient D emerging from the mean square displacement computation. We have shown that all these quantities could be extracted for shorter tracks : V is almost instantaneously obtained and we require a track of duration $T_{obs} > 30\,\mathrm{s}$ to fit the orientation ACF on the three first seconds to extract Ω and D_r. In the next section we present 24 tracks of about 50 s, in which the flagella have been tagged. The quality of the bacterial visualization is optimal at surface. We confront the kinematic variability to the morphological variability and finally provide a range of diffusion coefficent D for these non-tumbling bacteria at surface.

III.3 Population variability : kinematics and morphology

Alex Le Guen, intern and now PhD student in the group, participated to this work.

Variability is inherent to biological systems. Variability can come from different sources :

- stochasticity of internal biochemical processes.
- gene expression that can vary from an individual to another (known as phenotypic variability).
- bacteria observed at a given time do not all have the same age and are not at the same step of their reproduction. The reproduction, during which a bacterium grows to finally divide, leading to a parent and a child.

This variability can lead both to different qualitative behavior (for instance some bacteria from the same culture will adhere to surfaces whereas some others will not) or quantitative differences (for instance bacterial speed, as well as the body size, can vary from simple to double). One must be aware of this and eventually take it into account to get a complete picture of the emerging phenomena for a given population. The literature lacks of data on this topic whereas the source of kinematic variability is often blindly attributed to the morphology. We take advantage of our set-up allowing for both visualization and trajectories, to investigate both morphological and kinematic properties of a collection of 24 bacteria. We provide new insights on their interplay.

III.3.1 Morphological parameters

To the best of our knowledge, this work is the first to relate directly the number of flagella of a swimming E. coli to its motion properties. To achieve this, we send high intensity UV light while tracking, progressively slowing down the speed of the bacterium to 0, typically in 100 s. We do that after the 50 s of tracking sufficient for extracting kinematic parameters. Debundling occurs making possible the counting of flagella individually (see figure III.8).

Based on progress in the visualization (by minimizing exposure time), we give a qualitative indicator of the quality of the bundle Q (see figure III.9) observed during the swimming. If the bundle looks like a unique helix we rate it 5/5. If flagella are not bundled at all we rate it 1/5.

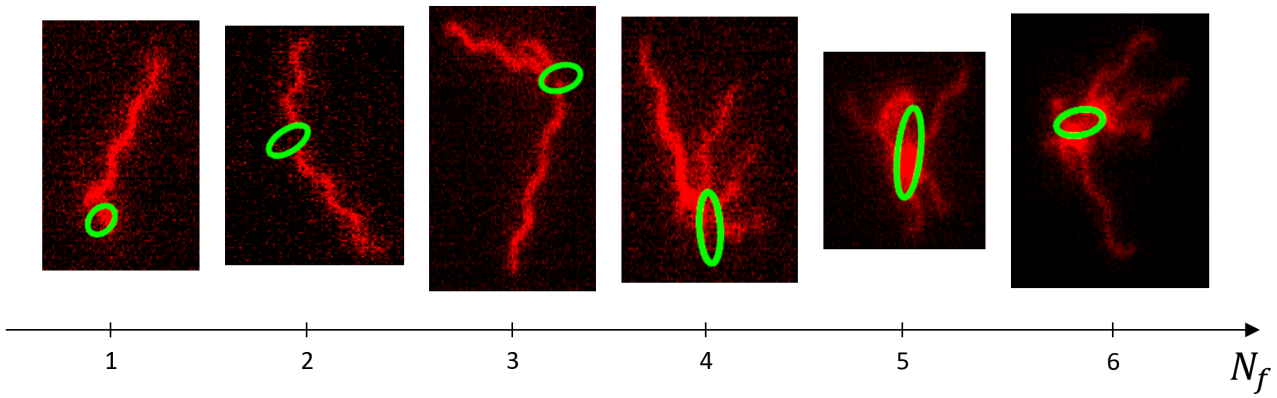

FIGURE III.8 – Snapshots of bacteria with different number of flagella N_f showing up after exposition to UV light causing motion stoppage. Body is replaced by its ellipsoidal fit for visualization. The number of flagella N_f is determined more precisely from a sequence of images.

3/5 corresponds to a case where a flagellum has shown to be hardly part to the bundle. We tried to extract more information on the bundle helicity (radius, pitch...) but, despite improvements, the visualization is generally not good enough and the variation between individuals not very significant. It could be achievable with more efforts.

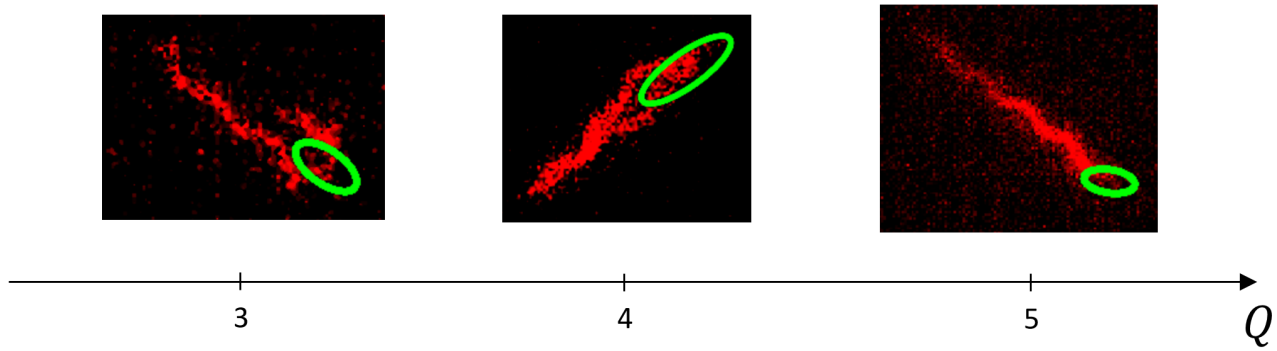

FIGURE III.9 – Snapshots of bacteria with different bundle quality. The quality increases with Q. $Q = 3$ if the bundle is composed of two distinct helices, $Q = 4$ if the bundle assembles far from the body, $Q = 5$ if the bundle really looks like a unique helix. At least two flagella compose the bundle for each displayed bacterium.

To get the body size and the bundle length, we first visualize a sequence of images and determine a pertinent image. We align the main axis of the bacterium with the horizontal axis of the image and plot the intensity profile along this axis (see figure III.10). The body length is the width at half-maximum. The bundle length is the distance between the back of the body and the ending point of the flagella (selected by eyes, the accuracy is less than $0.25\,\mu$m). For all measurements we obtained a constant body width $w_{body} = 1 \pm 0.1\,\mu$m. We intended to measure also the bundle width but the measurements turned out to be unreliable.

In figure III.11, we display the histograms and correlations between the measurable morphological quantities : body length $L_{body} = 2.5 \pm 0.5\,\mu$m, bundle length $L_{bundle} = 6 \pm 2.5\,\mu$m, number of flagella $N_f = 2 - 5$ and quality of the bundle $Q = 3 - 5$. The number of flagella depends on the body size : the longer is the body, the higher is the number of flagella (see figure III.11e). The bundle length does not increase with the number of flagella. Naively one could have thought that the growth of flagella was independent, leading to higher chance to find long flagella with higher number of flagella. Instead of that, it's more of the opposite. It can be interpreted as : the flagella share common resources to grow. Then, longer flagella are found

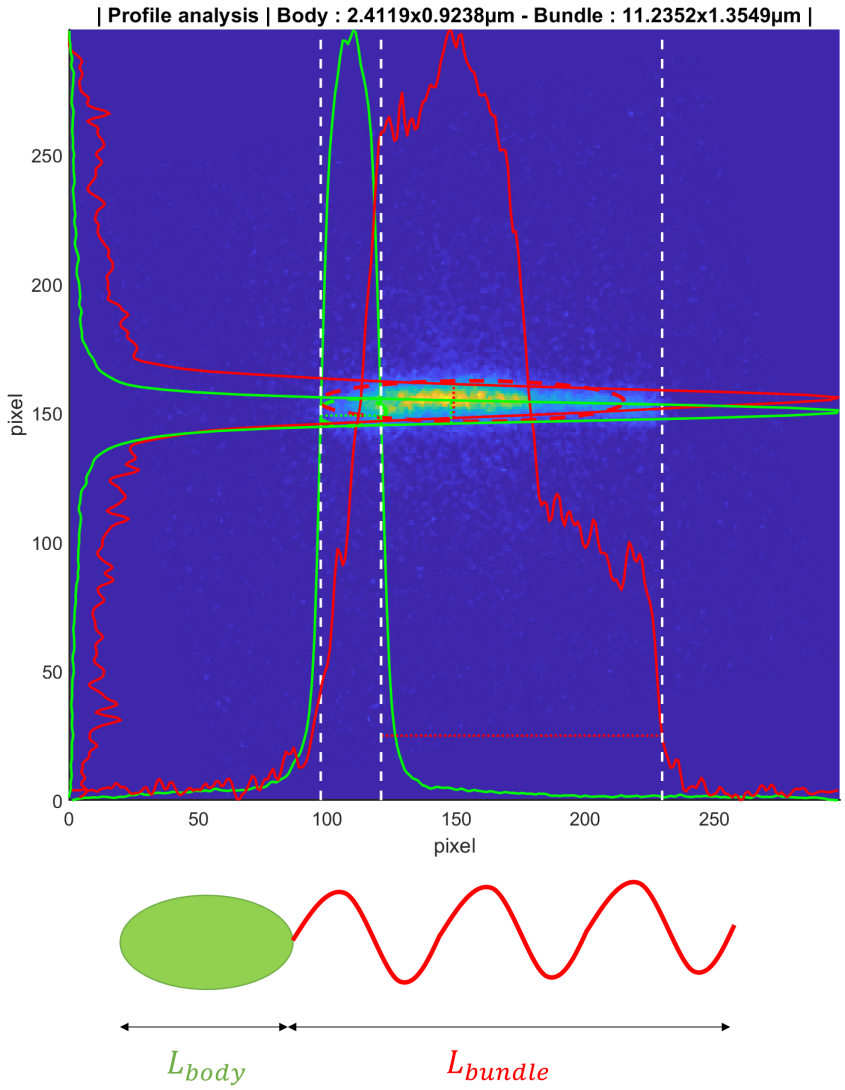

FIGURE III.10 – Extraction of geometrical parameters to characterize an E. coli swimmer : body size (green dotted line) and bundle length (red dotted line) through the intensity profile on the main axis. Background colormap is the light intensity. Red and green lines are light intensity profiles respectively for the flagella and the body.

with a smaller amount of them. Also, the bundle length is not correlated with the body length : one could think that longer body length would result in longer flagella because of maturation. It is not obvious from our data.

III.3.2 Kinematic parameters

In figure III.12 we display the histograms and correlations between the measurable motion quantities : the swimming speed $V = 28 \pm 7 \mu\text{m}\,\text{s}^{-1}$, the gyration radius $R = 10 - 40\mu\text{m}$ and the surface diffusion persistent time $\tau_p = 15 - 60\text{s}$.

Interestingly, despite variability, there is a significant correlation between the swimming speed and the gyration radius on surface : the faster the higher the gyration radius (see figure III.12e). From an hydrodynamic perspective, at low Re, the surface speed at surface should not affect the gyration radius. Indeed, at low Re, the system can be considered quasi-static, slow and fast kinematics result in the same motion provided no velocity-induced structural changes. Then we suggest that the speed is indirectly correlated with some morphological properties impacting the gyration radius, for instance a change of conformation of the flagellar bundle.

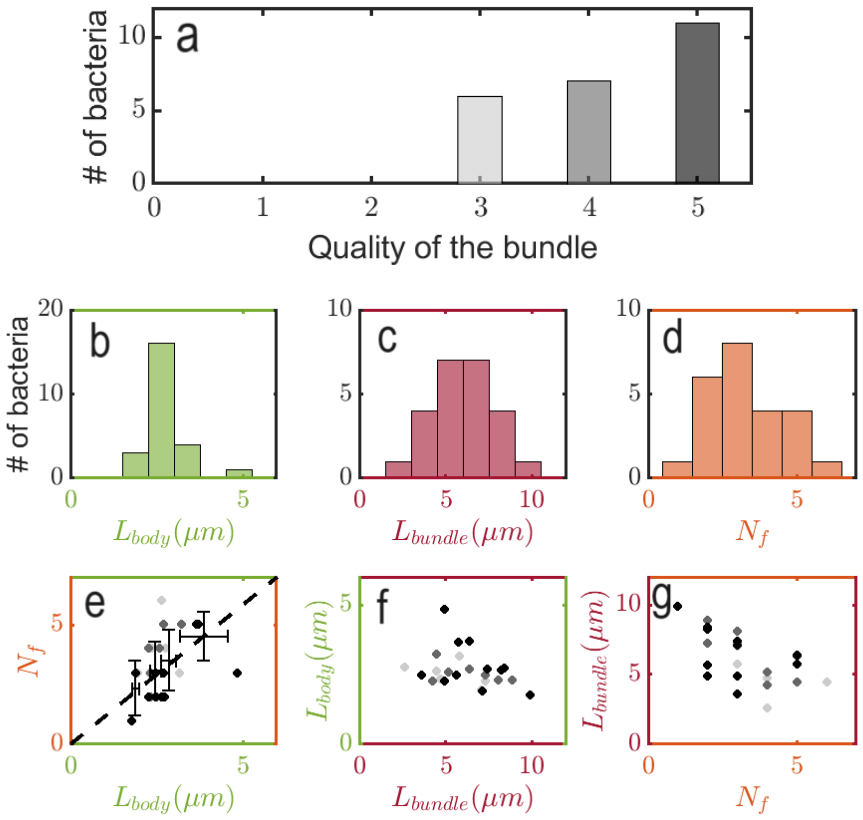

FIGURE III.11 – Morphological parameters : body length L_{body}, bundle length L_{bundle}, number of flagella N_f and quality of the bundle Q. (a) Histogram of the bundle quality. Note the grey color code that will hold for figure III.11, III.12 and III.13. (b,c,d) Histograms. (e,f,g) Raw cross-quantities.

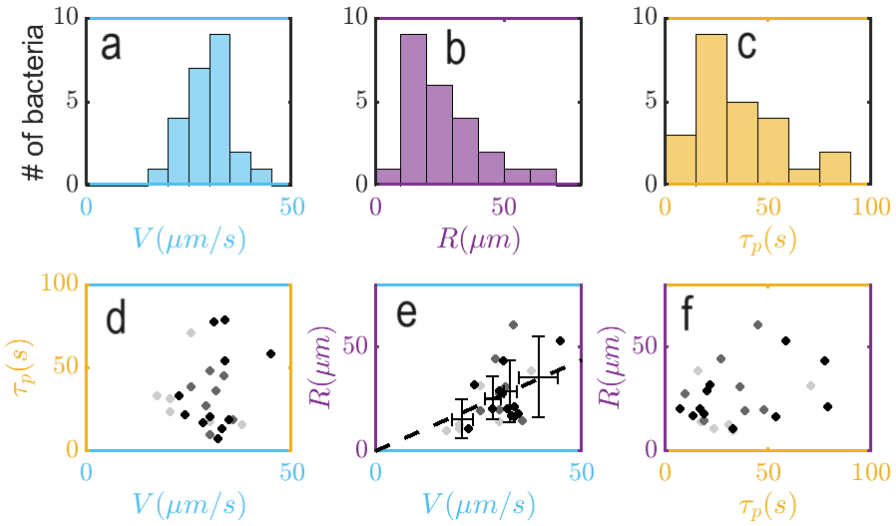

FIGURE III.12 – Kinematic parameters : speed V, the gyration radius R and the persistent time τ_p. Grey code corresponds to bundle quality Q. (a,b,c) Histograms. (d,e,f) Raw cross-quantities.

III.3.3 Influence of the morphology on kinematics

Let's now question the impact of the morphology on the motion of the bacteria. Morphological parameters are thought to be a major influence in the noticed variability in the motion of motile bacteria, as argued in many papers related to individual bacterial motion [93, 83]. We take the opportunity that our device allows for such a characterization to provide new insights in this debate. For the first time, we capture directly the number of flagella of swimming bacteria. We display histograms and correlations between morphological and kinematic parameters in figure III.13.

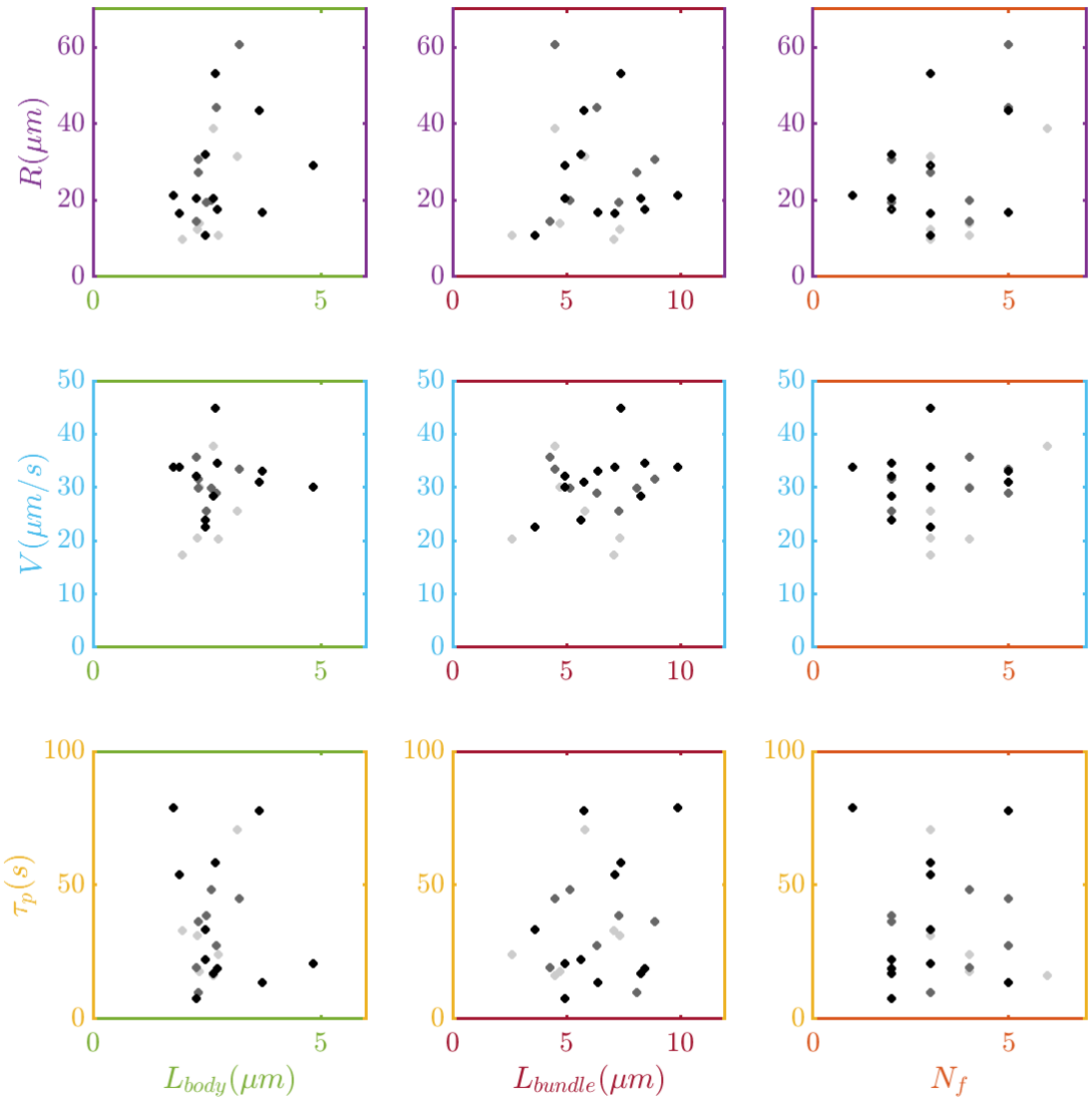

FIGURE III.13 – Mixing morphological and motion parameters. Raw cross-quantities. Grey code corresponds to bundle quality Q.

The principal component analysis (PCA) in figure III.14 has been kindly done by the statistical biologist Dr Arnaud Lheureux : L_{body} and N_f are correlated, together anti-correlated to L_{bundle}. V and R are correlated. However at this point we did not find any evidence for correlations between morphological and motion properties. Their relations are analyzed in a hydrodynamic context in the following.

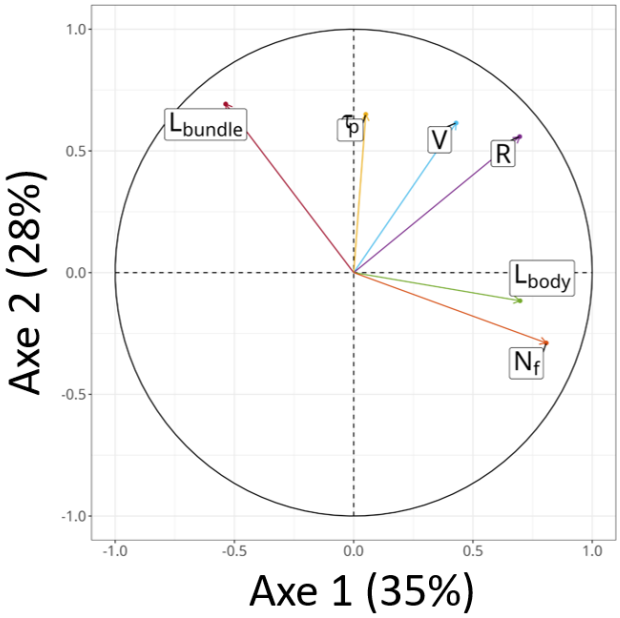

FIGURE III.14 – PCA analysis. Two vectors having close orientations are correlated. Two perpendicular vectors are uncorrelated. Two opposite vectors are anti-correlated.

Swimming speed

We compare the relation between the measured swimming speeds V as a function of the bundle length L_{bundle} with the ones presented in the introduction from Gaspard Junot (see figure III.15a). We note that our speeds are higher than his, because we add L-serine in our motility buffer. We lack of statistics to really confirm this trend, but for sure both datasets are not in contradiction.

Number of flagella is thought to explain the variability observed in the swimming speed. On the contrary, our data show an independence between the number of flagella and the swimming speed (fig. III.15b). This result suggests that the evolutionary advantage of multiflagellarity is not linked with speed.

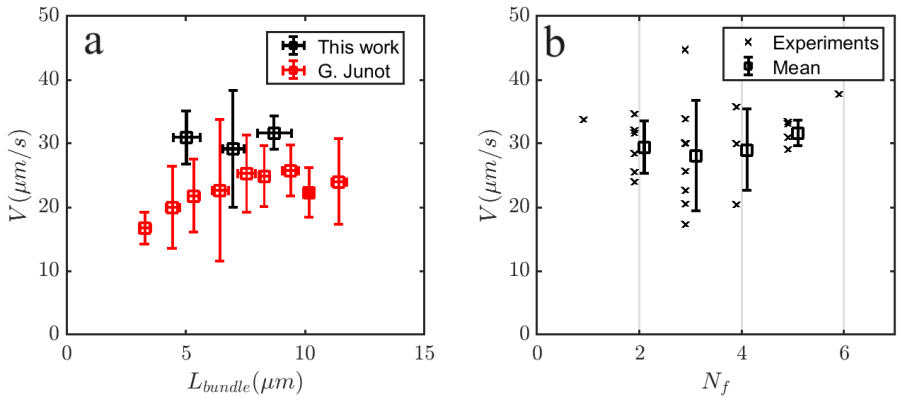

FIGURE III.15 – (a) Mean and standard deviations of the swimming speed V as a function of the bundle length L_{bundle}. Our data are not sufficient to confirm preliminary data from Gaspard Junot, previous PhD in the group (private communication). (b) Mean and standard deviations of the swimming speed V for fixed numbers of flagella N_f. Speed does not depend on the number of flagella.

Rotational diffusion coefficient

In a 3D passive case, the Brownian reorientation of an elongated object (of length L_{body} and width w_{body}) is [129] :

$$D_r = \frac{1}{\tau_p} = \frac{3k_bT\ln(2L_{body}/w_{body})}{\pi\eta L_{body}^3} \tag{III.13}$$

and a more precise expression for a prolate ellipsoid can be found in [130]. This model could apply to an unflagellated E. coli bacterium. In the active flagellated case that we study, this theory does not describe our observations (see figure III.16-left). However, the presence of flagella have been shown to stabilize E. coli orientation compare to unflagellated ones [107]. We find that mixing the body length with the bundle length :

$$L_{tot} = L_{body} + \alpha L_{bundle} \tag{III.14}$$

provides a better agreement with the theory (see figure III.16-right). $\alpha = 0.8$ provides the best agreement. This suggest that the rotational diffusion coefficient D_r is mostly from Brownian origin. It was not obvious since bacterial activity induce wobbling that could bring some hydrodynamic instabilities affecting the diffusion coefficient.

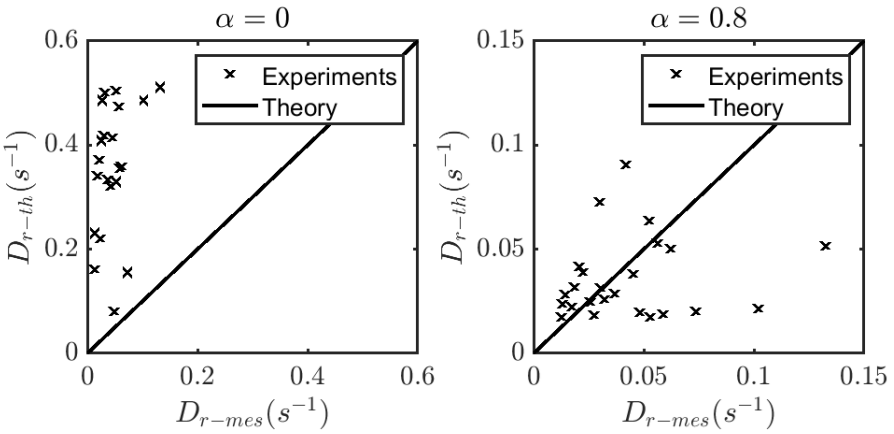

FIGURE III.16 – Rotational diffusion coefficient. Effective theory taking into account the bundle length as a function of the measured one using the mixing size model of equation III.13. (left) $\alpha = 0$: the bundle is not taken into account. (right) $\alpha = 0.8$: the bundle is taken into account.

Gyration radius

Finally, we revisited the problem of gyration radius studied experimentally and theoretically in [93] for E. coli that was cultured such as the body elongate. To compare with [93], we analysed our data using the radius of the sphere a that has the same viscous resistance as the prolate ellipsoid width $w = 1\,\mu$m and aspect ratio $\phi = L_{body}/w$:

$$a = \frac{4}{3}\frac{w}{\frac{2\phi^2-1}{(\phi^2-1)^{3/2}}\ln\left(\frac{\phi+\sqrt{\phi^2-1}}{\phi-\sqrt{\phi^2-1}}\right) - \frac{2\phi}{\phi^2-1}} \tag{III.15}$$

We confirm the same trend but with a shift (see figure III.17a,d) : increasing body length leads to increasing gyration radius, in disagreement with the theory that has been developed [93]. Our data match with a different explanation, the observed gyration radius can actually be related to the body size in an indirect way : longer bodies have more flagella (see figure III.17b,e). Depending on where they are located on the body, flagella could cause a steric hindrance, thus

repelling the body from the surface, enlarging the emerging circular motion. Thus the larger the number of flagella, the more likely the gyration radius is large (see figure III.17c,f). This explanation is quite convincing since it explains specifically the small gyration radius of the largest measured bacterium (blue circle in figure III.17a,b,c).

The shift observed on figure III.17 could also be explained by this argument. Anyway another possible explanation is based on the electrostatic interaction between the glass slide and the bacterium body. We suggest that salt concentration of the medium could be responsible of such a difference by screening the electrostatic interaction.

We attempted to take into account the bundle length in our analysis but it does not provide better insights.

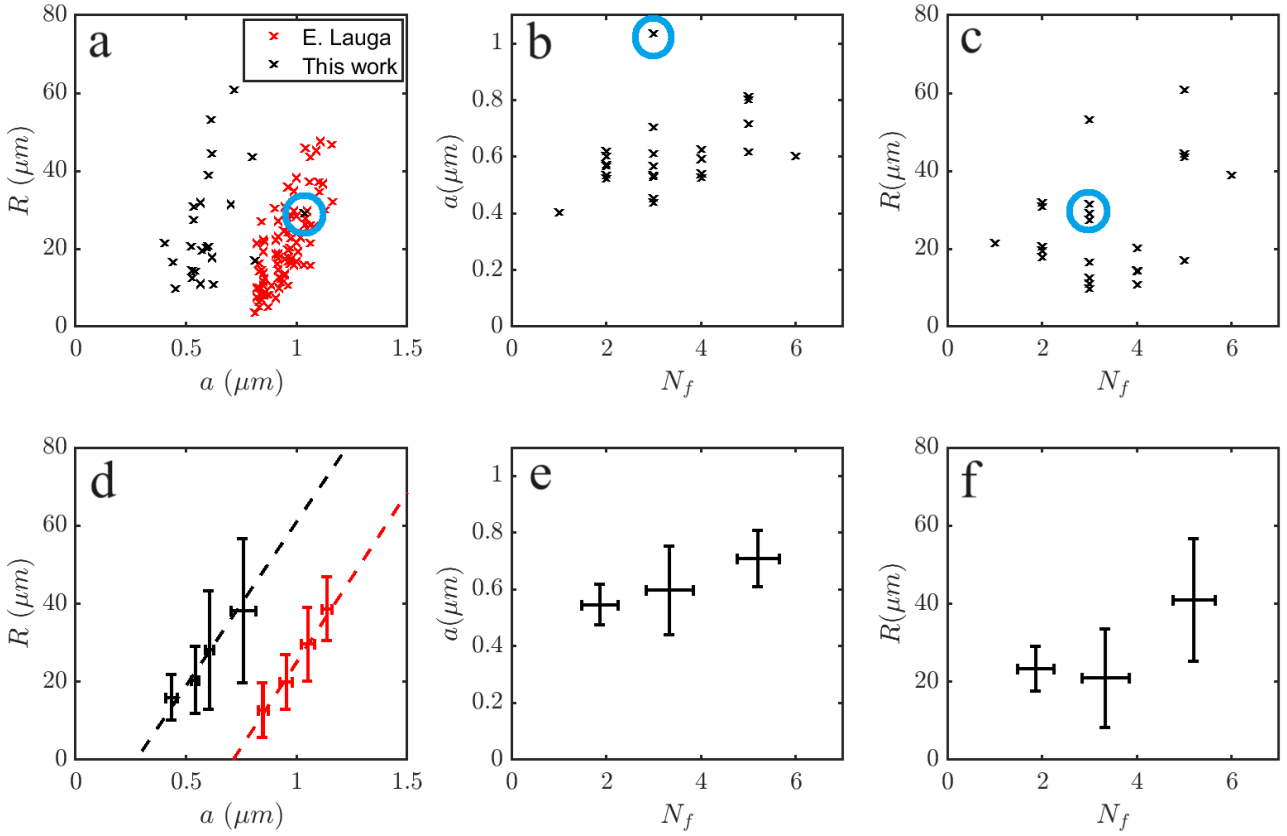

FIGURE III.17 – Gyration radius R as a function of morphological parameters : a new convincing explanation. (a,b,c) Raw data. (d,e,f) Bin-averages and standard deviations. (a,d) Gyration radius R as a function of the radius of the equivalent sphere a (formula III.15) and comparison with data from [93]. Dashed line : linear fit on bin-averages. The larger body point, far from the other, is surrounded by a "blue" circle and is not taken into account for the fit nor bin-average. (b,e) Radius of the equivalent sphere a as a function of the number of flagella N_f. N_f grows with a but blue point does not follow this trend with only 3 flagella. (c,f) Gyration radius R as a function of the number of flagella N_f. A larger amount of flagella causes a higher gyration radius, the "blue" point in no more far from the other points.

Translational diffusion coefficient

We finally compute the histogram of the emerging rescaled diffusion coefficient for each bacterium $\tilde{D}_\alpha = D/(0.5V_\alpha^2\tau_r) < 0.05$ with $\tau_r = 2.23\,\mathrm{s}$, where the scaling with the square of the velocity comes from equation III.10, that we will be introduced in the next section (equation III.21) which provides a typical order of magnitude for the diffusivity of smooth-swimmers at surface $\tilde{D}_{ss} = 0.01$.

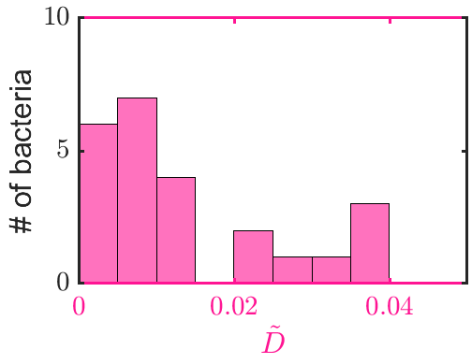

FIGURE III.18 – Histogram of the rescaled diffusion coefficient $\tilde{D} = D/(0.5V^2\tau_r) < 0.05$.

III.3.4 Discussion

We collected trajectories and videos of smooth-swimmers with their flagella at surface to understand in detail the movement of E. coli at the surface. Since they do not tumble, they stay at the surface very long time. The exploration of smooth-swimmers at surface is mostly explained with a simple stochastic model including their kinematic properties namely the speed, the gyration radius and the rotational diffusion coefficient. However, we cannot measure the speed fluctuations, which could slightly increase the ability of bacteria to explore surfaces. In the hope of understanding the variability between individuals, we compared the kinematic parameters with the morphological parameters we could extract : the body size, the bundle length and, most importantly, the number of flagella. Our data cannot confirm a previously measured relationship between the speed and the bundle length but, interestingly, we observed an independence between the speed and the number of flagella. The rotational diffusion coefficient can be estimated from the body and bundle length via a purely Brownian theory : the effects of activity, such as wobbling, do not seem to enhance the diffusion. Although it is known that the gyration radius increases with the body size, no hydrodynamic theory can explain it yet. Our data suggest an alternative mechanism, in which flagella could repel the body from the surface via a steric hindrance, and the variability arises from the randomness of the localisation of the flagella on the body.

For the non-tumbling mutant studied here, where the source of the reorientation is mainly passive, we provide a typical rescaled diffusion coefficient $\tilde{D}_{ss} = 0.01$. In the next section we compare this value in the context of the exploration of wild-type bacteria that not only reorient passively, but also actively, in a confined 3D environment.

III.4 Wild-type E. coli exploration in a confined 3D environment

This section is dedicated to the impact of confinement on transport properties. Experimental trajectories of bacteria are taken in the cell composed of two parallel plates separated by a height H described in introduction. For this part of my work, we collaborated with theorists Fernando Peruani and Marta Pedrosa Garcia-Moreno from the university of Cergy-Pontoise. Theoretical work resulting from this collaboration will not be discussed in this manuscript. Quentin Guigue and Solène Meinier, two interns in the group, also participated in this project.

III.4.1 From individual tracks to statistical analysis

From each experimental trajectory, we extract the kinematic characteristics from the track of the bacterium as well as an objective measurement of the height of the pool (see figure III.19). The speed distribution shows two Gaussian contributions coming from the runs and the tumble processes. We get the swimming speed V as the mode of the Gaussian fit on the values higher than the half-maximum (in dark green in figure III.19d). Since bacteria spend long times at surfaces, we use the Z-profile to determine by a double Gaussian fit the precise top and bottom location z_{top} and z_{bot}. We can then estimate objectively $H = z_{top} - z_{bottom}$ (see figure III.19c). The rotation rate Ω is measured via the orientation ACF taken on the aggregation of surface trajectories, with the same methodology discussed previously (see equation III.11 and figure III.19b). Hence, we obtained the gyration radius at the surface $R = V/\Omega$. The exploration is measured through the lateral diffusion coefficient D emerging from the self-averaged mean square displacement (MSD) computed like equation III.12 for the XY projection of the trajectory. The MSD is fitted via a "Fürth" function (equation III.17) for time lags less than one tenth of the total track duration $\Delta t < T_{obs}/10$ for statistical reasons to perform self-averaging (see figure III.19f) :

$$\left\langle X^2(\Delta t) \right\rangle = 2V_c^2\tau_c^2 \left(\frac{\Delta t}{\tau_c} - 1 + e^{-\Delta t/\tau_c} \right) \tag{III.16}$$

$$\underset{\Delta t \to 0}{=} V_c^2 \Delta t^2 \tag{III.17}$$

$$\underset{\Delta t \to \infty}{=} 2V_c^2\tau_c\Delta t = 2dD\Delta t \tag{III.18}$$

This function shows two limits, describing the ballistic and the diffusive regime depicted in II.3 and we can extract the lateral diffusion coefficient $D = V_c^2\tau_c/2d$. $d = 2$ in our study because of the XY-projection.

This methodology is rigorously applied to every track. Each track has been controlled by eye because, in addition to get better insights, it is important to check any problem that could have occurred during experiments.

We collected 92 tracks restricted in the range of tracking time $T_{min} = 200\,\mathrm{s} < T_{obs} < T_{max} = 300\,\mathrm{s}$. The lower bound is chosen such that the track is significant statistically. The higher bound is chosen such that the swimming speed is almost constant. Indeed a speed decay is observed after long tracking time due to the blue light used to excite the GFP fluorescence [76]. Experiments have been performed under different nominal heights $H \approx \{50; 105; 210\}\,\mu\mathrm{m}$ (see figure III.20b). However, for every experiment, because of some variability in adhesion and "sandwiching" process, an objective measurement of the height was performed which can vary by 5-10 microns from one experiment to the other.

Therefore, trajectories are analyzed to get from each track the objective confinement height H, the swimming speed V, the gyration radius on surface R and the emerging lateral diffusion coefficient D. Most of the measured gyration radius R are below $100\,\mu\mathrm{m}$ but some bacteria are shown to go almost straight ($R > 200\,\mu\mathrm{m}$) (see figure III.20a). The swimming speed V varies from $20\,\mu\mathrm{m/s}$ to $40\,\mu\mathrm{m/s}$ between individuals. Typically $V = 29 \pm 9\,\mu\mathrm{m/s}$ (see figure III.20c). The bulk speed looks a bit higher, less than 10%, than the surface speed and is the same at surface and in the bulk (see figure III.20e). The lateral diffusion coefficients $D = 200 - 2000\mu\mathrm{m}^2/\mathrm{s}$ are shown to be broadly distributed, varying on more than a decade (see figure III.20d). When looking at these raw quantities altogether in figure III.20f, we can guess the impact of the gyration radius and of the confinement height : the larger, the larger the diffusion coefficient. The mere scaling $D \propto V^2$ foreseen stemming from a run & tumble process in a boundless environment (equation II.25) does not show up obviously due to the large variability of the gyration radii and the impact of confinement.

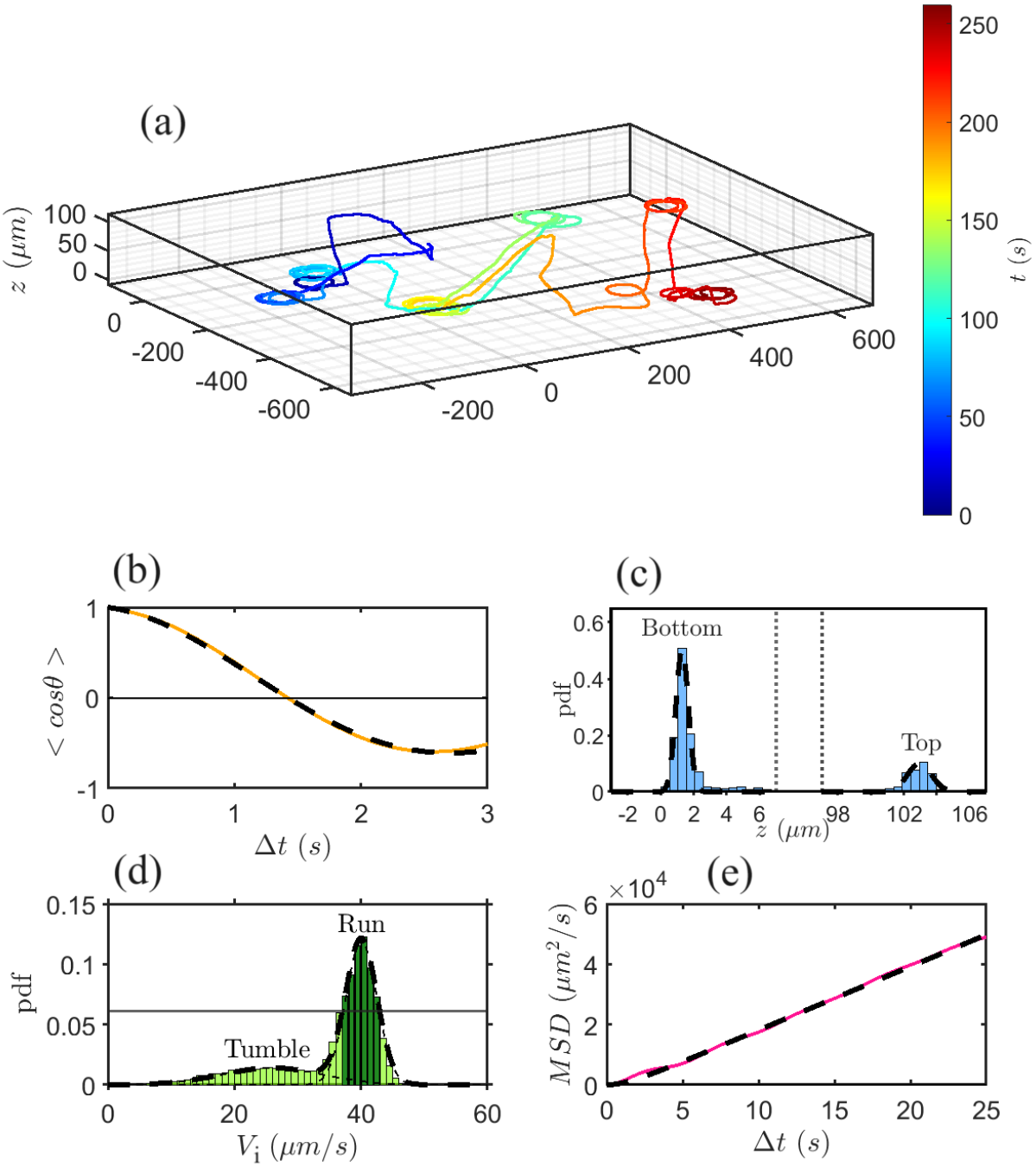

FIGURE III.19 – Example of an experimental bacterium track and extraction of the quantities of interest. (a) Bacterium trajectory. Straight run & tumble motion in the bulk are complemented with circular motion at the surface, still combined with tumbles. (b) Orientation auto-correlation function at the surface $< cos\theta >$ (orange line) fitted with the function III.11 ($\Omega = 1.2\,\mathrm{s}^{-1}$, $\tau_p = 5.1\,\mathrm{s}$, $= V/\Omega = 33\,\mu\mathrm{m}$ - dashed line). (c) Z-profile (blue) fitted by a double Gaussian ($z_{bot} = 1.3\,\mu\mathrm{m}$, $z_{top} = 103\,\mu\mathrm{m}$ - dashed line). (d) Distribution of the instantaneous speed V_i (green). The run speed $V = 40.1\,\mu\mathrm{m/s}$ is computed from the Gaussian fit (right light dashed line) on the values above half-maximum (above solid line - dark green). Here is also shown the total fit (heavy dash line) complemented by the tumble speed (left light dashed line). (e) Self-averaged mean square "lateral" displacement MSD (pink curve) fitted by a Fürth function providing the lateral diffusion coefficient $D = 527\,\mu\mathrm{m}^2/\mathrm{s}$.

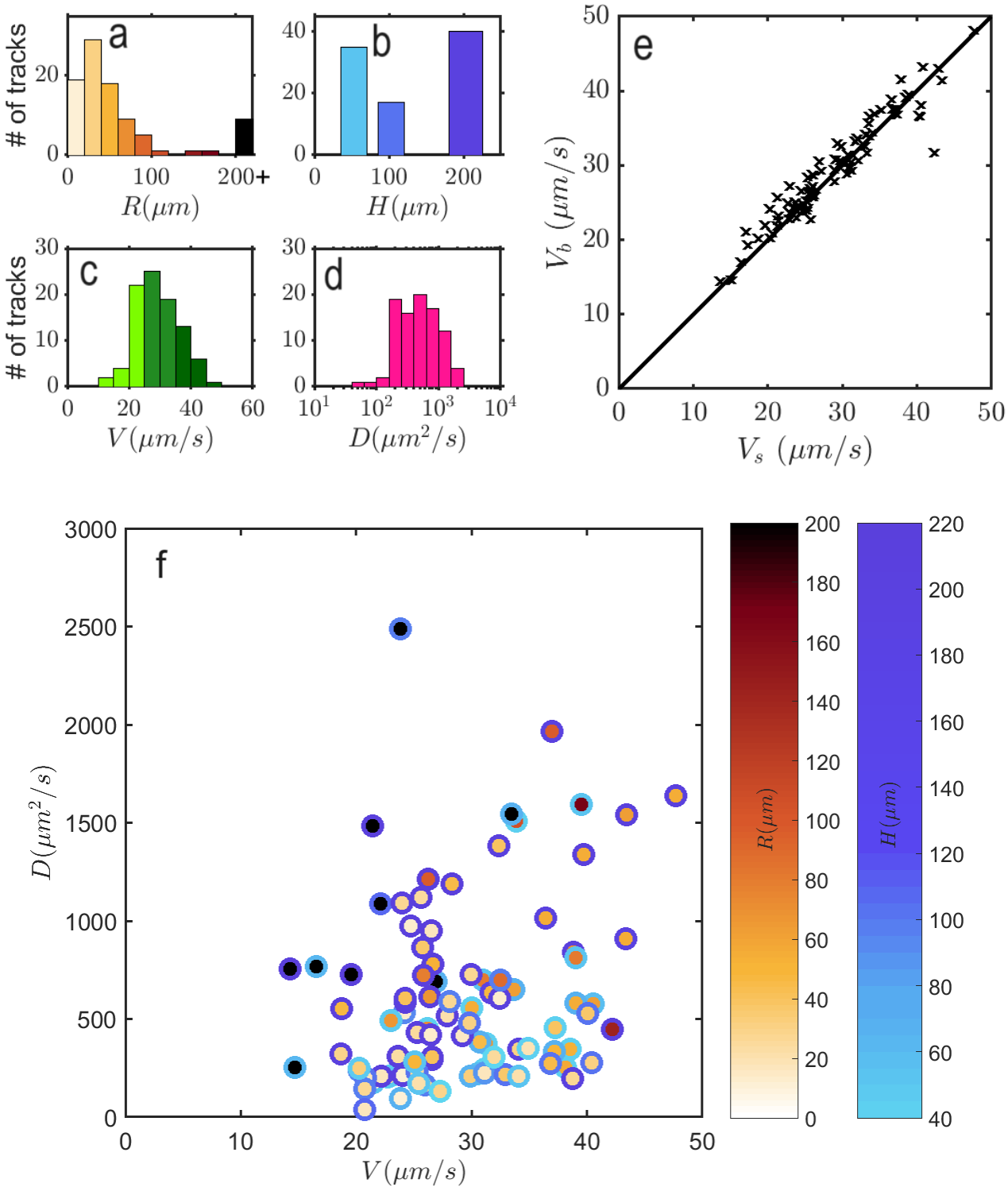

FIGURE III.20 – Experimental values (D, V, R, H) obtained from 92 tracks. Distribution of : (a) radius of gyration R, (b) confinement height H, (c) swimming speed V and (d) lateral diffusion coefficient D. (e) Speed measured in the bulk V_b and at surface V_s are very close. (f) Lateral diffusion coefficent D as a function of the swimming speed V, gyration radius R (disk color) and confinement height H (circle color). A simple scaling $D \sim V^2$ (II.25) fails to explain the data.

III.4.2 Dimensionless quantities and numerical stochastic model

In the framework of the BV model, phenotypic variability for the run times is negligible beyond behavioral variability and we can then rescale times by $\tau_r = 2.23\,\mathrm{s}$ the mean run time previously calibrated [115] and lengths by $l_p = V\tau_r$ the mean persistent length :

$$\tilde{R} = R/l_p = 1/\tilde{\Omega} \tag{III.19}$$

$$\tilde{H} = H/l_p \tag{III.20}$$

$$\tilde{D} = D/D_p \tag{III.21}$$

where $D_p = 0.5V^2\tau_r$ is the diffusion coefficient expected from equation II.25 in 2D with a Poisson process for the run rimes and random reorientations. Thus parameters space (D, V, R, H, τ_r) is transformed to $(\tilde{D}, \tilde{R}, \tilde{H})$.

In parallel to the experiments, we performed numerical simulations of run & tumble "behavioral noiseless circle" model containing the following kinematic rules :

- Space is delimited by two infinite parallel surfaces separated by a confinement height H.
- Time is discretized : $\Delta\tilde{t} = \Delta t/\tau_r = 10^{-3}$
- The bacterial internal "mood" δX fluctuates according to the BV model calibrated in earlier work [115] ($\tau_0 = 4.62\,\mathrm{s}$, $\Delta_n = 1.62$, $T_M = 19\,\mathrm{s}$). The model is detailed in II.3.3.
- Run mode
  - Constant speed $\tilde{V} = 1$.
  - Run times dynamics : the current tumble rate depends on the "mood" such that $k_r(t) = exp\left(-\Delta_n \delta X(t)\right)/\tau_0$.
  - At the end of the run mode, the bacterium enters the tumble mode.
- Tumble mode (from [92])
  - No speed.
  - Reorientation : rotational diffusive process of coefficient $D_r = 9.65\,\mathrm{s}^{-1}$.
  - Tumble times : Poisson process of rate $k_t = 1/\tau_t = 2.5\,\mathrm{s}^{-1}$.
  - When a tumble ends, the bacterium enters the run mode.
- In the bulk : straight 3D motion
- At surface (see figure III.21)
  - The bacterium is considered at surface as soon as it touches it and keeps the incoming direction projected on the plane of the surface.
  - Circular motion of radius R, CW on one surface and CCW on the other.
  - When a tumble occurs, the bacterium exits the surface if the new orientation points out of the plane. Otherwise it stays in and the new swimming direction is simply projected on the plane of the surface.

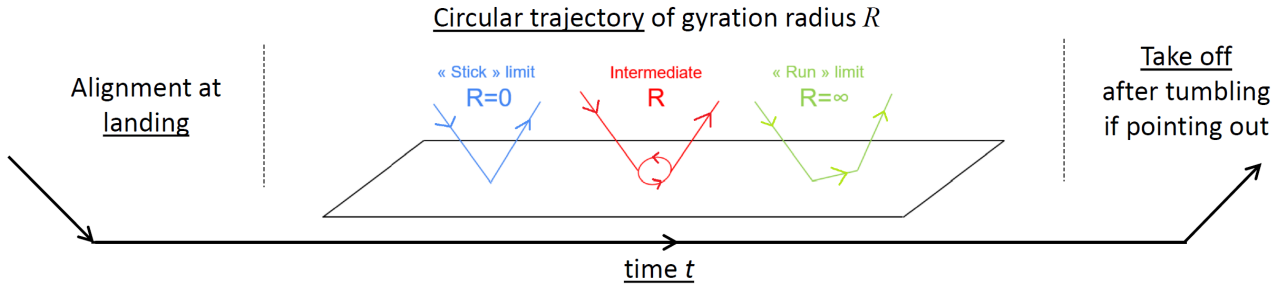

FIGURE III.21 – Surface kinematic rules. When a bacterium lands on the surface, it keeps its original direction and starts moving circularly until a tumble occurs making it either stay at surface or taking off. The gyration radius is a parameter that can be varied continuously from the "sticking" limit $R = 0$ to the "run" limit $R = \infty$.

This is a calibrated model without any adjustable physical parameters. The resulting numerical tracks are analyzed the same way as the experimental ones. We can vary the dimensionless gyration radius $\tilde{R}$ and confinement height $\tilde{H}$, defined in equations III.19 and III.20, to see the impact on the dimensionless lateral diffusion coefficient $\tilde{D}$ defined in equations III.21. From now on, to avoid heaviness, the quantities we discuss are implicitly dimensionless quantities, for instance gyration radius will refer to $\tilde{R}$. On figure III.22, for all $\tilde{R}$, the diffusion coefficient seems to converge to the no wall limit $\tilde{D}^{no-wall} = 2.14$ computed numerically in the no-wall limit (boundless environment). Interestingly, even if the BV model for the run times is not Markovian, this value corresponds to formula II.25 outcome provided the values extracted from the simulations $\tau_r = 2.23\,\mathrm{s}$, $\langle \tau_r^2 \rangle = 34.57\,\mathrm{s}^2$, $\tau_r = 0.4\,\mathrm{s}$ and $\alpha = 0.1147$. In the "stick" limit $\tilde{R} = 0$, in which there is no exploration of surfaces, the diffusion coefficient increases with the confinement height. In the "run" limit $\tilde{R} = \infty$, the diffusion coefficient is maximal in the limit of full confinement $H = 0$ and $D^{run-2D} = 3/2 \times D^{no-wall}$ and then decreases with the height. Note that the factor $3/2$ comes from the 2D-projection of the speed when the system is 3D. We isolated the effect of the rotational noise in the previous section, extracting a typical value $\tilde{D}_{ss} = 0.01$. It might be non-negligible only for very confined situations $\tilde{H} << 1$ and confirm our approach that does not take into account passive diffusion at surfaces.

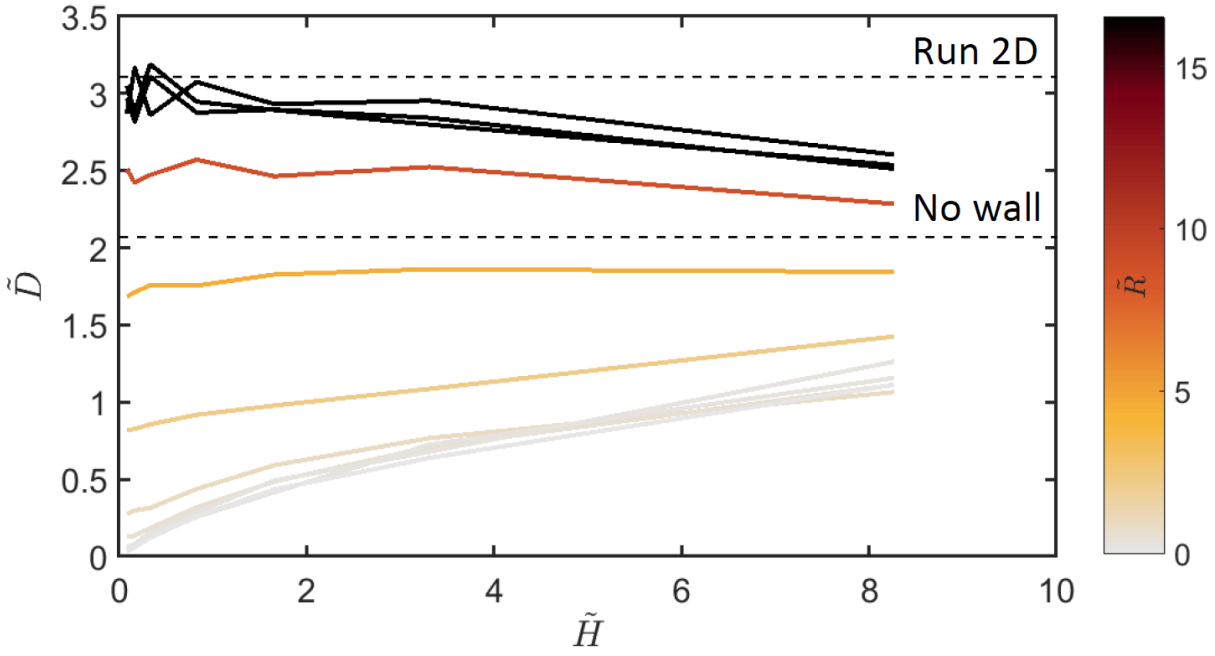

FIGURE III.22 – Lateral diffusion coefficient $\tilde{D}$ as a function of confinement height $\tilde{H}$ and gyration radius $\tilde{R}$ (in red scale) from numerical simulations.

In figure III.23 are compared experimental and numerical outcomes. We separate our experimental data in different ranges of $\tilde{H}$ like in figure III.23a such that every range contains the same amount of tracks. We also classify the radii in each range. We choose the radii ranges like in figure III.23b such that the numerical simulations predict significant variations in the lateral diffusion coefficient. We can now average in our heights-radii intervals and compare with numerical simulations (see figure III.23c). Experiments are in very good quantitative agreement with the numerical predictions : our results show that confinement indeed has a strong impact on the exploration and gyration radii are a key parameter that has to be considered.

About 70% of bacteria are found to have a gyration radius $\tilde{R} < 0.89$. In this regime, there is almost no diffusion at surfaces then the lateral diffusion coefficient vanishes in the limit $\tilde{H} \to 0$ while reaching the no-wall limit for $\tilde{H} \to \infty$. Note that the convergence is slow : $\tilde{D}(\tilde{H} = 8) = 0.5\tilde{D}_{no-wall}$. The confinement thus impacts the lateral spreading on large scale.

The higher is the confinement and the larger is the gyration radius, the larger is the bacterial exploration.

We confirmed experimentally the numerical predictions of the lateral diffusion under confinement, we can now have a deeper look at quantities linked to the exploration process such as the residence times.

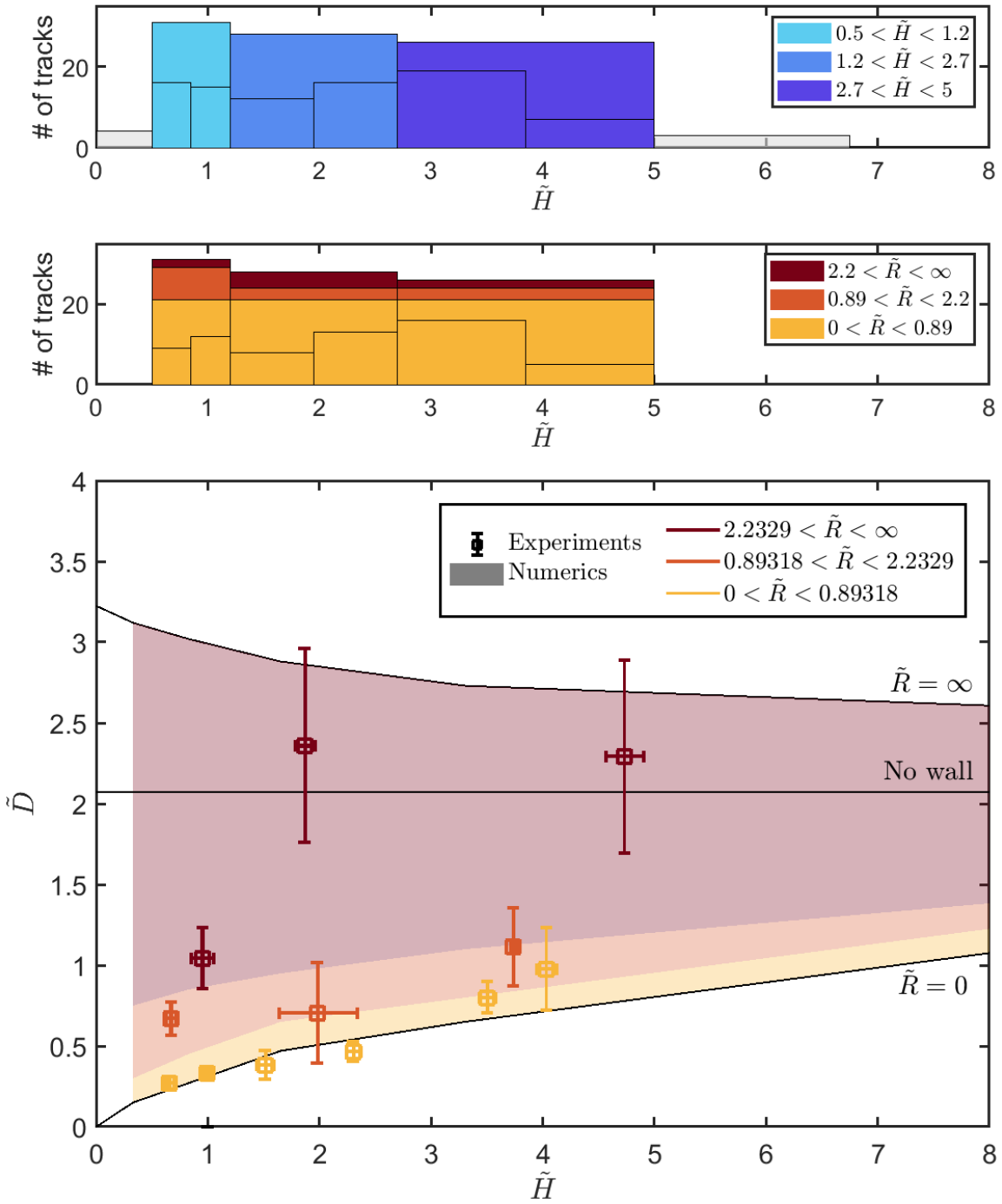

FIGURE III.23 – Impact of the confinement $\tilde{H}$ on the lateral diffusion coefficient $\tilde{D}$. (a) Distribution of the rescaled confinement height $\tilde{H} = H/(V\tau_r)$ in the relevant ranges (with sub-distribution in the binning intervals). (b) Distribution of the rescaled gyration radii $\tilde{R}$ in the chosen ranges of $\tilde{H}$. (c) Rescaled quantities : Averaged (according to the binning intervals above) $\tilde{D} = D/(V^2\tau_r/2)$ as a function of $\tilde{H} = H/(V\tau_r)$ and $\tilde{R} = R/(V\tau_r)$. $\tilde{D}$ grows with the rescaled confinement height $\tilde{H}$ and gyration radius $\tilde{R}$. Very good agreement between experiments and numerics (no adjustable parameters). Error bars are standard errors for the means.

III.4.3 Bulk and surface residence times

Residence time in the bulk (resp. at surface) is the duration in which the bacterium stays in the bulk (resp. at surface). Numerically those quantities are easy to define : if $z = 0$ or $z = H$ then the bacterium is at surface, else it is in the bulk. Experimentally the precision of the z-location is not perfect and Junot et al [92] proposed to use a double-threshold method (with parameters $z_s = 3\,\mu$m and $z_s = 8\,\mu$m) to define the residence times as explained in figure III.24. We then have two different definitions for the residence times : the first one can be used only for the numerical simulations whereas the second one can be implemented for both experiments and numerics. We will then use the second one when comparing numerical simulations and experiments.

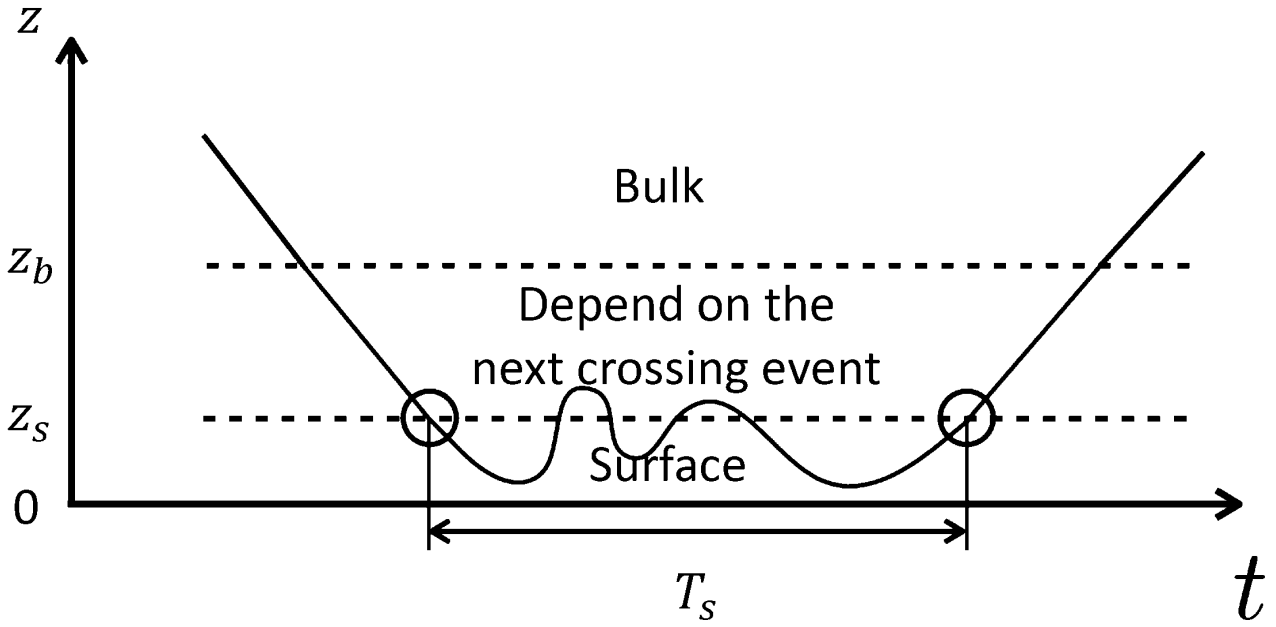

FIGURE III.24 – Sketch of the definition of surface and bulk with a double threshold method : a bacterium arrives at surface when it gets closer than z_s. It exits the surface at the last crossing of z_s that is follown by a crossing of z_b, defining a surface residence time T_s. When the bacterium is not at surface, then it is in the bulk.

Residence times from experiments and numerical simulations are compared on figure III.25 and III.26.

- Bulk residence times are in excellent quantitative agreement between experimental measurements and numerical predictions, both in the average and in the distribution (see figure III.25a,b). On figure III.25c, the tail of the distribution of bulk residence times is shown to decay exponentially, scaling with its average value.
- Experimental surface residence times are shown to be about 30% higher than the prediction of the numerical simulations and mostly independent on the confinement height (see figure III.26). In our simple model, we consider the same reorientation angles at surface and in the bulk. While it has been calibrated to reproduce experimental measurements in the bulk, the take off angles are shown to be slightly different when escaping from a surface [92] that could be the cause of such a difference and probably point on a limitation of the simplistic model as far as tumbles at surface are concerned. Surface residence times are log-normally distributed. In experiments, they decrease with the gyration radii R (see figure. III.26d). We suggest that a bacterium with higher gyration radius would increase its probability to hit an impurity, eventually leading to a take-off. In this simple scenario, higher speed should also decrease the surface residence times but this is not

what is observed (see figure. III.26e). We use the average of the logarithm of $\tilde{T}_s$ because $\tilde{T}_s$ is widely distributed : using the log allows very short times to have the same weight as very long times.

We have shown a good quantitative agreement between experimental measurements and numerical predictions for the residence times. We will revisit more theoretically the residence times in the next section and link it to the calculation of the diffusion coefficient.

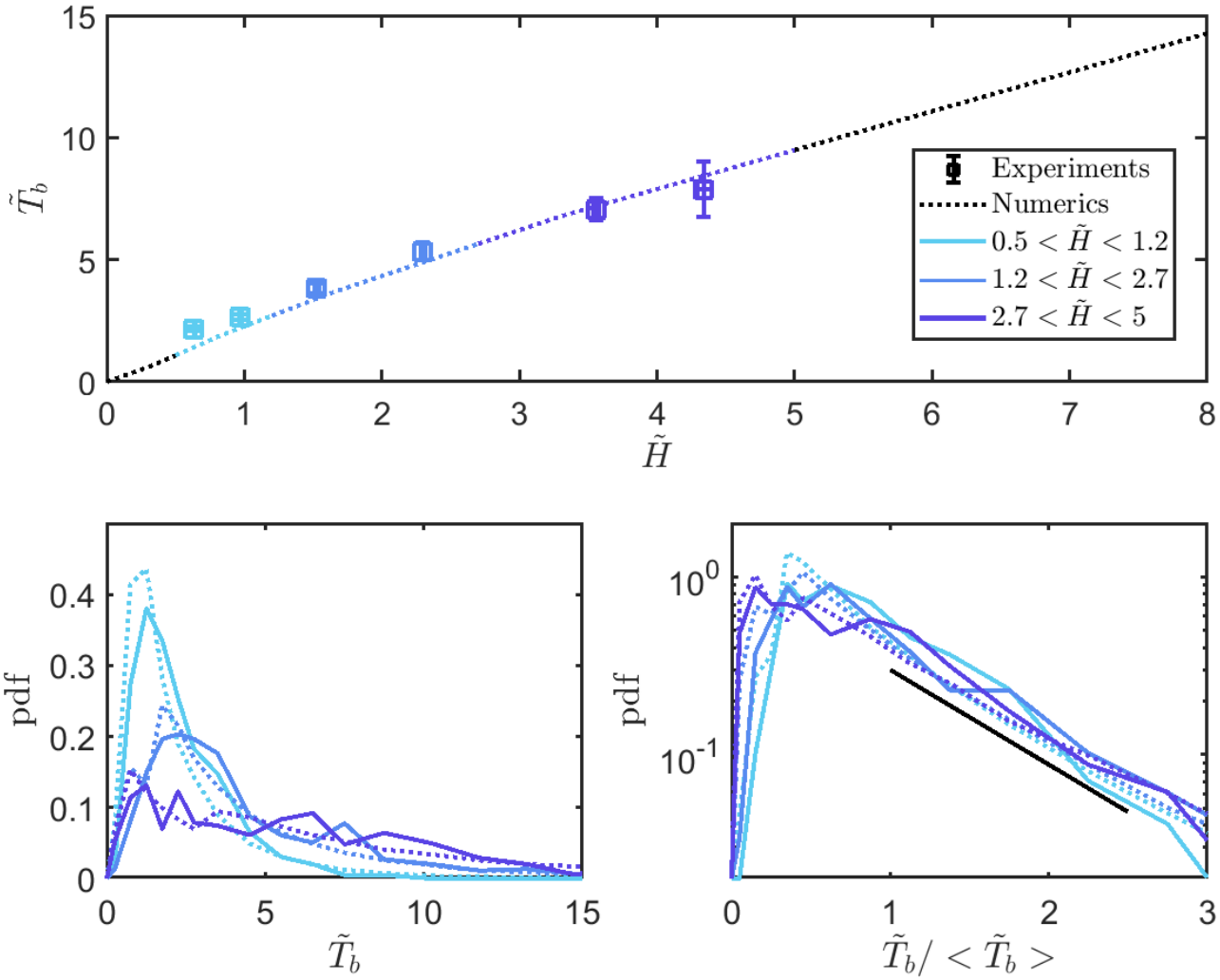

FIGURE III.25 – Impact of the confinement on the bulk residence times : i. (a) Bulk residence time $\tilde{T}_b$ as a function of the rescaled confinement height $\tilde{H}$. $\tilde{T}_b$ increases almost linearly with $\tilde{H}$. The dotted line is the Error bars are standard errors for the means. (b) Distribution of $\tilde{T}_b$. Very good agreement between experiments and numerics. (c) Distribution of the normalized value $\tilde{T}_b / < \tilde{T}_b >$ in log-normal scale. The tail of the distribution decays exponentially (black line : slope -4.2).

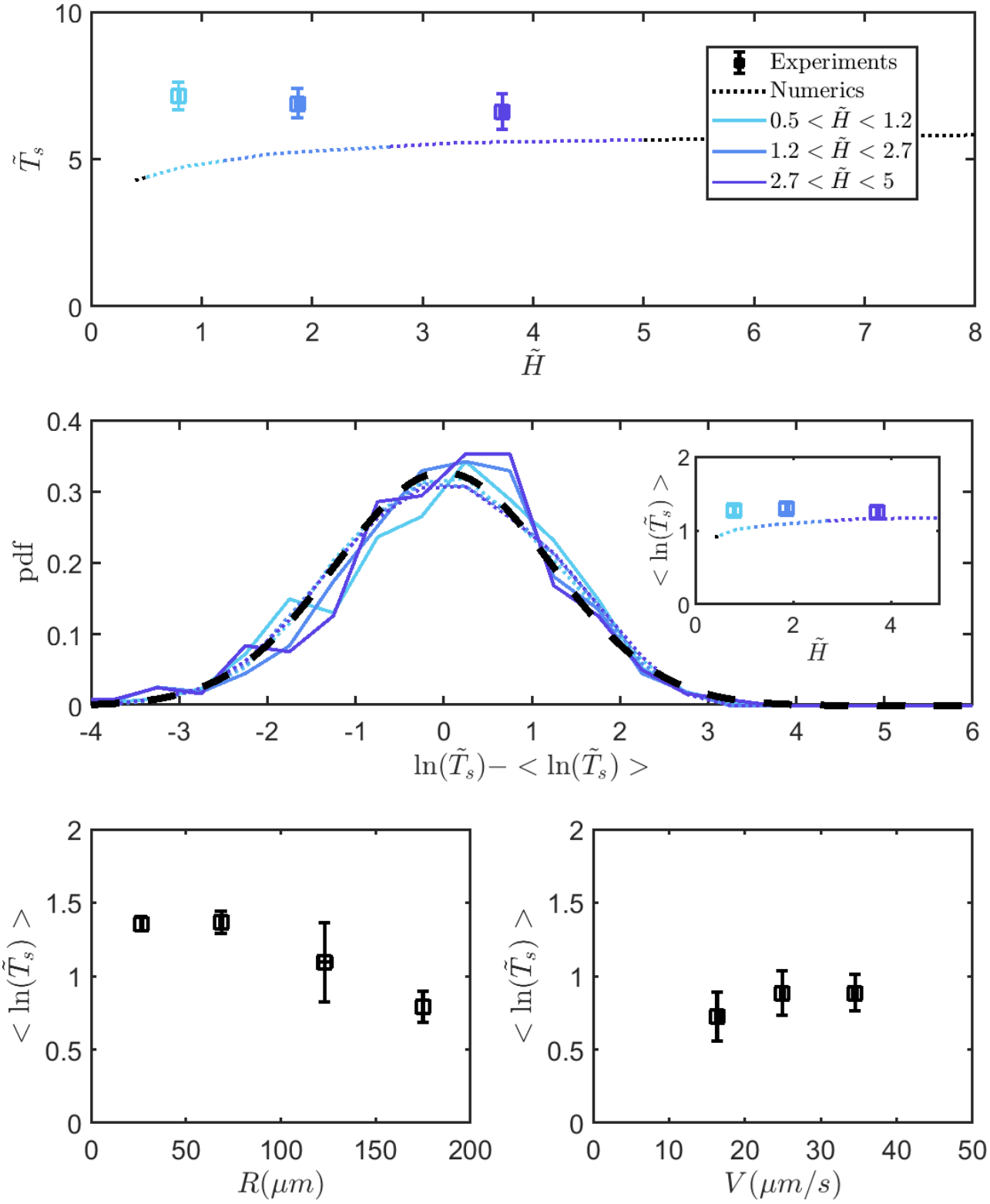

FIGURE III.26 – Impact of the confinement and the gyration radii on the surface residence times. (a) Surface residence time $\tilde{T}_s$ as a function of the rescaled confinement height $\tilde{H}$. $\tilde{T}_s$ is almost constant with $\tilde{H}$. (b) Distribution of $\ln(\tilde{T}_s) - < \ln(\tilde{T}_s) >$. The Gaussian fit (in black) has a width $\sigma = 1.22$. Inset shows the corresponding $< \ln(\tilde{T}_s) >$. Good agreement between experiments and numerics. $\tilde{T}_s$ is distributed log-normally. (c) $\ln(\tilde{T}_s)$ as a function of the gyration radius R. The residence times decrease with the gyration radius. (d) $\ln(\tilde{T}_s)$ as a function of the swimming speed V. Swimming speed does not play any role in the escape ability. For all graphs, error bars are standard errors for the means.

III.4.4 A "mixing" model for dispersion : the key ingredients

We now focus only on numerical simulations to get a more refined picture of bacterial exploration under confinement. We will now use the numerical definition of surfaces (simply $z = 0$ or $z = H$) to compute the residence times and the "free" runs.

We define as "free" runs in the bulk (resp. at surface) the runs only happening in the bulk (resp. at surface), taking into account the interruptions (resp. the starting) occurring when landing at surfaces. When landing at a surface, the current bulk "free" run stops and a surface "free" run starts. Runs are obviously also interrupted by tumbles.

Free runs distribution is clearly impacted by the confinement. In the bulk, the presence of surfaces imposes a cut-off for the bulk run times τ_b (see figure III.27a,c). For consideration, the cut-off in our situation is impacted by the angle of the run orientation with the z-axis. At surface, unexpectedly, the free surface run times τ_s increases with the confinement height (see figure III.27e,g) : Surfaces catch longer runs as $\tilde{H}$ increases. This effect is actually due to the memory of the internal "mood" . Following the theory described in chapter II.3 (see formula II.25), we can use those quantities, combined with a mean reorientation of $\alpha = 0.11$ which value is actually not of great importance but obtained numerically, to calculate surface and bulk effective diffusion coefficients. The bulk diffusion coefficient is shown to be highly impacted by the confinement (see figure III.27d), whereas the surface diffusion coefficient shown in figure III.27h is not but instead mostly depends on the gyration radius.

We use a simple model mixing bulk and surface behavior to calculate the emerging diffusion coefficient $\tilde{D}_{mix}$. We weight the effective bulk and surface effective diffusion coefficient $\tilde{D}_b$ and $\tilde{D}_s$ by the average time fraction spent in these regions :

$$\tilde{D}_{mix} = \frac{\tilde{T}_b}{\tilde{T}_b + \tilde{T}_s}\tilde{D}_b + \frac{\tilde{T}_s}{\tilde{T}_b + \tilde{T}_s}\tilde{D}_s \tag{III.22}$$

The idea behind this model is that you can permute the sequential order of the runs without changing the final quadratic displacement.

Average bulk residence times $\tilde{T}_b$ asymptotically scale linearly with $\tilde{H}$ (see figure III.28a) and we thus use an empirical determination $\tilde{T}_b = 1.5\tilde{H} + 2.6$. This result can actually be obtained in the analog gambler's ruin problem (return probability) [131]. The surface residence times $\tilde{T}_s = 5$ is taken as constant (see figure III.28b) since it is not much affected by the confinement and we do not have a theory yet to explain its increase with confinement. For a Poisson process, the effective diffusion coefficient at surface $\tilde{D}_s$ is :

$$\tilde{D}_s(\tilde{(R)}) = \frac{\tilde{R}^2}{1 + \tilde{R}^2}\tilde{D}_{s-m}(\tilde{R}) \tag{III.23}$$

where $\tilde{D}_{s-m}(\tilde{R})$ is taken as the asymptotic value for large $\tilde{H}$. In our BV model case, it corresponds an effective gyration radius R_{eff}, rescaling the actual gyration radius : $R_{eff} = R/4.5$ (see figure III.28d). This empirical effective gyration radius is not understood theoretically. For $\tilde{D}_b$, we use directly our computation (see figure III.28c). Indeed, there is no theory yet to obtain the first and second moment of the bulk free run times distribution $p(\tilde{\tau}_b)$, needed to compute $\tilde{D}_b$.

We show that the "mixing" model for dispersion, contains all the important features to predict correctly the lateral diffusion coefficient : $\tilde{D}_{mix}$=$\tilde{D}_{mes}$ (see figure III.28e). We only show data for $\tilde{H} \gtrsim 1$ for the clarity in the use of theoretical arguments, but the "raw" (without theoretical arguments, just ad-hoc values) model of mixing works in any regime. We have no theoretical arguments to describe $D_b(\tilde{H})$ yet.

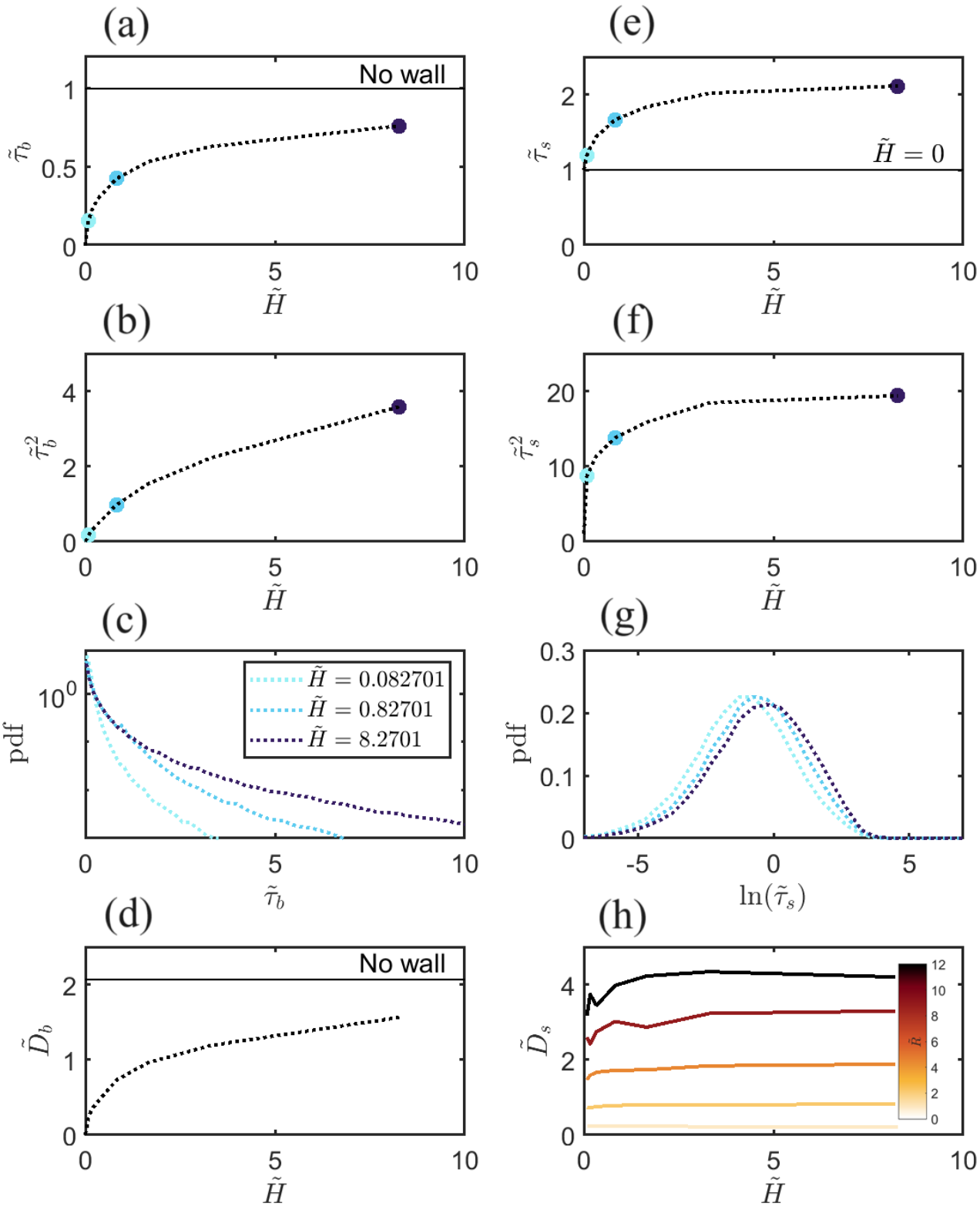

FIGURE III.27 – "Free" run times and emerging diffusion coefficient from formula II.25 : in the bulk (left) and at surface (right). (a-c) Bulk free runs as a function of the rescaled confinement height $\tilde{H}$. Free bulk runs last longer as $\tilde{H}$ increases. Confinement "cuts" the bulk runs. (d) Rescaled emerging bulk diffusion coefficient $\tilde{D}_b$ is highly impacted by the confinement. (e-g) Surface free runs as a function of the rescaled confinement height $\tilde{H}$. Free surface runs increase with $\tilde{H}$ until saturation. Surfaces catch longer runs as $\tilde{H}$ increases (effect of the memory, not shown explicitly). (h) Rescaled emerging surface diffusion coefficient $\tilde{D}_s$ for different $\tilde{R}$ (color code). It increases slightly with $\tilde{H}$ until saturation.

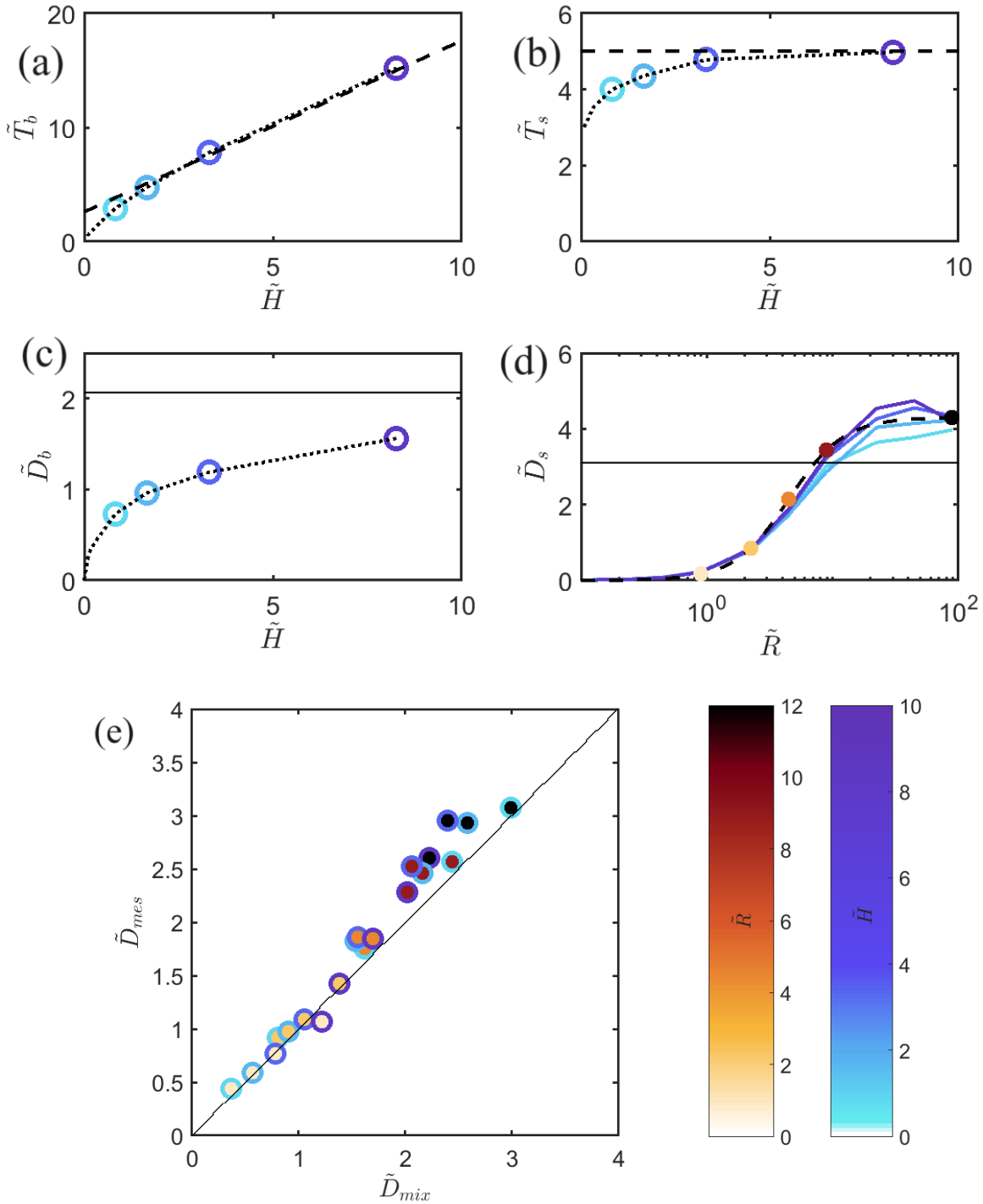

FIGURE III.28 – Test of the mixing model for the lateral diffusion coefficient under confinement. (a) Bulk residence time $\tilde{T}_b$ as a function of the rescaled confinement height $\tilde{H}$ (dotted line) adjusted with an empirical linear fit $y = 1.5x + 2.6$ (dashed line). (b) Surface residence time $\tilde{T}_b$ as a function of the rescaled confinement height $\tilde{H}$ (dotted line) with a constant limiting value $y = 5$ (dashed line). (c) Bulk diffusion coefficient computed from the distribution of "free" bulk (dotted line) runs and the no wall limit (solid line). (d) Surface diffusion coefficient computed from the distribution of "free" surface runs at various heights (solid blue lines) fitted accordingly to the formula III.23 with $\tilde{R}_{eff} = \tilde{R}/4.5$. 2D limit for straight runs $\tilde{R} = \infty$ is shown in solid line. (e) Comparison between measured (from MSD) diffusion coefficient $\tilde{D}_{mes}$ and the "mixing" one $\tilde{D}_{mix}$ predicted from formula III.22. Data collapse on the master curve $y = x$ demonstrating that the "mixing" approximation contains all the most important features to handle the effect of confinement.

III.4.5 Bacteria distribution at the surfaces vicinity

The Z-profiles are the distribution of the Z-position of bacteria through time. Experimentally, we need to impose a threshold $z_{thresh} = 3\,\mu$m because of the precision on the acutal surface determination. We can then rescale z into the dimensionless $\tilde{z} = z/(V\tau_r)$. The Z-profiles are symmetrized with respect to $\tilde{H}/2$ to improve the statistics.

To compare experiments and numerics, all the profiles start at the most constraining value $\tilde{z}_{start} = max(z_{shift}/(V\tau_r)$ and, for a given $\tilde{H}$ interval, end at the most constraining value $\tilde{z}_{end} = min(\tilde{H}/2)$. Also, we impose that the integrals of experimental and numerical Z-profile must be equal for a given interval. We observe that the decay observed close to the surface is faster in the experimental outcomes : bacteria get away far from surfaces faster in experiments than in the numerical model. It points a limit of this simple stochastic model, probably related to a limitation already discussed for the surface residence times : the tumbling process at surfaces could be different than in the bulk (like hydrodynamic hindrance suggested in [132]).

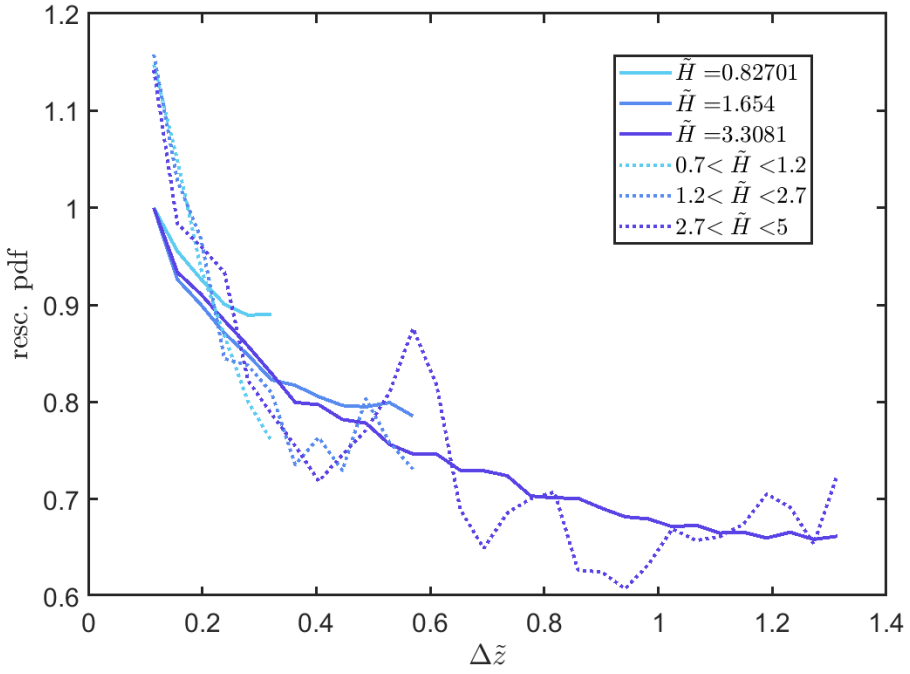

FIGURE III.29 – Z-profile of the bacteria distribution under confinement. The PDF is rescaled to the first value of the numerical profile so that it starts at 1. Numerics are in solid line, experiments in dotted line. Experimental Z-profiles decay typically twice faster than in numerics close to the surface.

III.5 Conclusion

We studied bacterial exploration in an archetypal confined environment where bacteria swim between two parallel plates. We demonstrated the importance of confinement, which occurs in many natural environments explored by microorganisms, in the emergent parameters such as lateral diffusion coefficients and residence times. The more bacteria are confined, the less they explore space laterally. We also show that gyration radii and, to some extent, swimming speeds are highly distributed and depend on details that could not be directly identified. Consequently, in the quantitative approach we present, we explicitly consider these parameters as a quantitative measure. We find that the higher the confinement heights and gyration radii, the more

the bacteria explore their environment laterally.
It would be interesting to observe bacteria in even more confined environments, with a height comparable to the bacterial size ($1-2\,\mu$m), to test for some hydrodynamic effects. Also, our experimental conditions limit our measurements to a rescaled height $\tilde{H} = H/(V\tau_r) < 5$. Slowing down the bacteria would allow to reach experimentally higher rescaled heights.

Numerical simulations have been carried out with a previously calibrated BV model, which is in good quantitative agreement with experiments. The BV model is characterized by an internal variable that controls the tumble rate. This internal variable is therefore referred as the "mood" and fluctuates on a characteristic memory time $T_M = 20\,$s. It would be interesting to compare the results of this BV model with a mere Poisson model for the run times, in which the tumble rate is constant, to assess the impact of such a memory process.
A first result of this internal memory is that surfaces tend to select bacteria in a "long run" mood, increasing the observed average run times at surface. This effect is stronger as the confinement height increases.

We identified two main effects induced by the confinement. First, the confinement controls the amount of time the bacteria spend at surface compared to in the bulk. Since total diffusion is a weighted average of bulk and surface behaviour, small environments give more weight to surface behaviour, while large environments give more weight to bulk behaviour. Secondly, from a bulk perspective, the runs are interrupted by the surface, which reduces the average run length. Since smaller runs lead to less diffusion, confinement reduces the "effective" diffusion in the bulk.

In the context of bacteria entering the epithelium through cracks in the dense mucus barrier, we confirm that this is a plausible mechanism, although surfaces tend to trap bacteria rather than promote their spread. Indeed, for a typical bacterium to cross a breach in the mucus barrier, of typical length $\Delta X = 100\,\mu$m and of thickness as small as $H = 10\,\mu$m [49], we predict a typical order of magnitude for the invasion time $T_{inv} = \Delta X^2/2D = 50\,$s.

This result, and this study in general, has implications that go beyond ecological and medical aspects. Indeed, most quantitative experiments with bacteria are carried out in the presence of confinement, an element that is often neglected. We hope that this study will provide the keys to understanding and characterising its effects in future studies.

Confinement with different geometries, for instance with curved surfaces instead of a flat plane, could be considered since it could impact the localization and the spreading of bacteria in a non-trivial way, maybe depending on the details of the take-off.

We have shown successful and high quality tracking experiments in simple fluids. However, for turbid fluids such as mucus, the tracking algorithm does not work well. Indeed the rules of the algorithm cannot be applied in such environments since we cannot find simple rules from the Z-pattern (see figure III.30). In the next following chapters, we will study bacteria in mucus, first in chapter IV with a static picture where a population of bacteria have invaded a mucus barrier and then in chapter V by developing a new algorithm allowing for Lagrangian tracking in mucus.

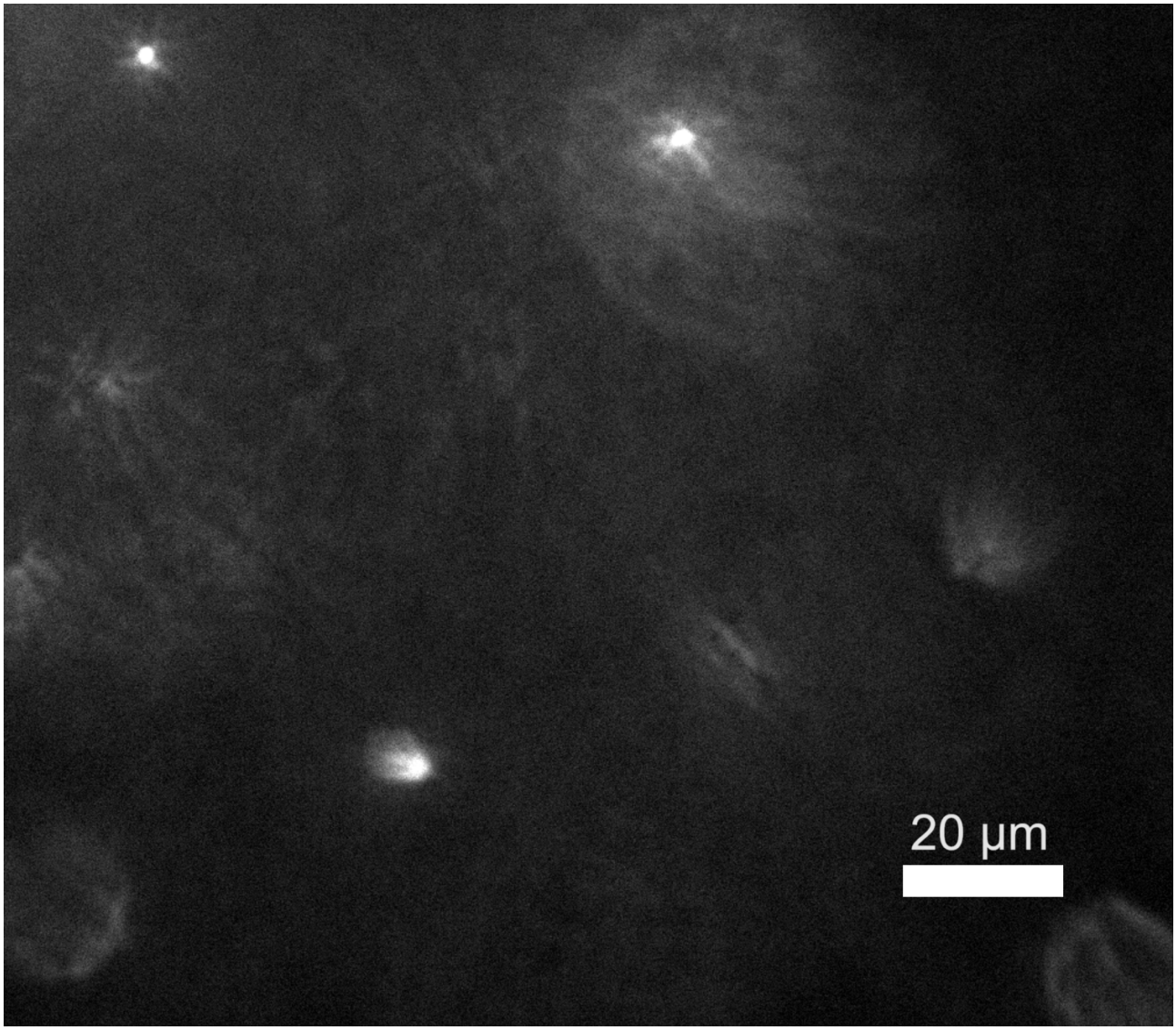

FIGURE III.30 – Snapshot of fluorescent bacteria in mucus. The brightness comes from the GFP on the bacterial body. Mucus scatters this light perturbating the tracking.

Chapter IV

Bacterial penetration of piglets gut mucus barriers

IV.1 Introduction

IV.1.1 The gastrointestinal tract : microbiota and mucus

The human gastrointestinal tract (GI) starts with the stomach (see figure IV.1a). The gastric environment is acidic with a pH oscillating between 1.5 and 5. This pH is good to decompose proteins, but very deleterious for bacteria (only 10 bact/g). Then comes the so-called "small" intestine, long of 6 meters, constituted by the duodenum, the jejunum and the ileum. This neutral environment is full of enzymes (proteases, lipases, glycosidases) and most of the nutrients and water are already absorbed when reaching the large intestine, also called the colon.

The gut microbiota, i.e the bacteria, viruses and fungi living in our intestines, is denser and denser through the tract : from only about 10 bacteria/gram in the stomach, to 10^{11} bacteria/gram in the large intestine. We have about 10^{14} of bacteria in the GI tract, in which about 500 different species coexist [134]. The composition of the microbiota is very variable from an individual to the other. In the digestion process, some commensals (i.e bacteria living in our body without causing harm) are known to ferment dietary fibres otherwise non-digestible, breaking them down to short-chain fatty acids, such as butyrate, often associated with good

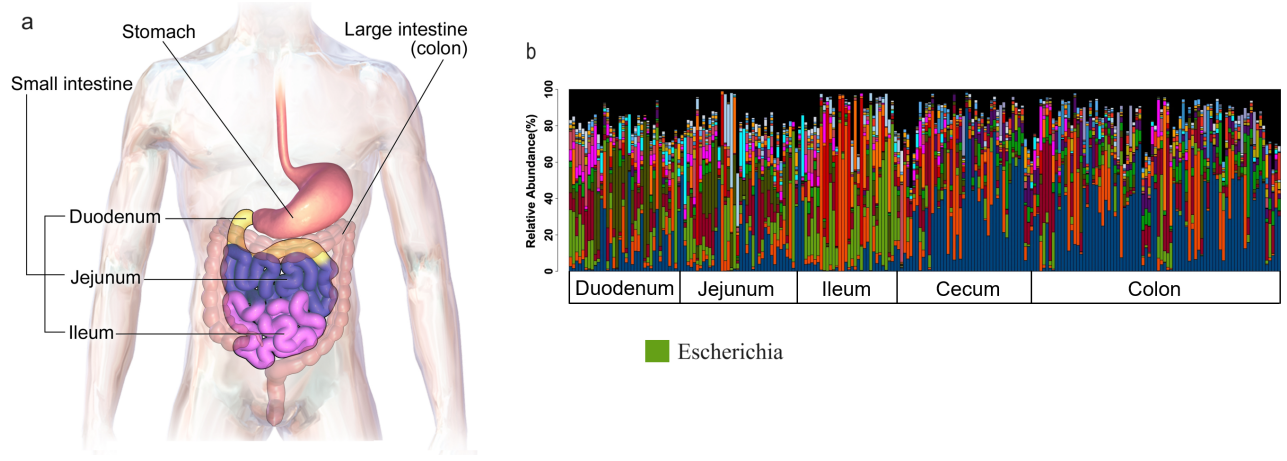

FIGURE IV.1 – (a) Sketch of the GI tract. From wikipedia. (b) 16s rRNA gene sequencing from a piglet along the gut. Bacterial populations (colors) vary along the track. E. coli are mostly in the ileum. Adapted from [133].

health condition [135]. It is possible to determine the bacterial composition of a sample by a method called "16s rRNA sequencing". The bacterial composition varies along the intestines [133] (see figure IV.1b). Most of E. coli are located in the small intestine and we will focus on this part.

Among all bacteria, some of them are pathogens. They are separated from our intestinal epithelial cells (IECs) by the mucus barrier. The mucus barrier of the small intestine is essentially composed of an entangled network of mucins MUC2, highly glycosylated proteins of molecular weight of order 1 MDa (see figure IV.2b), and antimicrobial peptides. They are secreted by specialized IECs, respectively the "goblet" and the "paneth" cells [136] (see figure IV.2a). The glycosylation of the mucin happens in the Golgi apparatus of the goblet cell (see figure IV.2c). The mucus barrier is often described with two layers : the sterile inner mucus layer and the outer mucus layer hosting bacteria. An order of magnitude of the thickness of these layers in mice is provided in [137], varying along the gut : the dense inner mucus layer, thought to be the protective layer [49], is 20-100 microns thick whereas the the loose outer mucus layer, thought to be a habitat for the microbiota [48], is 100-800 microns thick.

Epithelium is not a straight interface (IV.2a), but instead it is formed by villi and crypts which are known to increase the area of exchange of nutrients. Thus the mucus barrier must

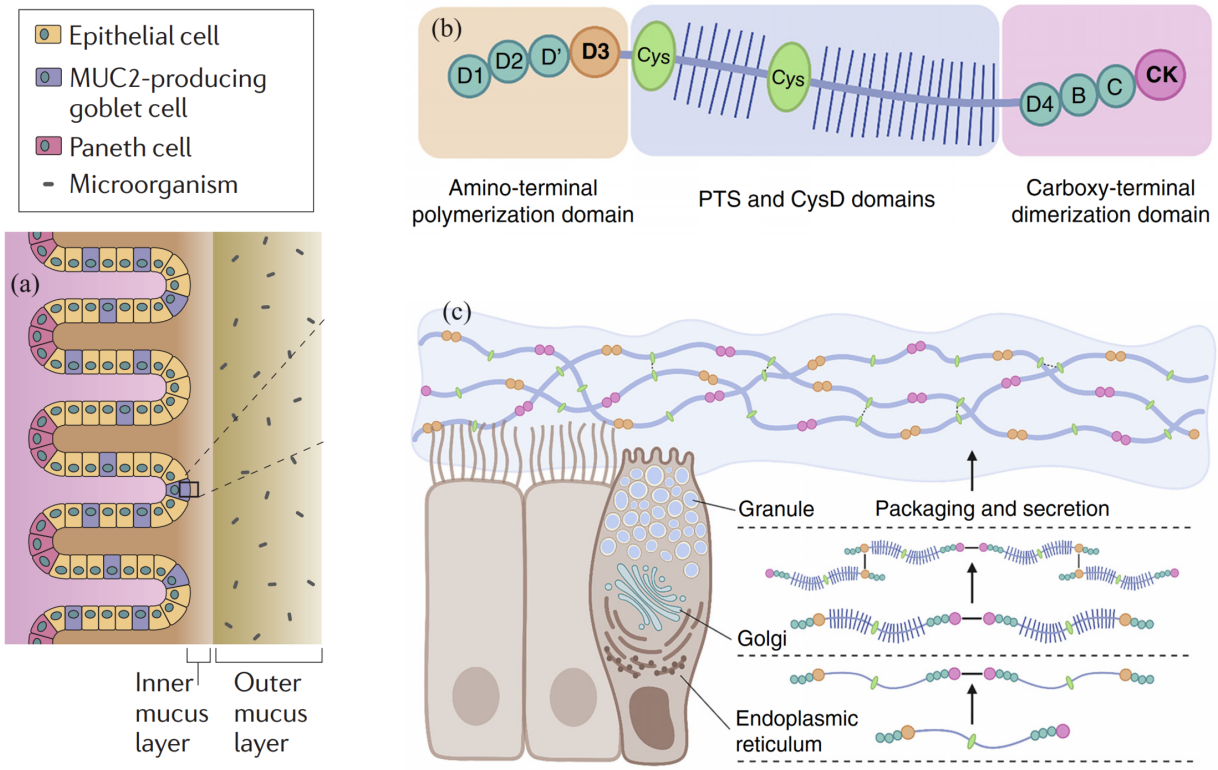

FIGURE IV.2 – The gut mucus barrier. (a) Sketch of a transverse cut of the gut. The epithelium surface (epithelial cells) is geometrically structured in villi and crypts. On the epithelium, goblet cells produce the mucin and paneth cells produce the antimicrobial agents. Both prevent from bacterial invasion. (b) MUC2 mucin protein (the main constituent of mucus) and its different domains. The dimerization is irreverisble while the polymerization and the central domains promote reversible bonds. The mucin network is dynamic because of the reversible bonds. (c) Formation and secretion of the mucin by a goblet cell. After transcription and translation of the MUC2 gene forming the protein backbone, mucins are dimerized in the endoplasmic reticulum, glycosylated and multimerized in the Golgi, packed into vesicles (granules), ready to be secreted on-demand. Granules will expand and join the existing dynamical mucin network. Figures adapted from [138].

let the nanoscale nutrients diffuse while preventing from microscale pathogens invasion.

IV.1.2 Bacterial motility and mucus penetrability in IBD

Inflammatory bowel disease (IBD) is a term for two conditions : Crohn's disease (CD) and ulcerative colitis (UC). Both are characterized by chronic inflammation of the gastrointestinal tract. "Inflammation" is the body's natural reaction against injury and infection. An infection is the invasion of tissues by pathogens, possibly causing some damages. In IBD, the mucus barrier is found to be degraded. It is disrupted in UC and more permeable in CD, due to a dysfunction in the glycosylation process. Mice fed with dietary emulsifiers have also expressed similar symptoms [47] (see figure IV.3a), pointing the importance of diet in those pathologies [48]. Omics-based studies, allowing the identification of virulence factors (flagellation [139]) and pathogens (adherent-invasive E.coli (AIEC)), have led to great advances and still constitute a very active field of research with the recent "mucosal microbiology" investigating specifically the mucosa-associated microbiota [140]. In parallel, new techniques aim at mimicking the intestinal host/pathogen interaction in biological conditions [141], reviewed in [142]. They allow to study bacterial invasion while monitoring at the same time the environmental conditions, the bacterial species and the mucus production. This led to discoveries : for instance the AIEC LF82 penetrates the mucus barrier by promoting mucin degradation with proteases [143]. Importantly, the motile bacteria seem to penetrate the mucus barrier more than the non-motile ones [139, 50] (see figure IV.3b).

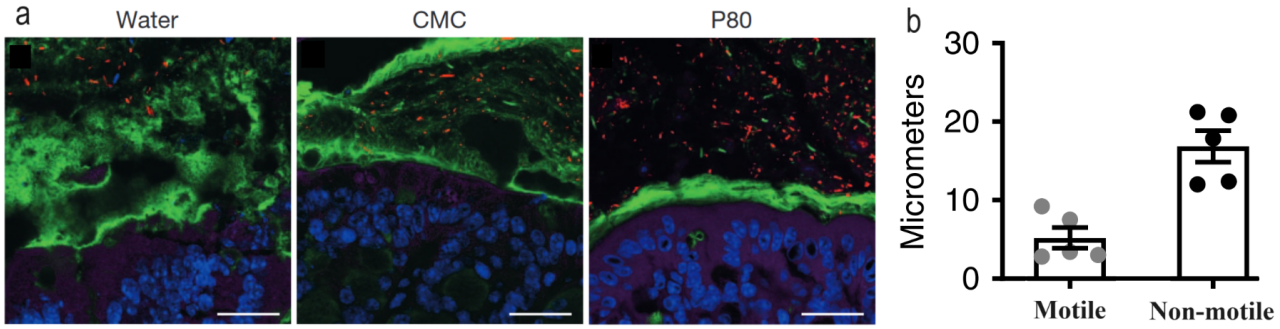

FIGURE IV.3 – Bacterial localization close to intestinal epithelial cells. (a) Bacterial (in red) invasion of intestinal epithelial cells (in blue) through mucus (in green) of mice fed with different diets. CMC and P80 are dietary emulsifiers and result in a more permeable mucus (CMC) or a disruption of the mucus barrier (P80). Scale bar 20 μm. From [47]. (b) Distance of bacteria to the epithelium. Motile bacteria come closer to the epithelium than non-motile ones. From [50].

Most of the current approaches are based on correlations, we are interested in causality. Few is known on the underlying swimming properties of bacteria in biological mucus : Furter et al [49] observes circular trajectory on the surface of the dense gut mucus layer in well-preserved mice mucus barriers, whereas Figueroa-Morales et al [45] reports bacterial alignment in sheared cervical mucus, like observed in liquid crystals by Goral et al [41]. The state-of-the-art is completed by the recent work of Hector Urra in the group [144] characterizing bacterial motility in model complex fluids (carbopol and commercial mucin) linked with their macro-rheological properties, and Bhattacharjee et al [43] pointing to intermittent motion with a new orientation after a stop. A better understanding of the fundamental swimming mechanisms in mucus could pave the way for new treatments and cures with impact in health and animal farming [145].

IV.2 Gut mucus from piglets

Bringing physicists and biologists together allow to combine the physicist view of soft matter on the relevant biological matter of interest. Especially, we could access piglets, in two limiting cases in term of diet, as a starting point. We aim at bringing a first physicist point-of-view on the problem of the bacterial penetration of the mucus barrier, establishing a methodology to study the mucus from the intestines of animals, from the extraction to the physical characterization. This works constitutes a first exploratory attempt.

After the extraction and the preparation of the mucus, we propose a first picture of the bacterial penetration in this biological fluid through an original model experiment, complemented with rheological and optical characterization, to eventually compare the results from both populations. I emphasize now that a key point when working with mucus is to keep it in a frozen state as much as possible to avoid degradation, defrosting it only for experimental purposes, and refreezing it as soon as possible.

IV.2.1 Cohort of piglets

We aim at comparing the piglets intestinal mucus properties of a cohort separated into two groups :

- Twelve "suckling" piglets which have been fed with milk only during their 21 days of existence.
- Twelve "weaned" piglets which started to complement their diet with solid food at their 21^{st} day, before complete weaning at their 28^{th} day. They have been slaughtered after 35 days.

"Suckling" and "weaned" piglets are thus different from two points : their age and, more interestingly, their diet. Piglets have been raised in the INRAE Toulouse by Martin Beaumont.

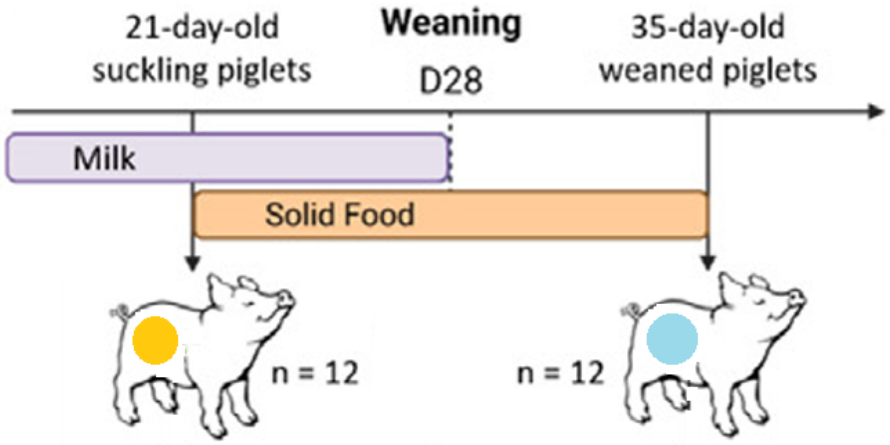

FIGURE IV.4 – "Suckling" (yellow dot) piglets only got milk. Mucus was extracted after 21 days. "Weaned" (blue dot) piglets have been weaned completely after 28 days and then started to eat solid food. Mucus was extracted after 35 days. They correspond to two limiting situations in term of diet. Adapted from [146].

IV.2.2 Mucus sampling

The sampling was made in collaboration with the biologists Tiphaine Le Roy and Marta Vazquez Gomez from the laboratory Nutriomics, Hôpital Pitié-Salepêtrière, Paris. Their ex-

perience with biological protocols was determinant to initially collect mucus and define the working protocols.

Extraction and purification

The method to collect the mucus is similar to the one described in [147] and recapitulated in figure IV.5. We took some special care to keep the intestines as cold as possible using ice bath during manipulations and to reintegrate the samples in the frozen state as soon as possible.

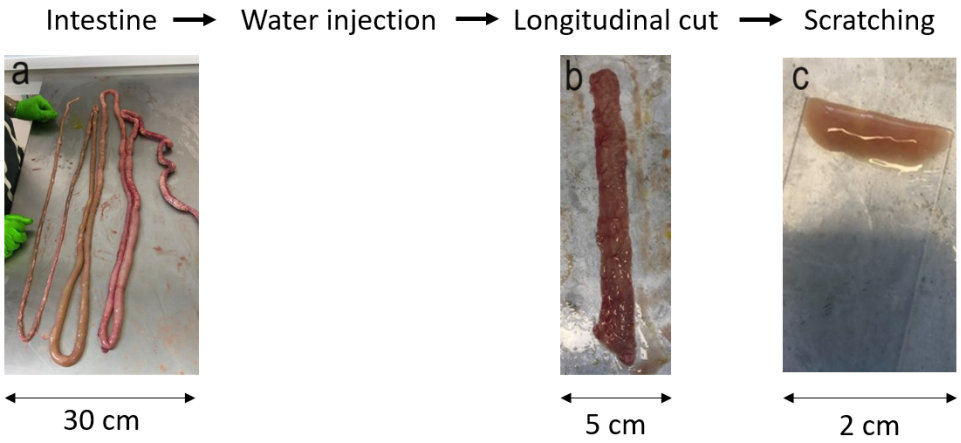

FIGURE IV.5 – Extraction of the mucus. Intestines (a) are washed by injecting water inside the gastrointestinal tube. They are then segmented into smaller parts and opened via a longitudinal cut (b). The inside part of the lumen is then scratched with a microscope slide. The mucus is apparent as reddish colored highly viscous and jellified fluid (c).

The purification protocol has been made by Tiphaine Le Roy, based on the literature [148] and adapted with available equipment. The process is recapitulated in figure IV.6. Importantly, the dialysis is made in the fridge at 4 °C for seven days. Water is renewed everyday. Centrifugation is also done at 4 °C, 20 000 g for 30 minutes. The supernatant is again centrifugated until no mucus can be collected.

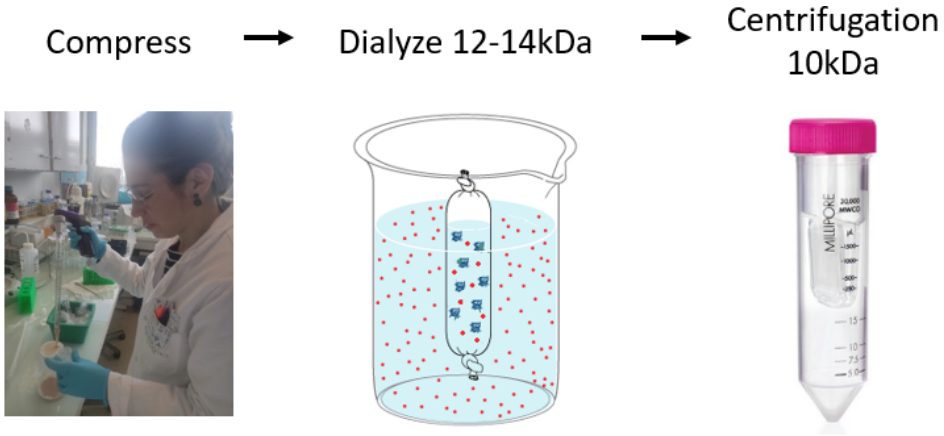

FIGURE IV.6 – Purification of the mucus. Big impurities are removed by passing the mucus through a compress. It is then dialyzed to remove small particles such as antimicrobials. A dialyzis consists in letting particles smaller than the membrane pore size ($12 - 14$kDa) diffuse in the surrounding fluid (pure water). The concentration of small particles inside the membrane thus decreases while keeping the same concentration of big particles (mainly mucins). Finally, mucus is centrifugated with a filter 10 kDa, removing most of the water and the ultimate small particles.

Purified mucus stocks

We are now in possession of purified mucus stocks, stored at $-20\,°C$. A summary is provided in figure IV.7. Total mass, pH and dry mass percentage have been measured for each piglet before and after purification. The mass of mucus collected, unlike the $pH \sim 6.5$ and the dry mass percentage, is very different between individuals. The purified mucus is concentrated at $8.52 \pm 0.94\%$ averaged on individuals. The total dry mass has been divided by three during the purification.

	Before purification			After purification		
Pig ID	masse (g)	pH	% dry mass	masse (g)	pH	% dry mass
1	11.00	6.47	16.86	**6.41**	**6.31**	**9.28**
3	9.30	6.67	15.37	**5.42**	**6.34**	**9.57**
4	8.60	6.65	14.91	**5.08**	**6.48**	**7.41**
5	7.70	6.56	16.28	**6.39**	**6.39**	**7.88**
6	4.30	6.49	12.36	**1.94**	**6.18**	**9.05**
8	6.50	6.62	14.14	**2.74**	**6.16**	**8.43**
9	20.70	6.49	21.43	**19.09**	**6.35**	**8.77**
10	15.90	6.53	17.83	**10.79**	**6.40**	**8.68**
11	9.90	6.50	15.54	**2.76**	**6.18**	**6.50**
14	9.78	6.50	12.49	**3.87**	**6.28**	**8.28**
15	27.25	6.42	12.11	**14.63**	**6.33**	**8.32**
17	14.40	6.74	16.00	**7.73**	**6.56**	**8.16**
18	16.80	6.59	19.60	**13.08**	**6.49**	**8.89**
20	5.40	6.41	15.75	**6.20**	**6.37**	**10.33**
23	39.80	6.67	12.67	**27.19**	**6.30**	**7.48**
24	22.72	6.36	13.02	**6.44**	**6.28**	**9.39**
mean	14.38	6.54	15.40	**8.74**	**6.34**	**8.52**
std	9.42	0.11	2.67	**6.81**	**0.11**	**0.94**

FIGURE IV.7 – Summary of the extracted mucus samples. Total mass, pH and dry mass percentage have been measured for each piglet, before and after purification. In orange and blue : resp. "suckling" and "weaned" piglets. Piglets above the dashed line have been used for the rest of the ongoing study.

Let's start the physical characterization of our piglet intestinal purified mucus. I will first describe the protocols and methods developed to study optical properties, bacterial penetration and rheology, discussing their reproducibility. I will then compare the different piglets mucus extracts.

IV.3 Physical characterization

The mucus extract is defrosted one hour at room temperature, in a rotating platform, before manipulations. We use a rotating platform for two reasons : mixing and avoid rotting. Indeed, by keeping the fluid in motion the proliferation of microorganisms is altered.

IV.3.1 Optical characterization

Optical visualization is of great interest to characterize mucus and several techniques are proposed in the literature, with or without fluorescent markers (SEM [45, 149], lectin-based staining [150, 49], immunostaining [151, 47]). I did not have time to push the optical study far. However I was able to use simple brightfield microscopy on large scale as well as a more elaborated technique called optical coherence tomography (OCT [152]), thanks to a collaboration with Jean-Marie Chassot (Institut Langevin, ESPCI, Paris). OCT allows for the visualization of a well-resolved plane in brightfield. I provide here briefly my attempts.

Turbidity

Mucus is not transparent, but rather brownish as shown on figure IV.8a. We measured the light intensity decrease with depth by optical coherence tomography microscopy. Light intensity decreases with a depth scale $l_e = 49\,\mu$m (see figure IV.8).

Structure scales

In simple brightfield microscopy, mucus extracts show optical heterogeneities. We image the mucus on large scale ($500 \times 800\mu$m in figure IV.9) by combining several images together (called "stitching") after 3.5 h between parallel plates. The size of these heterogeneities can be described through the radial autocorrelation function that can be fitted by summing two exponential functions from which we extract two length scales $\lambda_{opt-1} < \lambda_{opt-2}$. By exposing the samples to a sufficiently intense light, we can still describe those heterogeneities at $80\,\mu$m depth and we find that measured structure size do not depend on the depth. Interestingly, no effect of sedimentation is observed, pointing that there is none. λ_{opt-1} is of order $0.1\,\mu$m and λ_{opt-2} is of order $1\,\mu$m. Note that such quantities measured for the same extract can vary by a factor 4, which is surprisingly not very reproducible (see figure IV.10). We suggest that better results would be obtained with the OCT technique.

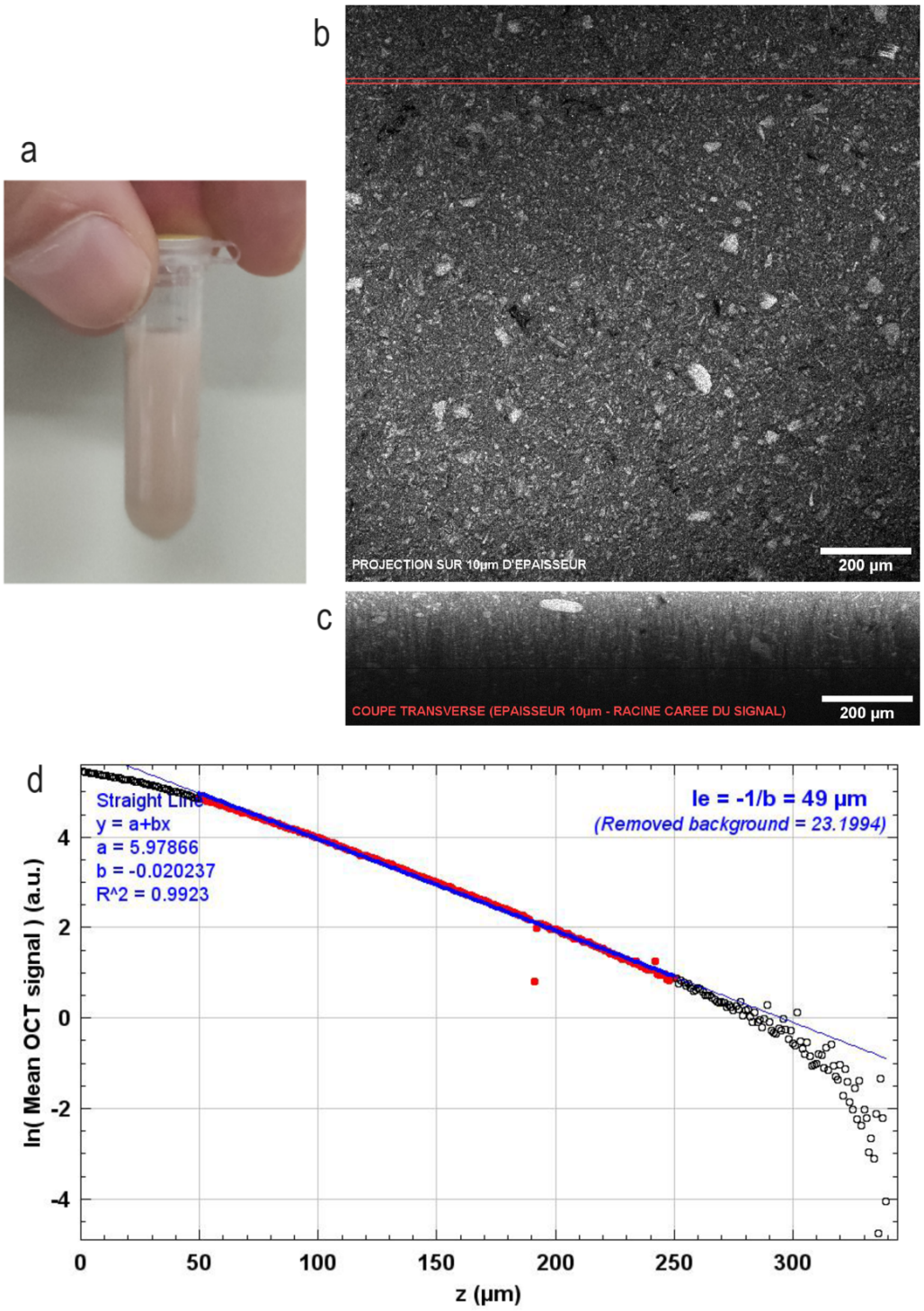

FIGURE IV.8 – Turbidity of the mucus extracts. (a) A tube filled with mucus. Mucus is not transparent. (b) Mucus imagery of a plane done by optical coherence tomography (OCT) and (c) corresponding cross-section. Mucus is turbid : light intensity decays with the depth of visualization (d) on characteristic scale $l_e = 49\,\mu$m.

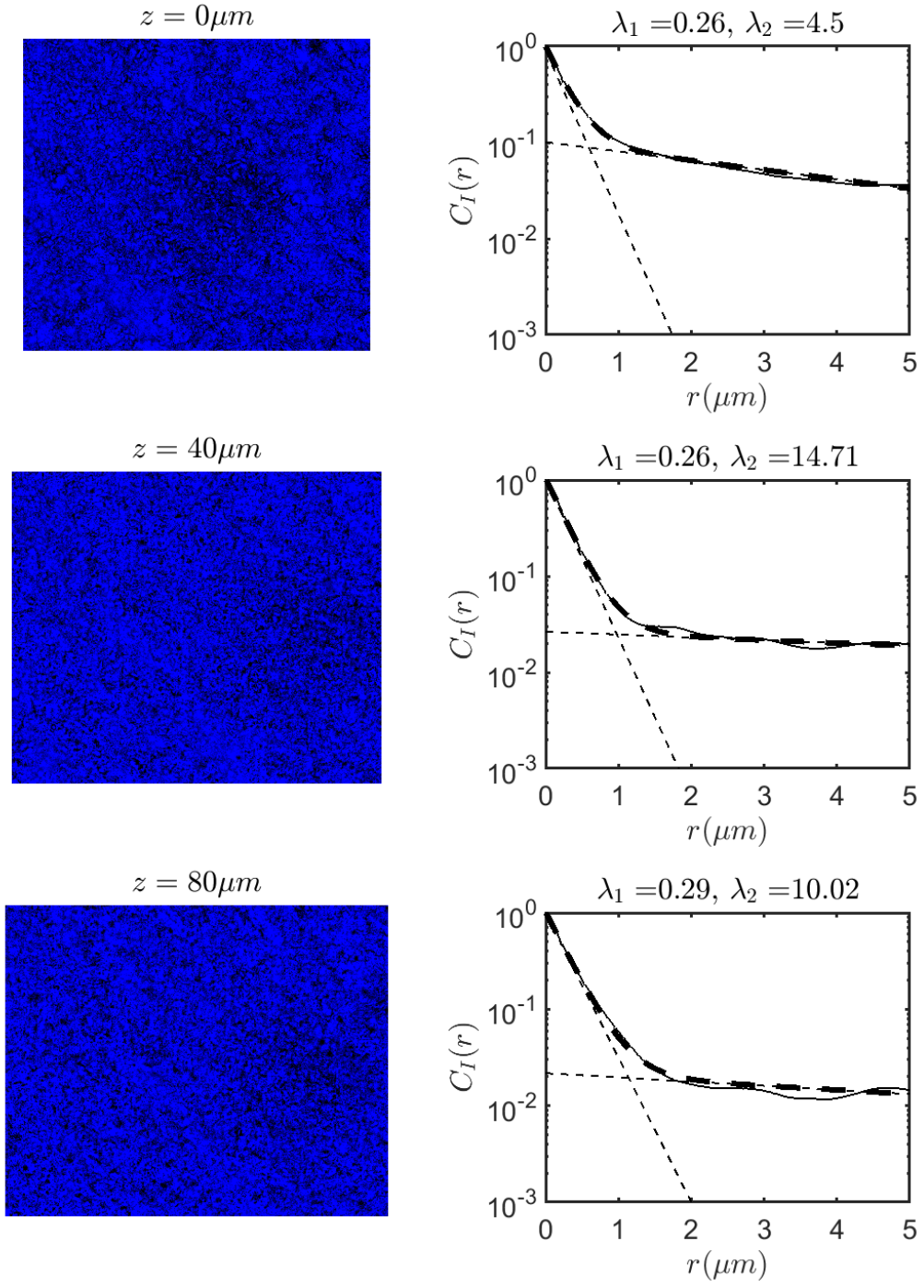

FIGURE IV.9 – Mucus (in blue) brightfield image via optical microscopy with a pixel resolution of 100 nm of size $500\mu m \times 800\mu m$ (left) and associated radial intensity autocorrelation function $C_I(r)$ (right) at different heights : (top) $z = 0\mu m$, (middle) $z = 40\mu m$ and (right) $z = 80\mu m$. Mucus shows microscale heterogeneities, that seem independent of the depth in the sample. The structures are revealed by the radial autocorrelation function $C_I(r)$, which is fitted by the sum (thick dashed line) of two exponentials (thin dashed lines) from which are extracted two characteristic structural length scales $\lambda_1 = \lambda_{opt-1} < \lambda_2 = \lambda_{opt-2}$.

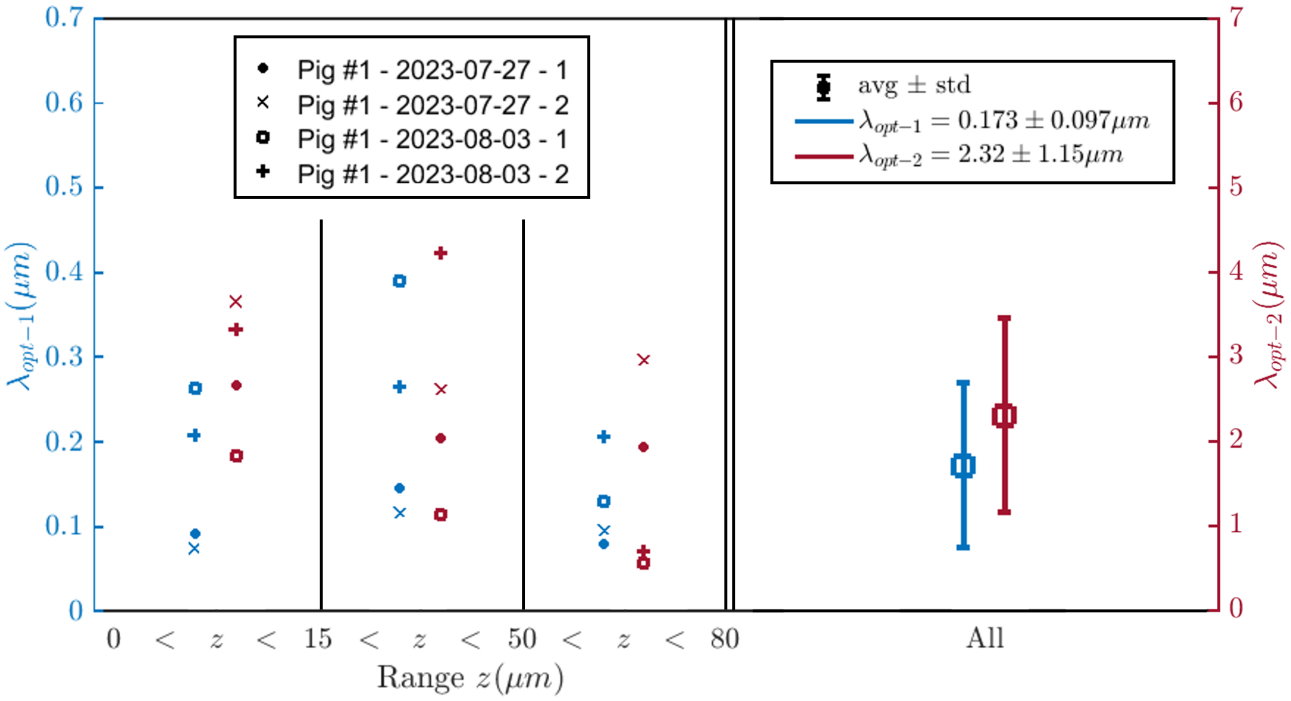

FIGURE IV.10 – Reproducibility of optical structures measurements λ_{opt-1} (left axis) and λ_{opt-2} (right axis) for piglet #1 done on four different samples of the same piglet prepared at two different days. Error bars are the standard deviations.

IV.3.2 Rheological characterization

During this thesis, many efforts have been performed to improve rheological measurements. We upgraded the software from the commercial rheometer Anton Paar MCR501 to get raw data directly and perform the analysis using an home-made software.

Rheometer measurement protocol

Hugo Legalois, intern in the team, participated to the elaboration of the protocols.

The measurement tool is a cone-plate CP25-2, which means a radius $r = 25\,\text{mm}$ and a cone angle $\alpha = 2°$. We inject $160\,\mu\text{L}$ of fluid. We perform a rotational test at fixed shear rates $\dot{\gamma}$, measuring the resulting shear stress σ. The time of measurement $T(\dot{\gamma})$ is calculated such that the rheometer completes one full rotation :

$$T(\dot{\gamma}) = \frac{2\pi}{\dot{\theta}} = \frac{2\pi}{\dot{\gamma}\tan(\alpha)} \tag{IV.1}$$

with $\dot{\theta}$ the angular speed. For our cone plate of angle $\alpha = 2°$, this leads for $\dot{\gamma} = 1\,\text{s}^{-1}$ to $T = 180\,\text{s}$. We seek to probe the rheological behavior from low to high shear rates. Low shear rates impose long experiments and as a compromise, we use the profile of figure IV.12a : from $\dot{\gamma} = 0.5\,\text{s}^{-1}$ to $\dot{\gamma} = 50\,\text{s}^{-1}$ in six logarithmic steps. To check any changes in the materials due to shear, the profile is made symmetric : first increasing shear values, then decreasing shear values. As a standard procedure when studying the rheology of complex fluids, the fluid is initialized to a given state by preshearing it (here $\dot{\gamma} = 50\,\text{s}^{-1}$ for $50\,\text{s}$). The complete test lasts a bit less than one hour, a duration that makes possible both quality and repeatability.

The tests are performed in an environment saturated in humidity by encompassing the "measurement cage" in wet paper (see figure IV.11) to prevent evaporation.

Resulting flow curves

The resulting shear stresses σ are displayed as a function of time t in figure IV.12b,d. Some samples are shown to have a symmetric response, whereas some others are impacted by their shear history. An hypothesis for this history-dependent behavior could be an isotropic to nematic transition as reported by [45] that we intend to check under the microscope between cross-polarizer. We extract the median value of shear stress σ in each of the intervals to finally get the flow curves IV.12(c,e). These flow curves point to a Herschel-Bulkley fluid, with the relation :

$$\sigma = \sigma_0 + \eta \frac{\dot{\gamma}}{1 + (\tau_0 \dot{\gamma})^{1/2}} \tag{IV.2}$$

where σ_0 is the yield stress, τ_0 a characteristic relaxation time of the fluid and η an effective viscosity. This fluid combines yield stress, viscoelasticity and shear-thinning that can all affect microswimming (see the introduction : swimming in complex fluids). Shear history and aging can also impact the mucus' rheology : since the phenomenology can be different from an extract to another, the rheological reproducibility, aging, and impact of defrosting will be discussed when comparing the mucus from different piglets.

We have developed a robust protocol to measure the flow curve of mucus. Mucus is a Herschel-Bulkley fluid and our results suggest that its rheological properties can vary depending on its shear history. Other tests, like oscillation tests, could bring some new insights on the mucus rheological properties. As a suggestion for future works, one could get some inspiration from Larobina et al [153]. They combine X-ray photon correlation spectroscopy to a stress-controlled rheometer, observing an enhancement of the microscopic pig gastric mucus gels dynamics upon applying a modest shear stress (i.e. in the linear viscoelastic regime).

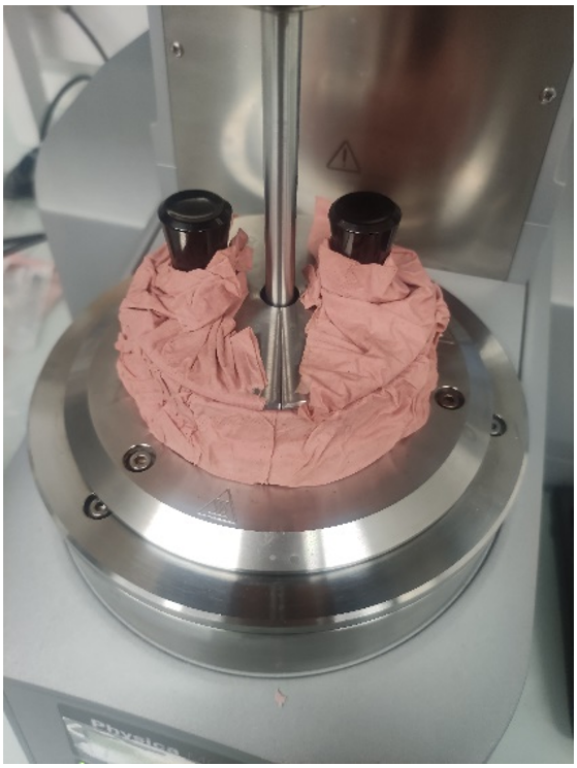

FIGURE IV.11 – Photography of the rheometer. The measurement is done inside the cage enveloped in wet paper to prevent evaporation.

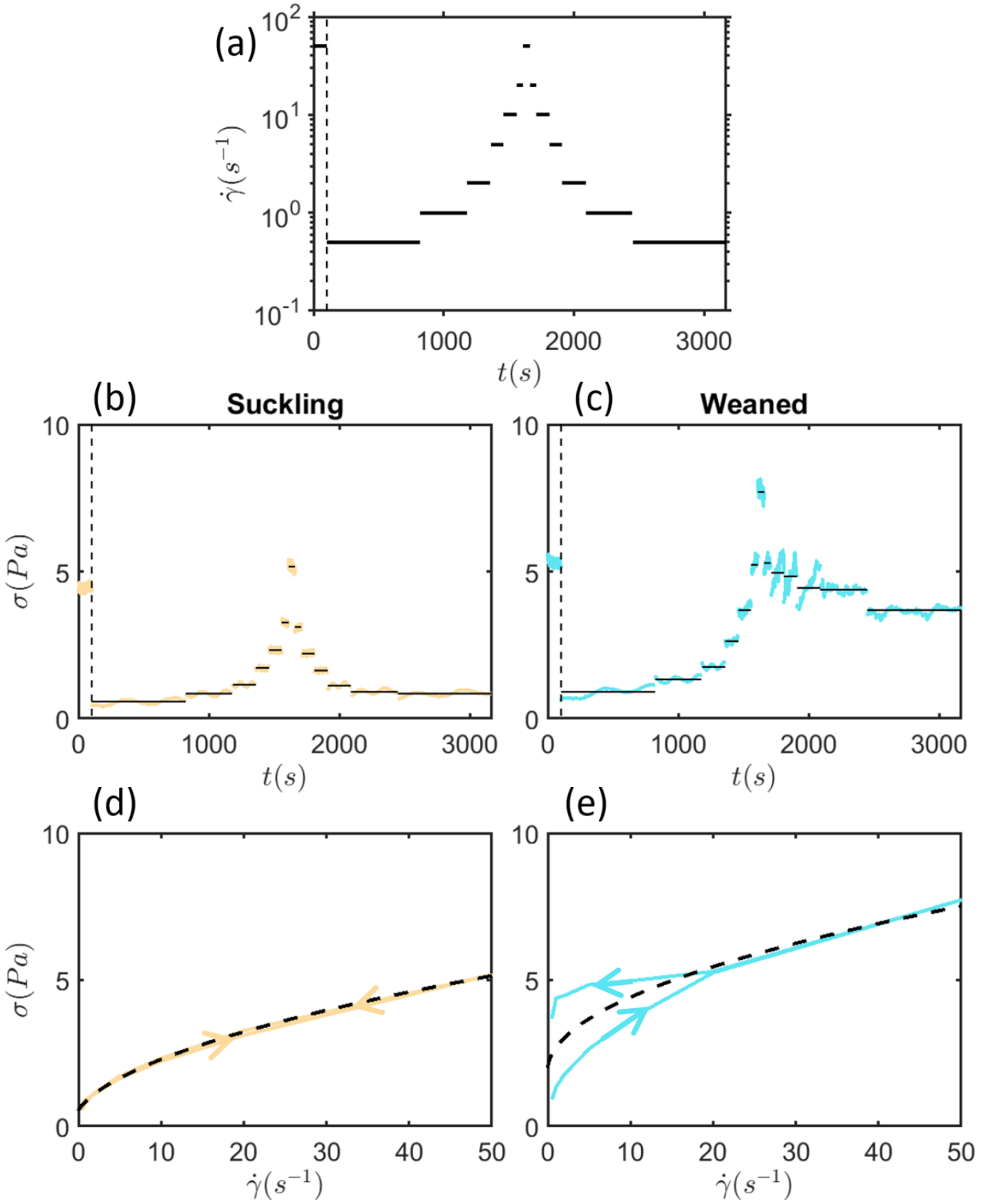

FIGURE IV.12 – Shear test methodology and typical result for suckling (left) and weaned (right) pigs. (a) Shear rate profile. Values of the shear rate $\dot{\gamma}$ come from $0.5\,\mathrm{s}^{-1}$ to $50\,\mathrm{s}^{-1}$ with logarithmic steps. Time intervals are chosen such that the rheometer does a complete turn. The profile is symmetric (increasing then decreasing shear rates). A preshear is done (before dashed line). (b/c) Resulting shear stress for a typical suckling/weaned pig (colored curves) and extracted median values for each interval (black line). The measured shear stress can differ qualitatively : the profile for the suckling pig is symmetric, whereas it is not symmetric for the weaned one, pointing to an effect of the shear history. (d/e) Flow curves $\sigma = f(\dot{\gamma})$ associated to the tests (colored curves) and Herschel–Bulkley fit (dashed line). Suckling pig mucus flow curve is stable and can be fitted whereas weaned one does not superpose back and forth.

IV.3.3 Bacterial penetration

To study the bacterial penetration of a mucus barrier, one needs to create an interface between a bacterial suspension and the mucus extract. We tried many methods, with or without flow. As a brief summary, due to its complex heterogeneous structure at the microscale, mucus is hard to handle in thin microfluidic wires, excluding the possibility to achieve some stable interface dynamically, for instance with a Y-junction. We propose an easy way to achieve the creation of a stable interface. To enhance the statistics on the number of bacteria and take into account the possible impact of the distance from surfaces, we developed an automated module to obtain what we coin as "3D-cartography" on large scale. The 3D exploration is obtained by scanning the sample from the surface to a certain height z_{max} by incremental step z_{step}. The objective 63xW we use, with a resolution and depth of field pertinent for this study, provides image of around $100\,\mu\text{m} \times 100\,\mu\text{m}$. We aggregate adjacent images to reconstitute a wider view, a process known as "image stitching". Combining the scans in Z with the wide images, we get our large scale 3D-cartography. The scans are done at $80Hz$, i.e a scan from $z = 1\,\mu$m to $z = 80\,\mu$m with step $\Delta z = 1\,\mu$m only takes 1 s. To get all the images that constitute the final large view, the stage moves sequentially to specific locations along the x and y axis.

Interface formation

The method to achieve the formation of an interface between mucus and bacteria is sketched in figure IV.13. A $10\,\mu$L droplet is sandwiched in a pool of thickness $H = 220\,\mu$m for 1.5 h. Letting the mucus at rest between slides consolidates its interface when mixed with another solution. Without this, fluids mix more resulting in less sharp interface (but still one can try). We then fill the pool by capillarity with a bacterial solution concentrated at $OD = 0.01$, that enters in contact with the mucus. To avoid any perturbating chemical interactions with the mucus, the bacteria are diluted in a solution of BMB without salt and without L-serine. The pool is then closed with silicone to prevent evaporation.

Analysis of the stationary state

After 2 h of bacterial penetration, most of the bacteria are found to be located in the mucus, not moving any longer. We thus consider it as a stationary state and trigger a cartography of the penetration of bacteria at this moment.

A volume delimited by 1 mm from each side of the interface, a width of $600\,\mu$m and a height $100\,\mu$m, is assessed. We take $z_{step} = 1\,\mu$m corresponding typically to the size of a bacterium. We image the mucus in brightfield, the bacteria in fluorescence. We also added $1\,\mu$m fluorescent beads to check for the penetration of passive objects. Bacteria and beads can be visualized independently. In all the figures, mucus is shown in blue, bacteria in green and beads in red.

The analysis is shown and detailed in figure IV.14 and IV.15, resulting in the 3D assessment of the localization of the bacteria and the 3D position of the interface. We then calculated the distances d between bacteria and the mucus interface : $d < 0$ when bacteria are in the motility buffer, $d > 0$ when bacteria are in the mucus. The resulting distribution $p(d)$ shows three distinct zones (see figure IV.16) : 1) very few bacteria are found in water, 2) when entering mucus, the concentration increases sharply with d until a maximal concentration at a transition distance $d = \lambda_T$ is reached. 3) Then the concentration decreases as we go deeper in mucus, characterized by a penetration length λ_P obtained via an exponential fit.

The distribution of bacteria along the mucus barrier is independent on the height in the sample (see figure **??**) : the presence of a glass surface does not seem to control, perhaps surprisingly, the bacterial transport properties in mucus. It would be interesting to measure

the surface residence times of bacteria in this case to check for an effect of mucus, compared to water.

The bacterial concentration fluctuates locally in the mucus (see figure IV.17), pointing to the presence of mechanical heterogeneities. It would be interesting to characterize optically those heterogeneities, for instance simply with a static picture with OCT microscopy, to check for a link between optical and mechanical characteristics. Also microrheology could reveal the local mechanical landscape of mucus.

The experiments have been replicated four times for the piglet #1 to check the reproducibility. The total penetration length $\lambda_P + \lambda_T = 224 \pm 34\mu$m is a more stable quantity than its constituents $\lambda_T = 92 \pm 58\mu$m and $\lambda_P = 132 \pm 43\mu$m (see figure **??**). A variation of only 15% for the total penetration length is very good given the complexity of the biological mucus and of the analysis. This quantity is also pertinent biologically and its order of magnitude is the hundred of microns, comparable to the in-vivo thickness of the loose mucus layer.

Most (loosely 99%) of the bacteria are found to be immobile in the mucus, while flagella can still be moving : they are blocked. How bacteria arrived at their trapped location ? Does the interface formation possesses some crucial properties, for instance due first to the drying and then to the wetting, or does it have the same mechanical properties as the rest of the mucus ? That is the kind of question we want to answer in details in the future with the Lagrangian tracking microscope.

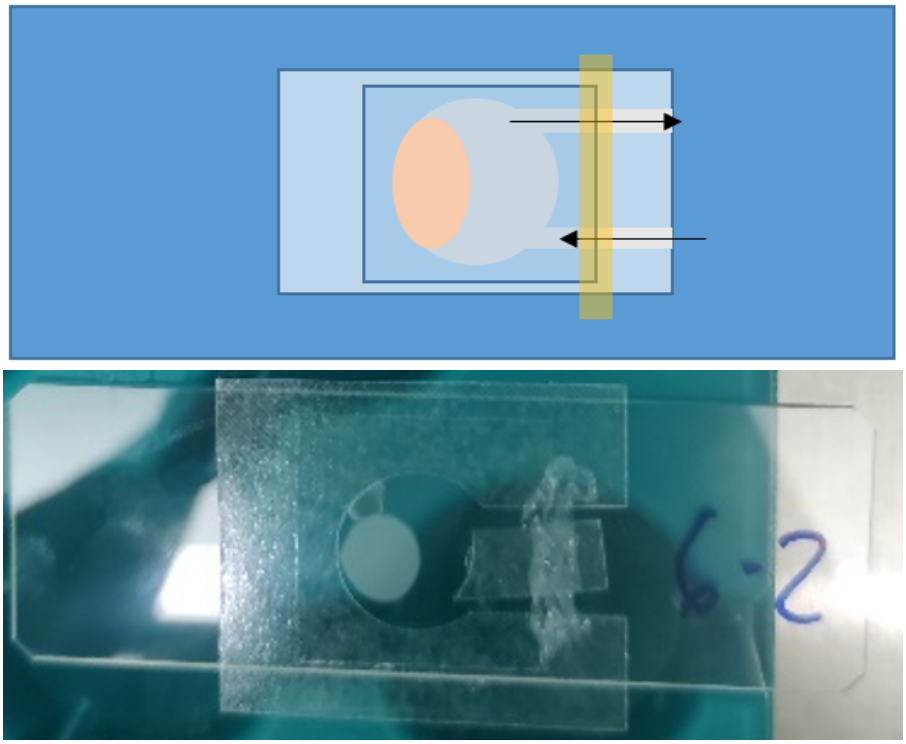

FIGURE IV.13 – Pool design to create a mucus interface. (top) Sketch of the pool set-up. Mucus (in orange) is sandwiched in a circular pool. Bacterial solution is injected by capillarity (left arrow), entering in contact with the mucus. Silicone (in yellow) finally closes the pool. (bottom) Final practical realization. The resulting interface between the mucus (white) and the bacterial solution (transparent) is sharp.

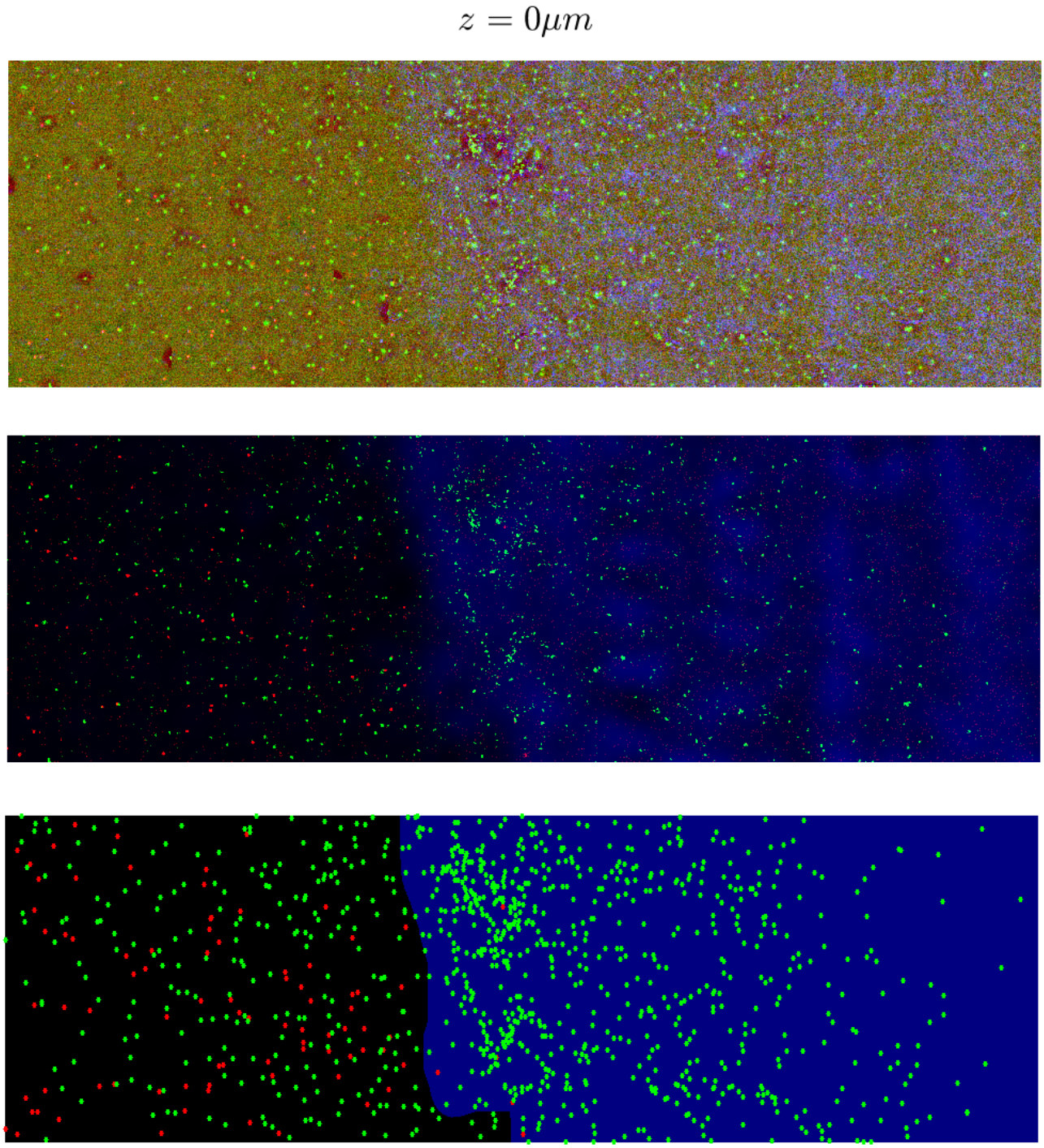

FIGURE IV.14 – Image analysis of a cartography plan (here the plane $z = 0\mu m$). The size of the image is around $2000\mu m \times 600\mu m$. Mucus is in blue, bacteria in green, and beads in red. (top) Combination of the raw images. The mucus barrier, the bacteria and the beads are visible. (middle) Binarization by thresholding of the raw images. (bottom) Detection of the different elements. Bacteria and beads are selected given a minimum area of $1\mu m^2$. Mucus is determined via a watershed algorithm. Unlike beads, bacteria penetrate into the mucus. There is no flow through the mucus interface. The interface is stable.

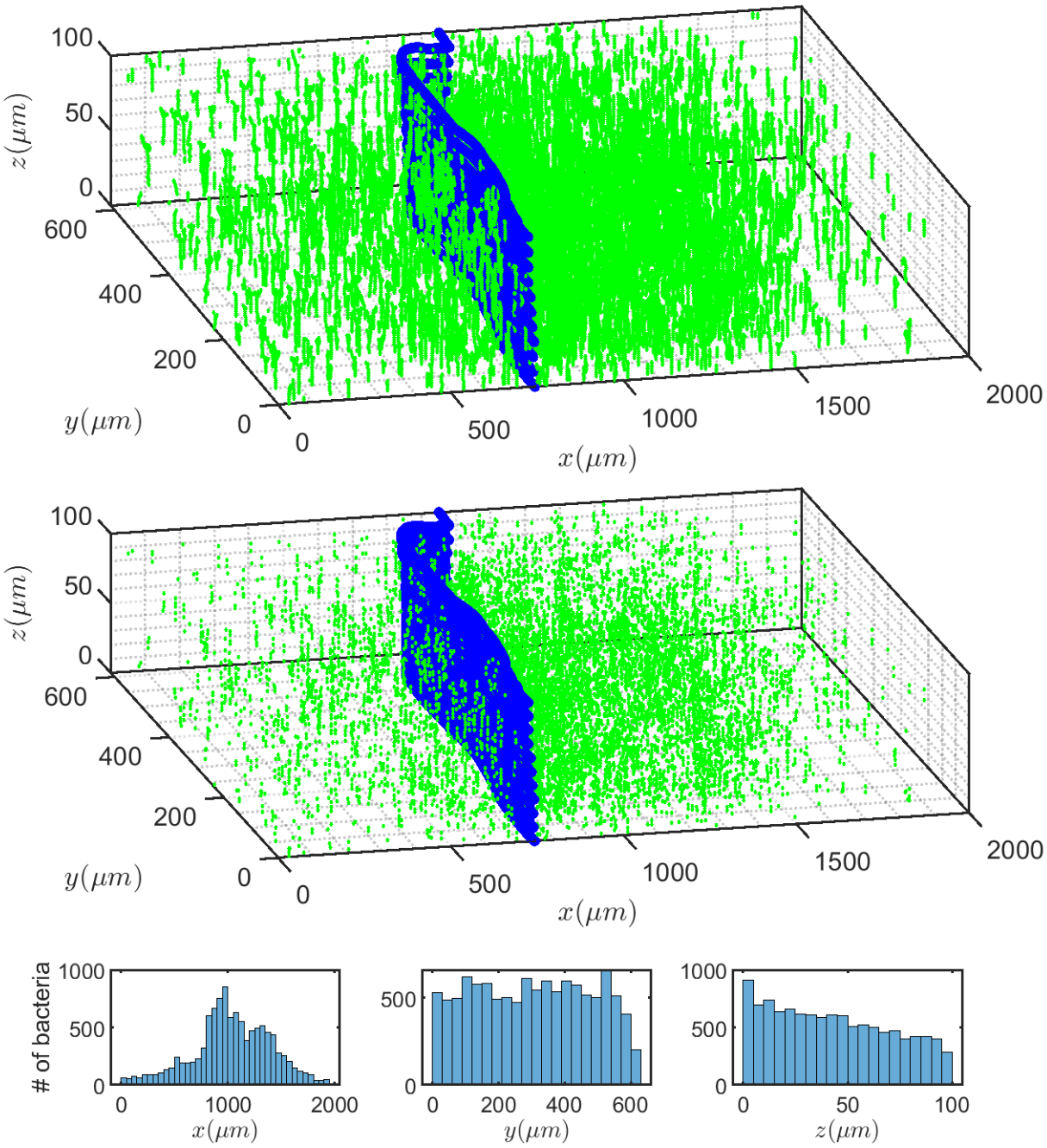

FIGURE IV.15 – 3D reconstruction of the cartography after image analysis. (a) Raw positions of the mucus interface (blue lines - every $10\mu m$ in height) and of the bacteria (green dots) on all cartographied plans. (b) Interpolated mucus interface (now a 2D surface) and selection of the bacteria through a tracking algorithm to make unique a bacteria present on successive plans. (c/d/e) Distribution of the number of bacteria along x/y/z axis. (c) On the x-axis, the mucus barrier impacts strongly the distribution. (d) On the y-axis, the distribution is constant (consistent with what is expected). (e) On the z-axis, there is first an accumulation at the bottom surface (range of order $15\mu m$), then a rather constant number (range of order 50 μm) and finally a decay, probably due to an increasing difficulty to detect the bacteria. We will restrict our study in height between 0 and $80\mu m$.

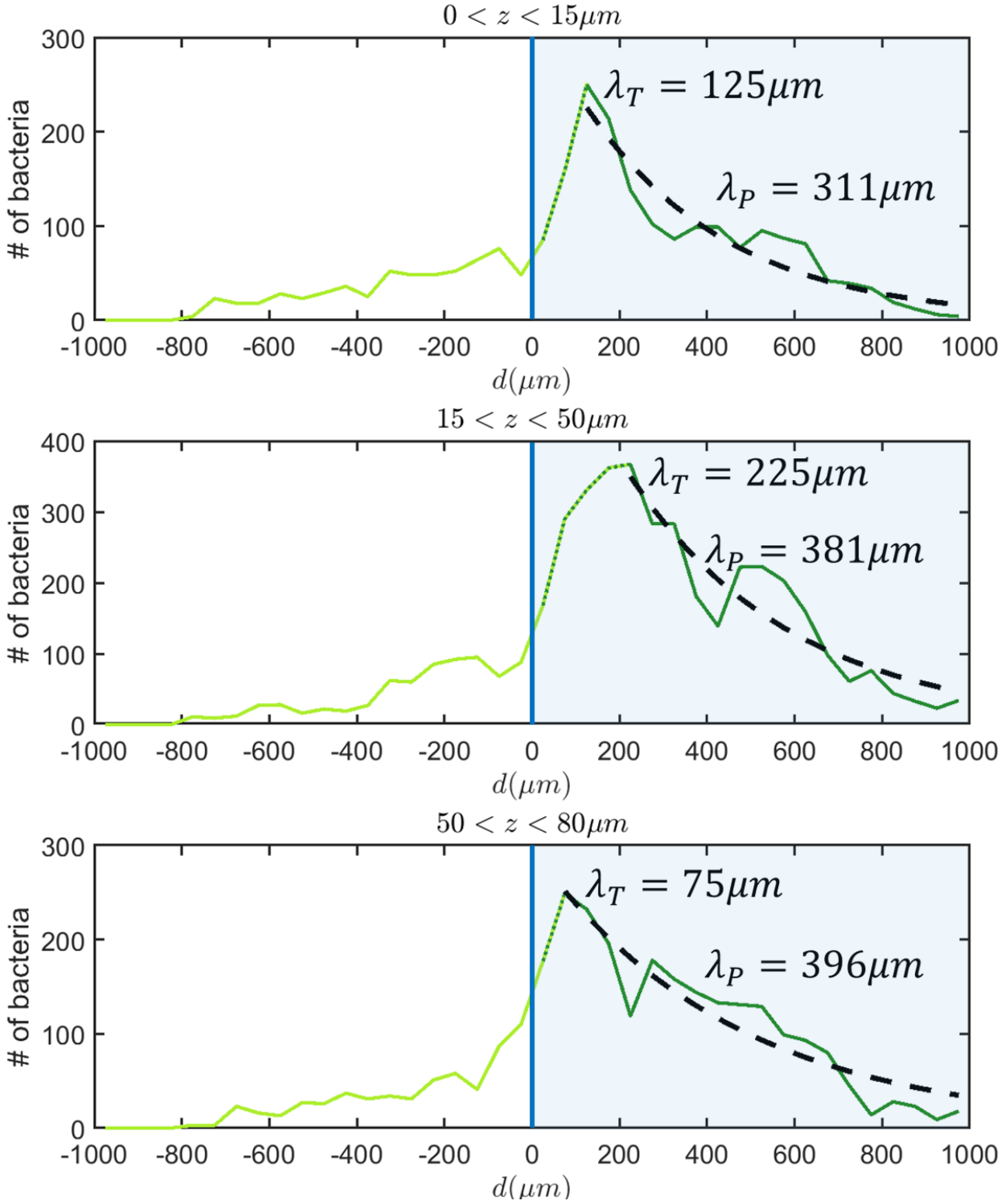

FIGURE IV.16 – Distribution of the number of bacteria depending on their distance d to the mucus interface $d = 0$ (solid blue line) for different height intervals : (a) $0 < z < 15\mu m$, (b) $15 < z < 50\mu m$ and (c) $50 < z < 80\mu m$. Light blue area represents mucus. Three areas are defined : the "water" area $d < 0$ in light green in which there are the bacteria remaining in water, very diluted. Then the "transition" area $0 < d < \lambda_t$ in light green superposed with dotted dark green where the bacterial concentration increases in the mucus. λ_t is the distance of the maximal number of bacteria. Finally the "mucus" area $d > \lambda_t$ in dark green where the bacterial concentration decreases as we go deep in the mucus. This part of the distribution is fitted (dashed line) by an exponentially decaying function to characterize a penetration length scale λ_p. Height does not show to have a major influence on the distribution.

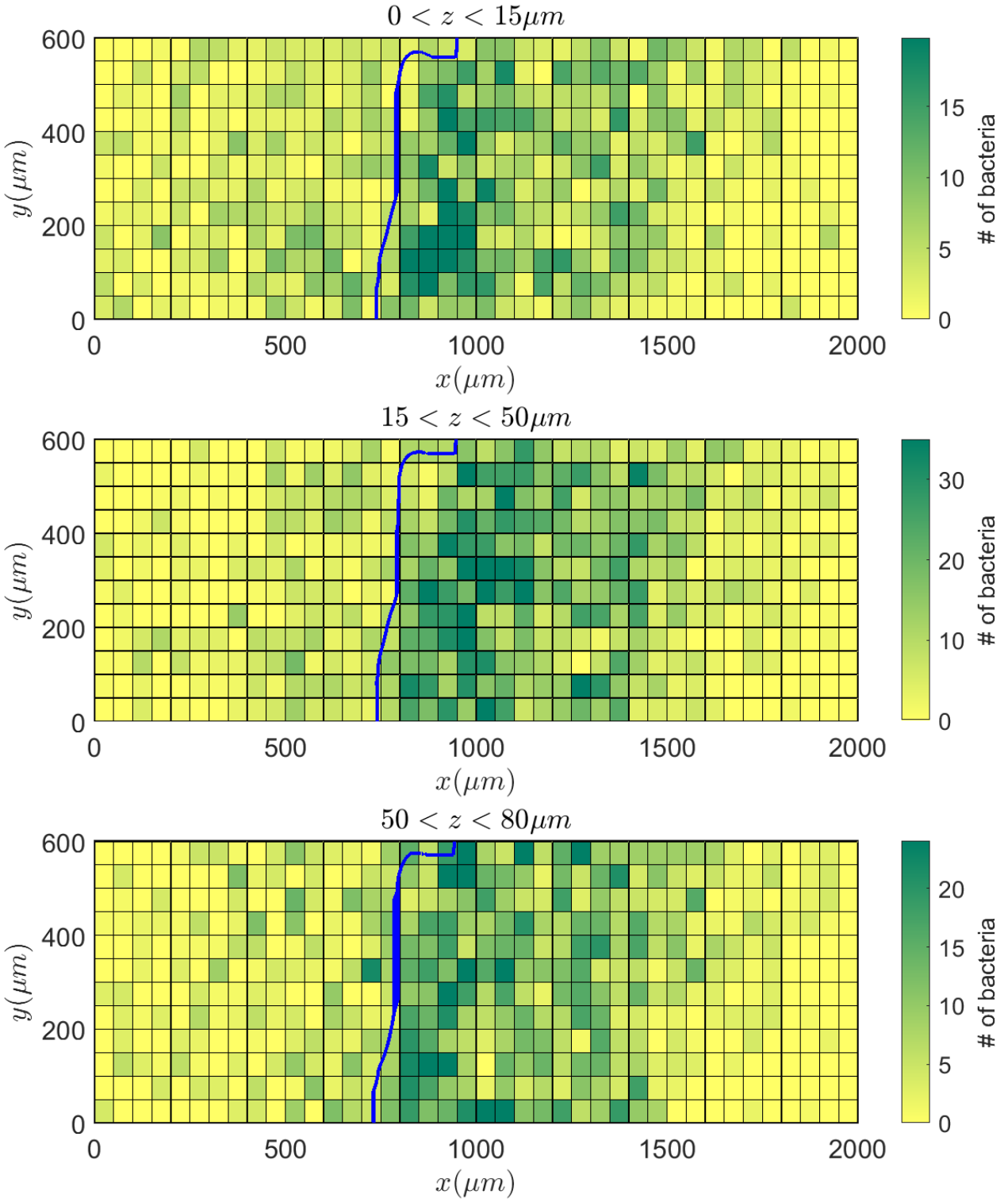

FIGURE IV.17 – Heatmap of the number of bacteria (in green color scale) on the XY plane for different height intervals. The associated mucus interface is the blue line (mucus covers the rightmost region of the line). (a) $0 < z < 15\mu m$, (b) $15 < z < 50\mu m$ and (c) $50 < z < 80\mu m$. Heatmaps are similar for the different height intervals : Bacteria accumulate at the beginning of the mucus barrier and the deeper one penetrates the mucus, the less bacteria are present. Local heterogeneities appear, reflecting heterogeneities in the mucus.

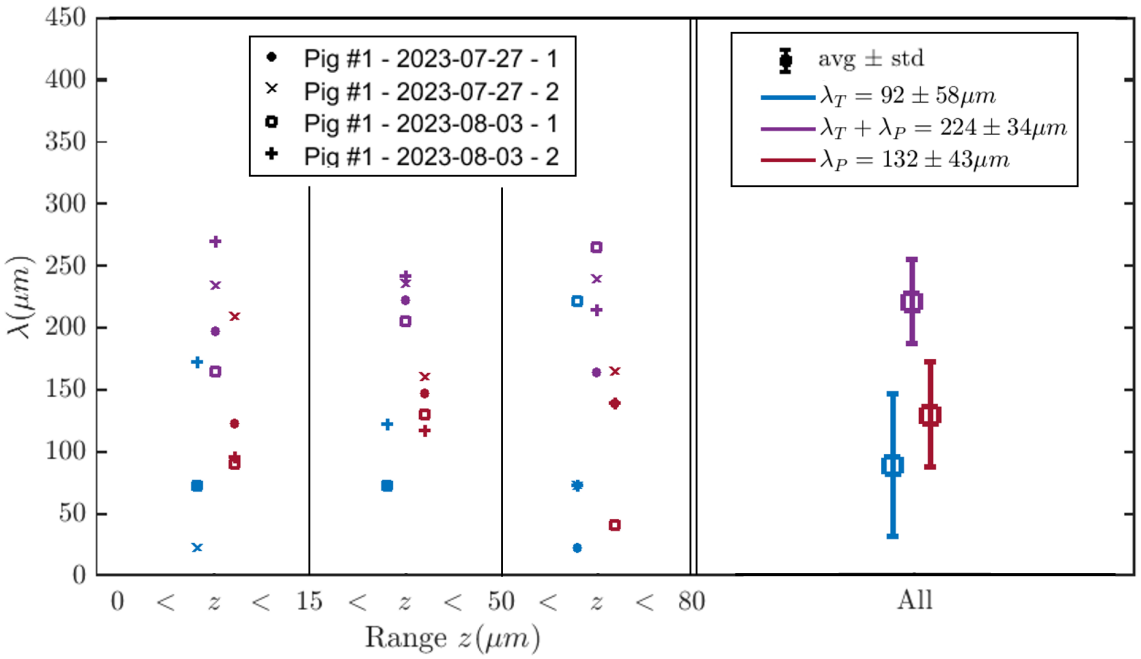

FIGURE IV.18 – Reproducibility of the bacterial penetration features for the piglet #1 done on four different slides prepared at two different days. Transition length λ_T (in blue), penetration length λ_P (in red) and total penetration length $\lambda_T + \lambda_P$ (in violet) as function of the distance from the surface z and for different experiments with the same piglet mucus. These quantities λ do not depend on the distance from the surface z. λ_P and λ_T show some variability, either inside an experiment at different heights, either from an experiment to another. Conversely, $\lambda_P + \lambda_T$ is a very robust quantity (only 15% variability). Error bars are standard deviations.

IV.3.4 Optimizing the throughput

These experiments are time-consuming while we need statistics. For the moment we had time to characterize three piglets for each group. We will characterize three more for each group in the future to enhance statistics. Standards in biology typically require five samples for each group. To achieve that in a reasonable amount of time, we use the schedule of figure IV.19, allowing for three samples a day. We detail here the schedule for only one sample :

1. 8 :00 : Reculture bacteria in TB.
2. 8 :45 : Mucus defrosting in eppendorf and the rheometer turned on.
3. 9 :45 : Mucus goes under the rheometer and the rotational test starts.
4. 10 :00 : Mucus is sandwiched in three preliminary prepared pools. We prepare three pools to cope with eventual failures and always keep a back-up sample. Mucus eppendorf goes back to the freezer.
5. 11 :00 : Bacteria are washed and transferred to their motility medium.
6. 12 :00 : Injection of the bacterial solution into the pools. The bacterial penetration starts. Injection must be done carefully.
7. 13 :30 : Two conform slides (i.e. with a sharp interface) are selected and cartographied at an appropriate place (far from walls, far from eventual bubbles...).
8. 14 :00 : Data are transferred to the hard drive.
9. 16 :45 : Clean everything. Run the pre-analysis overnight. It is a long process : about 8 hours.
10. 17 :15 : Prepare new bacteria and start again for the next day.

The procedure can be parallelized for three samples, but one should be aware that the resulting working day is intense and requires to be experienced with all the steps. The pre-analysis is in general not sufficient yet and a step of analysis with some changes in the parameters must be performed for a proper recognition of the interface.

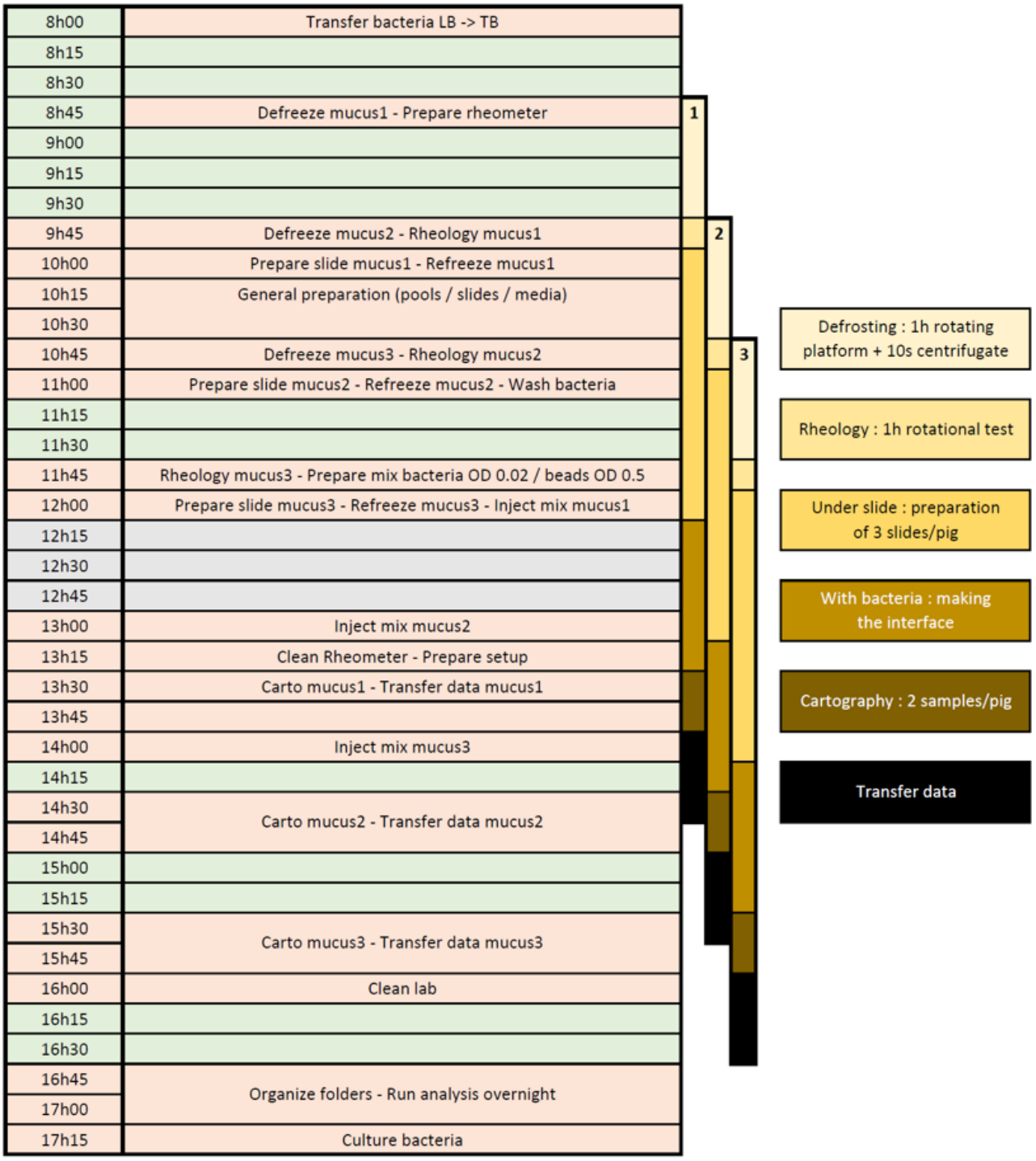

FIGURE IV.19 – Schedule to optimize a day of experiment. Details in the text.

IV.3.5 "Weaned" and "suckling" piglets : a comparative study

We first go back to the rheology measurements to discuss the data reproducibility and then synthesize the results over all the piglets, enhancing the presence of two different groups : "suckling" and "weaned" piglets. We show in figure IV.20a,b the resulting flow curves for every piglets. All "suckling" piglets flow curves are shown to be reversible and of the same order of magnitude, unlike "weaned" piglets flow curves which show an irreversible flow curve, pointing an effect of the shear history, which could be the signature of a nematic transition occurring in the mucus. An element of proof is the outcome of a yield stress, i.e a transition to a more "solid" state, occurring during the return of the shear rate. Before this "shear-history" effect, the first measured shear stress, at low shear rate, are of the same order of magnitude for the two groups. Since the rotational test lasts less than one hour, we could also check the effect of aging (see figure IV.20c,d) and the reproducibility after cycles of defrosting/refreezing (see figure IV.20e,f). Some mucus show a slight increase in the measured shear stress after resting some time T_{rest} in the rheometer. However the order of magnitude of the stresses obtained remains the same. The cycles of defrosting/refreezing does not affect much the material. We hypothesize that what matters more is the time during which the mucus is let in a defrosting state. In our case we defrost our samples during one hour in a rotating platform to avoid any form of degradation, and put it back in the freezer right after manipulations, typically fifteen minutes.

We noticed a strong difference in the rheological behavior between the two groups. What about the optical and bacterial penetration properties ? The extracted parameters are sketched in figure IV.21.

From the bacterial penetration experiment, we extract two characteristic length :

- the transition length λ_T is the distance between the mucus interface and the distance at which the maximal concentration of bacteria is measured.
- the penetration length λ_P is the characteristic length describing the decay of the bacterial concentration after its maximal.

The importance of the precise location of the maximum in those parameters, which in practice is not always very peaked, is reduced by looking at the total penetration length $\lambda_T + \lambda_P$ and we thus focus on this quantity..

From optical measurements, we extract two structure sizes : $\lambda_{opt-1} < \lambda_{opt-2}$ emerging from the radial autocorrelation function.

The results are presented in figure IV.22, where the piglets are classified depending on their group. The mucus of piglet #3 is shown to be very permeable and full of biofilms. Its resulting bacterial concentration profile is shown to be very flat and the measurement of $\lambda_T + \lambda_P$ is more than the measurement limit of this technique. For this mucus, only one structure size is pertinent, the bigger one is huge and not significant. Another mucus that looks quite different from the others is the mucus from piglet #1. Its penetration length (also reflected in the total penetration length) is far less than the other mucus, and it does not reflect in rheological nor optical measurements. For the other mucus we obtain typically the following parameters : $\lambda_T \approx 130\,\mu$m, $\lambda_P \approx 400\,\mu$m, $\lambda_T + \lambda_P \approx 550 \mu m$, $\lambda_{opt-1} \approx 0.13\,\mu$m, $\lambda_{opt-2} \approx 1\,\mu$m. The absence of relationship between rheological, optical and bacterial penetration measurements is surprising. Indeed in the previous work of Hector Urra on commercial mucin and carbopol [144] and also of Nazari et al in yield-stress fluids [44], the rheology is thought to control the motion of bacteria. The pH of all mucus extracts has been measured and is constantly close to 7. An hypothesis is that the purified mucus we use contain some chemicals affecting the probability of bacteria to adhere to the mucus. Characterizing systematically the mucus extracts optically with more convincing techniques such that OCT or probing its structure with neutron scattering are interesting perspectives that could lead to interesting results.

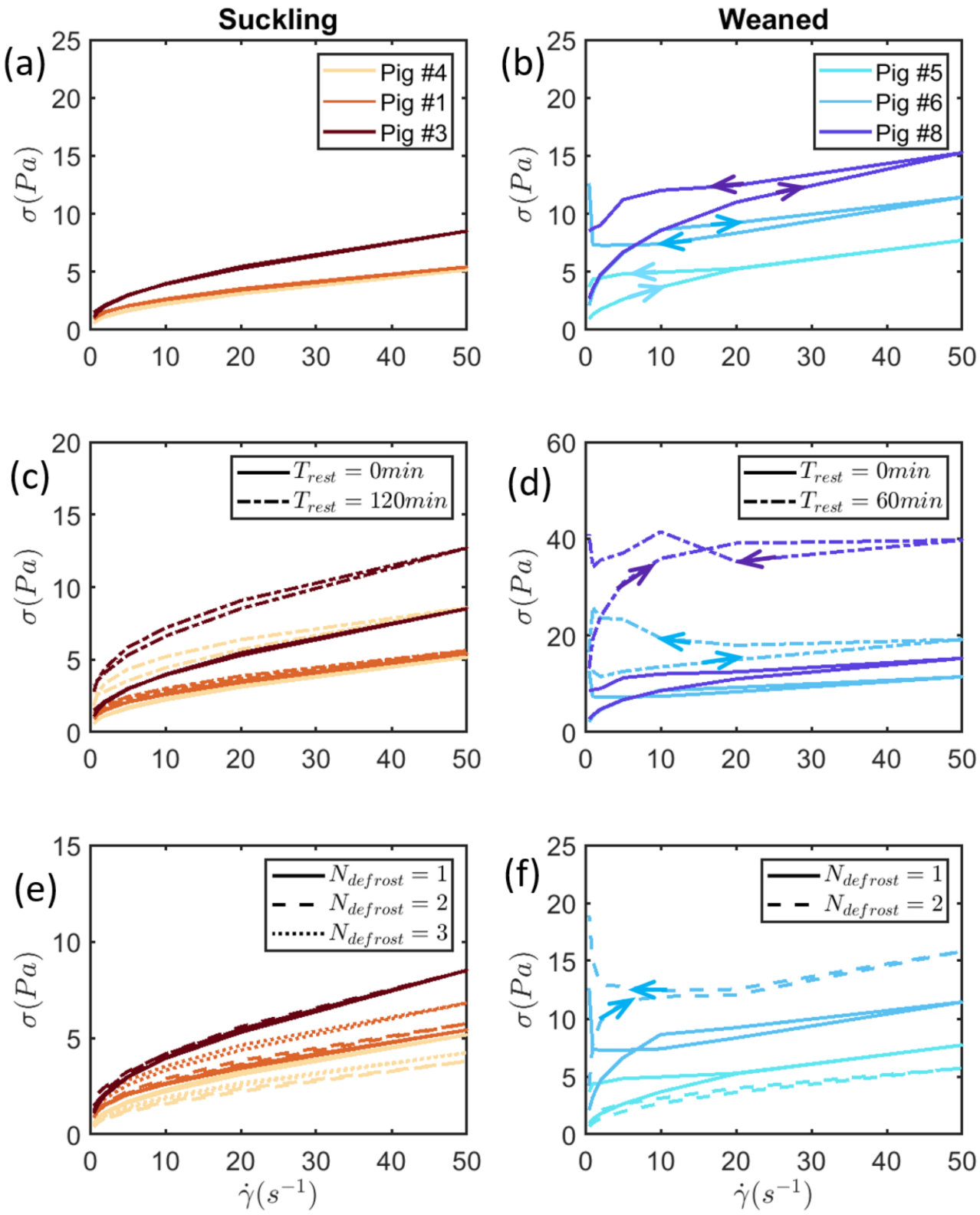

FIGURE IV.20 – Comparison of the flow curves for the mucus extracted from suckling (left) and weaned (right) piglets groups. On each curve are displayed up going (right arrows) and down going (left arrows) flow curves. Arrows are not always indicated to simplify the reading of the graphs. (a/b) Flow curves superpose / do not superpose. The measured shear stress are of the same order of magnitude in both groups. (c/d) Aging of the mucus. Mucus are let during a resting time T_{rest} in the rheometer before measurement. The shear stress increases with resting time (except for pig #1) in both groups. (e/f) Effect of the defrosting. The flow curves do not change significantly after several cycles of defrosting/refreezing $N_{defrost}$.

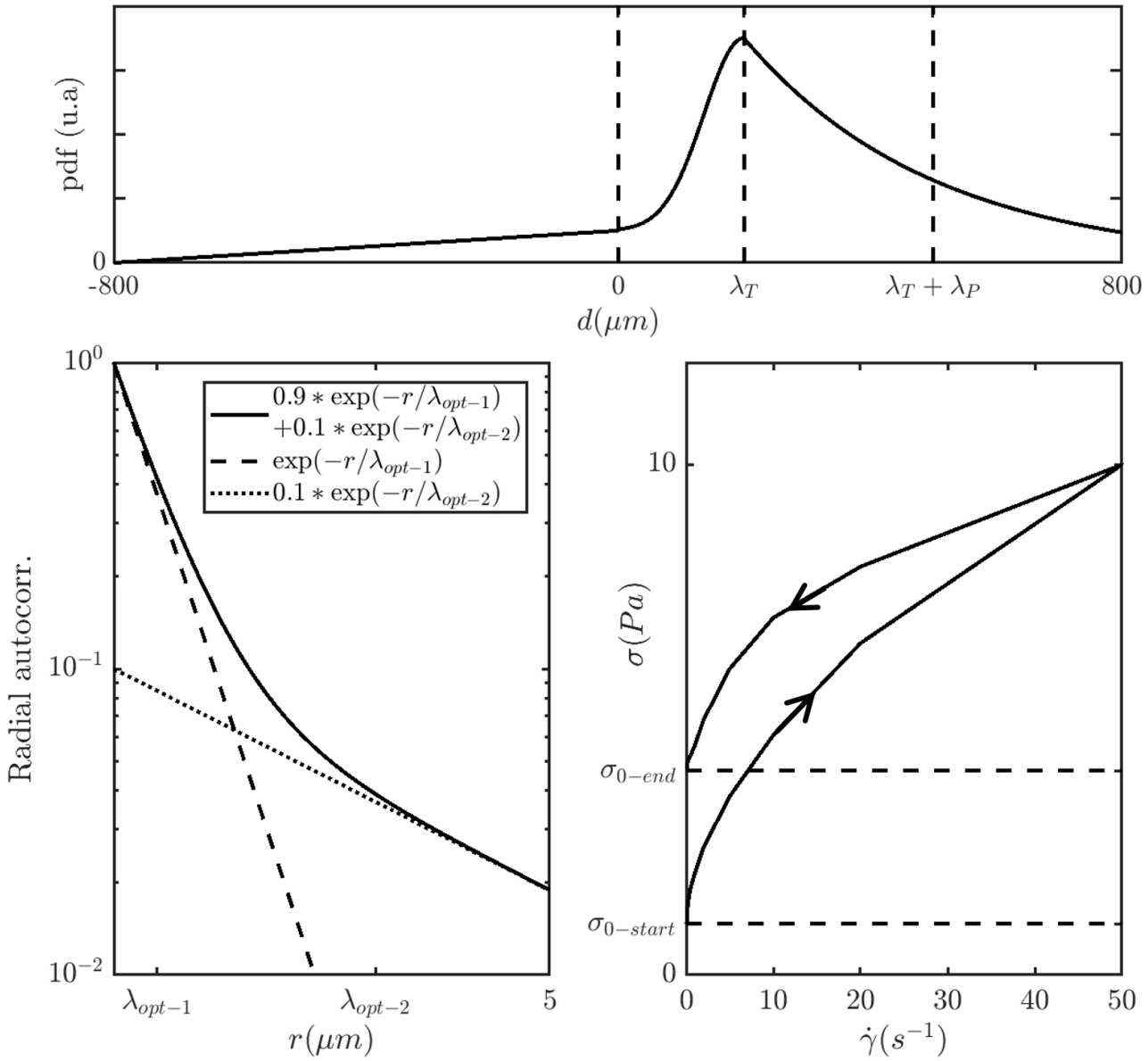

FIGURE IV.21 – Sketch of the different quantities extracted from the different mucus analysis. (a) Distribution of the number of bacteria as a function of their distance to the mucus interface. $d > 0$ in mucus. λ_T is the distance at which occurs the maximal value. λ_P is the characteristic length of the decay. (b) Radial autocorrelation function of the intensity from mucus imagery in log-scale (solid line). $\lambda_{opt-1} < \lambda_{opt-2}$ are the characteristic structure sizes fitted by the sum of two exponentials (in dashed and dotted line). In this example $\lambda_{opt-1} = 0.5\,\mu$m and $\lambda_{opt-1} = 3\,\mu$m. (c) Shear stress σ as a function of the shear rate $\dot{\gamma}$ (flow curve). The rotational test goes from increasing to decreasing values of shear rate (arrows). The two values obtained in the limit of low shear rate are $\sigma_{0-start}$ and σ_{0-end}.

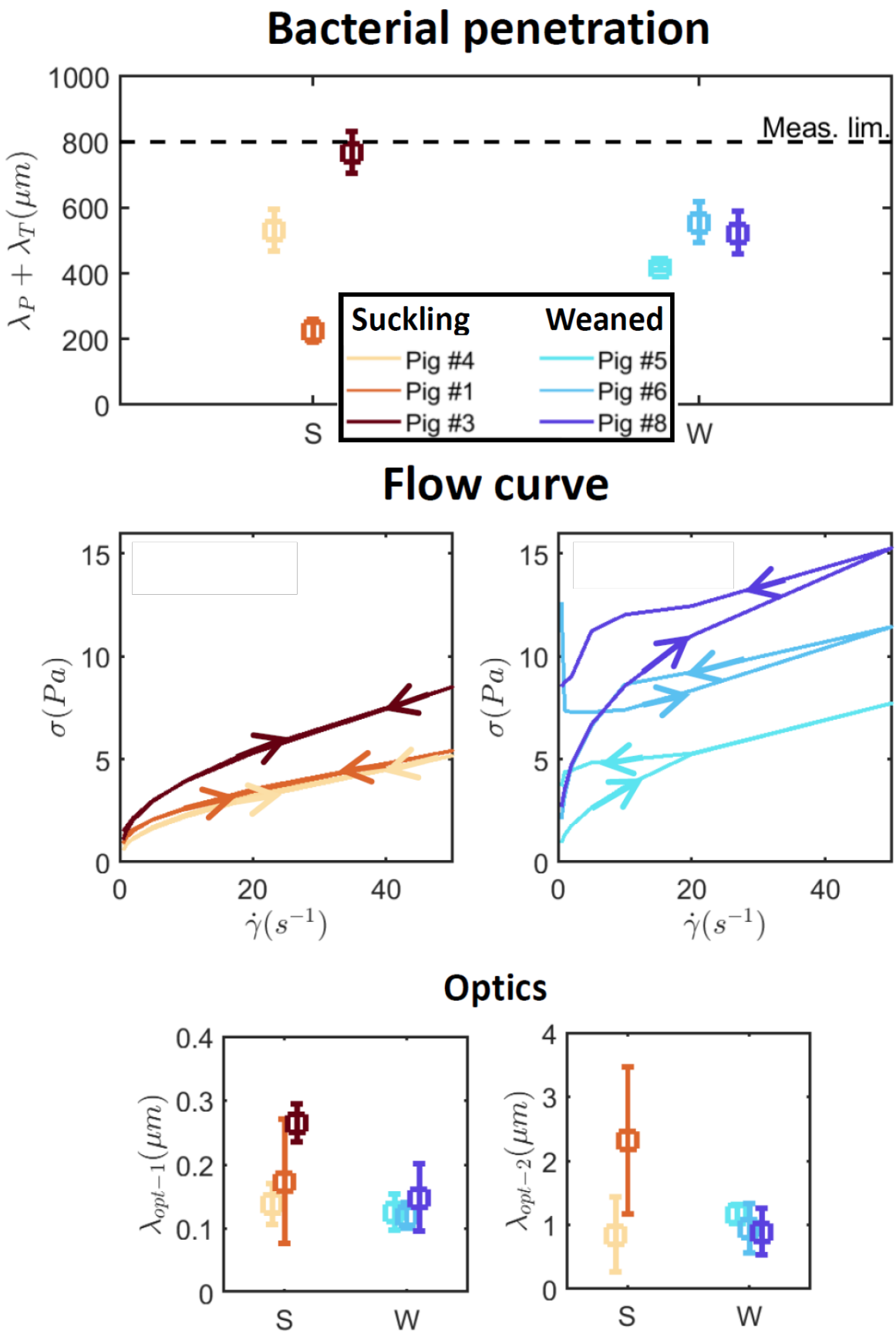

FIGURE IV.22 – Synthesis of the measured quantities from bacterial penetration, rheological and optical experiments. (S) Suckling. (W) Weaned. Error bars are errors on the mean. The broad range of bacterial penetration, from 200 to 800 μm are not directly linked with the rheological flow curve nor the optical structure sizes λ_{opt-1} and λ_{opt-2}.

IV.4 An heuristic view on bacteria penetration of mucus layers

Here, we present two simple models aiming at capturing the essential features found in the mucus bacteria penetration experiments. The purpose of the analysis is merely heuristic. We do not seek here for quantitative agreement or any fit with the experiments. The objective is to built on rational grounds a critical view of the results and to highlights some possible physical mechanisms, that will structure future investigations.
In both models, we consider the spatial exploration undertaken by motile bacteria as diffusive. For the moment, the diffusion coefficients in the mucus and in the fluid are assumed to be identical. In the mucus layer there is a trapping probability for the swimmers. This trapping process could be due to remnant peptide molecules dispersed in the mucus killing the bacteria, some geometrical blockade or chemical processes that hinder the swimming ability.

The first model PEN1, highlights the initial presence of attractant molecules in the mucus, like sugars constituting the mucin, that spread in the fluid and deplete the mucus layer. The attractant gradients hence created, are driving a chemotactic response of the bacteria towards the mucus deepest layers and competes with the trapping process. The second model PEN2 assumes an alteration of the mucus barrier in contact with the fluid. The modification of the barrier properties can be due to a dilution problem or a structural reorganization of the mucine molecules in presence of a solvent. Note that both models are not necessary exclusive and in reality, chemotaxis and mucus alteration could occur both at the same time.

An essential objective of the models is to be able to reproduce the maximum observed for the particle trapping distribution as well as the final decay that defines the penetration limit. Both models are unidimensional along a direction x perpendicular to the interface. The fluid layer width is L_F and the mucus layer L_M The fluid/mucus interface is situated at $x = X_M$. In both models the edges display reflective boundary conditions for diffusion. The bacteria diffusion coefficient is D_B and the trapping rate $\kappa(x)$. The concentrations of motile and stuck bacteria are respectively $n(x,t)$ and $n^s(x,t)$. The initial bacteria concentration profile is uniform in the fluid ($n = n_0$) and no bacteria are in the mucus.

IV.4.1 Model PEN1 - chemotaxis

In model PEN1, the attractive ligand concentration is $L(x,t)$. Starting at $t = 0$, from an initial Heaviside step of concentration L_0 for $x > X_M$, at $t > 0$ the concentration profile is then : $L(x,t) = L_0 erf(\frac{x-X_M}{\sqrt{4D_L t}})$, where D_L is the ligand diffusion coefficient. In the mucus layer ($x > X_M$) the trapping rate is constant : $\kappa(x) = \kappa_0$. The dynamical equations for the motile and stuck bacteria are then :

$$\dot{n} = D_B n_{xx} + \nabla_x(\chi L_x n) - \kappa_0 n \quad \text{(IV.3)}$$

$$\dot{n}^s = \kappa_0 n \quad \text{(IV.4)}$$

χ is a chemotactic response coefficient taken here as a constant. This macroscopic chemotactic response corresponds to the simplest form of a macroscopic Keller-Segel model. This picture induces a natural space/time re-scaling with a penetration length scale $\lambda = \sqrt{D_B/\kappa_0}$ and a time scale $1/\kappa_0$. Hence, in dimensionless variables the dynamical equations are :

$$L(x,t) = erf(\frac{\beta(x - X_M}{2\sqrt{t}}) \quad \text{(IV.5)}$$

$$\dot{n} = n_{xx} + \alpha\nabla_x(L_x n) - n \quad \text{(IV.6)}$$

$$\dot{n}^s = n \quad \text{(IV.7)}$$

Here, the concentration fields are normalized ($L \to L/L_0$, $n \to n/n_0$ and $n^s \to n^s/n_0$) and therefore the dimension less coefficient α (chemotactic strength) and β (diffusion ratio) are :

$$\alpha = \frac{\chi L_0}{D_B} \tag{IV.8}$$

$$\beta = \sqrt{\frac{D_B}{D_L}} \tag{IV.9}$$

The set of equations IV.7 is solved numerically with a Matlab solver (pdepe) suited for 1-D parabolic and elliptic PDEs. In figure IV.23, the time development of the penetration process is monitored. One can observe the ligand spreading across the system, in association with a penetration of motile bacteria and a progressive emergence of stuck cells. The stuck cell profile displays a maximum followed by a final exponential decay in the depth of the mucus layer. In figure IV.24 are displayed the terminal profiles of stuck bacteria for different chemotactic strengths α at a constant diffusivity ratio $\beta = 1$. In figure IV.25, one can observe a weak, quasi-logarithmic evolution of the penetration depth l_p with α from a value $l_0 \approx 1.34$. Above $\alpha \approx 80$, a peak shows up in the stuck cells distribution which position in the layer depth increases quasi-logarithmically with α such that the final exponential decay remains quasi constant and of the order l_0. Therefore in this framework the measurement of the final decay is a characterization of the trapping process and the peak position a characterisation of the chemotactic process.

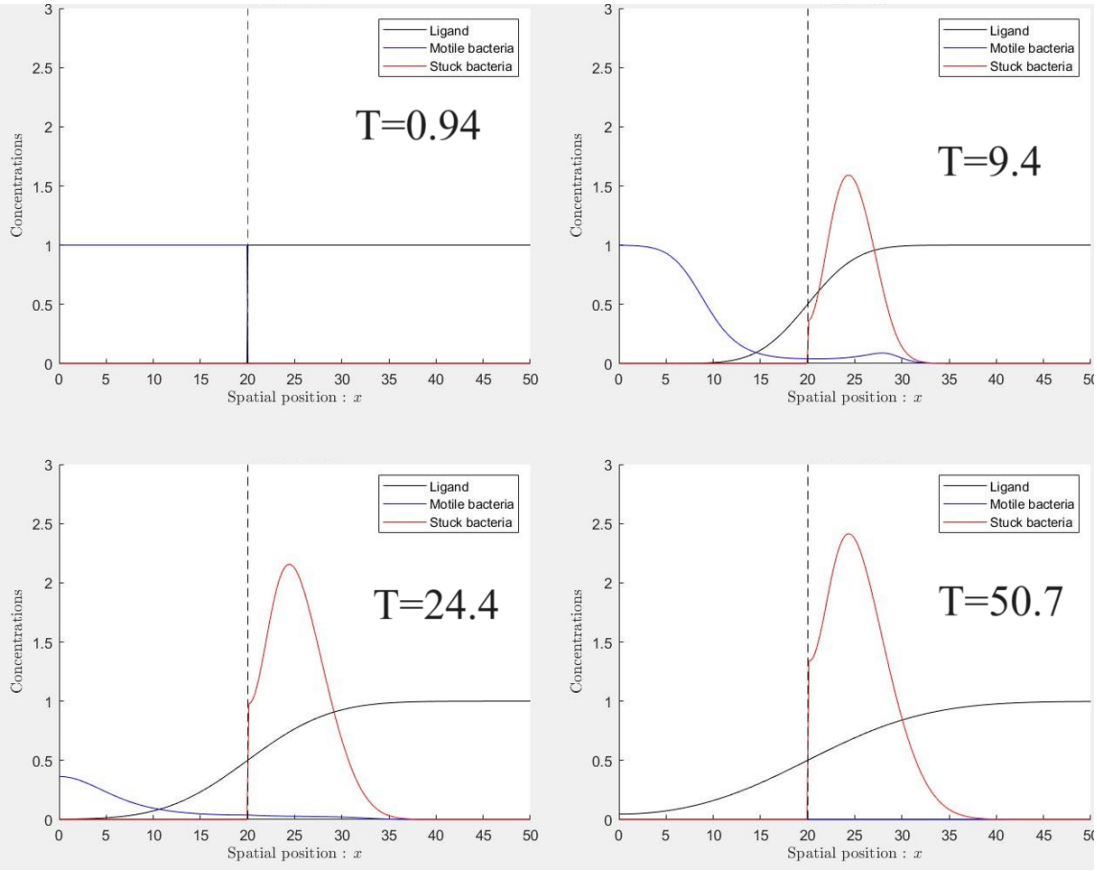

FIGURE IV.23 – PEN1 Model - Time evolution of the ligand $L(x,t)$, motile bacteria $n(x,t)$ and stuck bacteria $n^s(x,t)$ concentrations ($t = 0.94, 9.4, 24.44, 50.76$), for a fluid layer $L_F = 20$ in contact with a mucus layer $L_M = 30$. The chemotactic strength is $\alpha = 150$ and diffusion ratio $\beta = 1$.

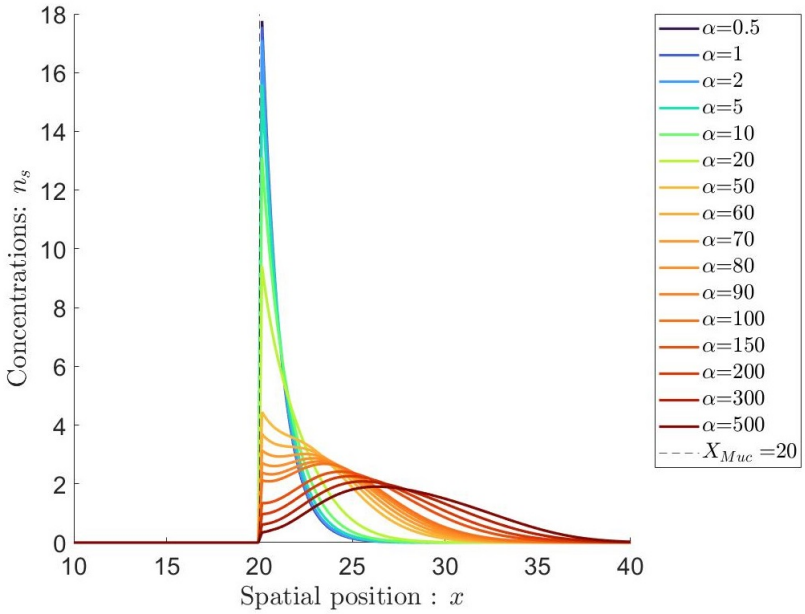

FIGURE IV.24 – PEN1 Model - Final concentration profile of stuck bacteria $n^s(x, \infty)$ as a function of the chemotactic strength α. Fluid layer $L_F = 20$, mucus layer $L_M = 30$ and diffusion ratio $\beta = 1$.

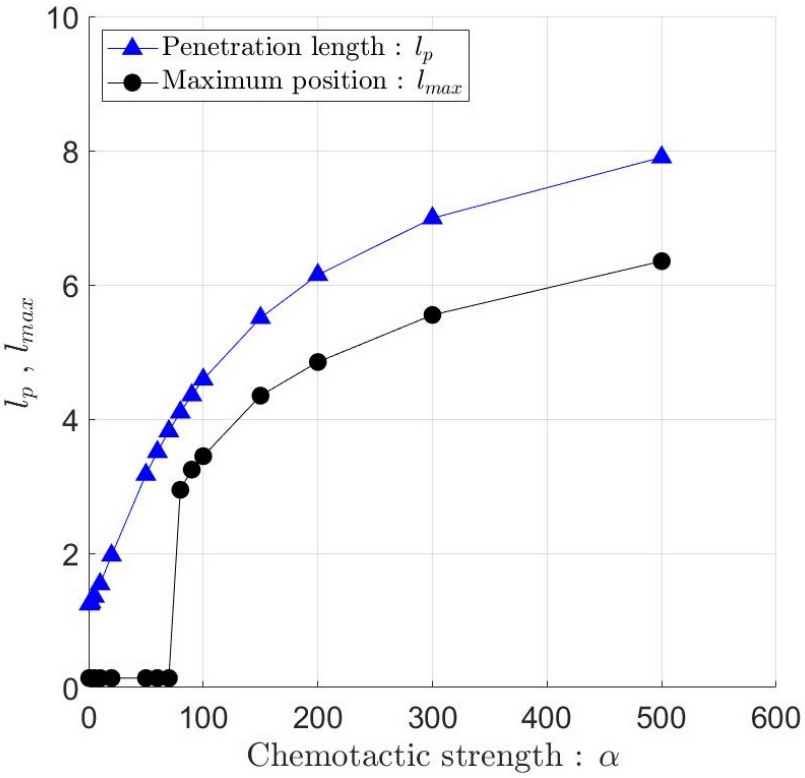

FIGURE IV.25 – PEN1 Model - Penetration length l_p and position of the maximum l_{max} of stuck bacteria as a function of the chemotactic strength α. Fluid layer $L_F = 20$, mucus layer $L_M = 30$ and diffusion ratio $\beta = 1$.

IV.4.2 Model PEN2 - mucus barrier alteration

The second PEN2 model assumes a space dependent trapping rate : $\kappa(x) = \kappa_0(1-exp(-x/\Delta)$ where Δ is a length characterizing the alteration of the mucus barrier.
Re-scaling for space and time ($x \to x/\lambda$ and $t \to \kappa_0 t$) and for densities ($n \to n/n_0$ and $n^s \to n^s/n_0$), yields a set of dimensionless equations for $n(x,t)$ and $n^s(x,t)$:

$$\dot{n} = n_{xx} - (1 - exp(-x/\delta)n \quad \text{(IV.10)}$$

$$\dot{n^s} = (1 - exp(-x/\delta)n \quad \text{(IV.11)}$$

where $\delta = \Delta/\lambda$. The PDEs are solved using the Matlab solver pdepe. On figure (IV.27) are displayed the time evolution of the motile and stuck bacteria for a mucus alteration length $\delta = 10$. One can observe that the stuck bacteria profile also displays a maximum followed by a final decay. On figure (IV.28) are displayed the terminal profiles of stuck bacteria for different δ values. On figure (IV.28) are represented the penetration length l_p and the peak position l_{max} as a function of δ. Both lengths seems to follows asymptotically, for large δ, a power law as : $l_p \propto \delta^a$ with an exponent $a \approx 1/3$.

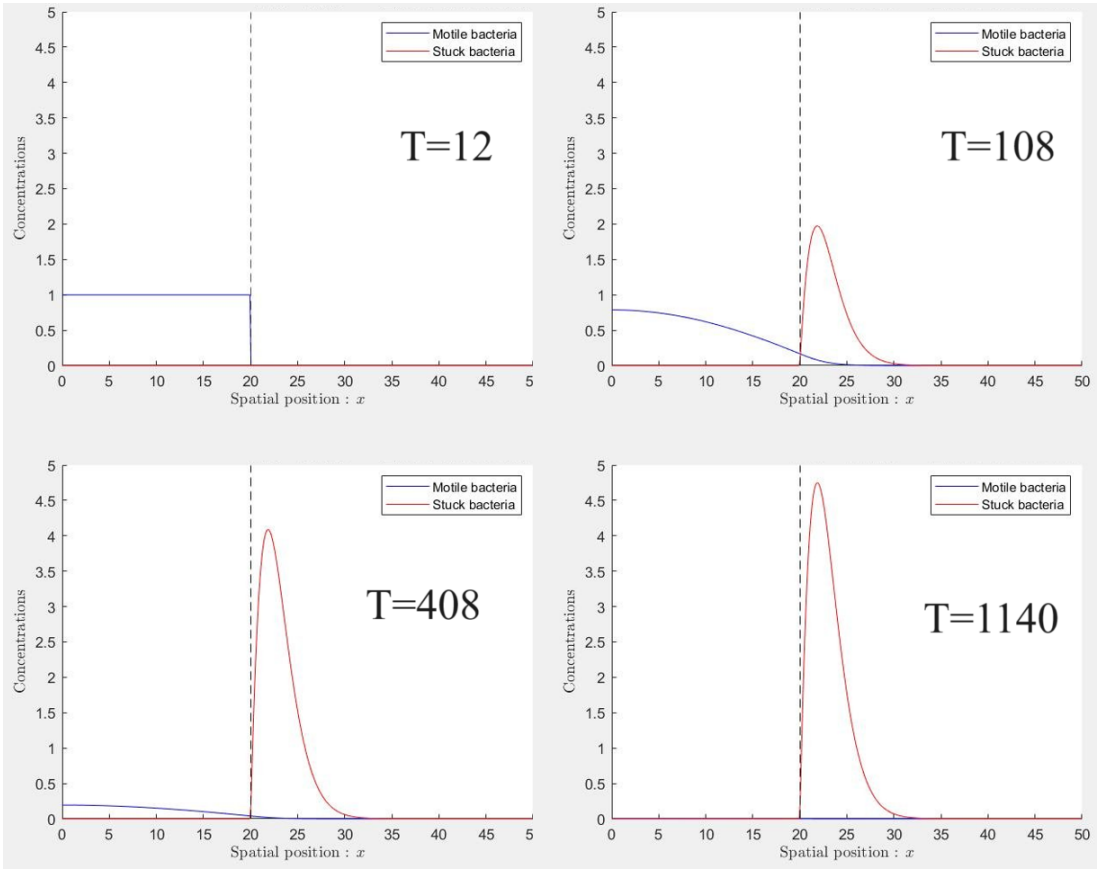

FIGURE IV.26 – PEN2 Model - Time evolution of the motile $n(x,t)$ and stuck $n^s(x,t)$ bacteria concentrations ($t = 12, 108, 408, 1140$), for a fluid layer $L_F = 20$ in contact with a mucus layer $L_M = 30$. The mucus alteration length is $\delta = 10$.

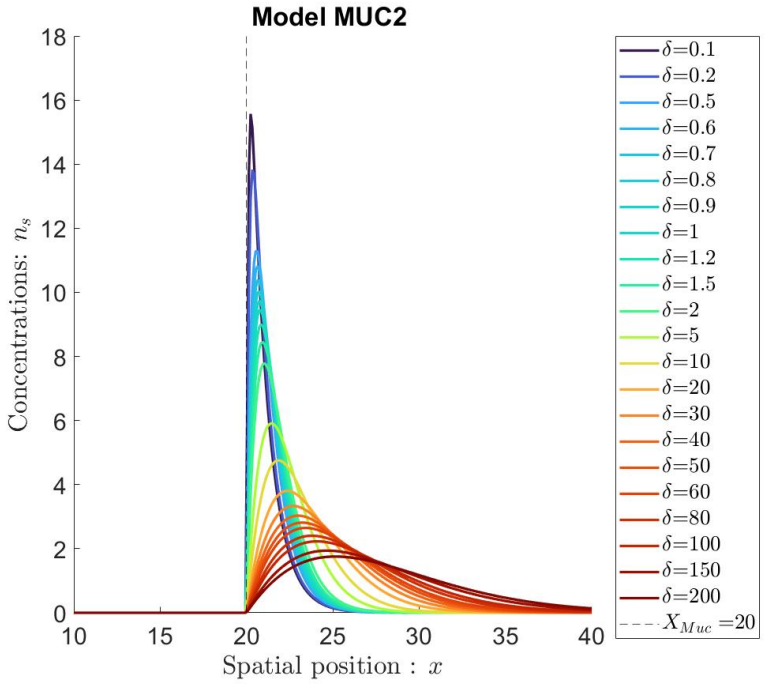

FIGURE IV.27 – PEN2 Model - Final concentration profile of stuck bacteria $n^s(x, \infty)$ as a function of the mucus alteration length δ. Fluid layer $L_F = 20$, mucus layer $L_M = 30$.

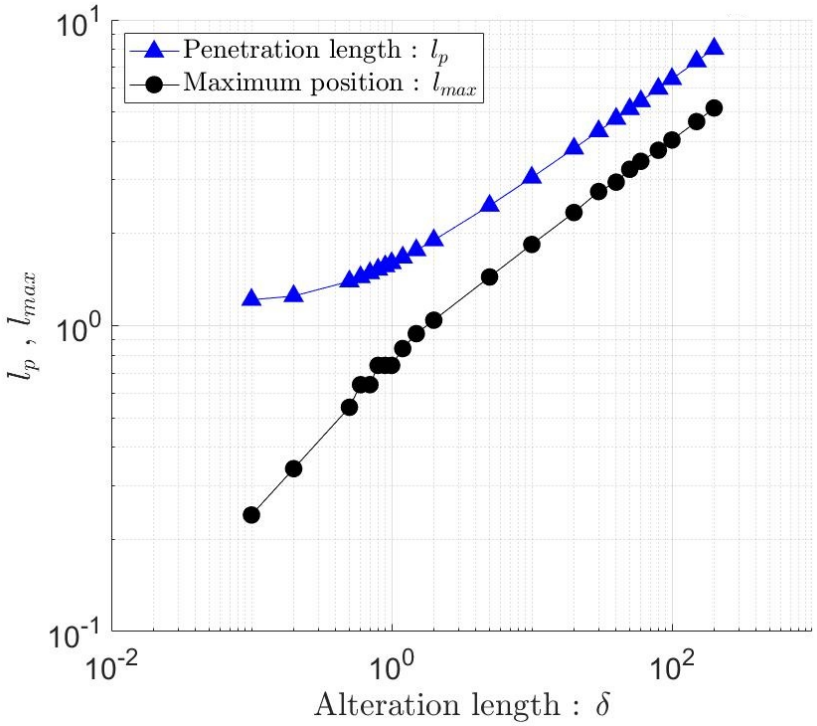

FIGURE IV.28 – PEN2 Model - Penetration length l_p and position of the maximum peak l_{max} of stuck bacteria as a function of δ. Fluid layer $L_F = 20$, mucus layer $L_M = 30$.

IV.4.3 Discussion

Both models seem to reproduce qualitatively the emergence of the most salient features observed experimentally in the bacteria penetration experiments.
A very important step would be first to find out whether in the mucus , even though it was dialyzed quite thoroughly, would remains some chemical elements of interest in the building of the penetration model. First, it would be possible to dilute the mucus and filter out the supernatant fluid and test directly whether a chemo-attractant response is still present for the bacteria. Also, in this fluid, the eventual presence of peptides, a natural bacteria killer in intestinal mucus, could be tested. Along those lines, it would also be important to provide an estimation of the typical molecular diffusion constant in the mucus layer, for example using a fluid initially mixed with a fluorescent dye and measure the penetration kinematic within the mucus layer using confocal microscopy. Another, strong hypothesis of the model is the assumption of diffusive exploration modes for bacteria in both media (fluid ans mucus). The first chapter of this thesis was dedicated to a deeper understanding of the emerging transport properties in a minimal fluid and in presence of confinement. Some results obtained there can be transferred to this problem. However, for the exploration processes in the mucus layer, hardly anything is known. The new Lagrangian tracking tools developed in the next chapter, in particular the AI algorithm, would be of upmost interest to be able to track bacteria individually when crossing from the fluid to the mucus layer. From those results, a much more refine model of the kinetic processes undertaken by bacteria in the mucus environment would be obtained. Finally, it could be of great interest to test at a microscopic level the local mechanical status of the mucus. To this purpose, micro-rheological tools could be developed to probe in-situ resistance and rheology of the mucus layer.

IV.5 Conclusion and perspectives

Our mucus is obtained directly from the intestines of piglets, which are divided into two groups according to their diet. The mucus is purified to remove most of the chemical components, such as nutrients or peptides, to focus on the properties of the "mucin" network : the main molecular component of this biological fluid. How the mucus extracts obtained are close to in vivo conditions is difficult to assess. However, we provide a first methodology to physically characterize them in the laboratory. This exploratory work is reported, both successes and failures, and many perspectives are suggested for future studies.

The core of this work is based on an experimental setup in which bacteria cross a mucus barrier. A sharp and stable interface between a bacterial fluid and mucus is achieved. Bacteria are found to migrate and become trapped in the mucus portion. Bacterial penetration of this in vitro mucus barrier is quantified with a static picture after two hours of bacterial invasion, which we refer to as the steady-state because most bacteria are found to be immobile. The steady-state bacterial concentration profile from water to mucus has several characteristics : 1) few bacteria are found in the water, 2) bacteria accumulate in the mucus : a maximum is observed, followed by an exponential decay. These observations can be rationalized by a simple scenario : 1) Bacteria can diffuse both in water and in mucus. 2) Most of the bacteria are localized in the mucus because they get stuck there with a certain probability (or rate), which also explains the decay observed in the profile. 3) The observation of a maximum in the profile after the measured interface can be explained by hydration of the mucus at the interface (which locally reduces the probability of entrapment) or by an effect of chemotaxis (indeed, mucus is highly glycosylated, i.e. full of carbohydrates). This static picture provides already some elements of understanding on the bacterial penetration of the mucus barrier. However a temporal picture is missing : a simple assessment of the migration process could already

provide valuable information, but the full dynamics of individual bacteria starting from the water tank and then penetrating the mucus barrier, while visualizing their flagella, could lead to the detailed exploration mechanisms. Note that the time $t = 0$ of the penetration of a bacterium allowed by the presence of a sharp interface is interesting to avoid biases in the selection of a bacterium. It is necessary to develop a Lagrangian tracking technique suitable for bacteria in mucus, which is the subject of the next chapter.

The penetration of bacteria in mucus is biologically relevant in itself. However, the structure and rheological properties of the mucus can be helpful to understand the swimming properties. Optically, mucus exhibits heterogeneities at the microscopic level. We have used simple bright field microscopy to optically characterize these heterogeneities with two "structure lengths", because this technique is easily accessible in the laboratory. However, we suggest that the results obtained should be compared with more sophisticated techniques such as OCT microscopy [152]. Confocal microscopy of stained mucus would also be a way to compare our purified mucus extracts with mucus closer to the "in vivo" situation reported in the literature [49, 48]. Rheologically, we established a reproducible protocol to determine the mucus flow curve. Mucus exhibits yield stress and shear thinning, which can be described by a Herschel-Bulkley fluid. Surprisingly, some mucus extracts are affected by their shear history, suggesting a structural change such as a nematic transition previously reported in mucus [45]. This could be checked under cross polarizers after inducing a shear, using a method similar to that used to characterize the nematic order of liquid crystals [41].

We compared mucus samples extracted from three "suckling" and three "weaned" piglets. These two groups differ by a change in diet (milk vs. solid food), but also by age (21 days old vs. 35 days old). From our rheological measurements, the mucus of the "suckling" group appears more stable (with ageing and thawing) and not affected by the shear history, whereas the mucus of the "weaned" group shows less stability and a strong effect of the shear history. This difference needs to be verified with more samples. However, all flow curves are of the same order of magnitude and this does not affect the bacterial penetration experiment. In fact, the measured total penetration length can vary from 200 to more than $800\,\mu$m, typically the thickness of the mucus barrier [137].

Four of the six characterized samples have the same total penetration length of $600\,\mu$m as well as the same "structure lengths". Interestingly, and despite having the same rheological behaviour and the same dry mass percentage, piglet #1 is shown to be a stronger barrier with a total penetration length of $200\,\mu$m whereas mucus from piglet #3 shows no barrier effect with a total penetration length greater than the measurement limit of $800\,\mu$m. For both samples, the optical measurements show larger structure lengths with higher variability. These two "extreme" cases could be a starting point for deeper comparisons. A simple macrorheology experiment does not therefore explain the bacterial penetration in our extracts : this could be due to the presence of antibacterial chemical residues (for example, this could explain the results for piglet #1) or to different mucus structures (for example, larger meshes in the mucus of piglet #3 could explain why the barrier function is not guaranteed).

There is a need for further characterisation. One could try to do microrheological experiments with smaller PEG-coated beads [154], typically of tens of nanometers, i.e. the thickness of flagella, or magnetic wires [155]. Neutron or X-ray [156] scattering could also be used to quantify the mesh size.

We proposed this pioneering work to understand the swimming properties of bacteria in biological mucus. We hope that these new experimental protocols and analysis pipeline, as well as the suggestions, will be helpful for future investigations on the penetration of microswimmers into complex fluids. To this end, the next chapter is dedicated to a new Lagrangian tracking method that aims to extend the use of the Lagrangian setup to optically complex environments such as our mucus extracts.

Chapter V

Lagrangian tracking : a paradigmatic change based on AI

The aim of this chapter is to extend the use of the 3D Lagrangian tracking already implemented for fluorescent bacteria in simple environment to the more general case of any object in more complex environments, specifically in mucus which is optically turbid. This work was done in collaboration with Thierry Darnige, engineer in the PMMH. We collaborated with Pr. Giovanni Volpe and Dr. Daniel Midtvedt (from the University of Gothenburg, Sweden) who are experts in machine learning for active matter. They have developed the framework "DeepTrack" [157] based on "TensorFlow" [158] that aims at simplifying the powerful use of machine learning methods for microscopy [159].

V.1 On the different methods of tracking

Different methods to study the motility of micro-objects exist :

- Optical tweezers allow to keep the object in a localized area. Knowing the force applied on the object, one can a posteriori determine some properties of the motion [160]. It's also a method that has been used to study the R&T dynamics [106].
- Digital holographic microscopy (DHM) [161] successfully implemented in [132] using the principle of holography.
- Defocussed imaging methods [162] using a library of defocussed images to determine the actual z-position of the tracked object.
- Lagrangian methods (unlike the previously described Eulerian methods which focus on what happens in a fixed location), first developed by H. Berg in 1971 [163], aim at keeping the tracked object in focus of the objective during its motion [164, 165].

The implementation of any of these methods require image or signal analysis at some point. In addition to classical algorithms, machine learning has shown to be generally very efficient in those topics and is getting more and more used in active matter [159].

The Lagrangian methods are the gold standard since it allows for precise high-speed, long-time and large-scale observations while directly visualizing the object and its surrounding environment. It's also less-dependant to optical heterogeneities that can be present in complex environments. However, Lagrangian methods are costly and hard to implement. It is also not high-throughput (objects can only be tracked one at a time) so it can be quite demanding to get some statistics.

V.2 Motivations

Beyond the need to find a new method to track bacteria in optically complex fluids, the tracking algorithm based on rules (detailed in chapter III.1) has limitations that can be conceptually overcome by a method based on machine learning :

- Due to the rules (see figure V.1left) :
  - The tracked object must be capture close to its focus to initialize some parameters.
  - Determinism : the algorithm looks for a quantity to minimize and can thus lead to an indetermination in the refocusing direction close to the focal plane. The next correct move is found, after trials and errors.
  - Live-tracking performances are directly impacted by the time needed to compute the new position, limiting the frame rate. The current algorithm needs 12 ms to determine the next position, then limiting the frame rate to 80 Hz.
- Due to the objects to be tracked
  - The object must be fluorescent. In some instances it can be biologically complicated to make such microorganisms fluorescent (like the magnetotactic bacteria MSR-1 studied in out laboratory). Moreover, the excitation light near blue may catalyze photochemical reaction ultimately affecting the biological integrity of the microorganism [166, 167].
  - The rules need to be parameterized depending on the object size.
  - Objects with a "far-from-spherical" shape cannot be tracked easily.
- Due to the presence of optical heterogeneities, that can be inherent to the medium such as in complex fluids or external such as the presence of surfaces or suspensions, which can locally deteriorate the quality of the tracking.

We aim at developing a unique method based on artificial intelligence (AI) in order to track any object in any environment with the best accuracy and versatility. Especially, the performances of machine learning in pattern recognition could lead to a "zero-crossing" method (see figure V.1right), i.e. a fully deterministic method where the distance from the focal plane is improving the former "optimization" method stemming from the simple rules described earlier (see figure V.1left).

V.3 Training the neural network

The idea behind machine learning is to optimize a function such that an input will correspond to the expected output. This function with its parameters is called a "neural network" (NN). The complexity of the function is exponentially increased by using several successive layers of parameters interacting with the previous layer (deep neural network) [168]. These layers are equivalent to nested functions. Generic models of neural networks have been shown to be very versatile in their application for image analysis, composing convolutional layers with pooling layers that reduce the dimensions of data. Here we use a standard one composed of 90000 parameters. In our case, the neural network is set to recognize specific optical aberrations of the microscope the same way as it would classify dogs, cats and rabbits from a random collection of images.

The methodology we developed is sketched in figure V.2. The idea is to determine, from the image of an object, what is its distance to the center (Δx, Δy) and the focal plane (Δz). It is based on experimental datasets. For the moment we have made two independent datasets for bacteria that will be used to train the AI : one in fluorescence and the other in bright field. To this purpose, we take a Z-sweep of our object, i.e images of our object in our experimental conditions at different distances from the focal plane Δz and at different positions z. To have a good training set, we must make our object quasi immobile during the sweep process. We

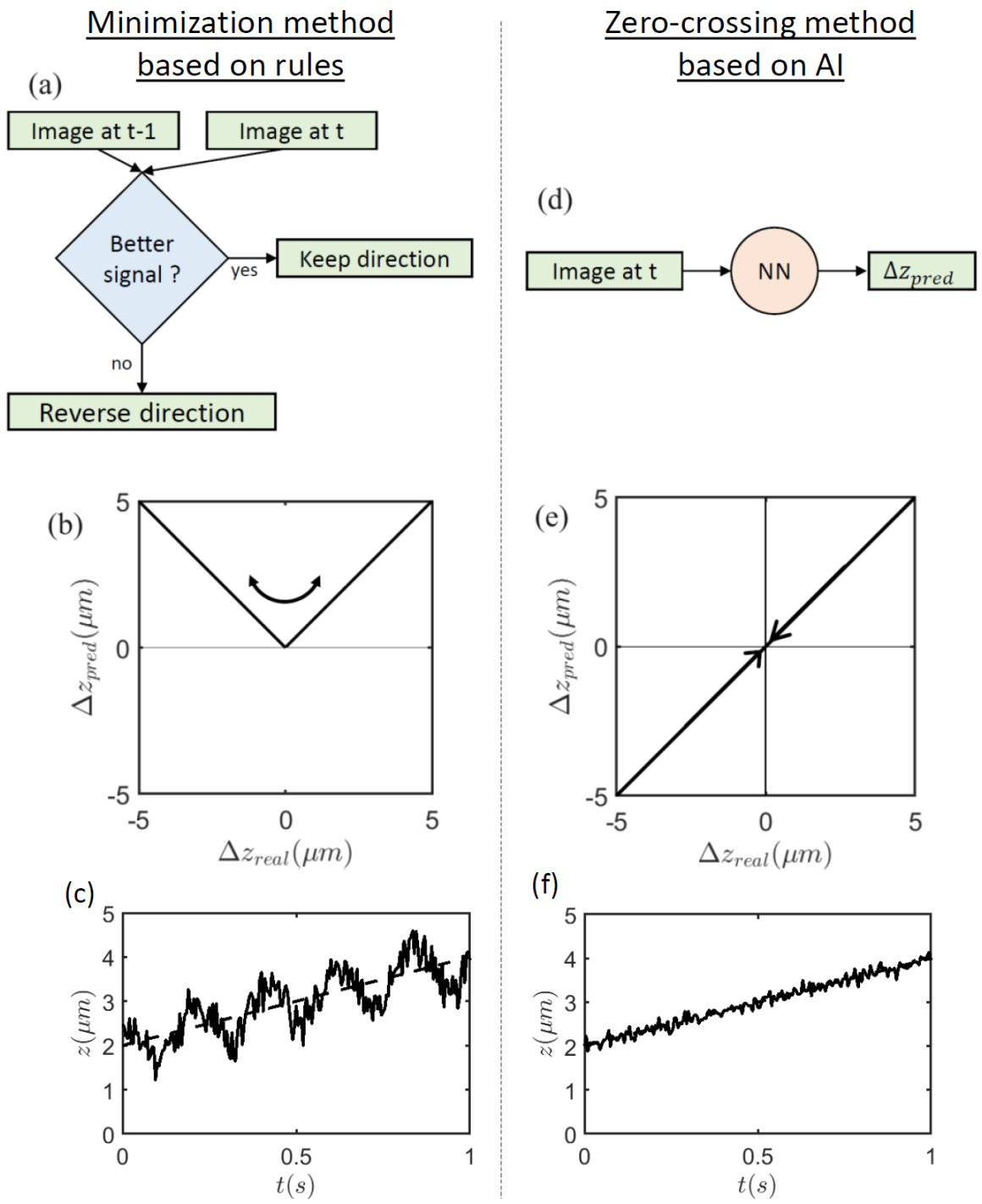

FIGURE V.1 – Sketch of the conceptual difference between tracking algorithm based on rules previously developed (left side) ill-adapted for feedback and new one based on AI (right side), well adapted for accurate feedback. (b) Close to the focus, the sign of the displacement to get closer to the focus $\Delta z_{real} = \pm \Delta z_{pref}$ cannot be guessed by simple rules. It is a minimization method. (a) A memory variable is used to guess the direction of the motion and can change depending on the variations of the signal between two successive images. (c) This leads to high-frequency oscillations in the z-position (real position is the dashed line). (d) An image is provided to a trained neuron network (NN) predicting the defocused position of the image $\Delta z_{real} = \Delta z_{pred}$. It yields a "zero-crossing" method as the position with respect to the focal plane is detected by the AI. (e) The finding of the actual position of the object is then deterministically predicted and results in a more accurate tracking (f).

avoid sedimentation by diluting 1 :1 in Percoll solution and achieve a non-buoyant bacterial suspension. To suppress swimming activity we use a small quantity of ethanol. For our bacteria our Z-sweep starts from $\Delta z = -10\,\mu$m to $\Delta z = 10\,\mu$m by step $\delta z_{step} = 100\,$nm and the duration of this recording is less than 5 s, making the translational noise negligible. Since the off-focus optical aberrations depend on the position z of the focal plane , the Z-sweep is made at different heights z. The experimental dataset consists in about hundred Z-sweeps of bacteria taken at random heights $0 < z < 220\,\mu$m. Moreover, the quality of the centering of the dataset have been shown to be a crucial step. The efficient "LodeSTAR" algorithm [169] (Localization and detection from Symmetries, Translations And Rotations), developed in Gothenburg, is used to center the images in XY whereas the focus position $\Delta z = 0$ is selected manually. Details of the following steps are facilitated using the "DeepTrack" library [157] : the centered experimental dataset is then augmented by translation, rotation and artificial noise addition from which a training dataset and a validation dataset, respectively 80% and 20% of the total dataset, are extracted. Parameters of the neural network are then adjusted (trained) recursively via a stochastic gradient descent algorithm. The idea behind the stochastic gradient descent algorithm is to progressively minimize a loss function, which is a function minimized when the predicted output is equal to the real output. The learning rate l_r, determining how much parameters will change between two steps, is determined empirically, though its value is not very sensitive. A criterium on the loss function determines when the neural network is sufficiently trained (when it has converged), while it is checked in parallel with the validation dataset that the AI is not overtrained, i.e. the parameters are trained too specifically. After convergence, we use a validation dataset (that has not been used for the training) to check the predictions. We show, at the end of figure V.2, the resulting predictions for both the fluorescent and brightfield training.

The results are similar in both cases : our AI method can indeed predict deterministically the displacement in the three directions : we have now a quite accurate "zero-crossing" method. Parallel to the plane of visualization (XY), the algorithm is trained in the range $-3\,\mu$m to $3\,\mu$m and the accuracy is less than $\sigma_X = \sigma_Y < 0.3\,\mu$m, it is nearly one tenth of the size of a bacterium. In the perpendicular plane (Z), for the first time the prediction is deterministic. The algorithm is trained in the range $-10\,\mu$m to $10\,\mu$m and the accuracy is $\sigma_Z < 0.75\,\mu$m which is again less than the size of a bacterium. In figure V.3, we get a closer look to the errors on the predictions for both the fluorescent and the brightfield algorithms. Some systematic bias can appear : for instance, the Z-prediction for the fluorescent algorithm is systematically higher than the real displacement far from the focus. This could probably be improved by implementing rotations in the training step.

The neural network is now trained and the issue is to implement it on the computer driving the motorized stages suited to track microorganisms in real-time.

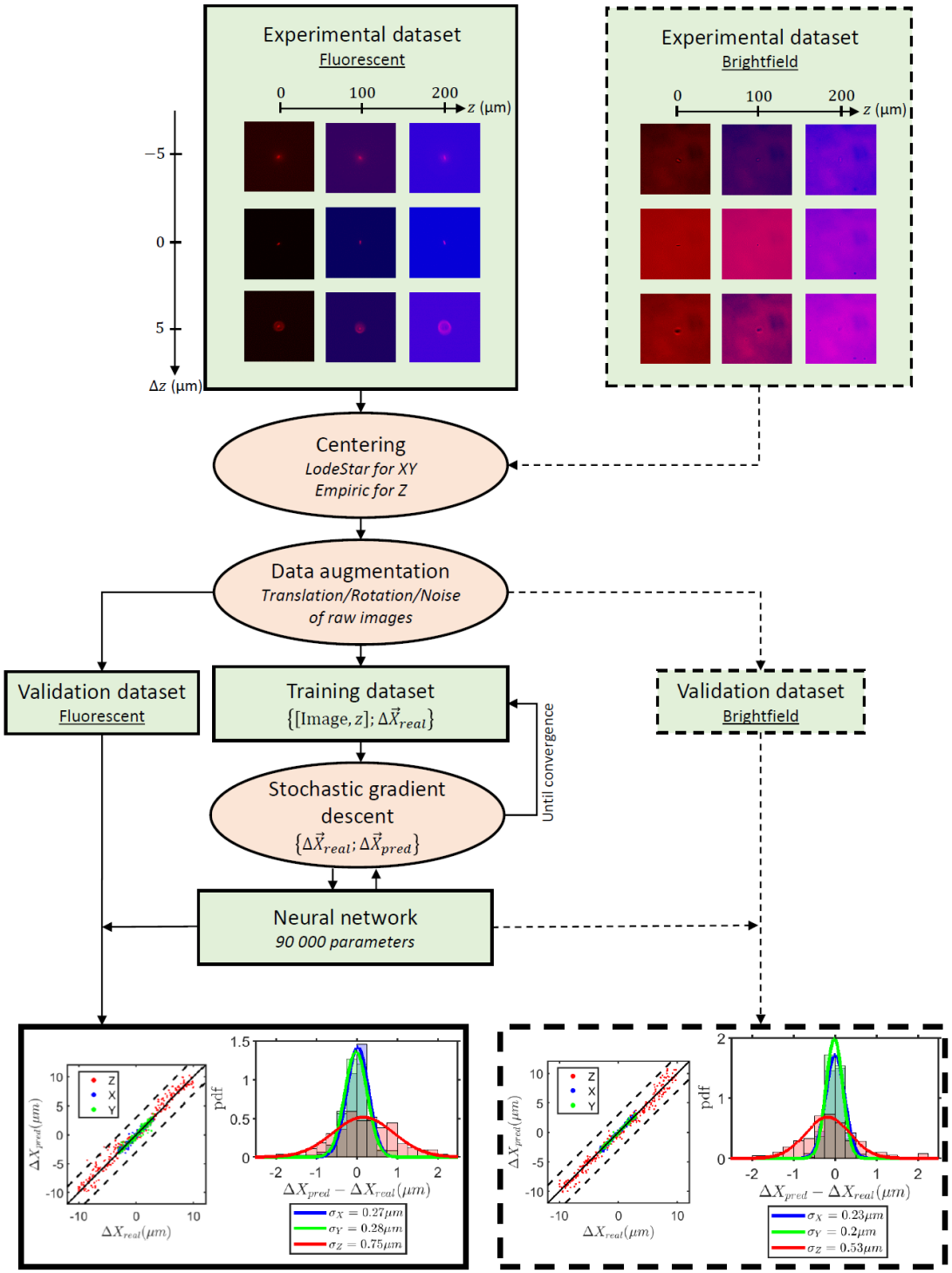

FIGURE V.2 – Sketch of the training procedure in two optical cases : fluorescence (left) and brightfield (right). The experimental dataset is a collection of ≈ 100 Z-sweep of bacteria that are labelled with the position of the focus z relative to the bottom surface and their position Δz relative to the focal plane. Images are coded in 8bit RGB with z encoded in the blue channel. Data are then centered and augmented with translations $\Delta\vec{X}_{real}$ constituting a validation dataset and a training dataset. The training dataset is used to improve the NN predictions $\Delta\vec{X}_{pred}$ through a stochastic gradient descent algorithm , done recursively until convergence. After convergence, the validation dataset is injected into the neural network and the predictions $\Delta\vec{X}_{pred}$ are compared to the real displacements $\Delta\vec{X}_{real}$ for the three directions. The predictions are deterministic (zero-crossing method) and the errors σ are smaller than the size of a bacterium even in the Z-direction.

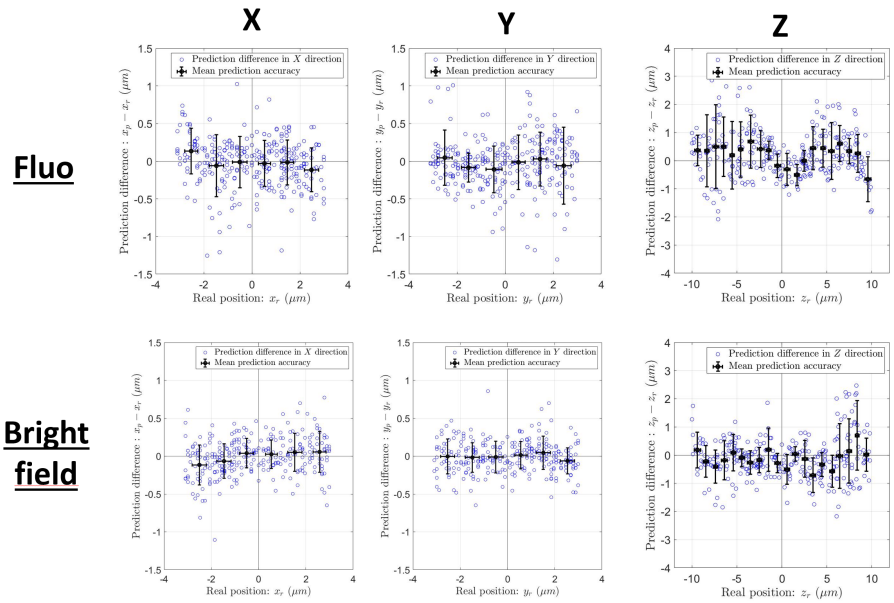

FIGURE V.3 – Error on the prediction $\Delta X_{pred} - \Delta X_{real}$ as a function of the real displacement ΔX_{real} in all the directions. This is indeed a zero-crossing method. However systematic biases can eventually appear in the prediction. This is in particular the case for fluorescent training on the z axis. However close to the focal plane the bias is significantly less than 1 μm.

V.4 Real-time tracking in a simple fluid

The integration of the neural network into the "LabVIEW" [170] software monitoring the tracking has been done using the "TensorFlow implementation for GPU" with a home-made DLL to interface with LabVIEW.

Predictions with this AI method are calculated in 8 ms, an improvement compared to the 12 ms required by the algorithm based on rules, hence paving the way to increase the tracking framerate to more than 100 Hz.

In figure V.4, we present and compare tracks obtained with the different models. The trained algorithms, shown in the previous figure, have not been used yet for tracking, this project is still in progress. We use older versions. We have been able to track successfully bacteria for more than 500 s in each cases. Remarkably it is the first time that Lagrangian 3D tracking of bacteria in brightfield is achieved for such a long period. We combine white light with a 495-nm long-pass filter as proposed in [76] to suppress the speed decay of order 30 μm/s/h observed under the blue light used for excitation. Impurities, unlike in fluorescence, are visible in bright field. The tracked bacterium can, for the moment, be lost when passing too close to "impurities" of the same size, such as dusts or other bacteria. We compare the Z-accuracy of each algorithm by taking the standard deviation $\sqrt{< (z - z_{fit})^2 >}$ of the difference between the resulting raw z-position $z(t)$ to the smoothed ones $z_{fit}(t)$ as described in the previous chapter. In fluorescence, more light intensity is needed for the AI-based algorithm to work. We want to improve this aspect by adding noise to the training dataset. However, we already show a slight improvement on the Z-accuracy.

We have successfully tracked bacteria for more than 500 s by implementing a "zero-crossing" AI-based method for real-time tracking. The methodology that we developed is in principle applicable to any objects. For the first time, bacteria can be tracked in bright field. The accuracy is already comparable to the previous algorithm. Many ideas are still under development.

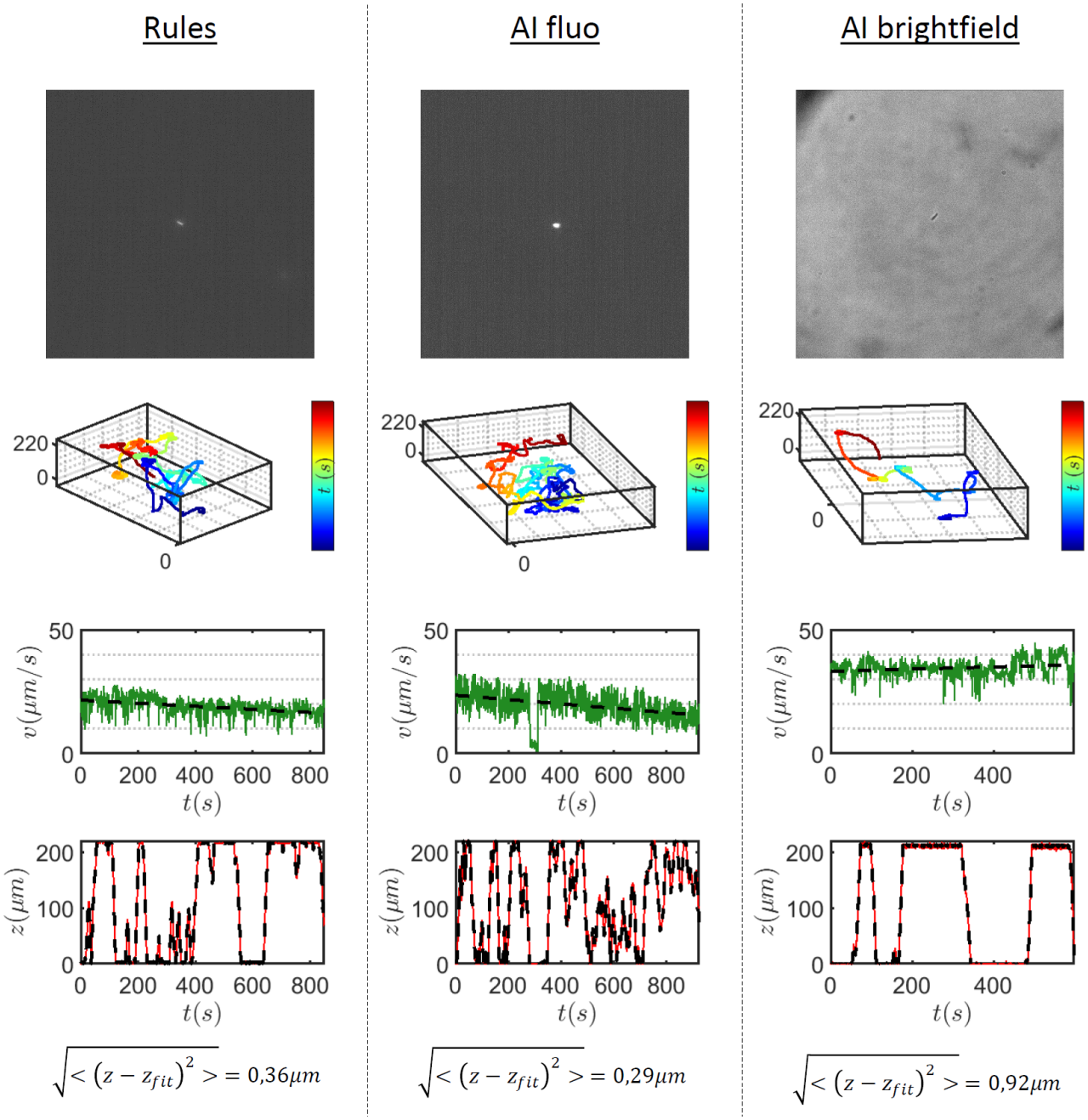

FIGURE V.4 – Comparison of the different tracking algorithms. First column corresponds to the algorithm based on rules, second and third are the ones based on AI. These algorithms were trained respectively for fluorescence and brightfield imaging. 1st row : snapshots of the tracked objects. Less fluorescence intensity is currently needed for the rules based algorithm. In brightfield, there are some impurities in the landscape. 2nd row : trajectories of more than 500 s. 3rd row : Smoothed speed (on 1 s) as a function of time and linear fit (dashed line). The speed of the bacterium decreases under blue light ($\approx 30\,\mu$m/s/h) but not in brightfield (the light is filtered with a 495-nm long-pass filter). 4th row : Raw z-trajectories fitted by smoothing (dashed line) allowing to estimate the accuracy of the z-detection.

V.5 Application to fluorescent bacteria in mucus : a first track

At the very end of my PhD, we successfully applied this methodology to mucus from piglet #4, leading to the first 3D tracking of a fluorescent bacterium in this optically complex fluid (see figure V.5).

In this track, the bacterium has a "stop & go" dynamics of the same type as the one reported in hydrogels in Hector Urra's PhD thesis [144] and S. Datta et al [43] where the reorientations are controlled by the fluid via "medium-assisted tumbles". The bacterium used is a tumbling bacterium and we cannot fully judge whether these dynamics are due to the active tumbles or the passive "medium-assisted tumbles". However the measured persistence time $\tau_p = 0.8\,\mathrm{s}$, which is lower than that expected in water, favours medium-assisted tumbles. The bacterium speed, when swimming, is about $V = 20\,\mu\mathrm{m/s}$, comparable to the speed observed in water. The measured emerging diffusion coefficient $D = 35\,\mu\mathrm{m}^2/\mathrm{s}$, influenced by the many reorientations, is ten times lower than would be expected in a water-like fluid. After $T_{trap} = 50\,\mathrm{s}$ of tracking, the bacterium has shown to stop moving, compatible with a tracking probability $\kappa_0 = 1/T_{trap} = 0.02\,\mathrm{s}^{-1}$ associated with a mucus sample as discussed in the model of mucus penetration IV.4. The whole phenomenology is quantitatively consistent with H. Urra's measurements [144] in mucin 7.5%, comparable to the mucus from piglet #4, concentrated at 7.4%, in which we track.

In addition to the bacterial track, we are able to visualize the mucus indirectly. In fact, we have implemented the ability to 'replay' the recorded trajectory of the bacterium on the microscope, with no restrictions on the optical conditions. We then "replay" the trajectory of the bacterium, but this time in bright field, to visualize the optical heterogeneities of the mucus (we hypothesize that the optical landscape of the mucus does not change over a sufficiently short period of time). It is then possible to combine the film taken during the tracking and the film taken during the "replay" to visualize both the bacterium and the mucus. We want to check whether the optical heterogeneities of the mucus correlate with some mechanical heterogeneities that would affect the bacterium. However, as it requires good precision, this "replay" function needs to be carefully checked before studying these correlations.

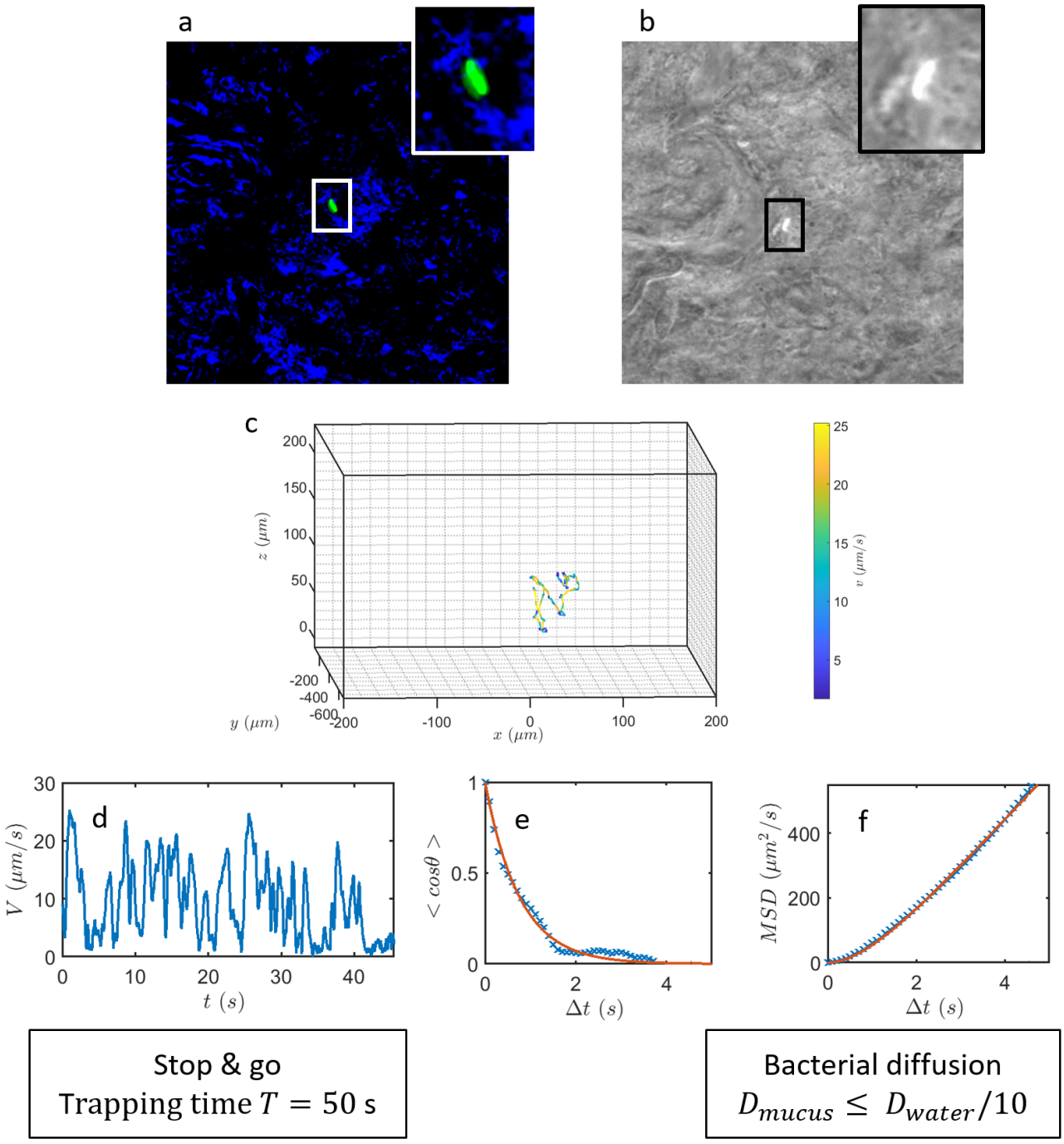

FIGURE V.5 – First track of a fluorescent bacterium. (a) Snapshot of a tracked bacterium (green channel) navigating through mucus (blue channel). (b) Same but in grey scale. (c) 3D trajectory. There is no interaction with surfaces. (d) Speed of the bacterium V (smoothed on 0.5s on XY and 1s on Z) as a function of time t. The bacterium swims at $V = 20\,\mu$m/s, comparable to the speed observed in water but displays a stop & go dynamics until getting fully blocked after 50s of tracking. (e) Orientation ACF as a function of time lag Δt with a fitted (red curve) persistent time $\tau_p = 0.8$ s, smaller than in water and compatible with "medium-assisted tumbling". (f) MSD as a function of time lag Δt with a fitted (red curve) diffusion coefficient $D = 35\,\mu\text{m}^2/\text{s}$, about ten times lower than expected in water.

Chapter VI

Conclusion

Inspired by the understanding of bacterial swimming mechanisms hypothetically involved in the medical problem of bacterial infection in the gut, we experimentally studied the spread of the model motile microorganism E. coli in two model experiments : first in a geometrically confined environment, mimicking breaches in a mucus barrier, and second, in purified mucus extracts from the gut of piglets, rendering the mechanical properties of a mucus barrier.

In the first part, we used a Lagrangian tracking system to study the spread of bacteria between two parallel solid plates at the level of individuals. The plates are separated by a height H that is varied from tens to hundreds of microns.

E. coli perform a well-known run & tumble process, i.e. continuous trajectories interrupted by sudden reorientations. The hydrodynamic interactions occurring at the surface change their trajectory, from straight to circular, and trap them so that they only take off after a tumble. As a result, they alternate between a straight 3D motion interrupted by reorientations in the bulk and a circular 2D motion at the surface in which a tumble can lead either to a change in orbit or to take-off. The interplay between phases in the bulk and phases at the surface affects the transport properties. This is the focus of this work. Following the work of Figueiroa et al, we use the Behavioral Variability (BV) model to describe the run times dynamics of our swimmers. In this model, the temporal fluctuations of an internal variable, called "the mood", predominate over the phenotypic variability between individuals to explain the large distribution of run times observed in the experiments.

Interestingly, a bacterium can be characterized by its constant kinematic parameters (the swimming speed V and the gyration radius at the surface R) but these parameters show a large variability within a population. We complemented the measurement of the kinematic parameters with some anatomical parameters (the body size, the bundle size and the number of flagella). Speed is actually independent of the anatomy. In particular, there is no relationship between swimming speed and the number of flagella. On the other hand, our results suggest that the gyration radius of an individual can be explained by the number of flagella. In a simple scenario, flagella tend to repel the body from the surface by steric hindrance, reducing the hydrodynamic forces in play and thus increasing the gyration radius on average. The observed variability could then result from the detailed localization of the flagella on the body. Bacterial selection based on anatomy does not eliminate the variability in kinematic properties. This led us to explicitly include the kinematic parameters of each individual in our model as an objective measurement.

We have shown experimentally that confinement slows down the lateral exploration of E. coli. We also measured the residence times, both at the surface and in the bulk. The mean surface residence time is essentially independent of confinement height and its distribution is log-normal. The mean bulk residence time scales linearly in our confinement range and

its distribution decays exponentially. These measurements are compared with a numerically implemented model. In this model, the previously calibrated BV model for the run times is combined with simple rules at the surface. In particular, the gyration radius R can be varied from the "sticking" limit $R = 0$ to the "straight" limit $R = \infty$. In the limit of small heights, the diffusion is zero in the "sticking" limit and it is maximized in the "straight" limit. In between is the "no wall" limit, which is also the limit for large heights for all radii. In the range of measurements, experimental and numerical outcomes are in quantitative agreement, with no adjustable parameters, both for the lateral diffusion coefficient and for the residence times.

Two effects of the confinement on the lateral spreading have been identified : First, the global diffusion coefficient resulting from the interplay between bulk and surface phases is mainly their weighted average. The more confined the environment, the more bacteria will spend time at the surface rather than in the bulk. Smaller heights then increase the diffusion in the "straight" limit, but decrease it in the "sticking" limit. Secondly, the surfaces induce a time cut-off for the runs that take place in the bulk. As shorter runs lead to a decrease in the diffusion coefficient, this effect reduces the lateral diffusion with decreasing height. However, it is not clear to what extent the results of the two parallel plates geometry described here, would apply to more complex geometries.

Quantitative experiments with bacteria are often carried out in the presence of confinement, an element that is often neglected. Beyond the fundamental interest, our results could be applied to medical and ecological issues, such as infections through physiological ducts or the search for ecological niches in natural soils. In the context of breaches in mucus, which can be dense enough to act as a solid surface, our results suggest that even in the "sticking" limit, a bacterium swimming as slowly as $V = 20\,\mu$m/s would invade the surface of the epithelium in a reasonable time ($T_{inv} < 100\,$s for a breach as long as $\Delta X = 100\,\mu$m and as thin as $H = 10\,\mu$m).

The second part of this thesis is dedicated to bacteria swimming in biological mucus. Mucus was extracted from the intestines of a cohort of piglets divided into two groups : "suckling" and "weaned", and then purified to focus on the mechanical properties of the mucin network, rather than on the effects of chemical residues. It is not clear how the purification process affects the mucus properties compared to "in vivo" situations. However, a methodology will be developed to characterize and compare the mucus extracts obtained.

An experiment based on the elaboration of a microfluidic cell in which a population of bacteria penetrates a mucus barrier is proposed. An interface is created between a bacterial fluid and mucus, and a static picture is assessed in a stationary state (after two hours) : unlike passive beads, motile bacteria do indeed penetrate this "mucus barrier". Most of the bacteria have migrated from the bacterial fluid to the mucus portion, where they finally get stuck. Interestingly, the bacterial concentration profile across the "mucus barrier" is such that there is a maximum followed by an exponential decay from which a "penetration length" can be quantified. The concentration profile is rationalized with a simple model based on diffusion on both sides of the interface and a trapping probability. Interestingly, the observed maximum could be attributed to mucus hydration at the interface but also to chemotaxis. This "penetration length" can be interpreted as an indicator of "mucus quality". This characterization is complemented by optical measurements in phase contrast microscopy leading to two structure sizes, and rheological measurements leading to flow curves describing a Herschel-Bulkley fluid, i.e. a yield stress and shear thinning fluid. Reproducibility is assessed by repeating these experiments for a given piglet.

Six mucus extracts, corresponding to six different piglets balanced between the two groups, have been characterized. A large variability in "penetration length" is observed for the different purified mucus, ranging from $200\,\mu$m to more than $800\,\mu$m. These sizes are in the range of a typical "in vivo" mucus barrier. Surprisingly, this variability is not reflected in the rheological

measurements which are all in the same order of magnitude. However, the rheological behaviour can differ qualitatively from one sample to another : the rheology of some extracts depends on the shear history, while others do not. Nevertheless, four of the samples have the same "penetration length" and share the same optical structure sizes. This suggests that the mesh size, or the microscopic heterogeneities, may be more important than the macrorheological properties in understanding the swimming properties of bacteria.

The static picture of the bacterial penetration of a "mucus barrier" provides some new information about the underlying process, but a temporal picture would provide more. We have extended the use of the Lagrangian tracking device with an AI-based method that is applicable to a wide range of objects in more complex optical environments. The principle of the method is to train a neural network to associate out-of-focus images of an object with its actual displacement from the focal plane. A collection of labelled out-of-focus images is generated experimentally on immobile objects in the optical conditions in which we want to track them. This method has been successfully implemented for real-time tracking. Compared to the previous algorithm based on empirical rules and live image analysis, it is more accurate ("zero crossing method" vs. "minimum method"), faster (7 ms vs. 10 ms) and offers new possibilities, such as the tracking of non-fluorescent objects. Importantly, this method was successfully applied to fluorescent bacteria in mucus, resulting in the first 3D trajectory of a bacterium in mucus. The tracked bacterium swims for $T_{trap} = 50\,\mathrm{s}$ before being trapped. Its persistent time is $\tau_p = 0.8\,\mathrm{s}$ and its diffusion coefficient is $D = 35\,\mu\mathrm{m}^2/\mathrm{s}$, much lower than expected in water, in agreement with previous experiments in model fluids such as hydrogels or commercial mucin. Systematic work remains to be done.

This study, which remains preliminary, does not lead to strong conclusions. However, the new experimental protocols and analysis pipelines pave the way for future work.
More needs to be understood about the structure of the mucin network. Neutron scattering, microrheology experiments and OCT microscopy could provide valuable new information. For medical applications, the biological relevance of the experimental conditions needs to be demonstrated, for example by replicating the mucus staining proposed in recent work close to in vivo situations, and ultimately by reproducing these situations. Potentially, the "mucus quality" proposed here can provide a novel diagnostic tool, especially for patients with obesity, diabetes and IBD. The evolution of the mucus barrier with drugs or chemicals could be studied. A comparison between selected bacterial strain could also be considered.

In summary the main results of this thesis consist of new measurements of bacterial swimming in confined geometries and a new methodology to study their accumulation and trapping in intestinal mucus layers. The results and the new experimental protocols extend the state of the art on the bacterial exploration and their penetration in viscoelastic fluids. This work opens up many perspectives and could form the basis for future studies.

Annexe A

Protocols : Bacteria from the freezer to their trajectory

Before going into details of the preparation, I want to emphasize that from the moment bacteria are in their final tube, one must try to imagine himself in this tube. Simple elements must be considered : there are surfaces where some of the bacteria adhere, some impurities can be present and there are some non-motile bacteria. Depending on the configuration, shaking or not shaking a tube can lead to different sampling. For instance, if impurities and non-motile bacteria sediment, then do not shake the tube and pipet far from surfaces to get more motile bacteria. Simple but efficient tips.

- List of ingredients :
  - LB : Lysogeny Broth Lennox (commercial). Preculture medium.
  - TB : Tryptone Broth (10 g/L of tryptone + 5 g/L of NaCl). Filtered at 0.22 μm. Culture medium.
  - PB : Phosphate Buffer 100 mM (61 mM K_2HPO_4 + 39 mM KH_2PO_4). Keep $pH = 7$ constant.
  - BMB : Berg's Motility Buffer (3.9 g/L of NaCl + 0.1 mM EDTA + 25 g/L of L-Serine + 10 mM PB). Filtered at 0.22 μm). Motility medium.
  - BMB x2 (BMB with double concentration of every solute). Filtered at 0.22 μm). To be diluted 1 :1 with Percoll.
  - Percoll (Reference P1644). Colloidal silica particles of 15-30 nm diameter (23% w/w in water) coated with polyvinylpyrrolidone (PVP). Density 1.13 g/mL.
  - Alexa solution (Reference A20347 Fischer scientific + 200 μL DMSO). Solution to color flagella. Kept in $-20\,^{\circ}$C.
  - Bacterial starters (30 mL preculture at $OD = 2$ + 6.5 mL glycerol 87%). Single-use tube containing bacteria. Kept in $-20\,^{\circ}$C.
- Culture steps :
  1. Preculture : 100 μL starter + 5 mL LB + 100 μg/mL Ampicillin. $\approx$ 14 h (overnight).
  2. Culture : 100 μL preculture + 5 mL TB + 100 μg/mL Ampicillin. $\approx$ 4 h ($OD \approx 0.5$).
  3. Washing by centrifugation 4590 RCF $\times$ 5 min : Replace supernatant by 1 mL BMB x2.
  4. (Flagellar coloration : 30 min with Alexa solution 1% v/v. Then double washing by centrifugation.)
  5. Mix 1 : 1 with Percoll for isodensity (no bacterial sedimentation).
- Good practice to avoid contamination and dust :
  - Manipulate under the hood.
  - Use UV light to clean the hood.

  - Sterilize media by autoclaving (120 °C - 20 min) or filtering 0.22 μm.
  - Clean surfaces with 70% ethanol.
- Settings of the setup :
  - Frame rate : 80 Hz.
  - Light source monocolor : Colibri blue LED. Starting from 2% and increasing it as slowly as possible to counter photobleaching. For long trajectories.
  - Light source bicolor : Colibri blue LED 20% and red LED 100%. For flagellar visualization while tracking.
  - Objective : 63x Water. Correction ring on 0.19 μm.
  - Reflector : 90HE.
- Settings of the track : Bacteria are captured at surface. Trajectories are smoothed to avoid mechanical noise with a polynomial of degree 2 (Savitsky-Golay algorithm). Smoothing time on X and Y (parallel to surface) is 0.2 s and on Z (perpendicular to surface) is 0.5 s. Speeds are computed as the derivative of the Savitsky-Golay fit.

Bibliographie

[1] Yinon M. Bar-On, Rob Phillips, and Ron Milo. The biomass distribution on earth. *Proceedings of the National Academy of Sciences*, 115(25) :6506–6511, May 2018.

[2] Jos M. Raaijmakers and E. Toby Kiers. Rewilding plant microbiomes. *Science*, 378(6620) :599–600, November 2022.

[3] Ranganathan Vasudevan. Biofilms : Microbial cities of scientific significance. *Journal of Microbiology and Experimentation*, 1(3), June 2014.

[4] Howard C. Berg, editor. *E. coli in Motion*. Springer New York, 2004.

[5] Louis Pasteur. *Nouvelle communication sur la rage*. Gauthier-Villars, 1886.

[6] Christoph Gradmann and Robert Koch. Die ätiologie der tuberkulose (1882). *Robert Koch : Zentrale Texte*, pages 113–131, 2018.

[7] Heiman Wertheim. *Small bugs, big data ; clinical microbiology in a digitising world (Inaugural lecture 2017)*. 01 2017.

[8] Theodor Escherich. *Die darmbakterien des neugeborenen und säuglinge. Fortschritte der Medizin. 3 :515-528 ;547-554*. Enke, 1885.

[9] www.pasteur.fr/en/institut-pasteur/history/middle-years-1862-1877, Nov 2016.

[10] Willem M de Vos, Herbert Tilg, Matthias Van Hul, and Patrice D Cani. Gut microbiome and health : mechanistic insights. *Gut*, 71(5) :1020–1032, February 2022.

[11] Jérémy O'Byrne, Alexandre Solon, Julien Tailleur, and Yongfeng Zhao. An introduction to motility-induced phase separation. 2021.

[12] Paulo E. Arratia. Life in complex fluids : Swimming in polymers. *Physical Review Fluids*, 7(11), November 2022.

[13] Saverio E. Spagnolie and Patrick T. Underhill. Swimming in complex fluids. *Annual Review of Condensed Matter Physics*, 14(1) :381–415, March 2023.

[14] Alison E. Patteson, Arvind Gopinath, and Paulo E. Arratia. Active colloids in complex fluids. *Current Opinion in Colloid : Interface Science*, 21 :86–96, February 2016.

[15] Clemens Bechinger, Roberto Di Leonardo, Hartmut Löwen, Charles Reichhardt, Giorgio Volpe, and Giovanni Volpe. Active particles in complex and crowded environments. *Reviews of Modern Physics*, 88(4), November 2016.

[16] Gaojin Li, Eric Lauga, and Arezoo M. Ardekani. Microswimming in viscoelastic fluids. *Journal of Non-Newtonian Fluid Mechanics*, 297 :104655, November 2021.

[17] Li-Heng Cai, Sujit S. Datta, and Xiang Cheng. Editorial : Active matter in complex environments. *Frontiers in Physics*, 10, September 2022.

[18] Christina Kurzthaler, Luigi Gentile, and Howard A. Stone, editors. *Out-of-equilibrium Soft Matter : Active Fluids*. Royal Society of Chemistry, London, 1st edition edition, March 2023.

[19] Albane Théry, Yuxuan Wang, Mariia Dvoriashyna, Christophe Eloy, Florence Elias, and Eric Lauga. Rebound and scattering of motile chlamydomonas algae in confined chambers. *Soft Matter*, 17(18) :4857–4873, 2021.

[20] Thomas D. Montenegro-Johnson, David A. Gagnon, Paulo E. Arratia, and Eric Lauga. Flow analysis of the low reynolds number swimmer c. elegans. *Physical Review Fluids*, 1(5), September 2016.

[21] Adama Creppy, Olivier Praud, Xavier Druart, Philippa L. Kohnke, and Franck Plouraboué. Turbulence of swarming sperm. *Physical Review E*, 92(3), September 2015.

[22] Anup V. Kanale, Feng Ling, Hanliang Guo, Sebastian Fürthauer, and Eva Kanso. Spontaneous phase coordination and fluid pumping in model ciliary carpets. *Proceedings of the National Academy of Sciences*, 119(45), November 2022.

[23] Maxime Deforet. Long-range alteration of the physical environment mediates cooperation between pseudomonas aeruginosa swarming colonies. *Environmental Microbiology*, 25(8) :1451–1464, March 2023.

[24] Jérémie Palacci, Benjamin Abécassis, Cécile Cottin-Bizonne, Christophe Ybert, and Lydéric Bocquet. Colloidal motility and pattern formation under rectified diffusiophoresis. *Physical Review Letters*, 104(13), April 2010.

[25] Jonathan R. Howse, Richard A. L. Jones, Anthony J. Ryan, Tim Gough, Reza Vafabakhsh, and Ramin Golestanian. Self-motile colloidal particles : From directed propulsion to random walk. *Physical Review Letters*, 99(4), July 2007.

[26] Adrien Izzet, Pepijn G. Moerman, Preston Gross, Jan Groenewold, Andrew D. Hollingsworth, Jérôme Bibette, and Jasna Brujic. Tunable persistent random walk in swimming droplets. *Physical Review X*, 10(2), May 2020.

[27] Sébastien Michelin. Self-propulsion of chemically active droplets. *Annual Review of Fluid Mechanics*, 55(1) :77–101, January 2023.

[28] Gaspard Junot, Marco De Corato, and Pietro Tierno. Large scale zigzag pattern emerging from circulating active shakers. *Physical Review Letters*, 131(6), August 2023.

[29] Benoit Vincenti, Gabriel Ramos, Maria Luisa Cordero, Carine Douarche, Rodrigo Soto, and Eric Clement. Magnetotactic bacteria in a droplet self-assemble into a rotary motor. *Nature Communications*, 10(1), November 2019.

[30] Ricard Alert, Alejandro Martínez-Calvo, and Sujit S. Datta. Cellular sensing governs the stability of chemotactic fronts. *Physical Review Letters*, 128(14), April 2022.

[31] Andrea Villa-Torrealba, Simón Navia, and Rodrigo Soto. Kinetic modeling of the chemotactic process in run-and-tumble bacteria. *Physical Review E*, 107(3), March 2023.

[32] Nicola Pellicciotta, Matteo Paoluzzi, Dario Buonomo, Giacomo Frangipane, Luca Angelani, and Roberto Di Leonardo. Colloidal transport by light induced gradients of active pressure. *Nature Communications*, 14(1), July 2023.

[33] Antoine Bricard, Jean-Baptiste Caussin, Debasish Das, Charles Savoie, Vijayakumar Chikkadi, Kyohei Shitara, Oleksandr Chepizhko, Fernando Peruani, David Saintillan, and Denis Bartolo. Emergent vortices in populations of colloidal rollers. *Nature Communications*, 6(1), June 2015.

[34] Yow-Ren Chang, Eric R. Weeks, and William A. Ducker. Surface topography hinders bacterial surface motility. *ACS Applied Materials & Interfaces*, 10(11) :9225–9234, February 2018.

[35] Maryam Khatami, Katrin Wolff, Oliver Pohl, Mohammad Reza Ejtehadi, and Holger Stark. Active brownian particles and run-and-tumble particles separate inside a maze. *Scientific Reports*, 6(1), November 2016.

[36] Stanislaw Makarchuk, Vasco C. Braz, Nuno A. M. Araújo, Lena Ciric, and Giorgio Volpe. Enhanced propagation of motile bacteria on surfaces due to forward scattering. *Nature Communications*, 10(1), September 2019.

[37] Shashank Kamdar, Seunghwan Shin, Premkumar Leishangthem, Lorraine F. Francis, Xinliang Xu, and Xiang Cheng. The colloidal nature of complex fluids enhances bacterial motility. *Nature*, 603(7903) :819–823, March 2022.

[38] Christoph Lohrmann and Christian Holm. Optimal motility strategies for self-propelled agents to explore porous media, 2023.

[39] Christina Kurzthaler, Suvendu Mandal, Tapomoy Bhattacharjee, Hartmut Löwen, Sujit S. Datta, and Howard A. Stone. A geometric criterion for the optimal spreading of active polymers in porous media. *Nature Communications*, 12(1), December 2021.

[40] Saverio E. Spagnolie. *Complex Fluids in Biological Systems : Experiment, Theory, and Computation*. Springer, softcover reprint of the original 1st ed. 2015 édition edition, September 2016.

[41] Martyna Goral, Eric Clement, Thierry Darnige, Teresa Lopez-Leon, and Anke Lindner. Frustrated 'run and tumble' of swimming escherichia coli bacteria in nematic liquid crystals. *Interface Focus*, 12(6), October 2022.

[42] Chuanbin Li, Boyang Qin, Arvind Gopinath, Paulo E. Arratia, Becca Thomases, and Robert D. Guy. Flagellar swimming in viscoelastic fluids : role of fluid elastic stress revealed by simulations based on experimental data. *Journal of The Royal Society Interface*, 14(135) :20170289, October 2017.

[43] Tapomoy Bhattacharjee and Sujit S. Datta. Bacterial hopping and trapping in porous media. *Nature Communications*, 10(1), May 2019.

[44] Farshad Nazari, Kourosh Shoele, and Hadi Mohammadigoushki. Helical locomotion in yield stress fluids. *Physical Review Letters*, 130(11), March 2023.

[45] Nuris Figueroa-Morales, Leonardo Dominguez-Rubio, Troy L. Ott, and Igor S. Aranson. Mechanical shear controls bacterial penetration in mucus. *Scientific Reports*, 9(1), July 2019.

[46] Andreas Zöttl and Julia M. Yeomans. Enhanced bacterial swimming speeds in macromolecular polymer solutions. *Nature Physics*, 15(6) :554–558, March 2019.

[47] Benoit Chassaing, Omry Koren, Julia K. Goodrich, Angela C. Poole, Shanthi Srinivasan, Ruth E. Ley, and Andrew T. Gewirtz. Dietary emulsifiers impact the mouse gut microbiota promoting colitis and metabolic syndrome. *Nature*, 519(7541) :92–96, February 2015.

[48] George M.H. Birchenough, Bjoern O. Schroeder, Sinan Sharba, Liisa Arike, Christian V. Recktenwald, Fabiola Puértolas-Balint, Mahadevan V. Subramani, Karl T. Hansson, Bahtiyar Yilmaz, Sara K. Lindén, Fredrik Bäckhed, and Gunnar C. Hansson. Muc2-dependent microbial colonization of the jejunal mucus layer is diet sensitive and confers local resistance to enteric pathogen infection. *Cell Reports*, 42(2) :112084, February 2023.

[49] Markus Furter, Mikael E. Sellin, Gunnar C. Hansson, and Wolf-Dietrich Hardt. Mucus architecture and near-surface swimming affect distinct salmonella typhimurium infection patterns along the murine intestinal tract. *Cell Reports*, 27(9) :2665–2678.e3, May 2019.

[50] Hao Q. Tran, Ruth E. Ley, Andrew T. Gewirtz, and Benoit Chassaing. Flagellin-elicited adaptive immunity suppresses flagellated microbiota and vaccinates against chronic inflammatory diseases. *Nature Communications*, 10(1), December 2019.

[51] Gabe Buckley. Prokaryotic cell - definition, examples & structure, Nov 2020.

[52] Nadège Philippe. *Mécanismes moléculaires de l'adaptation au cours de 20 000 générations d'évolution expérimentale chez Escherichia coli.* PhD thesis, Université Joseph-Fourier-Grenoble I, 2006.

[53] Mahesh Madyagol, Hend Al-Alami, Zdeno Levarski, Hana Drahovská, Ján Turňa, and Stanislav Stuchlík. Gene replacement techniques for escherichia coli genome modification. *Folia Microbiologica*, 56(3) :253–263, May 2011.

[54] Jana Schwarz-Linek, Jochen Arlt, Alys Jepson, Angela Dawson, Teun Vissers, Dario Miroli, Teuta Pilizota, Vincent A. Martinez, and Wilson C.K. Poon. Escherichia coli as a model active colloid : A practical introduction. *Colloids and Surfaces B : Biointerfaces*, 137 :2–16, January 2016.

[55] Pushkar P. Lele, Basarab G. Hosu, and Howard C. Berg. Dynamics of mechanosensing in the bacterial flagellar motor. *Proceedings of the National Academy of Sciences*, 110(29) :11839–11844, July 2013.

[56] Jasmine A. Nirody, Richard M. Berry, and George Oster. The limiting speed of the bacterial flagellar motor. *Biophysical Journal*, 111(3) :557–564, August 2016.

[57] Tohru Minamino, Miki Kinoshita, and Keiichi Namba. Directional switching mechanism of the bacterial flagellar motor. *Computational and Structural Biotechnology Journal*, 17 :1075–1081, 2019.

[58] Haidai Hu, Mònica Santiveri, Navish Wadhwa, Howard C. Berg, Marc Erhardt, and Nicholas M.I. Taylor. Structural basis of torque generation in the bi-directional bacterial flagellar motor. *Trends in Biochemical Sciences*, 47(2) :160–172, February 2022.

[59] Eric Lauga. Bacterial hydrodynamics. *Annual Review of Fluid Mechanics*, 48(1) :105–130, January 2016.

[60] Ashley L. Nord, Anaïs Biquet-Bisquert, Manouk Abkarian, Théo Pigaglio, Farida Seduk, Axel Magalon, and Francesco Pedaci. Dynamic stiffening of the flagellar hook. *Nature Communications*, 13(1), May 2022.

[61] A. L. Nord and F. Pedaci. Mechanisms and dynamics of the bacterial flagellar motor. *Physical Microbiology*, 1267, 2020.

[62] John S. Parkinson, Gerald L. Hazelbauer, and Joseph J. Falke. Signaling and sensory adaptation in escherichia coli chemoreceptors : 2015 update. *Trends in Microbiology*, 23(5) :257–266, May 2015.

[63] E. M. Purcell. Life at low reynolds number. *American Journal of Physics*, 45(1) :3–11, January 1977.

[64] S. Mahdiyeh Mousavi, Gerhard Gompper, and Roland G. Winkler. Wall entrapment of peritrichous bacteria : a mesoscale hydrodynamics simulation study. *Soft Matter*, 16(20) :4866–4875, 2020.

[65] G.I Taylor. Low reynolds-number flows, 1961.

[66] UNM Physics and Astronomy. Laminar flow, Mar. 2007.

[67] Eric Lauga and Thomas R Powers. The hydrodynamics of swimming microorganisms. *Reports on Progress in Physics*, 72(9) :096601, August 2009.

[68] Linda Turner, William S. Ryu, and Howard C. Berg. Real-time imaging of fluorescent flagellar filaments. *Journal of Bacteriology*, 182(10) :2793–2801, May 2000.

[69] Knut Drescher, Jörn Dunkel, Luis H. Cisneros, Sujoy Ganguly, and Raymond E. Goldstein. Fluid dynamics and noise in bacterial cell–cell and cell–surface scattering. *Proceedings of the National Academy of Sciences*, 108(27) :10940–10945, June 2011.

[70] Debasmita Mondal, Ameya G Prabhune, Sriram Ramaswamy, and Prerna Sharma. Strong confinement of active microalgae leads to inversion of vortex flow and enhanced mixing. *eLife*, 10, November 2021.

[71] Etienne Guyon, Jean-Pierre Hulin, and Luc Petit. *Hydrodynamique physique*. EDP Sciences, 2012.

[72] James Lighthill. Flagellar hydrodynamics. *SIAM Review*, 18(2) :161–230, April 1976.

[73] Bruce Rodenborn, Chih-Hung Chen, Harry L. Swinney, Bin Liu, and H. P. Zhang. Propulsion of microorganisms by a helical flagellum. *Proceedings of the National Academy of Sciences*, 110(5), January 2013.

[74] Maria Tătulea-Codrean and Eric Lauga. Elastohydrodynamic synchronization of rotating bacterial flagella. *Physical Review Letters*, 128(20), May 2022.

[75] Ashley L Nord, Emilie Gachon, Ruben Perez-Carrasco, Jasmine A. Nirody, Alessandro Barducci, Richard M. Berry, and Francesco Pedaci. Catch bond drives stator mechanosensitivity in the bacterial flagellar motor. *Proceedings of the National Academy of Sciences*, 114(49) :12952–12957, November 2017.

[76] Xiaobing Chen and Howard C. Berg. Torque-speed relationship of the flagellar rotary motor of escherichia coli. *Biophysical Journal*, 78(2) :1036–1041, February 2000.

[77] H.C. Berg and L. Turner. Torque generated by the flagellar motor of escherichia coli. *Biophysical Journal*, 65(5) :2201–2216, November 1993.

[78] Nicholas C. Darnton, Linda Turner, Svetlana Rojevsky, and Howard C. Berg. On torque and tumbling in swimming escherichia coli. *Journal of Bacteriology*, 189(5) :1756–1764, March 2007.

[79] Howard C. Berg. Bacterial flagellar motor. *Current Biology*, 18(16) :R689–R691, August 2008.

[80] Vincent A. Martinez, Jana Schwarz-Linek, Mathias Reufer, Laurence G. Wilson, Alexander N. Morozov, and Wilson C. K. Poon. Flagellated bacterial motility in polymer solutions. *Proceedings of the National Academy of Sciences*, 111(50) :17771–17776, December 2014.

[81] Jeremy P. Binagia and Eric S. G. Shaqfeh. Self-propulsion of a freely suspended swimmer by a swirling tail in a viscoelastic fluid. *Physical Review Fluids*, 6(5), May 2021.

[82] A. E. Patteson, A. Gopinath, M. Goulian, and P. E. Arratia. Running and tumbling with e. coli in polymeric solutions. *Scientific Reports*, 5(1), October 2015.

[83] Zijie Qu and Kenneth S. Breuer. Effects of shear-thinning viscosity and viscoelastic stresses on flagellated bacteria motility. *Physical Review Fluids*, 5(7), July 2020.

[84] Ding Cao, Mariia Dvoriashyna, Song Liu, Eric Lauga, and Yilin Wu. Reduced surface accumulation of swimming bacteria in viscoelastic polymer fluids. *Proceedings of the National Academy of Sciences*, 119(45), November 2022.

[85] Allison P. Berke, Linda Turner, Howard C. Berg, and Eric Lauga. Hydrodynamic attraction of swimming microorganisms by surfaces. *Physical Review Letters*, 101(3), July 2008.

[86] R. Di Leonardo, D. Dell'Arciprete, L. Angelani, and V. Iebba. Swimming with an image. *Physical Review Letters*, 106(3), January 2011.

[87] Jocelyn Dunstan, Gastón Miño, Eric Clement, and Rodrigo Soto. A two-sphere model for bacteria swimming near solid surfaces. *Physics of Fluids*, 24(1), January 2012.

[88] Margot A.-S. Vigeant, Michael Wagner, Lukas K. Tamm, and Roseanne M. Ford. Nanometer distances between swimming bacteria and surfaces measured by total internal reflection aqueous fluorescence microscopy. *Langmuir*, 17(7) :2235–2242, March 2001.

[89] Jinglei Hu, Adam Wysocki, Roland G. Winkler, and Gerhard Gompper. Physical sensing of surface properties by microswimmers – directing bacterial motion via wall slip. *Scientific Reports*, 5(1), May 2015.

[90] Guanglai Li and Jay X. Tang. Accumulation of microswimmers near a surface mediated by collision and rotational brownian motion. *Physical Review Letters*, 103(7), August 2009.

[91] Konstantin Schaar, Andreas Zöttl, and Holger Stark. Detention times of microswimmers close to surfaces : Influence of hydrodynamic interactions and noise. *Physical Review Letters*, 115(3), July 2015.

[92] Gaspard Junot, Thierry Darnige, Anke Lindner, Vincent A. Martinez, Jochen Arlt, Angela Dawson, Wilson C. K. Poon, Harold Auradou, and Eric Clément. Run-to-tumble variability controls the surface residence times of e. coli bacteria. *Physical Review Letters*, 128(24), June 2022.

[93] Eric Lauga, Willow R. DiLuzio, George M. Whitesides, and Howard A. Stone. Swimming in circles : Motion of bacteria near solid boundaries. *Biophysical Journal*, 90(2) :400–412, January 2006.

[94] Davide Giacché, Takuji Ishikawa, and Takami Yamaguchi. Hydrodynamic entrapment of bacteria swimming near a solid surface. *Physical Review E*, 82(5), November 2010.

[95] Francisca Guzmán-Lastra, Hartmut Löwen, and Arnold J. T. M. Mathijssen. Active carpets drive non-equilibrium diffusion and enhanced molecular fluxes. *Nature Communications*, 12(1), March 2021.

[96] Hanumantha Rao Vutukuri, Masoud Hoore, Clara Abaurrea-Velasco, Lennard van Buren, Alessandro Dutto, Thorsten Auth, Dmitry A. Fedosov, Gerhard Gompper, and Jan Vermant. Active particles induce large shape deformations in giant lipid vesicles. *Nature*, 586(7827) :52–56, September 2020.

[97] Laurence Lemelle, Jean-Francois Palierne, Elodie Chatre, and Christophe Place. Counterclockwise circular motion of bacteria swimming at the air-liquid interface. *J. Bacteriol.*, 192 :6310, 2010.

[98] Laurence Lemelle, Jean-Francois Palierne, Elodie Chatre, Cedric Vaillant, and Christophe Place. Curvature reversal of the circular motion of swimming bacteria probes for slip at solid/liquid interfaces. *Soft Matter*, 9 :9759, 2013.

[99] Hélène Bloch, Vincent Calvez, Benoît Gaudeul, Loïc Gouarin, Aline Lefebvre-Lepot, Tam Mignot, Michèle Romanos, and Jean-Baptiste Saulnier. A new modeling approach of myxococcus xanthus bacteria using polarity-based reversals. 2023.

[100] Marianne Grognot, Anisha Mittal, Mattia Mah'moud, and Katja M. Taute. Vibrio cholerae motility in aquatic and mucus-mimicking environments. *Applied and Environmental Microbiology*, 87(20), September 2021.

[101] Peter S. Lovely and F.W. Dahlquist. Statistical measures of bacterial motility and chemotaxis. *Journal of Theoretical Biology*, 50(2) :477–496, April 1975.

[102] Mariia Dvoriashyna and Eric Lauga. Hydrodynamics and direction change of tumbling bacteria. *PLOS ONE*, 16(7) :e0254551, July 2021.

[103] HOWARD C. BERG and DOUGLAS A. BROWN. Chemotaxis in escherichia coli analysed by three-dimensional tracking. *Nature*, 239(5374) :500–504, October 1972.

[104] Jonathan Saragosti, Pascal Silberzan, and Axel Buguin. Modeling e. coli tumbles by rotational diffusion. implications for chemotaxis. *PLoS ONE*, 7(4) :e35412, April 2012.

[105] Ekaterina Korobkova, Thierry Emonet, Jose M. G. Vilar, Thomas S. Shimizu, and Philippe Cluzel. From molecular noise to behavioural variability in a single bacterium. *Nature*, 428(6982) :574–578, April 2004.

[106] Taejin L Min, Patrick J Mears, Lon M Chubiz, Christopher V Rao, Ido Golding, and Yann R Chemla. High-resolution, long-term characterization of bacterial motility using optical tweezers. *Nature Methods*, 6(11) :831–835, October 2009.

[107] S. Tavaddod, M. A. Charsooghi, F. Abdi, H. R. Khalesifard, and R. Golestanian. Probing passive diffusion of flagellated and deflagellated escherichia coli. *The European Physical Journal E*, 34(2), February 2011.

[108] Gaspard Junot, Eric Clément, Harold Auradou, and Reinaldo García-García. Single-trajectory characterization of active swimmers in a flow. *Physical Review E*, 103(3), March 2021.

[109] A. P. Solon, M. E. Cates, and J. Tailleur. Active brownian particles and run-and-tumble particles : A comparative study. *The European Physical Journal Special Topics*, 224(7) :1231–1262, July 2015.

[110] Michael Rubinstein and Ralph H. Colby. *Polymer Physics.* OUP Oxford, Oxford ; New York, June 2003.

[111] Alexei R. Khokhlov, Alexander Yu Grosberg, and Vijay S. Pande. *Statistical Physics of Macromolecules.* American Institute of Physics, New York, english ed édition edition, March 2002.

[112] Howard C Berg. *Random walks in biology.* Princeton University Press, 1993.

[113] Mayukh K. Sarkar, Koushik Paul, and David Blair. Chemotaxis signaling protein chey binds to the rotor protein flin to control the direction of flagellar rotation in escherichia coli. *Proceedings of the National Academy of Sciences*, 107(20) :9370–9375, May 2010.

[114] Yunjie Chang, Kai Zhang, Brittany L. Carroll, Xiaowei Zhao, Nyles W. Charon, Steven J. Norris, Md A. Motaleb, Chunhao Li, and Jun Liu. Molecular mechanism for rotational switching of the bacterial flagellar motor. *Nature Structural & Molecular Biology*, 27(11) :1041–1047, September 2020.

[115] Nuris Figueroa-Morales, Rodrigo Soto, Gaspard Junot, Thierry Darnige, Carine Douarche, Vincent A. Martinez, Anke Lindner, and Éric Clément. 3d spatial exploration by e. coli echoes motor temporal variability. *Physical Review X*, 10(2), April 2020.

[116] Yuki Takaha and Daiki Nishiguchi. Quasi-two-dimensional bacterial swimming around pillars : Enhanced trapping efficiency and curvature dependence. *Physical Review E*, 107(1), January 2023.

[117] Daniel B. Amchin, Jenna A. Ott, Tapomoy Bhattacharjee, and Sujit S. Datta. Influence of confinement on the spreading of bacterial populations. *PLOS Computational Biology*, 18(5) :e1010063, May 2022.

[118] A. Alexandre, M. Mangeat, T. Guérin, and D. S. Dean. How stickiness can speed up diffusion in confined systems. *Physical Review Letters*, 128(21), May 2022.

[119] Arthur Alexandre, Maxime Lavaud, Nicolas Fares, Elodie Millan, Yann Louyer, Thomas Salez, Yacine Amarouchene, Thomas Guérin, and David S. Dean. Non-gaussian diffusion near surfaces. *Physical Review Letters*, 130(7), February 2023.

[120] Nuris Figueroa-Morales, Aramis Rivera, Rodrigo Soto, Anke Lindner, Ernesto Altshuler, and Éric Clément. E. coli super-contaminates narrow ducts fostered by broad run-time distribution. *Science Advances*, 6(11), March 2020.

[121] T. Darnige, N. Figueroa-Morales, P. Bohec, A. Lindner, and E. Clément. Lagrangian 3d tracking of fluorescent microscopic objects in motion. *Review of Scientific Instruments*, 88(5), May 2017.

[122] Gaspard Junot, Nuris Figueroa-Morales, Thierry Darnige, Anke Lindner, Rodrigo Soto, Harold Auradou, and Eric Clément. Swimming bacteria in poiseuille flow : The quest for active bretherton-jeffery trajectories. *EPL (Europhysics Letters)*, 126(4) :44003, June 2019.

[123] Gaspard Junot. *Transport of active bacteria : from micro-scale processes to macroscopic hydrodynamic dispersion*. PhD thesis, Sorbonne Université, 2019.

[124] Jacinta C. Conrad. Physics of bacterial near-surface motility using flagella and type IV pili : implications for biofilm formation. *Research in Microbiology*, 163(9-10) :619–629, November 2012.

[125] Luanne Hall-Stoodley, J. William Costerton, and Paul Stoodley. Bacterial biofilms : from the natural environment to infectious diseases. *Nature Reviews Microbiology*, 2(2) :95–108, February 2004.

[126] Stefan Otte, Emiliano Perez Ipiña, Rodolphe Pontier-Bres, Dorota Czerucka, and Fernando Peruani. Statistics of pathogenic bacteria in the search of host cells. *Nature Communications*, 12(1), March 2021.

[127] Emiliano Perez Ipiña, Stefan Otte, Rodolphe Pontier-Bres, Dorota Czerucka, and Fernando Peruani. Bacteria display optimal transport near surfaces. *Nature Physics*, 15(6) :610–615, March 2019.

[128] Premkumar Leishangthem and Xinliang Xu. An entropic effect essential for surface entrapment of bacteria, 2023.

[129] Francis Perrin. Mouvement brownien d'un ellipsoide - i. dispersion diélectrique pour des molécules ellipsoidales. *Journal de Physique et le Radium*, 5(10) :497–511, 1934.

[130] Gabriel Rosser, Ruth E. Baker, Judith P. Armitage, and Alexander G. Fletcher. Modelling and analysis of bacterial tracks suggest an active reorientation mechanism in rhodobacter sphaeroides. *Journal of The Royal Society Interface*, 11(97) :20140320, August 2014.

[131] Greg Orosi. Duration of play in the gambler's ruin problem : A novel derivation. *Applied Mathematics E-Notes*, 18 :268–274, 2018.

[132] Mehdi Molaei, Michael Barry, Roman Stocker, and Jian Sheng. Failed escape : Solid surfaces prevent tumbling of escherichia coli. *Physical Review Letters*, 113(6), August 2014.

[133] Ying Liu, Zhijun Zheng, Lihuai Yu, Sen Wu, Li Sun, Shenglong Wu, Qian Xu, Shunfeng Cai, Nan Qin, and Wenbin Bao. Examination of the temporal and spatial dynamics of the gut microbiome in newborn piglets reveals distinct microbial communities in six intestinal segments. *Scientific Reports*, 9(1), March 2019.

[134] Elizabeth Thursby and Nathalie Juge. Introduction to the human gut microbiota. *Biochemical Journal*, 474(11) :1823–1836, May 2017.

[135] Edward S. Chambers, Tom Preston, Gary Frost, and Douglas J. Morrison. Role of gut microbiota-generated short-chain fatty acids in metabolic and cardiovascular health. *Current Nutrition Reports*, 7(4) :198–206, September 2018.

[136] Charles L. Bevins and Nita H. Salzman. Paneth cells, antimicrobial peptides and maintenance of intestinal homeostasis. *Nature Reviews Microbiology*, 9(5) :356–368, March 2011.

[137] C. Atuma, V. Strugala, A. Allen, and L. Holm. The adherent gastrointestinal mucus gel layer : thickness and physical state in vivo. *American Journal of Physiology-Gastrointestinal and Liver Physiology*, 280(5) :G922–G929, May 2001.

[138] Michael A. McGuckin, Sara K. Lindén, Philip Sutton, and Timothy H. Florin. Mucin dynamics and enteric pathogens. *Nature Reviews Microbiology*, 9(4) :265–278, March 2011.

[139] Gwladys Sevrin, Sébastien Massier, Benoit Chassaing, Allison Agus, Julien Delmas, Jérémy Denizot, Elisabeth Billard, and Nicolas Barnich. Adaptation of adherent-invasive e. coli to gut environment : Impact on flagellum expression and bacterial colonization ability. *Gut Microbes*, 11(3) :364–380, March 2018.

[140] Noëmie Daniel, Emelyne Lécuyer, and Benoit Chassaing. Host/microbiota interactions in health and diseases—time for mucosal microbiology ! *Mucosal Immunology*, 14(5) :1006–1016, September 2021.

[141] María García-Díaz, Maria del Mar Cendra, Raquel Alonso-Roman, María Urdániz, Eduard Torrents, and Elena Martínez. Mimicking the intestinal host–pathogen interactions in a 3d in vitro model : The role of the mucus layer. *Pharmaceutics*, 14(8) :1552, July 2022.

[142] Lucie Etienne-Mesmin, Benoit Chassaing, Mickaël Desvaux, Kim De Paepe, Raphaële Gresse, Thomas Sauvaitre, Evelyne Forano, Tom Van de Wiele, Stephanie Schüller, Nathalie Juge, and Stéphanie Blanquet-Diot. Experimental models to study intestinal microbes–mucus interactions in health and disease. *FEMS Microbiology Reviews*, 43(5) :457–489, June 2019.

[143] Lucie Gibold, Estelle Garenaux, Guillaume Dalmasso, Camille Gallucci, David Cia, Benoit Mottet-Auselo, Tiphanie Faïs, Arlette Darfeuille-Michaud, Hang Thi Thu Nguyen, Nicolas Barnich, Richard Bonnet, and Julien Delmas. The vat-AIEC protease promotes crossing of the intestinal mucus layer by crohn's disease-associated escherichia coli. *Cellular Microbiology*, 18(5) :617–631, November 2015.

[144] Héctor Ignacio Urra. *Bacteria swimming in complex fluids*. PhD thesis, Sorbonne Université, 2021.

[145] Bing Xia, Ruqing Zhong, Weida Wu, Chengzeng Luo, Qingshi Meng, Qingtao Gao, Yong Zhao, Liang Chen, Sheng Zhang, Xin Zhao, and Hongfu Zhang. Mucin o-glycan-microbiota axis orchestrates gut homeostasis in a diarrheal pig model. *Microbiome*, 10(1), August 2022.

[146] Eloïse Mussard, Corinne Lencina, Lise Gallo, Céline Barilly, Maryse Poli, Katia Feve, Mikael Albin, Laurent Cauquil, Christelle Knudsen, Caroline Achard, Guillaume Devailly, Laura Soler, Sylvie Combes, and Martin Beaumont. The phenotype of the gut region is more stably retained than developmental stage in piglet intestinal organoids. *Frontiers in Cell and Developmental Biology*, 10, August 2022.

[147] A.J. Libao-Mercado and C.F.M. de Lange. Refined methodology to purify mucins from pig colonic mucosa. *Livestock Science*, 109(1-3) :141–144, May 2007.

[148] Veronika J. Schömig, Benjamin T. Käsdorf, Christoph Scholz, Konstantinia Bidmon, Oliver Lieleg, and Sonja Berensmeier. An optimized purification process for porcine gastric mucin with preservation of its native functional properties. *RSC Advances*, 6(50) :44932–44943, 2016.

[149] Adrian-Marie Philippe, Luca Cipelletti, and Domenico Larobina. Mucus as an arrested phase separation gel. *Macromolecules*, 50(20) :8221–8230, 2017.

[150] Elisabeth E. L. Nyström, Beatriz Martinez-Abad, Liisa Arike, George M. H. Birchenough, Eric B. Nonnecke, Patricia A. Castillo, Frida Svensson, Charles L. Bevins, Gunnar C. Hansson, and Malin E. V. Johansson. An intercrypt subpopulation of goblet cells is essential for colonic mucus barrier function. *Science*, 372(6539), April 2021.

[151] Malin E. V. Johansson and Gunnar C. Hansson. *Preservation of Mucus in Histological Sections, Immunostaining of Mucins in Fixed Tissue, and Localization of Bacteria with FISH*, page 229–235. Humana Press, December 2011.

[152] T Maldiney, H Greigert, L Martin, E Benoît, C Creuzot-Garcher, PH Gabrielle, JM Chassot, C Boccara, D Balvay, B Tavitian, et al. L'oct plein champ, une nouvelle technique pour le diagnostic d'artérite à cellules géantes. *La Revue de Médecine Interne*, 41 :A59–A60, 2020.

[153] Domenico Larobina, Angelo Pommella, Adrian-Marie Philippe, Med Yassine Nagazi, and Luca Cipelletti. Enhanced microscopic dynamics in mucus gels under a mechanical load in the linear viscoelastic regime. *Proceedings of the National Academy of Sciences*, 118(45), November 2021.

[154] Justin T. Huckaby and Samuel K. Lai. Pegylation for enhancing nanoparticle diffusion in mucus. *Advanced Drug Delivery Reviews*, 124 :125–139, January 2018.

[155] Milad Radiom, Romain Hénault, Salma Mani, Aline Grein-Iankovski, Xavier Norel, and Jean-François Berret. Microrheological study of human respiratory mucus. In *Mucus, Cilia and Mucociliary Interactions*, 2023.

[156] Paulo H. Michels-Brito, Volodymyr Dudko, Daniel Wagner, Paul Markus, Georg Papastavrou, Leander Michels, Josef Breu, and Jon Otto Fossum. Bright, noniridescent structural coloration from clay mineral nanosheet suspensions. *Science Advances*, 8(4), January 2022.

[157] Benjamin Midtvedt, Saga Helgadottir, Aykut Argun, Jesús Pineda, Daniel Midtvedt, and Giovanni Volpe. Deeptrack 2.0, 2020.

[158] TensorFlow Developers. Tensorflow. *Zenodo*, 2022.

[159] Frank Cichos, Kristian Gustavsson, Bernhard Mehlig, and Giovanni Volpe. Machine learning for active matter. *Nature Machine Intelligence*, 2(2) :94–103, February 2020.

[160] Declan J. Armstrong, Timo A. Nieminen, Itia Favre-Bulle, Alexander B. Stilgoe, Isaac C. D. Lenton, Mark A. Schembri, and Halina Rubinsztein-Dunlop. Optical force measurements illuminate dynamics of escherichia coli in viscous media. *Frontiers in Physics*, 8, October 2020.

[161] Pierre Marquet, Benjamin Rappaz, Pierre J. Magistretti, Etienne Cuche, Yves Emery, Tristan Colomb, and Christian Depeursinge. Digital holographic microscopy : a noninvasive contrast imaging technique allowing quantitative visualization of living cells with subwavelength axial accuracy. *Optics Letters*, 30(5) :468, March 2005.

[162] K.M. Taute, S. Gude, S.J. Tans, and T.S. Shimizu. High-throughput 3d tracking of bacteria on a standard phase contrast microscope. *Nature Communications*, 6(1), November 2015.

[163] Howard C. Berg. How to track bacteria. *Review of Scientific Instruments*, 42(6) :868–871, June 1971.

[164] Zijie Qu, Fatma Zeynep Temel, Rene Henderikx, and Kenneth S. Breuer. Changes in the flagellar bundling time account for variations in swimming behavior of flagellated bacteria in viscous media. *Proceedings of the National Academy of Sciences*, 115(8) :1707–1712, February 2018.

[165] Linda Turner, Liam Ping, Marianna Neubauer, and Howard C. Berg. Visualizing flagella while tracking bacteria. *Biophysical Journal*, 111(3) :630–639, August 2016.

[166] Anat Lipovsky, Yeshayahu Nitzan, Aharon Gedanken, and Rachel Lubart. Visible light-induced killing of bacteria as a function of wavelength : Implication for wound healing. *Lasers in Surgery and Medicine*, 42(6) :467–472, July 2010.

[167] Tatyana Perlova, Martin Gruebele, and Yann R Chemla. Blue light is a universal signal for escherichia coli chemoreceptors. *Journal of bacteriology*, 201(11) :10–1128, 2019.

[168] MacKay David J C. *Information theory, Inference, and learning algorithms*. Cambridge University Press, 2019.

[169] Benjamin Midtvedt, Jesús Pineda, Fredrik Skärberg, Erik Olsén, Harshith Bachimanchi, Emelie Wesén, Elin K. Esbjörner, Erik Selander, Fredrik Höök, Daniel Midtvedt, and Giovanni Volpe. Single-shot self-supervised object detection in microscopy. *Nature Communications*, 13(1), December 2022.

[170] Jeffrey Kodosky. Labview. *Proceedings of the ACM on Programming Languages*, 4(HOPL) :1–54, 2020.